

**GEOLOGICAL SURVEY OF FINLAND**

**Bulletin 404**

**2010**



**The Koillismaa Intrusion, northeastern Finland –  
evidence for PGE reef forming processes in the layered series**

Tuomo Karinen

**Geological Survey of Finland, Bulletin 404**

**THE KOILLISMAA INTRUSION, NORTHEASTERN FINLAND  
– EVIDENCE FOR PGE REEF FORMING PROCESSES IN THE  
LAYERED SERIES**

by

TUOMO KARINEN

with 176 pages, 90 figures, 22 tables and 1 appendix CD

ACADEMIC DISSERTATION

To be presented, with permission of the Faculty of Science, University of Oulu,  
for public criticism in the Auditorium GO101 of the Department of Geosciences,  
Linnanmaa, on February 12<sup>th</sup>, 2010, at 12 o'clock noon.

GEOLOGICAL SURVEY OF FINLAND  
ESPOO 2010

**Karinen, T. 2010.** The Koillismaa Intrusion, northeastern Finland – evidence for PGE reef forming processes in the layered series. *Geological Survey of Finland, Bulletin 404*, 176 pages, 90 figures, 22 tables and data CD as an appendix.

The 2440 Ma old Koillismaa Intrusion, located in northeastern Finland, forms the westernmost part of the Koillismaa-Näränkäväära Layered Igneous Complex. The intrusion originally formed an extensive sheet-like body that has been later tectonically dismembered into several blocks. The cumulate stratigraphy of the intrusion is divided into Marginal Series and Layered Series. The Marginal Series is up to 200 m thick and consists of gabbroic cumulates at the base that are overlain by progressively more magnesian rocks including pyroxenites and peridotites. The Layered Series is composed mostly of gabbroic cumulates. Its stratigraphic thickness in different intrusive blocks ranges from 1000 to 3000 m.

The Marginal Series includes contact-type base metal sulphide- and platinum group element mineralization, which contains up to 0.9 wt. % Cu, 1.1 wt. % Ni and 4.3 ppm Au+Pd+Pt. Palladium contents are significantly higher than Pt contents, resulting in a Pd/Pt ratio of 2.8. The average Cu/Ni ratio in the sulphide fraction of the Marginal Series is 1.3.

At present, only one PGE-Cu-Ni sulphide mineralized layer that is referred to as the Rometölväs Reef is known from the Layered Series. In the stratigraphic sequence of the Koillismaa Intrusion, this layer is marked by the appearance of cumulus clinopyroxene and inverted pigeonite and the disappearance of cumulus bronzite. The reef shows a close spatial relationship with small, 1-6 m thick, noncumulus-textured gabbroic bodies. These bodies can be considered as essential part of the reef, because the highest PGE grades (up to 0.3 wt. % Cu and 0.3 wt. % Ni and 1 ppm of Au+Pd+Pt) are found in sulphide-bearing portion of one noncumulus-textured gabbroic body. The mineralized cumulates surrounding these bodies typically have a mottled appearance due to small, up to 3 cm sized clusters of sulphide and low-temperature minerals that host a significant portion of the mineralization. The mottled cumulates of the reef contain up to 0.9 wt. % Cu, 0.3 wt. % Ni and 0.6 ppm of Au+Pd+Pt. The Pd/Pt ratios in both cumulates and noncumulate bodies are close to 1.0. The average Cu/Ni ratio in the sulphide fraction of the mottled cumulates is 4.1.

It is concluded that the origin of the mineralization of the Rometölväs Reef was triggered by emplacement of dykes of a new magma pulse into partially consolidated cumulates of the Koillismaa Intrusion. These dykes are presently represented by the noncumulus-textured gabbroic bodies of the reef. The stratigraphic level of the Koillismaa Intrusion at which bronzite gave way to inverted pigeonite and augite was the most favorable place for these dykes. The intruding magma was more primitive than that of the parental magma of the Koillismaa Intrusion and was saturated with ore-bearing fluid phase escaped from the magma upon emplacement in the form of late magmatic fluids, introducing PGE-Cu-Ni into host cumulates and recrystallizing them into mottled varieties. Sudden loss of volatiles from the intruding magma resulted in its supersaturation and related rapid crystallization to form the noncumulus-textured gabbroic bodies.

Keywords (GeoRef Therasaurus, AGI): layered intrusions, lithostratigraphy, igneous rocks, mineralogy, geochemistry, platinum group, copper, nickel, isotopes, Sm/Nd, genesis, magmatism, Paleoproterozoic, Koillismaa, Finland

*Tuomo Karinen  
Geological Survey of Finland  
P.O. Box 77  
FI-96101 Rovaniemi  
Finland*

*E-mail: [tuomo.karinen@gtk.fi](mailto:tuomo.karinen@gtk.fi)*

ISBN 978-952-217-092-7 (paperback)  
ISBN 978-952-217-093-4 (PDF)  
ISSN 0367-522X

Dedicated to the memory of  
Tuomo Alapieti  
(1946–2007)

## CONTENTS

1	INTRODUCTION .....	9
2	REVIEW OF PGE MINERALIZATION MODELS IN LAYERED INTRUSIONS .....	12
	2.1 Orthomagmatic models .....	13
	2.2 Orthomagmatic-metasomatic models .....	15
	2.3 Metasomatic models .....	16
3	MATERIALS AND METHODS .....	16
	3.1 Mapping and sampling .....	16
	3.2 Analytical techniques .....	17
	3.2.1 Mineral analyses.....	17
	3.2.2 Major and trace element analyses .....	19
	3.2.3 Sm-Nd isotope analyses .....	20
	3.3 Grain size and modal abundance of rock-forming minerals .....	21
	3.4 Nomenclature .....	22
4	GEOLOGICAL SETTING AND STRUCTURE OF THE KOILLISMAA INTRUSION .....	24
5	STRATIGRAPHY AND PETROGRAPHY .....	29
	5.1 Stratigraphic subdivision of the Koillismaa Intrusion .....	29
	5.2 Lotanvaara mafic rock unit .....	32
	5.3 Chilled margins .....	33
	5.4 Marginal Series and related PGE-mineralized layers.....	33
	5.5 Layered Series .....	35
	5.5.1 Lower Zone .....	35
	5.5.2 Middle Zone .....	37
	5.5.3 Upper Zone.....	38
	5.6 Granophyre.....	38
	5.7 Noncumulus-textured gabbro-norite bodies .....	38
	5.8 Rometölväs Reef .....	46
	5.8.1 Rometölväs.....	47
	5.8.2 Baabelinälkky.....	47
	5.8.3 Lanttioja .....	47
	5.8.4 Väливаара and Mustavaara.....	52
	5.8.5 Distribution of variably mottled cumulates in the sampling sites.....	52
	5.9 Summary.....	52
6	MINERALS AND MINERAL CHEMISTRY .....	54
	6.1 Silicates.....	54
	6.1.1 Olivine.....	54
	6.1.2 Pyroxenes .....	54
	6.1.2.1 Noncumulate rocks .....	55

6.1.2.2	Cumulate rocks .....	55
6.1.2.3	Solidus compositions of the pyroxenes in cumulate rocks .....	62
6.1.2.4	Compositional differences between the pyroxenes in the noncumulate and cumulate rocks.....	64
6.1.3	Feldspars .....	64
6.1.3.1	Noncumulate rocks .....	64
6.1.3.2	Cumulate rocks .....	66
6.1.4	Other silicate minerals.....	68
6.1.4.1	Amphibole group.....	68
6.1.4.2	Epidote group.....	69
6.1.4.3	Scapolite group .....	71
6.1.4.4	Phlogopite-biotite .....	71
6.1.4.5	Chlorite .....	71
6.2	Oxides.....	72
6.2.1	Spinel group .....	72
6.2.2	Ilmenite .....	74
6.3	Accessory silicates and oxides .....	75
6.3.1	Garnet.....	75
6.3.2	Loveringite .....	76
6.3.3	Rutile, pseudobrookite, zircon and baddeleyite .....	80
6.4	Phosphates .....	81
6.4.1	Apatite .....	81
6.5	Sulphides .....	82
6.6	Altaite, tellurobismutite and undefined Ni-Te-S mineral .....	83
6.7	PGE-, gold- and silver-bearing minerals .....	84
6.8	Summary.....	90
7	WHOLE-ROCK CHEMISTRY.....	90
7.1	Major and trace elements.....	90
7.1.1	Chilled margins and the weighted average composition of the Koillismaa Intrusion.....	90
7.1.2	Lotanvaara mafic rock unit and noncumulus-textured gabbro-norite bodies ..	95
7.1.3	Marginal Series, Layered Series and granophyre.....	103
7.2	Chalcophile elements.....	113
7.2.1	Marginal Series .....	113
7.2.2	Rometölväs Reef.....	113
7.2.3	Compositions of the sulphide fractions of the Marginal Series and the Rometölväs Reef.....	121
7.2.4	Chondrite- and mantle-normalized multi element patterns of the sulphide fraction of the Marginal Series and the Rometölväs Reef.....	124
7.3	Summary.....	128
8	SM-ND ISOTOPE CHEMISTRY .....	129
8.1	General features of the Sm-Nd isotopic systematics.....	129
8.2	Age determinations.....	133
8.3	Summary.....	136

9	CONDITIONS OF CRYSTALLIZATION IN THE KOILLISMAA INTRUSION.....	137
9.1	Pyroxene thermometer.....	137
9.2	Magnetite-ilmenite equilibrium.....	139
9.3	Summary.....	143
10	PARENTAL MAGMA OF THE KOILLISMAA INTRUSION.....	143
10.1	Methods to estimate parental magma composition .....	143
10.2	Estimation of the Koillismaa Intrusion parental magma composition .....	144
10.3	Summary.....	147
11	DISCUSSION AND CONCLUSIONS .....	150
11.1	Differentiation in the Koillismaa Intrusion .....	150
11.2	Noncumulus-textured bodies of the Koillismaa Intrusion.....	151
11.2.1	Review of the origin of noncumulus-textured igneous rocks.....	151
11.2.2	The origin of noncumulus-textured bodies of the Koillismaa Intrusion .....	151
11.3	Genetic aspects on the Rometölväs Reef.....	155
11.4	Genetic model of the Rometölväs Reef.....	158
12	ACKNOWLEDGEMENTS.....	162
13	REFERENCES .....	163
APPENDIX: DATA CD		



## 1 INTRODUCTION

The early Palaeoproterozoic (2500–2400 Ma) was a time of worldwide igneous activity, resulting in the formation of layered intrusions, mafic dyke swarms and volcanic formations on the cratonic areas of the Earth. These include the Jimberlana Intrusion (McClay & Campbell 1976) and the Widgiemooltha Dyke Suite (Compston & Arriens 1968; Glikson 1996) of the Yilgarn Block, the Hearst-Matachewan Dyke Swarm (Heaman 1988) and the East Bull Lake suite intrusions and supracrustal formations (Krogh et al. 1984) in the Superior Province of the Canadian Shield, the Scourie Mafic Dykes (Heaman & Tarney 1989) in Scotland, the dykes of the Dharwar Craton of the Indian Shield (Ikramuddin & Steuber 1976; Halls et al. 2007) and the mafic dyke swarms in the Vestfold Block and the Napier Complex of the East Antarctic Shield (Collerson & Sheraton 1986; Sheraton & Black 1981). The same igneous activity is also recorded in the Fennoscandian Shield, in the form of several layered intrusions, dykes and volcanic formations of different composition (Bogdanova & Bibikova 1993; Vuollo 1994; Amelin et al. 1995; Buiko et al. 1995; Puchtel et al. 1996, 1997; Balagansky et al. 1998, 2001; Manninen et al. 2001; Alapieti & Lahtinen 2002; Lauri & Mänttari 2002; Iljina & Hanski 2005).

This thesis deals with the early Palaeoproterozoic Koillismaa Intrusion of the Koillismaa-Näränkäväära Layered Igneous Complex, which is located in northeastern Finland, ca. 150 km northeast of the city of Oulu. The complex, which is referred to as the Koillismaa-Näränkäväära Complex, belongs to a group

of approximately twenty early Palaeoproterozoic mafic-ultramafic layered intrusions (Fig. 1.1). The Koillismaa-Näränkäväära Complex was dated by the U-Pb method on zircon to be  $2436 \pm 5$  Ma old (Alapieti 1982), which is close to the average age of all Fennoscandian early Palaeoproterozoic layered intrusions (2440 Ma, Alapieti & Lahtinen 2002). Appendices 1 and 2 include age data of these intrusions. According to Amelin et al. (1995) their magmatism occurred in two short episodes at 2505–2501 Ma and at 2449–2441 Ma.

The Koillismaa-Näränkäväära Complex comprises the Näränkäväära Intrusion, the Koillismaa Intrusion and a strong positive gravity anomaly, which connects these distant eastern and western parts of the complex (Fig. 1.2). The Näränkäväära Intrusion is surrounded by Archaean rocks. According to Alapieti (1982) the exposed Layered Series of the intrusion is ca. 1000 m thick, comprising an ultramafic lower and a mafic upper part. The margin of the intrusion is exposed in its north-western part where the rocks are composed of heterogeneous and altered gabbros. The strong positive gravity anomaly, which in this study is referred to as the connecting gravity anomaly zone or simply the connecting zone, is traceable on surface level by a narrow breccia zone. The anomaly has been interpreted to reflect the location of a dyke or layered intrusion that acted as a feeder zone for the Koillismaa Intrusion magmas (Piiirainen et al. 1978; Alapieti 1982; Iljina 2004). Alternatively, it could reflect the presence of mafic rocks belonging to the Archaean greenstone belt (T. Halkoaho, personal communication).

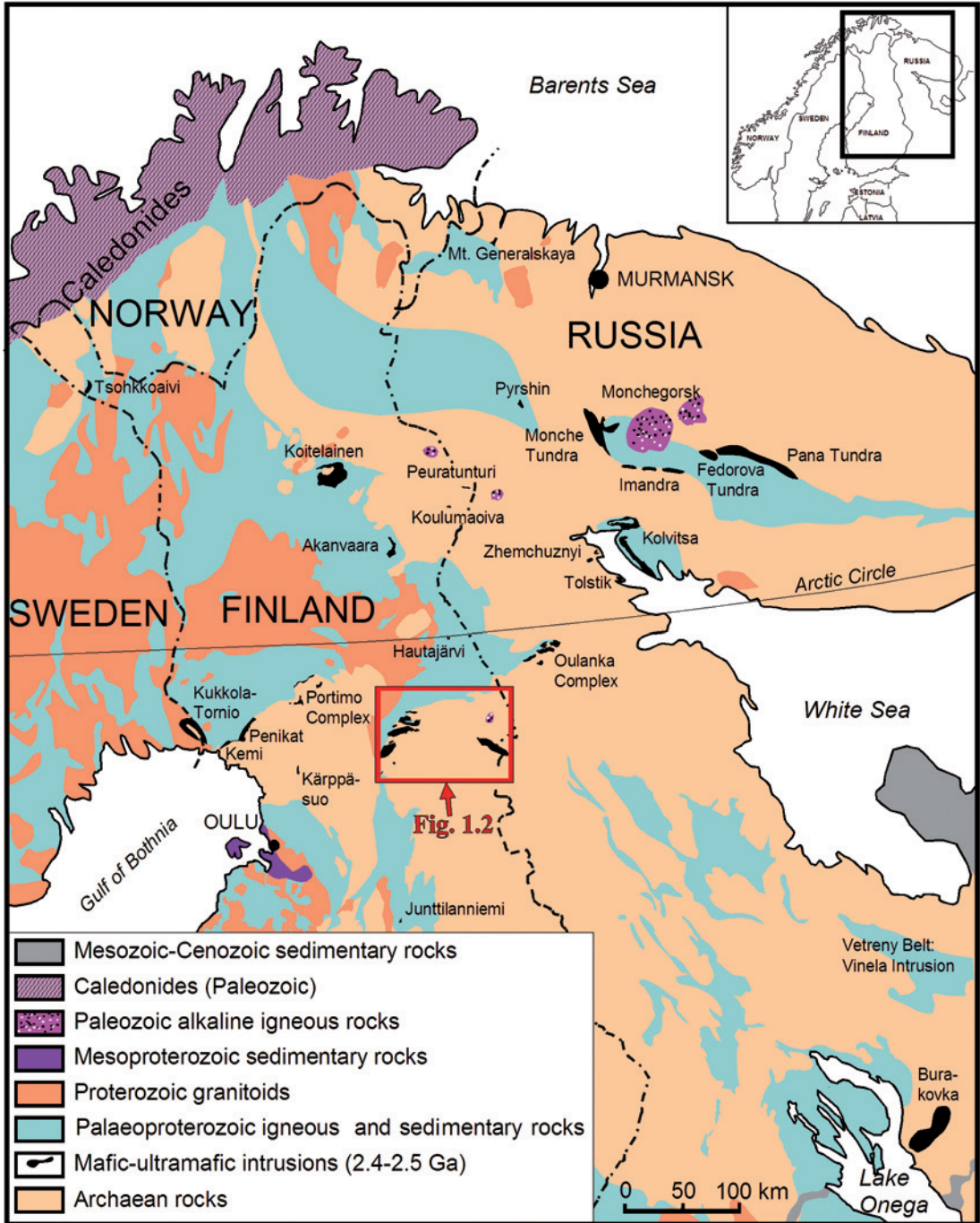


Fig. 1.1. Generalized geological map of the northeastern part of the Fennoscandian Shield, showing the locations of early Palaeoproterozoic mafic-ultramafic intrusions (modified from Alapieti et al. 1990 and Alapieti & Lahtinen 2002).

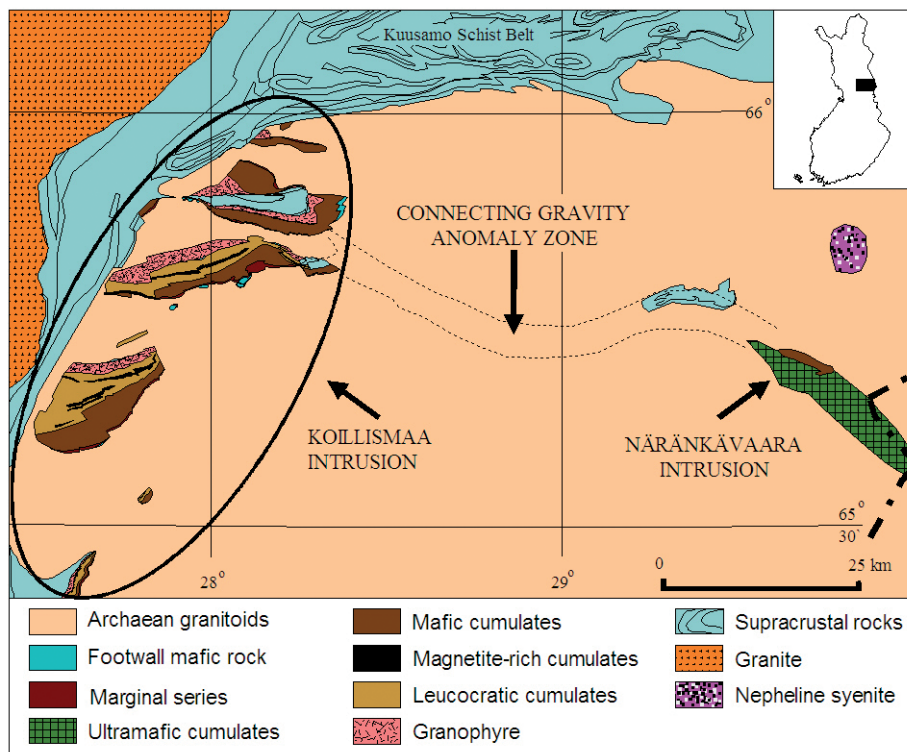


Fig. 1.2. Generalized geological map of the Koillismaa-Näränkäväära Complex (modified from Piirainen et al. 1978 and Alapieti 1982).

The Koillismaa Intrusion consists of separate bodies, which originally were considered to be the youngest rocks of the area and were envisaged to form separate sills (Enkovaara et al. 1953; Väyrynen 1954). However, Ohejola (1968) suggested that the bodies represent blocks of a single, sheet-like layered intrusion. Piirainen et al. (1974, 1978) proposed that the magma that formed this sheet-like intrusion was emplaced between the Archaean basement and supracrustal rocks.

The basement immediately below the Koillismaa Intrusion appears to have been partially melted and metasomatically altered to form a greyish coloured albite-quartz rock, which can be traced along the basal contact of all the segments of the intrusion. The rocks above the intrusion were considered by Piirainen et al. (1974, 1978), Juopperi (1976), Kerkkonen (1976) and Alapieti et al. (1979) to represent

mainly acid lavas below which the Koillismaa Intrusion crystallized. Due to their textural similarities to the granophyres of the Skaergaard intrusion and the Sudbury Complex, Alapieti (1982) renamed these rocks granophyre and included them into the Koillismaa-Näränkäväära Complex as a unique part of the complex. In some segments of the intrusion the granophyre is overlain by supracrustal rocks that may be correlated with the lowermost formations of the Kuusamo Schist Belt (Karinen 1998).

The Koillismaa Intrusion is divided into a Marginal Series and a Layered Series. The former is up to 200 m thick and contains base metal sulphide- and platinum-group element (PGE) mineralization. It displays a distinct basal reversal in that the cumulates grade upwards in the stratigraphy from gabbroic to ultramafic rocks. The Layered Series compris-

es mainly gabbroic cumulates and is between 1000 and 3000 m thick. In the upper part of the Layered Series, there is a layer of magnetite gabbro representing the only ore deposit that has been mined to date in the Koillismaa Intrusion (Mustavaara Vanadium Mine) (Alapieti 1982; Juopperi 1977).

The Layered Series has generally not been regarded as a potential target for significant PGE-Cu-Ni mineralization. Therefore, it has never been drilled completely, although extensive grab sampling was performed. Starting from the late 1960s, irregularly distributed sulphide- and PGE-enriched rocks were found in the middle part of the Layered Series in two blocks of the intrusion. A typical feature of these mineralized areas is the oc-

currence of a meter-sized noncumulus-textured, mostly fine-grained gabbro-noritic bodies hosted by sulphide-bearing pegmatitic or mottled gabbro-noritite. The noncumulus-textured bodies have been interpreted as dykes (Isohanni 1976; Piispanen & Tarkian 1984) or as xenoliths (Mutanen 1997; Iljina et al. 2001; Iljina & Hanski 2005).

The aim of the present thesis is to decipher the genesis of the aforementioned mineralization of the Koillismaa Intrusion. As the sulphide- and PGE-enriched cumulates are associated with noncumulus-textured bodies and are located in the middle part of the Layered Series, special attention is paid to the chemical and lithological stratigraphy of the Koillismaa Intrusion.

## 2 REVIEW OF PGE MINERALIZATION MODELS IN LAYERED INTRUSIONS

The models explaining the formation of PGE-enriched occurrences in layered intrusions, and especially the models of the reef-type deposits, generally fall into two main categories: orthomagmatic and metasomatic. The principal argument for an orthomagmatic origin of these occurrences is that the PGE reefs are typically associated with sulphides or oxides in thin, kilometer-long horizons or layers that define major petrological changes in the layered sequence and that show laterally broadly constant grades despite being underlain by footwall rocks of variable thickness (Crocket et al. 1976; Kruger & Marsh 1982, 1985; Todd et al. 1982; Campbell et al. 1983; Sharpe 1985; Naldrett et al. 1986). The orthomagmatic model involves primary magmatic immiscible sulphide liquid separation or chromite precipitation related to mixing of compositionally distinct magmas or contamination of magma. The most favourable situation for the formation of a PGE-rich reef is when the dense immiscible sulphide

melt or chromite grains can equilibrate with large amounts of silicate magma to effectively scavenge noble metals from the magma. This process is favoured by very high sulphide melt/silicate melt and chromite/silicate melt partition coefficients for the PGEs.

Several features of the PGE reefs have led some researchers to propose that the PGE were concentrated by metasomatic processes. These include the close association of pegmatitic textures, Cl-rich hydrous minerals and graphite with some reefs. Another indication of metasomatic origin is that the noble metal phases are rarely located within sulphide or oxide grains or at their boundaries, but are located mostly around the sulphides, e.g. in hydrous Cl-rich silicates. (Stumpfl 1974; Ballhaus & Stumpfl 1986; Stumpfl & Ballhaus 1986; Boudreau et al. 1986; Volborth et al. 1986; Ballhaus et al. 1988; Boudreau 1988; Boudreau & McCallum 1989; Hanley et al. 2005). The metasomatic model is consistent with several experimental studies that

found elevated solubility of Pt and Pd in hydrothermal fluids, e.g. by Mountain & Wood

(1988), Wood et al. (1989) and Gammons et al. (1992).

## 2.1 Orthomagmatic models

Campbell et al. (1983) developed a model in which PGE enrichment in layered intrusions is related to turbulent mixing between resident magma in the chamber and replenishing magmas. Depending on the density differences between the magmas and the momentum of the injection, new magma may spread out and hybridize with resident magma at any stratigraphic level in the magma chamber. The hybrid magma becomes supersaturated in an immiscible sulphide liquid and in chromite and the dense sulphide and chromite accumulate on top of the cumulate pile. The most advantageous scenario is one whereby the new pulse is lighter than the resident magma, or when the new pulse enters with sufficient momentum to form a magma fountain in the overlying lighter magma.

Several authors have suggested that two compositionally different parental magma types were involved in the genesis of the PGE reefs of the Stillwater and Bushveld Complexes (Irvine & Sharpe 1982; Kruger & Marsh 1982; Todd et al. 1982; Lambert & Simmons 1983; Longhi et al. 1983; Sharpe & Hulbert 1985; Lambert et al. 1989). The first magma type was a relatively PGE-enriched, but S-poor orthopyroxene-normative siliceous high-magnesian basalt and closely resembled modern boninites, while the second type was a less PGE-enriched, but S-saturated olivine-normative tholeiite. The two magma types have been termed U-type (ultramafic) and A-type (anorthositic) magma, respectively. Hamlyn et al. (1985) and Hamlyn & Keays (1986) suggested that boninites have less than 54 ppm sulphur but as much as 15 ppb Pd (for comparison, the averages of MORB are 800 ppm S and 0.83 ppb Pd). According to Hamlyn &

Keays (1986) magmas generated by low to moderate degrees of partial melting of fertile mantle cannot dissolve all the sulphide in the mantle and therefore leave a small amount of sulphide melt in the melting residue. Due to the high partition coefficients of noble metals into sulphide liquid, the residue is relatively PGE-rich. Second-stage magmas derived by further partial melting of the depleted mantle can dissolve the PGE-rich residual sulphides and therefore may be PGE-enriched yet S-undersaturated. Upon final emplacement of the magma sulphide saturation is triggered by mixing of the U- and A-type magmas.

In the case of the Bushveld Complex, Sharpe (1985) suggested that sulphide saturation was triggered by a large injection of relatively hot A-type magma into density-stratified magma chamber of U-type magma, which resulted in mixing of these two types of magma to form the Main Zone of the complex. Hatton (1989) suggested that the replenishing A-type magma was cooler and denser than the U-type magma in the chamber. This caused the U-type magma to become displaced towards the top of the magma chamber where a hybrid layer was generated. A further large pulse of A-type magma responsible for the Main Zone cooled the overlying hybrid magma and induced saturation in an immiscible sulphide. Sulphide liquid droplets and orthopyroxene crystals formed slurries that sank through the underlying magma to the top of the cumulate pile where they formed the Merensky Reef.

Maier et al. (2003) described magnetite-hosted PGE reefs in the Stella layered intrusion, South Africa. According to Maier et al. (2003), sulphide saturation in the Stella intrusion was reached in response to magnetite

crystallization that lowered the  $\text{Fe}^{2+}$  activity in the residual magma. The Stella intrusion reefs are poor in sulphur, which Maier et al. (2003) explained by late-magmatic reaction of FeS and  $\text{Fe}_2\text{O}_3$  to form magnetite and gaseous sulphur, or alternatively by sulphide resorption by late-magmatic fluids. The formation of Stella-type PGE reefs requires a PGE-rich and sulphide-undersaturated parental magma, a lack of contamination that would lead into early sulphide saturation, and a tholeiitic Fenner-type crystallization trend.

The models of Scoon & Teigler (1994) and Kruger et al. (2002) emphasize the role of chromite in the genesis of the PGE mineralization of the UG-2 and Merensky Reef of the Bushveld Complex. In these models, the magma becomes saturated in platinum-group minerals which are collected by and incorporated into chromite grains in hybrid zones of the magma chamber. Scoon & Teigler (1994) suggested that chromite saturation in the Bushveld magma chamber was achieved by lateral mixing of replenishing A-type magma with residual U-type magma. According to the model of Kruger et al. (2002), the pulses of the new magma were fountains of A-type magma that interacted with the granophyric roof rocks of the magma chamber. The magma fountains became contaminated with silica which caused precipitation of chromite. When the contaminated magma fountain collapsed a hybrid zone of U- and A-type magma was formed on top of the cumulate pile. Small grains of platinum-group minerals were collected by and incorporated into chromite in the hybrid zone.

Following the idea of two-phase convection originally suggested by Grout (1918) and later significantly reintroduced to petrology by Morse (1986a, b, 1988) and Brandeis & Jaupart (1986), Mutanen (1997) and Rice (2002) proposed a model of PGE enrichment by roof contamination in a single-pulse mag-

ma chamber. Rice (2002) explained the isotopic features of the Bushveld Complex with the effect of two-phase convection that served to split the magma chamber into a number of density-stratified layers. When crystal-bearing liquid packets slumped as density flows to the bottom part of the magma chamber, the hot residual liquid was forced upwards to replenish the heat flux to the roof zone. Therefore, in the initial stage of convection in the magma chamber, there was relatively insignificant contamination, but as the roof was continuously heated by residual magma, roof assimilation became more significant. Later, due to the cooling of the residual magma and probably because the roof had stripped off its low-melting components, the effect of assimilation decreased. Eventually, the lowermost parts of the magma chamber became compositionally closest to the parental magma, the middle ones became most significantly contaminated and the uppermost ones to possess a contamination level between that of the lower and intermediate areas of the intrusion. Contamination accounted for chromite and sulphide precipitation in the upper part of the magma chamber, below which the sulphide liquid and chromite grains collected PGEs from the magma to form the Merensky Reef on the cumulate pile. The model of Mutanen (1997) is similar to that of Rice (2002), but at least in the Keivitsa intrusion case he emphasized the role of Cl-bearing minerals in the genesis of PGE enrichments. Mutanen (1997) proposed that halogens derived from roof sediments of the magma chamber can form melt-soluble complexes with PGE, and when the complexes become unstable, PGEs can be liberated and associate with sulphide or oxide grains. Mutanen (1997) emphasized that the enrichment of PGEs is a mechanical rather than a chemical process, because PGE grains tend to be located at the grain boundaries of sulphides.

## 2.2 Orthomagmatic-metasomatic models

Vermaak (1976) and Von Gruenevaldt (1979) proposed a model for the genesis of the Merensky Reef, in which intercumulus liquids enriched in PGE were expelled during cumulate compaction and precipitated PGE on pre-existing magmatic sulphides at the reef horizon. Page et al. (1982) suggested that stratiform sulphides in the J-M Reef of the Stillwater Complex were orthomagmatic in origin, but that the sulphide liquid collected PGE from fluid-enriched intercumulus liquid that percolated upwards through cumulate pile during the compaction and adcumulus growth of the postcumulus phases.

Iljina (1994) proposed a genetic model for the PGE deposits of the Portimo Complex, suggesting that PGE-enriched sulphide liquid formed as an immiscible melt close to the margins of the intrusion but was later partially or totally dissolved in a Cl-bearing fluid to become precipitated some distance away from the site of the first sulphide segregation.

According to Halkoaho et al. (1990a, 2005) and Halkoaho (1993) the source of the PGEs of the SJ Reef of the Penikat Intrusion was the volatile- and fluid-enriched portion of residual liquid derived from Cr-rich magmas with a boninitic affinity (Megacyclic Units I-III of the intrusion). This residual liquid mixed with younger Cr-poorer magma pulses (Megacyclic Units IV-V of the intrusion), which were of tholeiitic lineage. The mixing occurred in a hybrid zone between these compositionally different magmas. Willmore et al. (2000) suggested an analogous model for the Merensky Reef of the Bushveld Complex. According to this model, sulphur-, volatile-, and Pt-Pd-enriched fluids escaped from the solidifying and compacting cumulate pile. The upward migrating fluids mixed with fluid-undersaturated intercumulus magma higher up in the cumulate pile. The fluids were dissolved in the magma and PGE precipitated. The sul-

phides were upgraded by successive waves of S-undersaturated fluids.

Latypov et al. (2008a, b) developed a concept of gravity-independent mineralization process to explain the Cu-Ni-PGE mineralization associated with the sill-like, fine-grained gabbro-norite bodies in the central part of the Lukkulaivaara intrusion, Russia. In this deposit, the ore components occur predominantly in association with anorthosite along the margins of the bodies and in pegmatitic segregations within the bodies. Latypov et al. (2008a, b) proposed that the sill-like bodies represent conduits in semi-consolidated magma chamber through which a large volume of magma passed through towards the overlying resident magma. The mineralization formed in response to local sulphide saturation along the conduit margins as a result of a flux of ore-bearing fluids from the conduit interior towards the margins. The transfer of ore-bearing fluids was attributed to a combination of a high internal volatile pressure and thermodiffusion forcing the fluids to move outwards from the interior of the conduit. The important point in the model is that initially the sulphides at the conduit borders were poor in PGEs, but became PGE-rich due to interaction with a large volume of magma and ore-bearing fluids passing through the conduits.

The model of Latypov et al. (2008a, b) shows some similarities to the hypothesis of Isohanni (1976) explaining the origin of the PGE mineralized occurrence in the Koillismaa Intrusion. Isohanni (1976) interpreted the noncumulus-textured gabbro-norite bodies as dykes, and assumed that their magma was relatively rich in volatile components when it intruded into the partially consolidated magma chamber of the Koillismaa Intrusion. During intrusion, the volatile phase escaped from the dykes to the surrounding cumulates. This resulted in local increase in oxygen fugacity of

the intercumulus melt causing crystallization of titanomagnetite. The resulting decrease in the iron content in the intercumulus melt caused local sulphide saturation in the cumu-

lates and along the dyke contacts. Isohanni (1976) assumed that the ore components in the mineralized occurrence were derived from the layered intrusion rather than from the dykes.

### 2.3 Metasomatic models

Perhaps the first to propose a purely metasomatic origin for PGE reefs was Lauder (1970) who suggested that an impervious layer may trap hydrothermal solutions at a late stage of crystallization. This could, for example, account for the pegmatitic nature of the Merensky Reef. Schiffries (1982) and Stumpfl & Rucklidge (1982) elaborated this idea further and interpreted the highly mineralized dunitic pipes (Driekop, Mooihoek and Onverwacht) of the Bushveld Complex as conduits of late-stage, upward percolating hydrothermal solutions, which became trapped by an impervious layer to form the Merensky Reef. Both Schiffries (1982) and Stumpfl & Rucklidge (1982) supposed that the PGEs deposited in these pipes were leached from the basal cumulates by hydrothermal solutions, but the former supposed that these solutions were derived from the country rocks, while the latter suggested them to be derived by the separation of an aqueous phase from the magma.

Boudreau & McCallum (1986) used the idea of Lauder (1970) to explain the genesis of the Picket-Pin deposit, which is located in the

Anorthosite Subzone II, the upper part of the Middle Banded Series of the Stillwater Complex. Boudreau & McCallum (1986) suggested that the monomineralic, medium-grained anorthosite member in the subzone acted as an impermeable zone trapping migrating HCl-, HF- and PGE-bearing fluids at its lower contact. The model of Mathez (1995) and Mathez et al. (1997) is similar to that of Boudreau & McCallum (1986), but with the exception that the principal PGE transporting medium is assumed to be upward percolating hydrous and incompatible element-enriched interstitial liquids rather than hydrothermal solutions.

Following the idea of Lauder (1970), Boudreau & McCallum (1992) proposed that chlorine-bearing hydrothermal solutions, exsolved from the underlying cumulate pile, could leach and transport upward minor amounts of sulphur and PGE present in cumulates of the intrusion. The noble metals can then precipitate at any stratigraphic physicochemical discontinuity such as changes in the fluid saturation temperature of the intercumulus liquid.

## 3 MATERIALS AND METHODS

### 3.1 Mapping and sampling

Most of the samples for this thesis were collected during 1999–2003 in the course of the Geological Survey of Finland (GTK) project “Layered Igneous Complexes in Northern

Finland”. During the field work, several profiles were mapped and sampled in different blocks of the intrusion to compare their igneous stratigraphy. The profile in one of the

central blocks of the intrusion is used in this research to establish the general stratigraphic sequence of the Koillismaa Intrusion. The profile also offered a comparison with the studies of Mäkelä (1975) and Alapieti (1982) who both used samples of the same area. When constructing the stratigraphic column of the intrusion, the dip of the layering and some fault zones were taken into account. Furthermore, distinct lower and upper contact zones of the intrusion were mapped in order to locate possible chilled margins. A further

mapping and sampling target were the noncumulus-textured gabbro-norite bodies and related sulphide- and PGE-mineralized occurrences in the Layered Series. The area was mainly studied using outcrops. In addition, two drill cores of the “Koillismaa Research Project” (1971–1976) of the University of Oulu were re-logged and sampled in detail. In these cores the sampling interval for cumulates was ca. 1 m, but for one relatively large noncumulate-textured gabbro-norite body, the sampling interval was smaller, ca. 20 cm.

### 3.2 Analytical techniques

#### 3.2.1 Mineral analyses

Petrographic studies were carried out using ca. 800 polished thin sections, of which ca. 250 were chosen for mineral analyses.

Altogether 2401 quantitative wavelength dispersive spectrometer (WDS) analyses on minerals were carried out using an electron microprobe. Of these 2357 were made at the Institute of Electron Optics, University of Oulu, with electron microprobes JEOL JCSA 733 and JEOL-8200. The standards used were jadeite for Na, orthoclase for K, BaF<sub>2</sub> for Ba and F, MgO for Mg, wollastonite and SiO<sub>2</sub> for Si, wollastonite for Ca, Al<sub>2</sub>O<sub>3</sub> for Al, tugtupite for Cl, P-apatite for P, pyrite for S, SrF<sub>2</sub> for Sr, LaF<sub>3</sub> for La, CeF<sub>3</sub> for Ce, rare earth element (REE) -glass for U and Th, synthetic InAs for As and pure metallic standards for the other elements. The remaining 44 analyses were made with a CAMECA SX50 electron microprobe at the Outotec Research Oy, Pori. The standards used were andradite for Si, Ca and Fe, manganese titanium oxide for Ti and Mn, chromite for Cr, MgO for Mg, vanadinite for V, NiO for Ni, sphalerite for Zn, Al<sub>2</sub>O<sub>3</sub> for Al, ClAl<sub>2</sub> for Cl, LaB<sub>6</sub> for La, UO<sub>2</sub> for U, ThO<sub>2</sub> for Th and pure elements for Hf and Zr. In both the Oulu and Pori laboratories,

the conversion of X-ray intensities to concentrations was made using the ZAF-correction. The number of mineral compositions determined with the electron microprobe is listed in Table 3.1. Appendices 3–21 include selected electron microprobe analyses from the study area. Furthermore, all analyses are compiled in the appended CD-ROM.

During the electron microprobe analyses, the accelerating voltage was set at 15, 20 or 25 kV. The beam current was usually 15 nA, but when analysing plagioclase it was lowered to 12 nA. Most analyses were made with a spot size of 1.5 or 10 µm, but sometimes a spot size of 20 µm was used to analyse plagioclase. The Fe<sub>2</sub>O<sub>3</sub>-FeO ratio in minerals was calculated using the methods described by Carmichael (1967), Droop (1987) and Bowles (1988), whereas the amounts of H<sub>2</sub>O or CO<sub>3</sub> were calculated on the basis of structural mineral formulae.

In total, 541 semi-quantitative identifications of PGE-, gold- and silver-bearing minerals were made with a JEOL JSM-6400 scanning electron microscope (SEM) equipped with a Link eXL energy dispersive spectrometer (EDS) at the Institute of Electron Optics, University of Oulu. During the identifications of these phases the nature of their host phases

were recorded. Due to their extremely small size, only 238 precise analyses were carried out using EDS. In addition, 78 other analyses, mostly of grains of galena-clausthalite solid solution were performed using EDS. When performing the analysis the accelerating voltage was set at 15 kV and the beam current was

usually 1.2 nA. Natural minerals and synthetic oxides or sulphides were used as standards. Appendix 22 includes selected EDS analyses of the PGE-, gold- and silver-bearing minerals from the study area. All analyses are compiled in the appended CD-ROM.

Table 3.1. Number of mineral compositions determined using the electron microprobe.

<b>Group</b>	<b>Mineral</b>	<b>University of Oulu</b>	<b>Outotec Research Oy</b>
Silicates, n = 1871	Olivine	11	
	Clinopyroxene	267	
	Orthopyroxene	214	
	Feldspars (plagioclase and orthoclase)	1123	
	Amphibole group minerals	81	
	Epidote group minerals	40	
	Scapolite group minerals	21	
	Phlogopite-biotite	31	
	Chlorite	51	
	Garnet	26	
	Zircon	6	
Oxides, n = 212	Spinel group minerals	54	
	Ilmenite	56	
	Lovingite	39	44
	Rutile	4	
	Pseudobrookite	1	
	Baddeleyite	14	
Phosphates, n = 122	Apatite	122	
Sulphides, n = 186	Chalcopyrite	57	
	Pyrrhotite	35	
	Pentlandite	40	
	Pyrite	17	
	Violarite	6	
	Sphalerite	7	
	Bornite	8	
	Millerite	7	
	Cobaltite	5	
	Geerite	4	
Others, n = 10	Undefined mineral	10	

Table 3.2. Analytical methods, laboratories and number of analyses used during whole-rock analysis.

Method	University of Oulu	Geological Survey of Finland	
XRF (major and trace elements)	218	578	(175X)*
TITRIMETRIC Fe <sub>2</sub> O <sub>3</sub> /FeO	136	5	(301T)*
ICP-MS (REE and other trace elements)	23	198	(308M)*
ICP-MS (Au, Ir, Os, Pd, Pt, Rh, Re, Ru)		62	(714M)*
FAAS (Au, Pd, Pt)	142		
GFAAS (Au, Pd, Pt)		143	(704U and 705U)*
		148	(521U)*
ICP-AES (Au, Pd, Pt)		412	(704P and 705P)*
FAAS (Fe, Cu, Ni)	39		
ICP-AES (Fe, Cu, Ni, Co, S)		338	(511P)*

\* Analytical code of the GTK, see detailed descriptions of the methods from Rasilainen et al. (2007).

### 3.2.2 Major and trace element analyses

Powders for geochemical analyses were prepared by crushing rock samples with a Mn steel jaw crusher and then pulverizing the samples with a carbon steel ring mill (GTK) or a tungsten carbide ring mill (Department of Geosciences, University of Oulu). The number of analyses made using different analytical methods and the laboratories regarding the 971 samples used in whole-rock geochemical investigations is listed in Table 3.2. The analytical raw data are compiled in the appended CD-ROM. Appendices 23–26 include average rock compositions of the study area. Detection limits for different methods are collected in Appendix 27 (detection limits for electron microprobe analyses are shown in the same appendix).

The concentrations of the major elements and selected trace elements were determined by X-ray fluorescence spectrometry (XRF) of pressed powder pellets at the geochemical laboratory of the GTK, Espoo, and at the Institute of Electron Optics, University of Oulu. Because it is not possible to determine the FeO/Fe<sub>2</sub>O<sub>3</sub> with the XRF technique, the ratio was determined titrimetrically in some sam-

ples, using HF-H<sub>2</sub>SO<sub>4</sub> digestion as a pre-treatment (same pre-treatment in both laboratories). For the rest of the samples the oxidation state of iron was estimated using the method proposed by Le Maitre (1976) who estimated the oxidation ratio for plutonic rock, using the following equation:

$$\text{Oxidation ratio} = 0.88 - 0.0016 \times \text{SiO}_2 - 0.27 \times (\text{Na}_2\text{O} + \text{K}_2\text{O}). \quad (1)$$

The oxidation ratio (OX) is used to estimate FeO (wt. %) in a sample:

$$\text{FeO} = (\text{OX} \times \text{Fe}_2\text{O}_3^{\text{TOT}}) / (1 - \text{OX} + \text{OX} \times M_{\text{Fe}_2\text{O}_3} / (2 \times M_{\text{FeO}})) \quad (2)$$

where M refers to the molecular mass of the subscribed oxide. The concentration of ferric iron as Fe<sub>2</sub>O<sub>3</sub> (wt. %) in a sample is estimated in the following way:

$$\text{Fe}_2\text{O}_3 = \text{Fe}_2\text{O}_3^{\text{TOT}} - \text{FeO} \times (M_{\text{Fe}_2\text{O}_3} / (2 \times M_{\text{FeO}})). \quad (3)$$

The analyses described in the text and used in diagrams are presented on the basis of normalization to 100 wt. % on a volatile-free basis. The normalized components are SiO<sub>2</sub>, TiO<sub>2</sub>, Al<sub>2</sub>O<sub>3</sub>, Fe<sub>2</sub>O<sub>3</sub>, FeO, MnO, MgO, CaO, Na<sub>2</sub>O, K<sub>2</sub>O and P<sub>2</sub>O<sub>5</sub>.

Trace elements including rare earth elements were analysed with inductively coupled plasma mass spectrometry (ICP-MS) at the geochemical laboratory of the GTK or at the Department of Chemistry, University of Oulu. In both laboratories the decomposition pre-treatment method was HF-HClO<sub>4</sub>-digestion.

The base metal content of samples with visible sulphide minerals was determined using flame atomic absorption spectrometric (FAAS) analysis at the Department of Geosciences, University of Oulu, or with inductively coupled plasma atomic emission spectrometry (ICP-AES) at the geochemical laboratory of the GTK. The pre-treatment in both laboratories was aqua regia digestion.

For analysing Au, Pd and Pt, the lead fire assay method combined with atomic absorption spectrometric analysis with flame atomisation (FAAS) was used at the Department of Geosciences of the University of Oulu. The lead fire assay preconcentration procedure was also adapted at the geochemical laboratory of the GTK, but the analysis was done using electrothermal atomisation (GFAAS) (704U and 705U in Table 3.2) or ICP-AES (704P and 705P in Table 3.2). In the early phase of the GTK project "Layered Igneous Complexes in Northern Finland" the pre-treatment in GFAAS method was aqua regia digestion followed by co-precipitation using Hg (521U in Table 3.2), but this was soon replaced by the lead fire assay.

Inductively coupled plasma mass spectrometry (ICP-MS) of the geochemical laboratory of the GTK was used for determining Au, Pd, Pt, Rh, Ir, Os, Re and Ru. The pre-treatment consisted of nickel sulphide fire assay with tellurium co-precipitation. For details of the methods used in the precious metal analyses, the reader is referred to Hoffman & Dunn (2002) and references therein.

As a useful approximation of mineral modes, the sample compositions in Appendices 23–26 are presented using molecular cationorms of Barth (1955, 1962) ("Barth-Niggli norm"

by Chayes & Métais 1964), whereas the composition of each normative mineral was calculated by CIPW norm (Cross, Iddings, Pirsson & Washington 1902, calculation rules given by Kelsey 1965). The molecular norm is expressed using cation percentages but the CIPW norm is presented on the basis of percentages by weight. Therefore the CIPW norm is actually a weight rather than a volume estimate of phases. Nevertheless, the correlation between individual parameters in the weight and molecular norms is usually very high. The modified differentiation index (MDI) and modified crystallization index (MCI) used as differentiation parameters were obtained by means of CIPW norms, following the method described by Von Gruenewaldt (1973).

Both the molecular cationorm and CIPW norm calculations contain potential errors since in the calculation procedure, the MgO/FeO of all coexisting mafic silicates is taken from the ratio in the whole-rock analysis. Generally the ratio in coexisting mafic phases varies slightly. For instance the ratio is highest in augite and lowest in olivine. In addition, norms slightly overestimate the amount of free silica. Fenner (1929) commented on the norm calculation: "*In the calculation, all of the Fe<sub>2</sub>O<sub>3</sub> present is attributed to magnetite, and an equal molecular amount of FeO is assigned to it. As a matter of fact, however, much of the Fe<sub>2</sub>O<sub>3</sub> seems to be dissolved in pyroxene crystals as an independent substance, and the equivalent FeO is actually combined with SiO<sub>2</sub>.*"

### 3.2.3 Sm-Nd isotope analyses

Isotope geochemical analyses were performed using whole-rocks and mineral fractions. Mineral fractions were collected from crushed whole-rock powders produced with an electric pulse disaggregator (EPD) at the GTK's Northern Finland Office, Rovaniemi. The sample was crushed using high-voltage electric pulses developed by a Marx cir-

cuit. The crushed rock samples were then sieved and the mineral fractions were collected with magnetic and heavy liquid separation. Fractions of plagioclase, clinopyroxene and orthopyroxene were collected. The sample preparation was continued at the isotope laboratory of the GTK, where the orthopyroxene fractions were further wind-abraded to obtain pure samples. Prior to final powdering with an iron pan of a swing-mill, all samples were cleaned ultrasonically. The whole-rock and mineral fraction powders (200–300 mg) were spiked with  $^{149}\text{Sm}$ - $^{150}\text{Nd}$  tracers. The spiked powders were dissolved in HF-HNO<sub>3</sub> solution in teflon beakers (Savillex screw cap) on a hot plate. The evaporation was repeated with HNO<sub>3</sub> and HCl until clear solutions were obtained. The elements Nd and Sm were separated from the same dissolved samples using standard ion exchange columns.

The isotopic ratios were measured with a VG SECTOR 54 mass spectrometer at the isotope laboratory of the GTK. Altogether 35 analyses were performed: Dr. Tapani Rämö performed 18 whole-rock analyses and the remaining 4 whole-rock and 12 mineral analyses were performed by Dr. Hannu Huhma and the author. For a detailed description of the Sm-Nd isotope analytical preparation at the GTK, the reader is referred to Hanski et al. (2001a).

In addition, 12 whole-rock samples were analysed for Sm-Nd isotopic compositions

using TRITON TI (thermal ionization multi-collector mass-spectrometry) at the Center of Isotopic Research of the VSEGEI, St. Petersburg. The samples were prepared at the Department of Geosciences of the University of Oulu by crushing them with a Mn steel jaw crusher and pulverizing with a tungsten carbide ring mill.

The best-fitting line used in the Sm-Nd dating was determined with the method of Williamson (1968), which accounts for the analytical uncertainties in both  $^{147}\text{Sm}/^{144}\text{Nd}$  and  $^{143}\text{Nd}/^{144}\text{Nd}$ . In comparison to the “least-squares cubic” procedure of York (1969), which is mostly used in geological age determinations, the Williamson method produces similar results but involves a simpler calculation procedure. All measured and calculated errors are reported at  $2\sigma$ -level (*i.e.* ~ 95 % of the values are within two standard deviations). The quality of the best-fitting line was estimated with mean squared weighted deviation (MSWD) as defined by Brooks et al. (1972). The  $^{143}\text{Nd}/^{144}\text{Nd}$  ratio relative to the Chondritic Uniform Reservoir (CHUR) at time *T* in geological history ( $\epsilon_{\text{Nd}}$ ) was defined by the Equation of DePaolo & Wasserburg (1976). The depleted mantle model age ( $T_{\text{DM}}$ ), which is the time at which the sample separated from a postulated light rare earth element (LREE)-depleted upper mantle source, was calculated iteratively assuming mantle evolution trend, using the Equation of DePaolo (1981).

### 3.3 Grain size and modal abundance of rock-forming minerals

The grain size of minerals was determined after verifying crystal outlines with a polarizing microscope or by SEM, by tracing manually the maximum intersection lengths of each grain on scanned thin section images or back-scattered electron images (BEI, BE-image) with a standard vector graphics program. The digital images were enlarged 10 times for eas-

ing the image analysis. The resolution used for thin section images was set at 4800 dpi (188.98 pixels/mm). The following grain size divisions were used: fine-grained (< 1 mm), small-grained (1–2 mm), medium-grained (2–5 mm), coarse-grained (5–10 mm), and pegmatitic (> 10 mm).

The mode of the major rock-forming phases was obtained by point-counting ca. 1000 points per thin section. In most samples alteration products were grouped together with their primary phases to yield an approxima-

tion of the original, pre-alteration mode. However, in the case of the sulphide- and PGE-mineralized occurrences studied in this work, the low-temperature minerals were included in the mode.

### 3.4 Nomenclature

In this study the terminology for layered intrusions follows the nomenclature and classification proposed by Wager et al. 1960, Wager & Brown (1967) and Irvine (1982, 1987). Alongside the cumulus terminology, the conventional rock names are used in accordance with the classification of Streckeisen (1976).

According to Irvine (1982, 1987), cumulate is defined as an igneous rock that is characterized by a cumulus framework of touching mineral crystals or grains that were evidently formed and concentrated through fractional crystallization. The fractionated crystals are called cumulus crystals and are normally cemented together by a texturally later generation of postcumulus material which crystallized from intercumulus liquid. Cumulates are divided into ortho-, meso-, and adcumulates according to the abundance of postcumulus material, which consist of intercumulus minerals. Orthocumulates are characterized by idiomorphic cumulus crystals and abundant intercumulus minerals, which make up 25–50 vol. % of the rock. Mesocumulates contain 7–25 vol. % of intercumulus minerals with the cumulus minerals adjoining partly along mutual grain boundaries. Adcumulates contain 0–7 vol. % of intercumulus minerals, and mutual interference boundaries are the norm for the cumulus phases. The intercumulus minerals may occur as large optically uniform crystals enclosing several cumulus crystals. In such cases these intercumulus crystals are called oikocrysts and the texture is called poikilitic; the rock can be described as poikilitic ortho-, meso- or adcumulate depending on

the abundance of intercumulus phases. Irvine (1982, 1987) did not give any specific name for the smaller crystals distributed as inclusions in oikocrysts, but Mathison (1987) and Tegner & Wilson (1995) described them as chadacrysts. Another term not defined by Irvine (1982, 1987) is megacryst, which is here used for significantly larger, pegmatitic crystals.

According to the current pyroxene nomenclature (Subcommittee on pyroxenes 1989) the mineral names “bronzite” and “hypersthene” should be replaced by the name “enstatite”. However, these obsolete names were retained in this study because they are still more readily understood by the intended audience of this work. Enstatite is magnesium-rich orthopyroxene with the  $\text{Mg}^{2+}$  partly replaced by small amounts of  $\text{Fe}^{2+}$  (up to 12 mol. %  $\text{Fe}_2\text{SiO}_6$ ). In bronzite, the  $\text{Fe}_2\text{SiO}_6$  ranges from 12 to 30 mol. %, and with still more iron there is a passage to hypersthene (30–50 mol. %  $\text{Fe}_2\text{SiO}_6$ ).

In this study the cumulus nomenclature and abbreviations are adopted from Irvine (1982) where the cumulus minerals are listed and abbreviated in order of decreasing modal abundance. An exception to Irvine’s classification is that intercumulus minerals are also included so that, for example, a bronzite-plagioclase cumulate with intercumulus augite is denoted by bpCa, and if the intercumulus mineral occurs as poikilitic, it is indicated by an asterisk. Thus, the rock would be called poikilitic bronzite-plagioclase cumulate with intercumulus augite, whose abbreviation would be

denoted by bpCa\*. The rocks that are characterized by igneous textures that cannot be described using the cumulus terminology are referred to as noncumulates. Crescumulates (“harrisitic textures”), ophitic texture and equigranular fine- to small-grained textures in chilled margins are well-known examples of these.

According to Irvine (1982, 1987) and Mc-Birney & Noyes (1979), igneous layering is an overall planar feature of cumulates, as manifested through a combination of laminae, lamination and layers. A lamina is a thin layer (1–3 cm), whereas lamination is characterized by minor planar features in the cumulate on the scale of its grain size, but which do not themselves define any distinctive planes. Igneous lamination may occur as planar lamination where the platy alignment of tabular minerals parallels cumulate layers. In lineate lamination minerals have lineation in the layering plane. Other examples of igneous lamination are imbricate, grain size, modal and textural laminations. A layer is a sheet-like cumulate unit that is a distinctive entity in its composition and/or textural features. It may be characterized as graded in terms of grain-size or texture, modal, uniform, schlieren or cryptic. A layer may be referred to by its thickness as being thin (< 5 cm), medium-thick (5 cm–1 m) and thick (1–3 m). A macrolayer is a layer which is 3–10 m thick and a megalayer is even thicker. Rhythmic layering is characterized by a systematic recurrence of distinctive layers or sequences of similar layers. On the basis of layer thickness, rhythmic layering may be called microrhythmic (inch-scale layering) or macrorhythmic. Intermittent layering is a special type of rhythmic layering, which comprises thin, modally graded layers alternating with layers of a uniform rock of

varying thickness. Cryptic layering refers to changes in the mineral compositions and is therefore not recognized with a naked eye.

Series refers to structural divisions comprising major stratigraphic cumulate successions. Zones and subzones are the first and second rank stratigraphic subdivisions of series. The basis for choosing zones and subzones depends on the target of investigation but are mostly defined by major cumulus minerals in the stratigraphic range of the intrusion. A unit is a specific and distinct feature that can be singled out, numbered or named for specific reference. It may be a part of anything in the layered intrusion, thus covering parts of zones, or even parts of many series. On textural basis, a unit may be called rhythmic unit. In contrast to the term rhythmic, which is descriptive, the term cyclic is genetic, and therefore a unit may be called cyclic unit only when there is evidence for repeated additions of fresh magma to the intrusion while it was solidifying. By layer thickness, cyclic and rhythmic units may also be further defined as micro-, macro- or megacyclic. A member is an outstanding single unit, whereas a group is a prominent combination of several similar units. (Irvine 1982).

In this study the prefix meta is generally omitted, although most of the rocks in the study area have undergone regional metamorphism. The typical metamorphic mineral assemblage of chlorite, albite, epidote, tremolite-actinolite and quartz in the mafic-ultramafic rocks of the study area implies conditions of greenschist or lower amphibolite facies. In the study area the original cumulus textures of plutonic rocks are usually well preserved as pseudomorphs thus enabling identification of original cumulus and intercumulus phases.

#### 4 GEOLOGICAL SETTING AND STRUCTURE OF THE KOILLISMAA INTRUSION

The individual blocks of the Koillismaa Intrusion are referred, from north to south, to as Murtolampi, Kaukua, Lipeävaara, Tilsa, Kuusijärvi, Porttivaara, Syöte, Pirivaara and Pintamo blocks (Fig. 4.1). They form a synformal structure where the block margins towards the E-W trending synform axis are faulted against the country rocks that mostly belong to the Archaean basement (Fig. 4.2). The Pintamo, Pirivaara, Syöte, Porttivaara, Tilsa and Kuusijärvi blocks dip towards the north or northwest whereas the Lipeävaara, Kaukua and Murtolampi blocks dip towards the south or southwest. In this structure the observed dip is steepest in the central part, amounting to 35–50° in the Porttivaara, Kuusijärvi and Lipeävaara blocks. In the Pintamo, Pirivaara, Syöte, Kaukua and Murtolampi blocks the dips are gentler, at ca. 10–30°. The Syöte block has a relatively large areal extent due to gently dipping igneous layering and faulting along the strike of the layering, which has led structural repetition of the Layered Series of the block. On the basis of gravimetric data, the Pirivaara and Syöte blocks extend to 1100 m below the present erosion level, whereas the Porttivaara, Kuusijärvi and Lipeävaara blocks extend deeper, to 2000–2500 m (Saviraro 1976; Ruotsalainen 1977; Piirainen et al. 1978).

The cross section in the upper part of Fig. 4.2 illustrates the sheet-like Koillismaa Intrusion in its original shape in which the present erosion level is marked and also indicated by the block names. The cross section reveals an angular discordance between the Layered and Marginal Series and a depression structure in the roof contact of the intrusion – features described earlier by Alapieti (1982). The angular discordance seems to be due to an inclined basal contact of the original magma chamber.

It is observable in the central parts of the Koillismaa Intrusion, in the Porttivaara block area, where the cumulate sequence includes stratigraphically lower LS members than those of other blocks. The depression structure is located in the Kuusijärvi and Lipeävaara block area where the stratigraphically uppermost cumulate layers are thin or lacking. This indicates a syn-intrusive roof collapse or an irregular roof contact of the magma chamber of the Koillismaa Intrusion.

Two stress field scenarios can be used to explain the break-up of the Koillismaa Intrusion, one tensional and the other compressional (Figs 4.2.A and B). Both would have resulted in a broadly similar pattern of fragmentation on surface, but with differently dipping faults separating the intrusion blocks. The compressional stress field is favoured in the present study, because it would account for 1) the reactivation of older rift-related normal faults related to the emplacement of the intrusion, 2) the uplift of the intrusive blocks above erosion level and 3) the folding of the supracrustal rocks in the depression structure.

It is suggested that a compressional stress field with a N-S oriented maximum principal stress axis ( $\sigma_1$ ) and vertical minimum principal stress axis ( $\sigma_3$ ) caused simultaneous tilting and structural duplication of the intrusive blocks and folding of the supracrustal formations above the intrusion, as lithologies of different competences would have undergone different deformation in a stress field. The supracrustal formations may be correlated with the lowermost formations of the Kuusamo Schist Belt, which itself is younger than 2405±6 Ma as indicated by zircon dating of quartz porphyry boulders in basal conglomerates of the schist belt (Silvennoinen 1991).

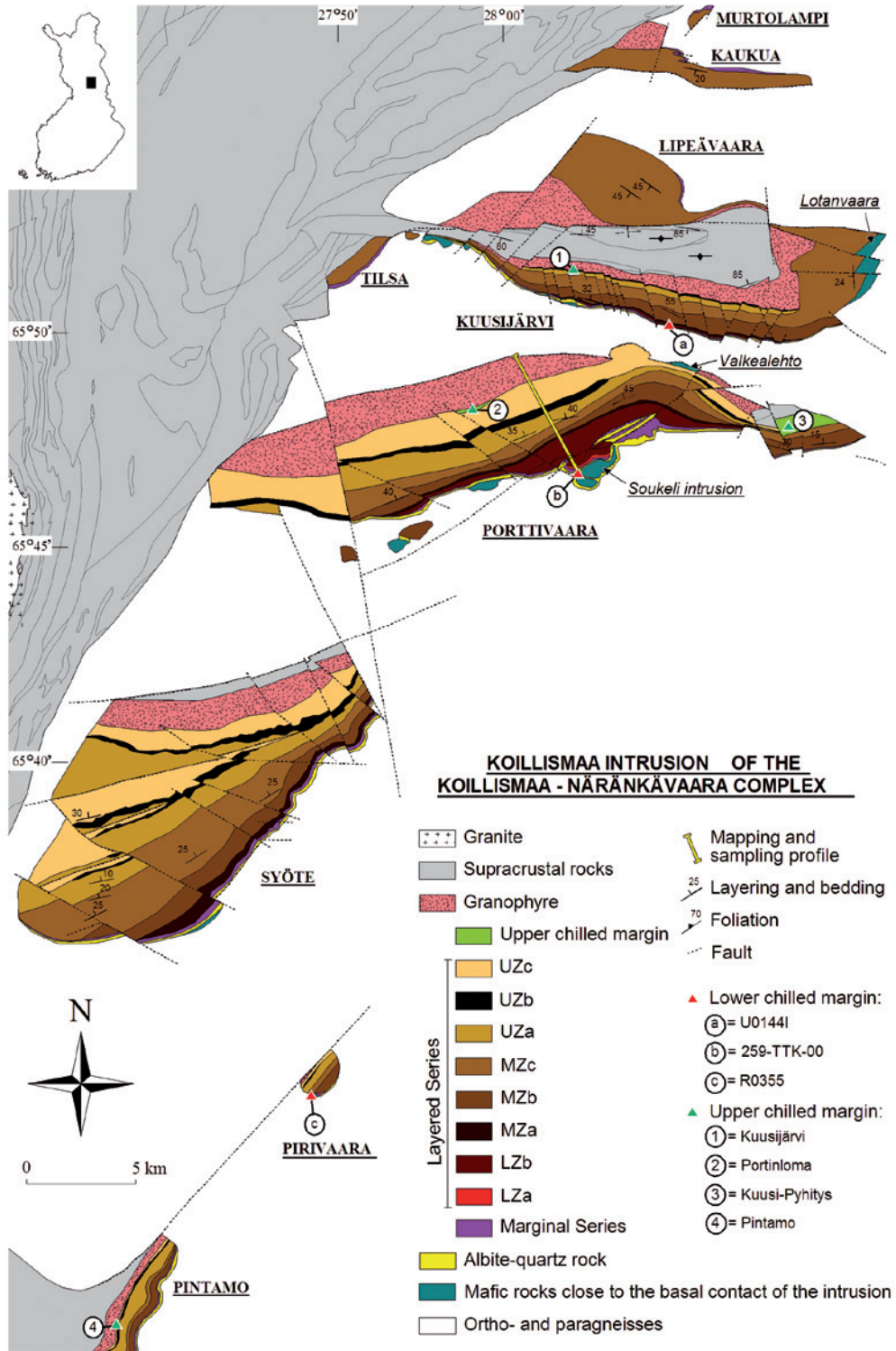


Fig. 4.1. Geological map of the Koillismaa Intrusion. Revised and redrawn partially after the maps compiled by Piirainen et al. (1978), Alapieti et al. (1979), Honkamo (1979), Lahti & Honkamo (1980), Alapieti (1982), Karinen (1998), Landén (1999) and Räsänen et al. (2003). Abbreviations: UZ = Upper Zone, MZ = Middle Zone, LZ = Lower Zone.

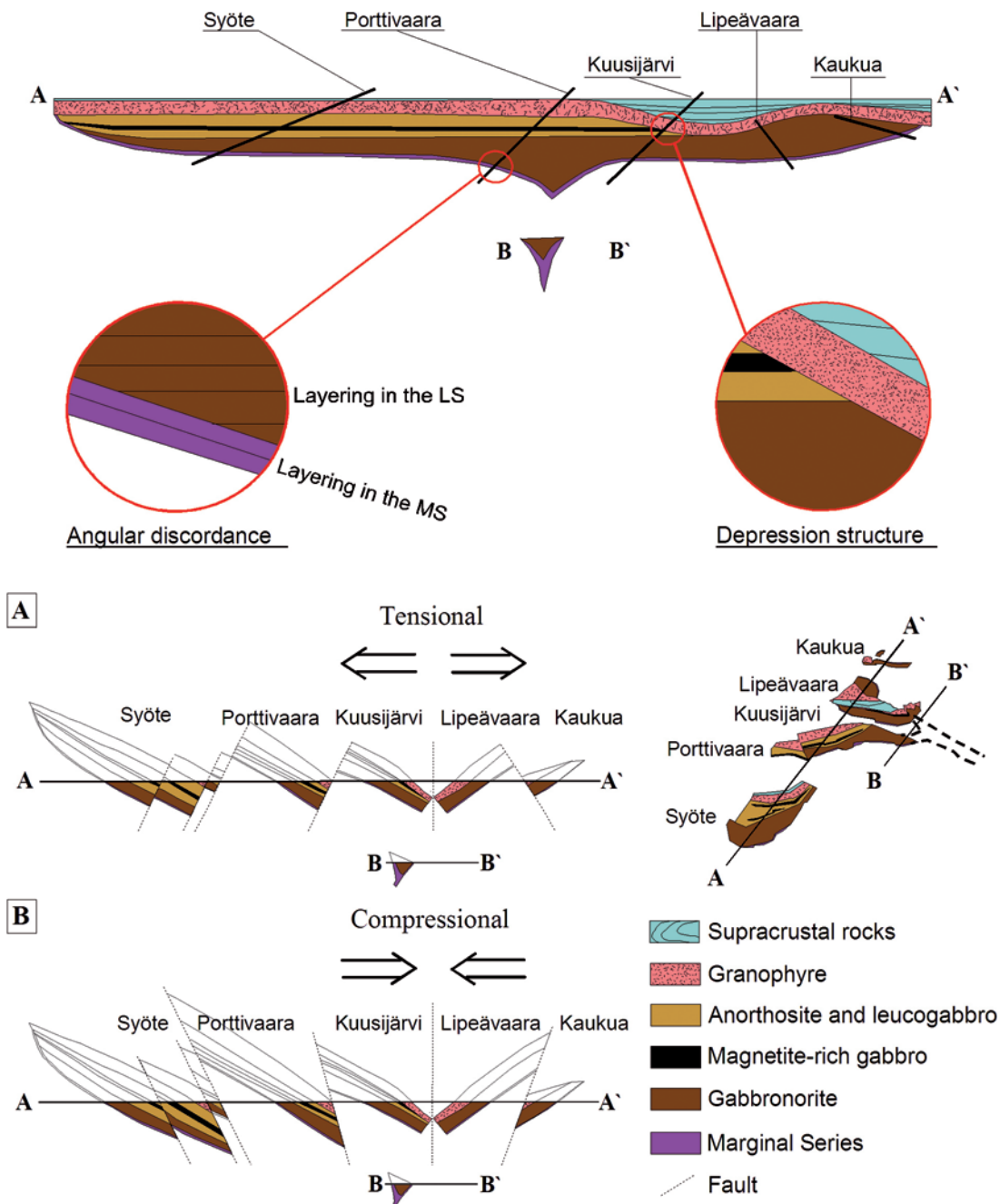


Fig. 4.2. Cross section of the original sheet-like Koillismaa Intrusion with current erosion levels of the blocks and two possible scenarios explaining the present intrusion structure: tensional (A) and compressional (B). Modified from Alapieti & Lahtinen (1984) and Karinen (1998). Abbreviations: LS = Layered Series, MS = Marginal Series.

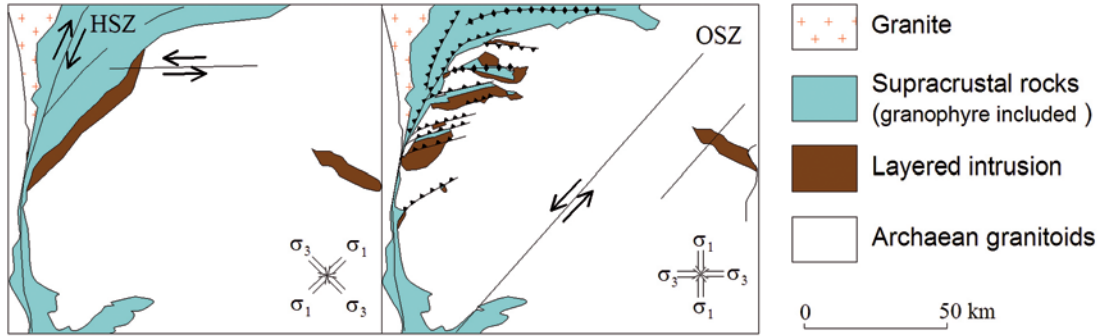


Fig. 4.3. Model of the tectonic evolution of the Koillismaa area. Abbreviations: HSZ = Hirvaskoski Shear Zone, OSZ = Oulujärvi Shear Zone.

The tilting may have taken place within the same stress fields, which has been attributed to the two major shear zones of the Koillismaa-Näränkäväära Complex area. Of these two shear zones the one that follows the western contact of the Kuusamo Schist Belt is dextral and is known as Hirvaskoski Shear Zone (HSZ in Fig. 4.3). The eastern, Oulujärvi Shear Zone (OSZ in Fig. 4.3), cuts the HSZ and is kinetically sinistral. By dating zircons of granitoids that tectonically predate the shear zones Kärki (1995) suggested that the maximum age of both the HSZ and OSZ is 1860 Ma. However, the paleomagnetic tests of Mertanen et al. (1989) provide strong evidence that the tilting occurred during the cooling of the intrusions. Therefore, it is concluded at this point that most probably the HSZ formed along an Archaean weakness zone (*cf.* Airo 1999), and the tilting of the Koillismaa Intrusion was a long-lasting event.

Karinen & Iljina (2009) divided the structural evolution of the intrusion into four main episodes (Fig. 4.4):

1. Initial rifting (2500–2450 Ma): the early stage of the rifting was characterized mainly by volcanism and formation of a graben structure above the feeder of the later magma chamber of the intrusion.
2. Main rifting (2450 Ma): volcanic activity was followed by intrusion of magma

below the volcanic pile resulting in the formation of the sheet-like intrusion. The granophyre originated from melting of the supracrustal rocks in the roof of the chamber, or by felsic magma injection below the supracrustal rocks. The depression in the hangingwall is the result of pre-intrusive graben faulting.

3. Continuation in the tensional regime resulted in the collapse of the central part of the intrusion, forming a basin, into which younger supracrustal material was deposited.
4. Compressional period (< 2450–? Ma): the tensional stress field changed to a compressional one, which caused reactivation and reverse motion along older rift-related normal faults. These reverse movements were strong enough to raise large segments of the Archaean basement which are presently separating the intrusion blocks, and to duplicate layers of the Syöte block. The N-S oriented stress field did not cause significant rotation or tilting of the Näränkäväära Intrusion because of its funnel-shaped structure, and therefore the intrusion retained its original position.

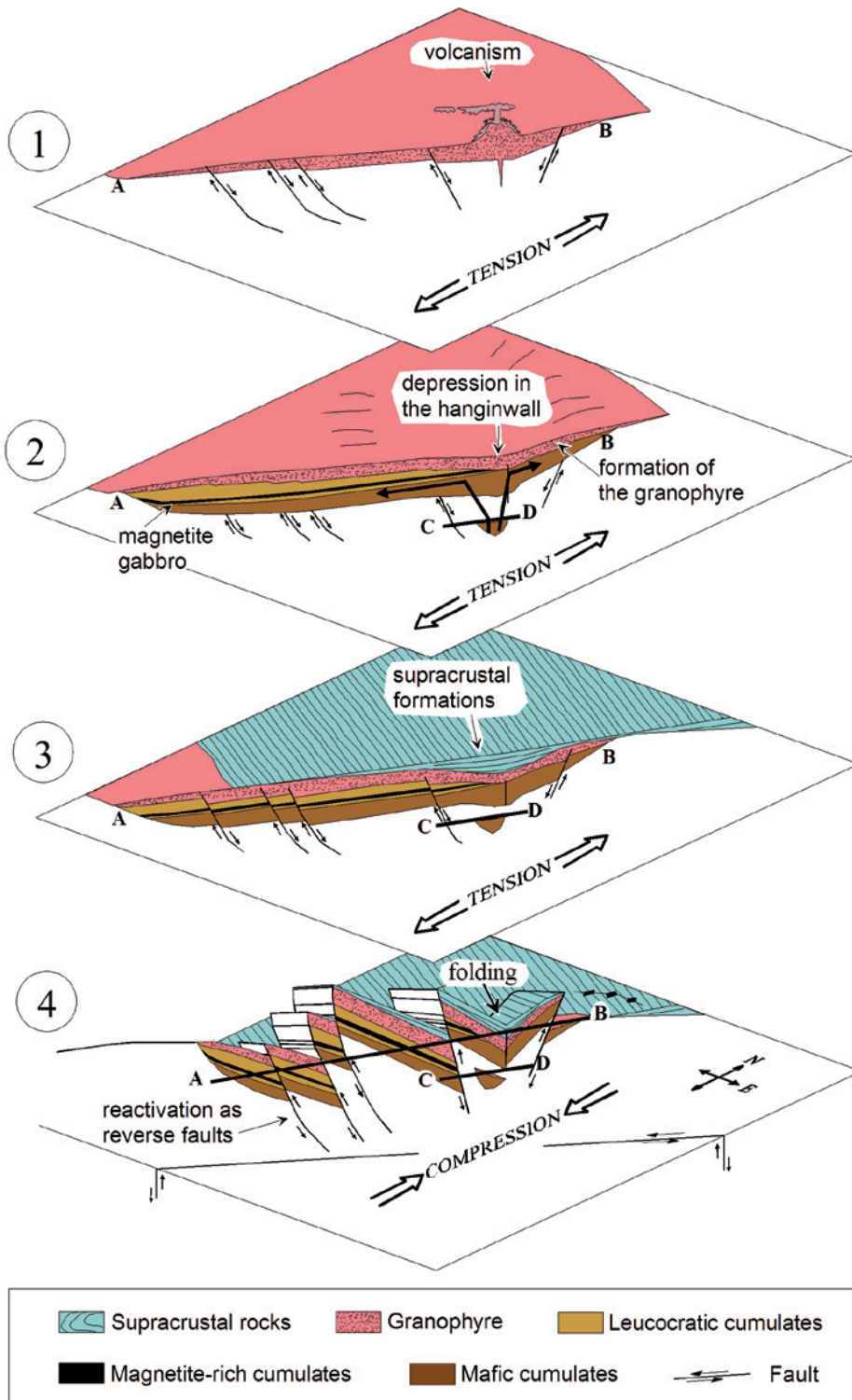


Fig. 4.4. Schematic diagram showing structural evolution of the Koillismaa Complex (modified from Karinen 1998, Iljina et al. 2001 and Karinen & Salmirinne 2001). See text for further explanation.

## 5 STRATIGRAPHY AND PETROGRAPHY

### 5.1 Stratigraphic subdivision of the Koillismaa Intrusion

The stratigraphic subdivision is based on the appearance of major cumulus minerals in the Koillismaa Intrusion. On the basis of the profile across the Porttivaara block, where the stratigraphic section is most complete and 2500 m thick, the intrusion is subdivided into two series, five zones and twelve subzones. One subzone is further divided into three units. (Fig. 5.1). From the roof to the base of the intrusion these are named as follows:

- Roof rocks (supracrustal rocks)
- Granophyre
- Upper chilled margin
- Layered Series (LS)
  - Upper Zone (UZ)
    - Upper Zone c (UZc)
    - Upper Zone b (UZb)
    - Upper Zone a (UZa)
  - Middle Zone (MZ)
    - Middle Zone c (MZc)
    - Middle Zone b (MZb)
    - Middle Zone a (MZA)
  - Lower zone (LZ)
    - Lower Zone b (LZb)
    - Lower Zone a (LZA)
      - Olivine gabbronorite unit II
      - Gabbronorite unit
      - Olivine gabbronorite unit I
- Marginal Series (MS)
  - Upper Zone of the MS (UZMS)
    - Upper Zone b of the Marginal Series (UZMSb)
    - Upper Zone a of the Marginal Series (UZMSa)
  - Lower Zone of the MS (LZMS)
    - Lower Zone b of the Marginal Series (LZMSb)
    - Lower Zone a of the Marginal Series (LZMSa)
  - Lower chilled margin
  - Basal rocks (mainly Archaean felsic gneisses)

In addition to the modal mineral variation in the stratigraphy of the Koillismaa Intrusion, the grain size of plagioclase distinguishes most of the subzones (Fig. 5.2).

Many layered intrusions show marginal reversals in their lower portions. The Koillismaa Intrusion is one of the first in which this feature has been described Alapieti (1982). Latypov (2003a, b) called the boundary between the marginal reversal and the overlying cumulates a “compositional crossover maximum”, since above that boundary, the modal and cryptic layering show normal trends of differentiation. In the Koillismaa Intrusion the border is located in the centre of the peridotitic subzone (UZMSb) of the MS. However, in this study the entire ultramafic portion is grouped to the MS, because the LS rests unconformably on the MS.

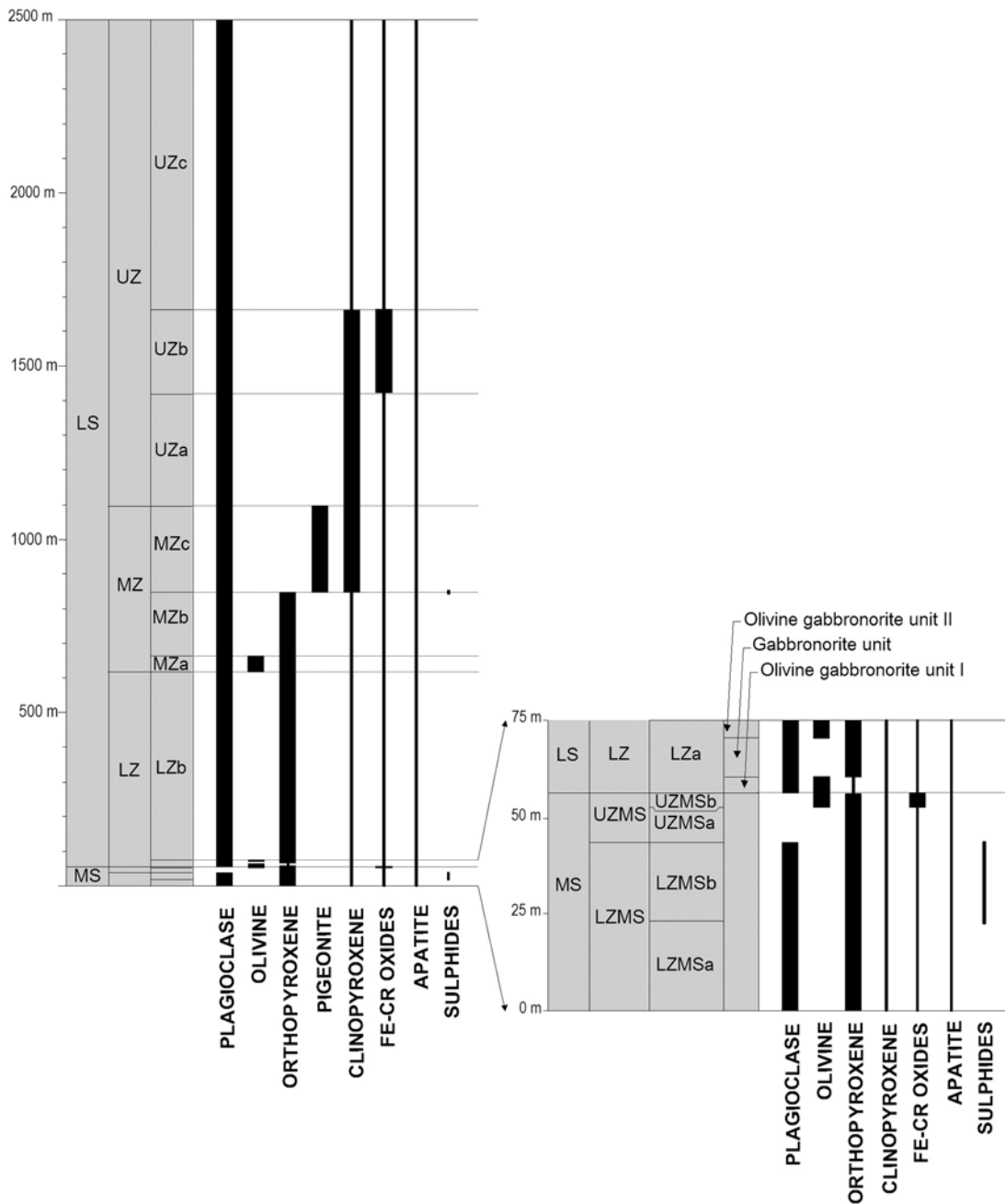


Fig. 5.1. Stratigraphic section and cumulus stratigraphy in the profile across the Porttivaara block (the profile is marked in Fig. 4.1). In the sequence thick vertical lines indicate cumulus minerals and thin vertical lines indicate intercumulus minerals.

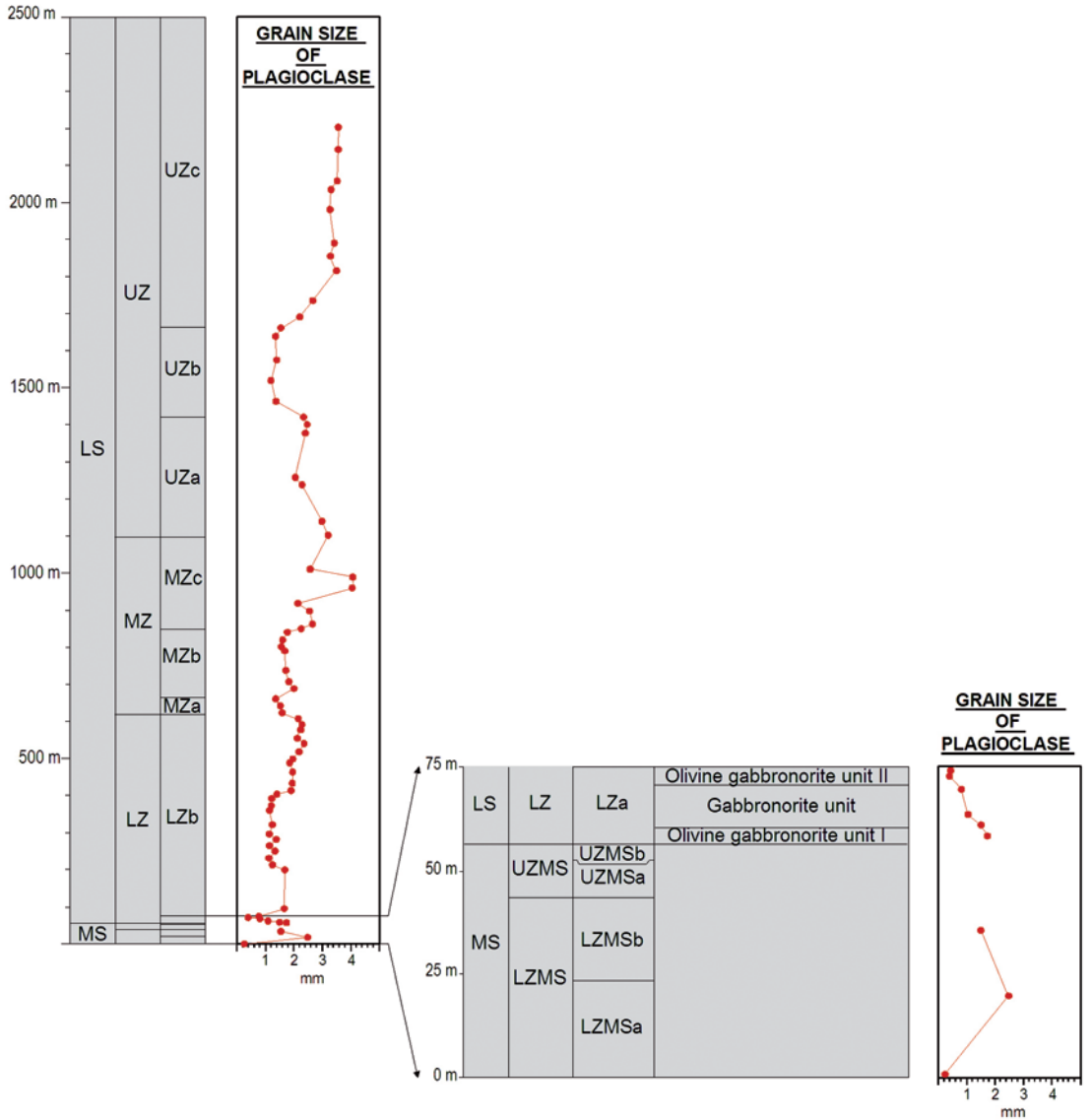


Fig. 5.2. Stratigraphic section and plagioclase grain size variation in the profile across the Porttivaara block (the profile is marked in Fig. 4.1).

## 5.2 Lotanvaara mafic rock unit

Close to the basal contact of the Koillismaa Intrusion blocks occur several small intrusions and other mafic rocks (Fig. 4.1). The most prominent of them is the Soukeli Intrusion near the southern contact of the Porttivaara block. Alapieti (1982) determined an Archaean age ( $2699 \pm 46$  Ma by the U-Pb method on zircon) for the Soukeli Intrusion. Another mafic rocks close to the basal contact locates in the eastern part of the Kuusijärvi and Porttivaara blocks, in the Lotanvaara and Valkealehto areas.

In this study only the rocks of the Lotanvaara area were investigated, since they have noncumulus textures and may therefore represent chilled margins. They may also provide a clue to the gabbronoritic noncumulate bodies within the LS (described in Chapter 5.7). Since the eastern part of the Kuusijärvi block shows no distinct layering, it is difficult to estimate the true stratigraphic thickness of the Lotanvaara unit. The distance between exposed contacts of the Archaean basement granitoids and cumulates of the Kuusijärvi

block is ca. 400 m, which is the maximum thickness of the unit. In the western part of the Lotanvaara area, the rock is penetrated by cumulus-textured gabbronoritic dykes that resemble in terms of their mode and rock texture to the MZc of the Koillismaa Intrusion. Photographs of these dykes are presented by Juopperi (1976) and Karinen (1998).

The rocks of the Lotanvaara unit are usually highly altered, but in some outcrops unaltered material has been found (Fig. 5.3). In these outcrops plagioclase occurs either in the form of idiomorphic, tiny chadacrysts, or as anhedral and larger crystals ( $\sim 0.3$  mm) in the matrix of bronzite and augite oikocrysts. Orthopyroxene oikocrysts are euhedral and show the same grain size as plagioclase in the matrix. Augite oikocrysts are larger ( $\sim 3$  mm) and typically also enclose small bronzite chadacrysts that tend to become larger (up to 0.1 mm) towards the edges of the oikocrysts. A small amount of fine-grained chromite is common in the rock.

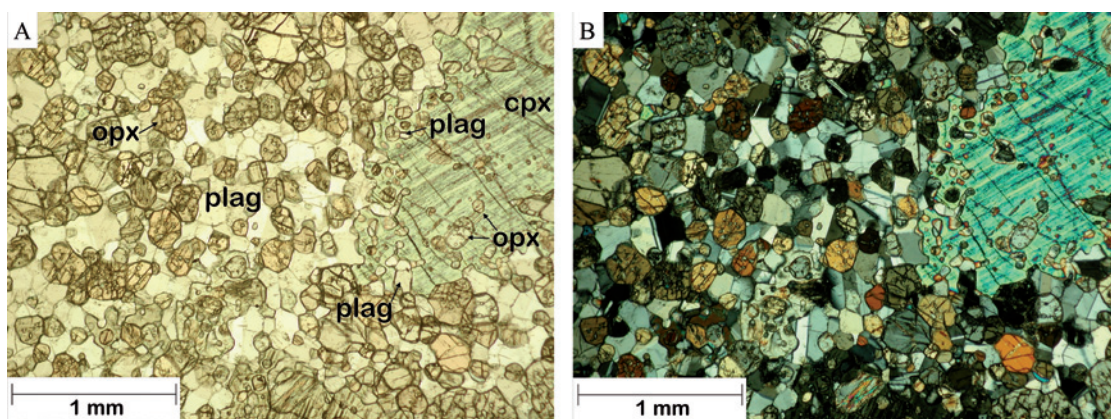


Fig. 5.3. Photomicrographs of texture of unaltered noncumulus-textured gabbronorite of the Lotanvaara rock unit (72-TTK-99, **A** with parallel nicols and **B** with crossed nicols). Abbreviations: plag = plagioclase, cpx = clinopyroxene, opx = orthopyroxene.

### 5.3 Chilled margins

The lower chilled margin (“U0144I” in Fig. 4.1), which Juopperi (1976) described from the Kuusijärvi block is texturally identical to that found during the present study in the Porttivaara block (“259-TTK-00” in Fig. 4.1). In both areas the rock is characterized by an equigranular gabbronorite with grain sizes between 0.2 to 0.5 mm (Fig. 5.4.A).

In a few places along the exposed contact between the cumulates and the overlying granophyre, there occurs a greenish rock, which Juopperi (1976) and Piirainen et al. (1978) interpreted as being of volcanic nature. In the present work the rock is interpreted to represent the upper chilled margin. In the Kuusijärvi block, the upper chilled margin may be exposed on an island in the western part of Lake Kuusijärvi (“Kuusijärvi” in Fig. 4.1) (see also Saini-Eidukat et al. 1997). However, due to the high degree of alteration and recrystallization, petrographic identification of the original texture is impossible. In the cen-

tre of the Porttivaara block (“Portinloma” in Fig. 4.1), the same contact zone includes a breccia with angular 5 to 10 cm-sized mafic fragments of fine-grained (< 0.3 mm) ophitic gabbronorite (5.4.B) in a granophyric or chlorite schist groundmass. In the eastern part of the Porttivaara block (“Kuusi-Pyhitys” in Fig. 4.1), a greenish and homogenous rock overlies the intrusion. Microscopically, the rock is a fine-grained (< 0.3 mm) and equigranular gabbronorite (Fig. 5.4.C). The layering is horizontal in the underlying LS cumulates and in many outcrops the rock is penetrated by gabbroic dykes, presumably from the intrusion (Fig. 5.4.D). Thus, the rock in the Kuusi-Pyhitys area forms a thin, sheet-like relict. In the Pintamo block area (“Pintamo” in Fig. 4.1) the upper chilled margin is well exposed. Within a few meters away from the intrusion, the fine-grained and greenish chilled rock becomes progressively coarser and resembles a cumulus-textured.

### 5.4 Marginal Series and related PGE-mineralized layers

The Marginal Series (MS) of the Koillismaa Intrusion is estimated to be 60 m thick in the stratigraphic section of the Porttivaara block (Fig. 5.1). Kerkkonen (1976) has noted that the basement topography is reflected in the shape of the basal contact of the intrusion. This is most distinctly visible in the southern Porttivaara block area where the strike of the MS and the layering in the Layered Series (LS) follows the depression shape as shown in Fig. 5.5.

The MS is divided into two zones, the gabbronoritic Lower (LZMS) and the ultramafic Upper Zone (UZMS). In the lowermost LZMS the rock contains albite-quartz veins and inclusions of silica-rich basement rocks that occasionally contain traces of gneissic fo-

liation. The abundance of inclusions and veins decreases upwards through the zone, with the rock becoming more monotonous. Thus, the LZMS is further divided into a relatively heterogeneous LZMSa subzone and a more monotonous LZMSb subzone. Both subzones consist of a plagioclase-bronzite cumulate with intercumulus augite (pbCa). The UZMS grades from pyroxenite (UZMSa) at the base to peridotite (UZMSb) at the top. The rocks in both subzones are typically highly altered but igneous textures are normally preserved. The pyroxenite is a medium-grained poikilitic bronzite orthocumulate (bCa\*) and the overlying peridotite is a medium-grained poikilitic olivine orthocumulate.

The sulphide- and PGE-minerals of the MS are mostly concentrated in the upper part of the LZMS and less in the lower part of the UZMS. The mineralized area is typically 15–40 m thick and has gradational lower and upper contacts. Sulphides comprise 1–5 vol. % of the rock and occur mostly as fine dissemination in the interstices of silicate grains. The

principal sulphide minerals are pyrrhotite, chalcopyrite, pentlandite and, in places, pyrite. They form composite grains, but pentlandite typically occurs with pyrrhotite within up to 2 cm-sized sulphide blebs, whereas chalcopyrite predominantly forms fine disseminations. Pyrite occurs in two textural varieties: as idiomorphic and as anhedral crystals.

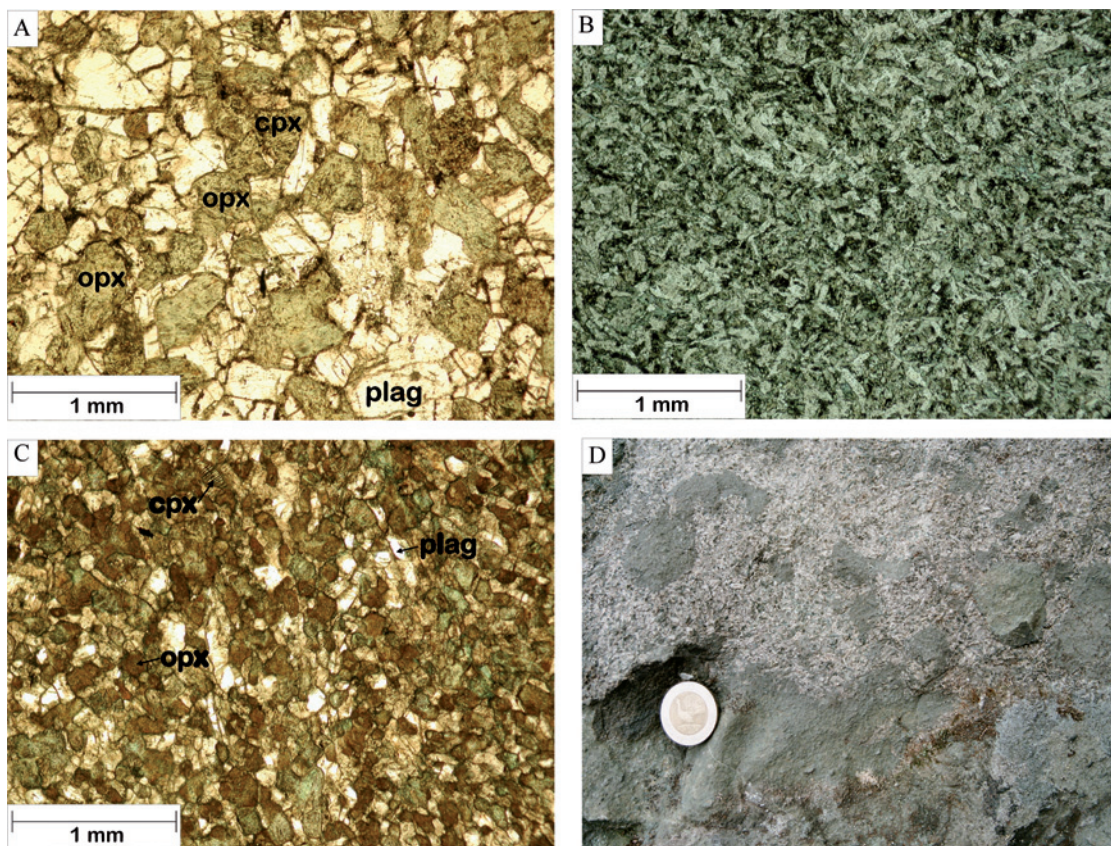


Fig. 5.4. Photomicrographs and outcrop photo of textures in the chilled margins. **A.** Partly altered small-grained equigranular gabbronorite at the lower contact of the Porttivaara block (259-TTK-00, parallel nicols). **B.** Partly altered fine-grained and ophitic gabbronoritic fragment in a breccia of the upper contact of the Porttivaara block (103.3-TTK-99, parallel nicols). **C.** Partly altered fine-grained equigranular gabbronorite representing the upper chilled margin in the Kuusi-Pyhitys area (10.2-TTK-98, parallel nicols). **D.** Fine-grained gabbronorite penetrated by coarse-grained gabbroic dykes in the Kuusi-Pyhitys area (10.2-TTK-98, the diameter of the coin is ca. 2.5 cm). Abbreviations: plag = plagioclase, cpx = clinopyroxene, opx = orthopyroxene.

## 5.5 Layered Series

### 5.5.1 Lower Zone

The Lower Zone (LZ) is 620 m thick in the Porttivaara stratigraphic section and is divided into two subzones (Fig. 5.1).

The LZa is best exposed in the southern part of the Porttivaara block where it is only ca. 20 m thick (Fig. 5.5). The subzone is divided into three units. The stratigraphically lowermost unit is a monotonous olivine gabbronorite (Olivine gabbronorite unit I) consisting of a poikilitic plagioclase-olivine orthocumulate (poCb\*a\*) with oikocrystic bronzite and augite (Fig. 5.6.A) and which includes garnet and brown igneous mica as typical accessory minerals. The central unit (Gabbronorite unit) is a microrhythmically layered poikilitic plagioclase-bronzite orthocumulate where augite is oikocrystic (pbCa\*) (Fig. 5.6.B). The uppermost unit (Olivine gabbronorite unit II) is a poikilitic plagioclase-olivine-bronzite orthocumulate with oikocrystic augite (pobCa\*) and accessory brown mica and garnet, but in

contrast to the lowermost unit, it shows distinct microrhythmic layering caused by variations in modal mineral proportions (Fig. 5.6.C). Detailed field mapping in the southern part of the Porttivaara block area (Fig. 5.5) where the LZa is best exposed revealed several elongate bodies of noncumulus-textured gabbronorite (described in Chapter 5.7).

The LZb is 600 m thick. It comprises mostly poikilitic gabbronorites (pbCa\*), where augite is oikocrystic and which typically show interstitial granophyric intergrowth of quartz and albite (Fig. 5.6.D). It is likely that the subzone is more complex than evident in the Porttivaara section since ca. 300 m east of the mapping profile, at a stratigraphic level of about 350 m above the base of the intrusion, there occur outcrops of fresh olivine gabbronorite (poCb\*a\*). In the mapping profile, this level is marked by a distinct increase in the plagioclase grain size (Fig. 5.2). Alapieti (1982) has also observed that the LZb includes cumulus olivine in places.

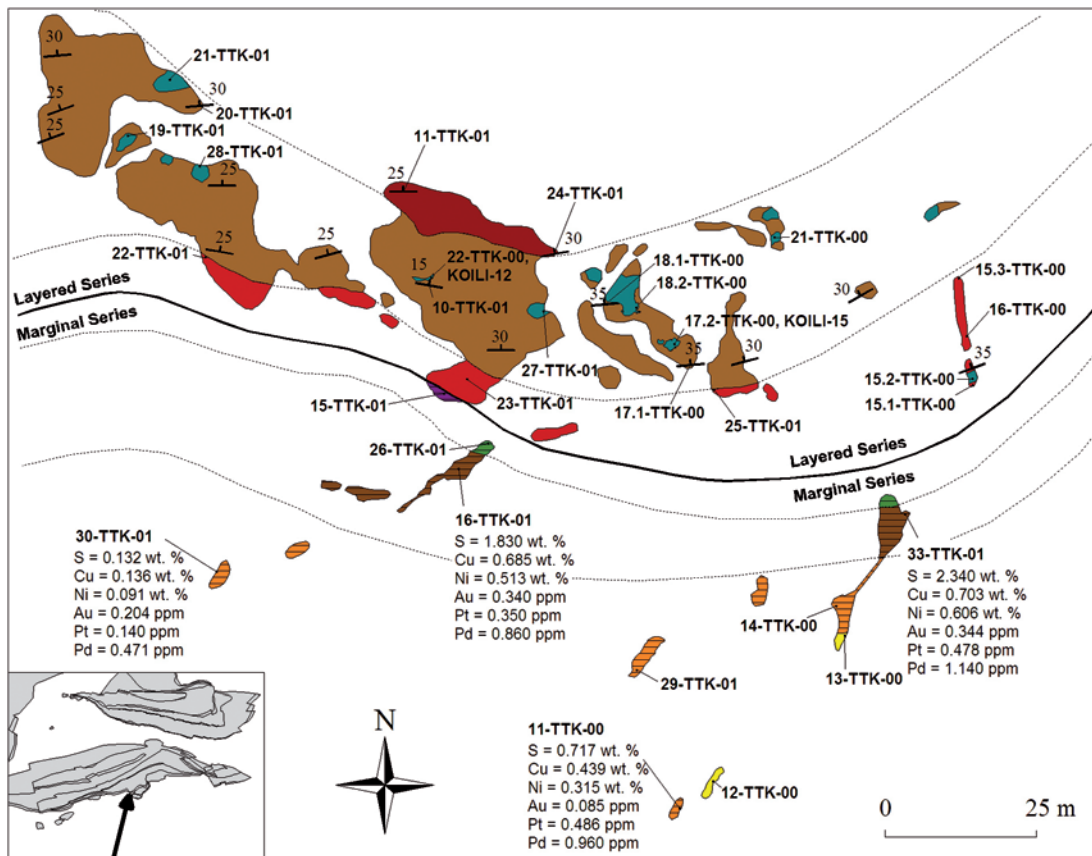


Fig. 5.5. Outcrop map of the southern Porttivaara block showing the Marginal Series and the lower part of the Layered Series.

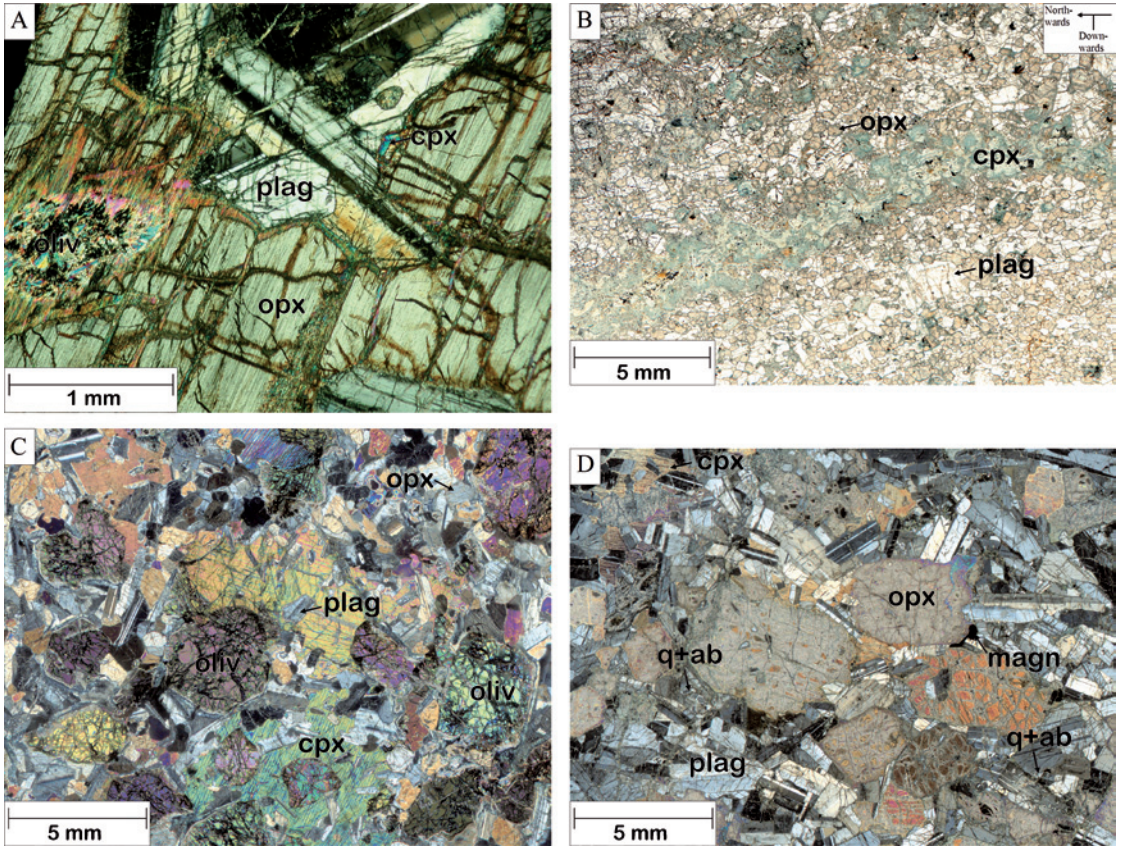


Fig. 5.6. Photomicrographs of textures in the Lower Zone. **A.** Partly altered poikilitic plagioclase-olivine mesocumulate (poCb\*a\*) of the LZa (23-TTK-01, crossed nicols). **B.** Microrhythmic layering in partly altered bronzite-plagioclase mesocumulate (bpCa) of the LZa (20-TTK-01, parallel nicols. Note the symbol indicating northwards-downwards directions in the photomicrograph). **C.** Unaltered poikilitic olivine-plagioclase-bronzite orthocumulate (opbCa\*) of the LZa (24-TTK-01, crossed nicols). **D.** Partly altered poikilitic plagioclase-bronzite mesocumulate (pbCa\*) of the LZb (284-TTK-00, crossed nicols). Abbreviations: plag = plagioclase, oliv = olivine, cpx = clinopyroxene, opx = orthopyroxene, magn = magnetite, q+ab = granophytic intergrowth of quartz and albite.

### 5.5.2 Middle Zone

The 450 m thick Middle Zone (MZ) (Fig. 5.1) is divided into three subzones that show monotonous layering and weak plagioclase lamination.

The MZa is ca. 50 m thick and represents the uppermost olivine-bearing subzone of the Koillismaa Intrusion. The subzone is composed of a poikilitic plagioclase-olivine-bronzite mesocumulate with oikocrystic augite (pobCa\*) (Fig. 5.7.A). Similarly to the LZa olivine gabbro-norites, garnet and brown

igneous mica are typical accessory phases in the MZa.

Using conventional classification, subzones MZb and MZc are gabbro-norites, but on the basis of the cumulus classification, the MZb is small to medium-grained plagioclase-bronzite mesocumulate (pbCa) containing interstitial granophytic intergrowths of albite and quartz (Fig. 5.7.B) whereas the MZc is a medium-grained plagioclase-hypersthene augite adcumulate (phaC) (Fig. 5.7.C). The boundary between MZb and MZc is marked by the disappearance of cumulus bronzite and the si-

multaneous appearance of cumulus augite and pigeonite, now inverted to hypersthene. The change in the nature of cumulus phases at the boundary between the two subzones is reflected in an increase in plagioclase grain size in MZc (Fig. 5.2). In addition, the boundary is characterized by an occurrence of noncumulus-textured gabbro-norite bodies (described in detail in Chapter 5.7). In the stratigraphic section of Fig. 5.1, the boundary is located at 850 m in the Porttivaara block.

### 5.5.3 Upper Zone

The 1250 m thick Upper Zone (UZ) accounts for about half of the entire thickness of the LS (Fig. 5.1). In the contact zone between the MZ and the UZ, the amount of inverted pigeonite diminishes gradually and gives way to cumulus plagioclase and augite.

The rocks of the ca. 170 m thick UZa are usually highly altered gabbros and leucogabbros (Fig. 5.7.D). These rocks are plagioclase adcumulates (paC) whose intercumulus material consists of granophyric intergrowths of quartz and albite. Locally these rocks also contain cumulus ilmenomagnetite.

In the following 240 m thick UZb plagioclase and augite crystallized with titaniferous magnetite as cumulus phases (pamC) (Fig. 5.7.E). The rock of the UZb is magnetite gabbro adcumulate that is characterized by its metallic lustre caused by grains of ilmenomagnetite.

The 840 m thick UZc is a massive and altered anorthosite, consisting of cumulus plagioclase with intercumulus augite (pCa) (Fig. 5.7.F). Other interstitial phases consist of granophyric intergrowth of quartz and albite.

## 5.6 Granophyre

The main minerals of the granophyre are plagioclase, quartz and biotite. The texture of the rock is typically medium-grained showing phenocrysts of unzoned albite in a matrix consisting of biotite and granophyric intergrowths of quartz and albite. The granophyre is texturally and mineralogically extremely uniform.

Only in the stratigraphically uppermost outcrops, the granophyric texture disappears and the grain size decreases towards the top of the granophyre layer (Karinen 1998). In the Porttivaara block, the granophyre forms a layer up to 1000 m in thickness.

## 5.7 Noncumulus-textured gabbro-norite bodies

In several parts of the Koillismaa Intrusion there occur lenticular noncumulus-textured gabbro-norite bodies that are conformable to the igneous layering of the intrusion. The bodies are found in LZa (see Fig. 5.5), LZb and also, as noted by Kerkkonen (1976), in MS. However, most of these bodies can be found at the level where MZb gives way to MZc. No bodies have so far been found at higher stratigraphic levels. Partly due to lack of exposure,

the dimensions of the bodies cannot be reliably measured. However, the largest bodies, measuring up to 6 m in thickness, are found near the boundary between the MZb and MZc, whereas bodies located in stratigraphically lower subzones are generally less than 1 m thick. The locations of the noncumulate bodies are shown by star symbols in the geological map of Fig. 5.8.

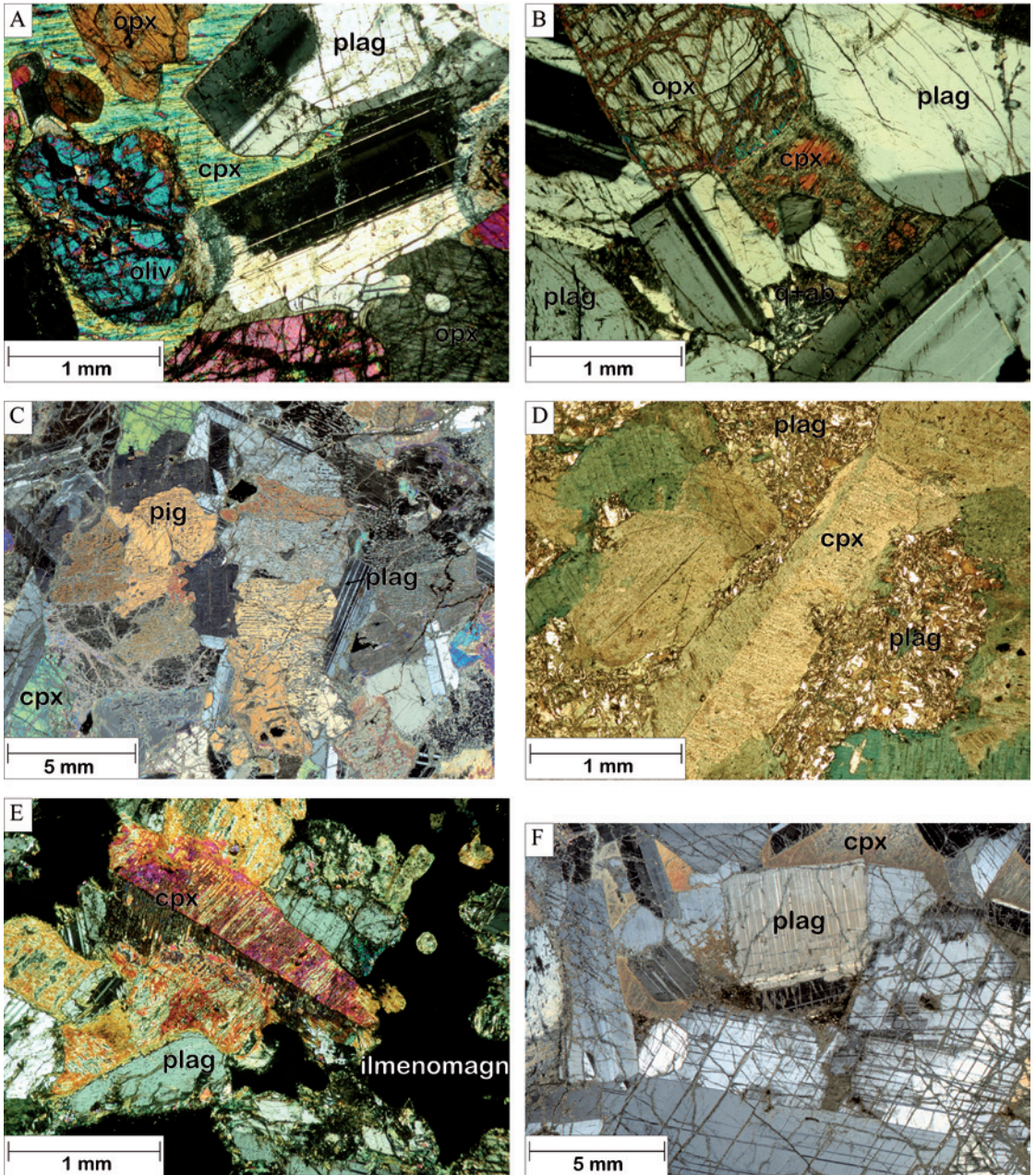
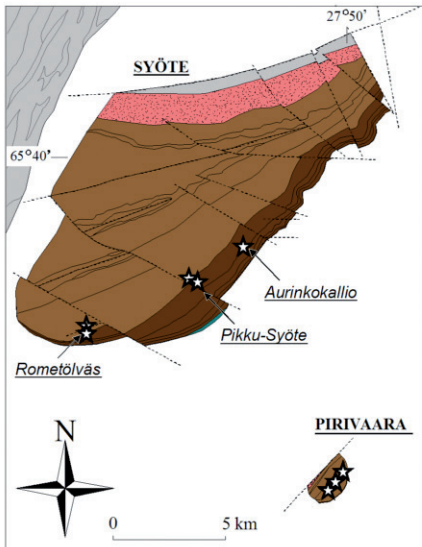
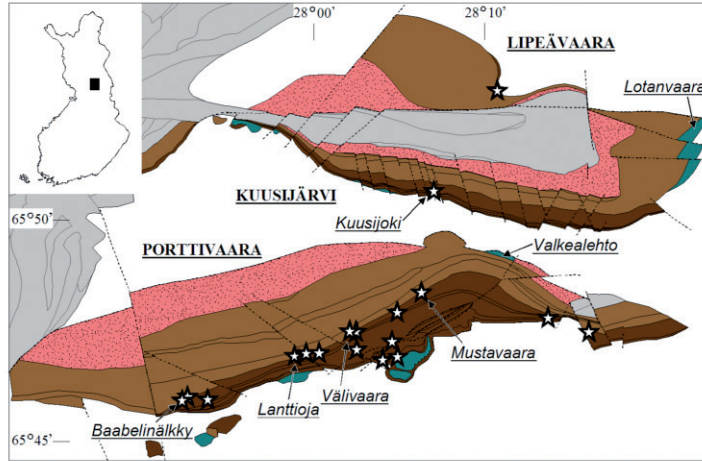


Fig. 5.7. Photomicrographs of textures in the Middle and Upper Zones. **A.** Unaltered poikilitic plagioclase-olivine-bronzite mesocumulate (pobCa\*) of the MZA (14-TTK-01, crossed nicols). **B.** Unaltered poikilitic plagioclase-bronzite mesocumulate (pbCa\*) of the MZb (311-TTK-00, crossed nicols). **C.** Unaltered plagioclase-hypersthene-augite adcumulate (phaC) of the MZc (6-TTK-03, crossed nicols). **D.** Highly altered plagioclase-augite adcumulate (paC) of the UZA (327-TTK-00, parallel nicols). **E.** Partly altered plagioclase-augite-magnetite adcumulate (pamC) of the UZb (335-TTK-00, crossed nicols). **F.** Coarse-grained and partly altered plagioclase mesocumulate (pCa) of the UZc (345-TTK-00, crossed nicols). Abbreviations: plag = plagioclase, cpx = clinopyroxene, opx = orthopyroxene, pig = inverted pigeonite, q+ab = granophyric intergrowth of quartz and albite, ilmenomagn = magnetite with ilmenite exolutions.



- Supracrustal rocks
  - Granophyre
  - Cumulates above the MZb
  - Cumulates below the MZc
  - Mafic rocks close to the basal contact of the intrusion
  - Noncumulus-textured gabbronorite body
  - Fault
- } Koillismaa Intrusion

Fig. 5.8. Geological map showing the locations of the noncumulus-textured gabbronorite bodies of the Koillismaa Intrusion.

The contact between the noncumulate bodies and their host cumulates are commonly sharp but lacking distinct chilled margins (Fig. 5.9.A). A typical microtexture of a small gabbronoritic noncumulate body is shown in Fig. 5.9.B. In terms of their textures and phase distributions most of these bodies are identical to the rocks of Lotanvaara unit (compare Fig

5.3.B and 5.9.B). However, exceptions do occur. For example, one small body in the Baabelinälkky area consists of cumulus-textured serpentinite. Some of the largest noncumulus-textured gabbronorite bodies include pockets of coarser bronzite segregations that host apatite and brown igneous mica (Figs 5.9.C and D).

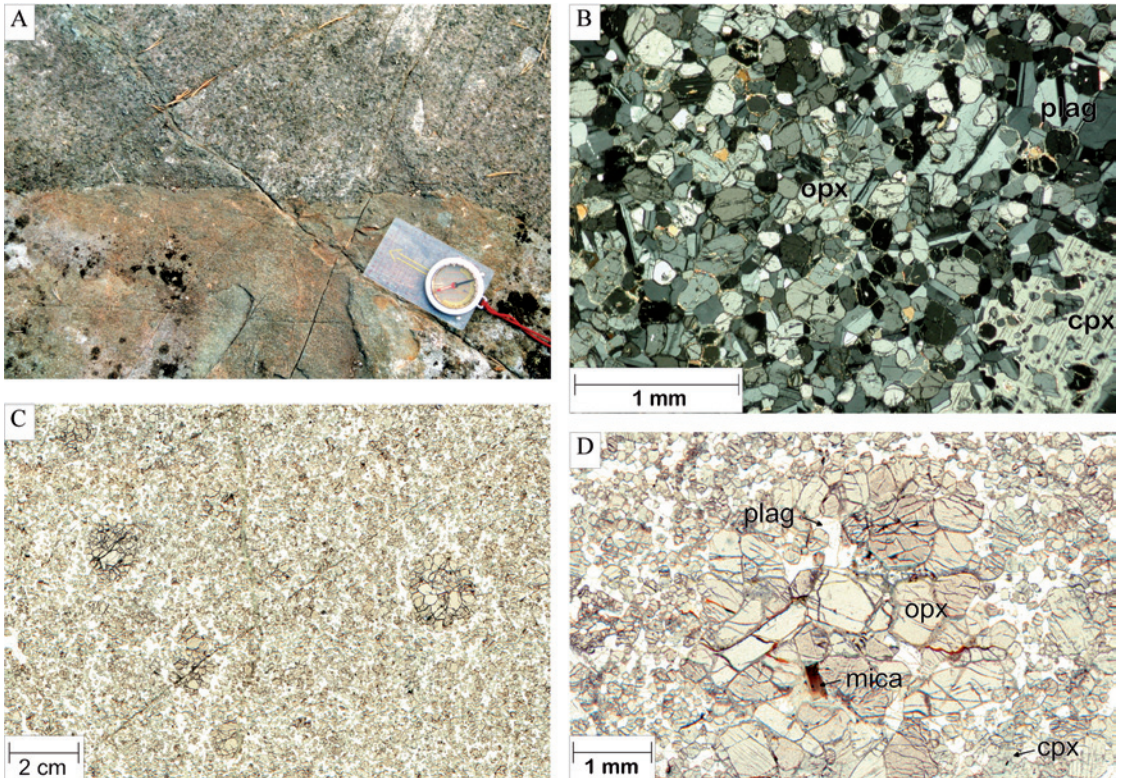


Fig. 5.9. Outcrop photo and photomicrographs of noncumulus-textured gabbronorite bodies. **A.** Contact of a noncumulus-textured body and gabbronorite of the MZ (81-TTK-00, length of the compass is 10 cm). **B.** Microtexture of an unaltered and fine-grained body (15.2-TTK-00, crossed nicols). **C.** Bronzite segregations in a body (15-TTK-03, parallel nicols). **D.** Bronzite segregation in a body (10-TTK-03, parallel nicols). Abbreviations: plag = plagioclase, cpx = clinopyroxene, opx = orthopyroxene.

The petrographic investigation of a 6 m thick noncumulate body in drill core B7 from the Rometölväs area revealed a systematic textural change from the body margins towards the interior. The analytical intervals and thin sections collected from the body are shown in Fig. 5.10, which also displays textures and modes of the principal rock-forming minerals in the section of the body.

The 6 m thick body is mostly unaltered; only pyroxenes at the margins of the body show alteration. The upper alteration zone is ca. 1 m thick and the lower one is less than 0.5 m thick. As shown in Fig. 5.10, both the upper

and lower margins belong to the “Quenched area” where the rock shows an equigranular and fine-grained assemblage of plagioclase, augite and bronzite. Towards the interior of the body, the rock develops a poikilitic texture of augite and bronzite oikocrysts up to 5 mm in size. These oikocrysts are sieved, enclosing numerous small (< 0.2 mm), euhedral plagioclase chadacrysts that occasionally show increasing grain size from the oikocryst cores to the margins. The matrix to the oikocrysts is mosaic-textured, comprising coarser (0.2–0.5 mm) plagioclase grains which show 120° triple junctions between the grains. (Fig.

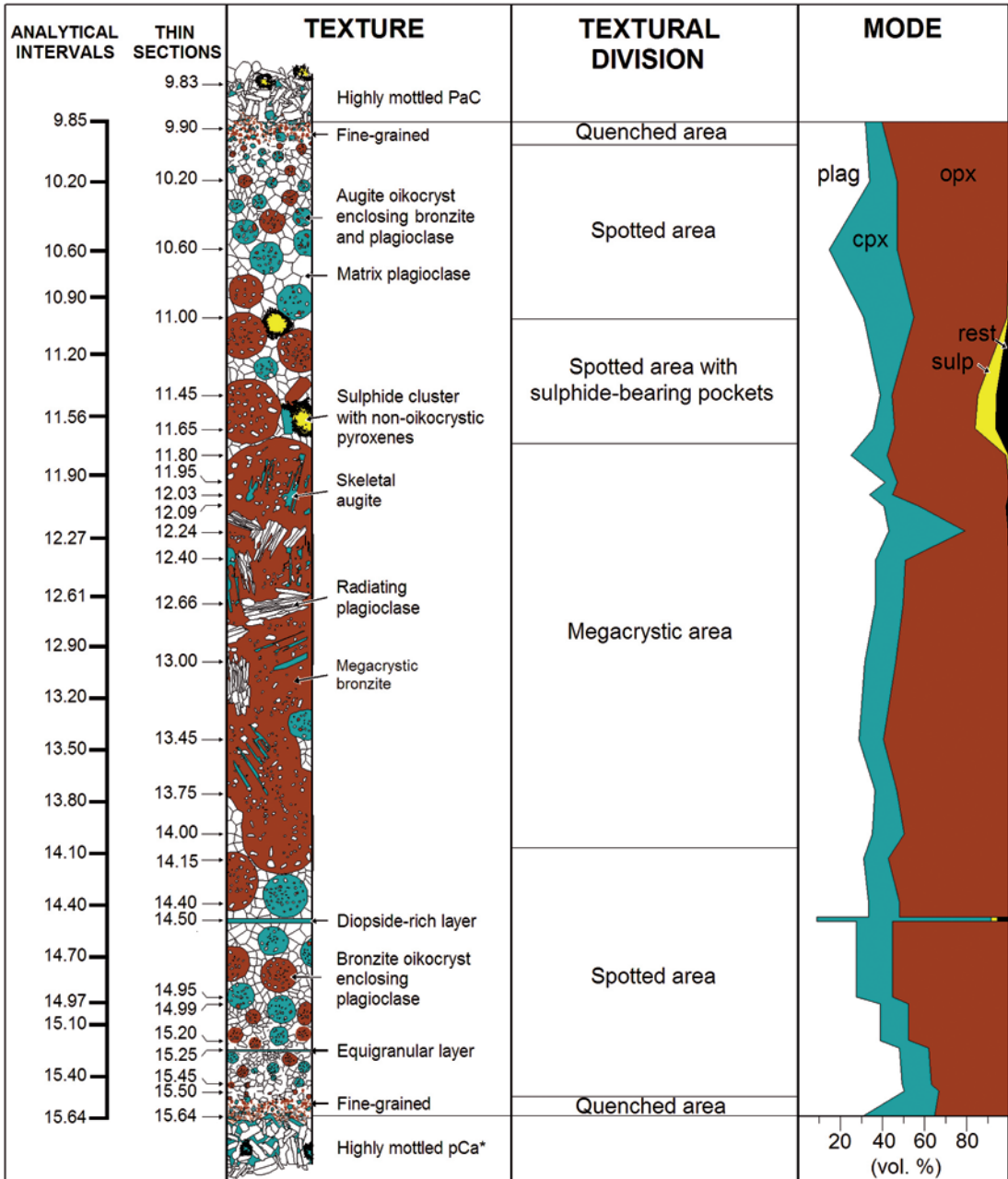


Fig. 5.10. Section through the noncumulus-textured gabbronorite body at 9.85-15.65 m in drill core B7, showing from left to right: analytical intervals, thin section sampling locations, schematic illustration of rock textures, textural subdivision and modal distribution of plagioclase (plag), clinopyroxene (cpx), orthopyroxene (opx), sulphide minerals (sulp) and amphibole+epidote+orthoclase+apatite+quartz (rest). Colours: brown = orthopyroxene, bluish green = clinopyroxene, white = plagioclase, yellow = sulphides, black = amphibole+epidote+orthoclase+apatite+quartz.

5.11.A). Due to the oikocrysts, the rock has a spotted appearance and therefore this portion of the body is termed the “Spotted area“. The interior of the noncumulate body is characterized by megacrystic bronzite that lacks exsolution lamellae and encloses numerous small (< 0.2 mm) euhedral plagioclase chadacrysts. This type of texture has been termed the “Megacrystic area“. In this part of the body, most of the augites appear as up to 5 mm long, skeletal and embayed hopper crystals,

which are also free of exsolution lamellae (Fig. 5.11.B). The mosaic-textured plagioclase surrounding the megacrysts mostly forms a similar mosaic-textured tortuous framework as that in the “Spotted area” (Fig. 5.11.C.). In the very middle part of the “Megacrystic area”, between 12.24 and 13.45 m depth in the drill core, exsolution-free bronzite megacrysts are tightly stacked and plagioclase exhibits radiating bunches of crystals (Fig. 5.11.D).

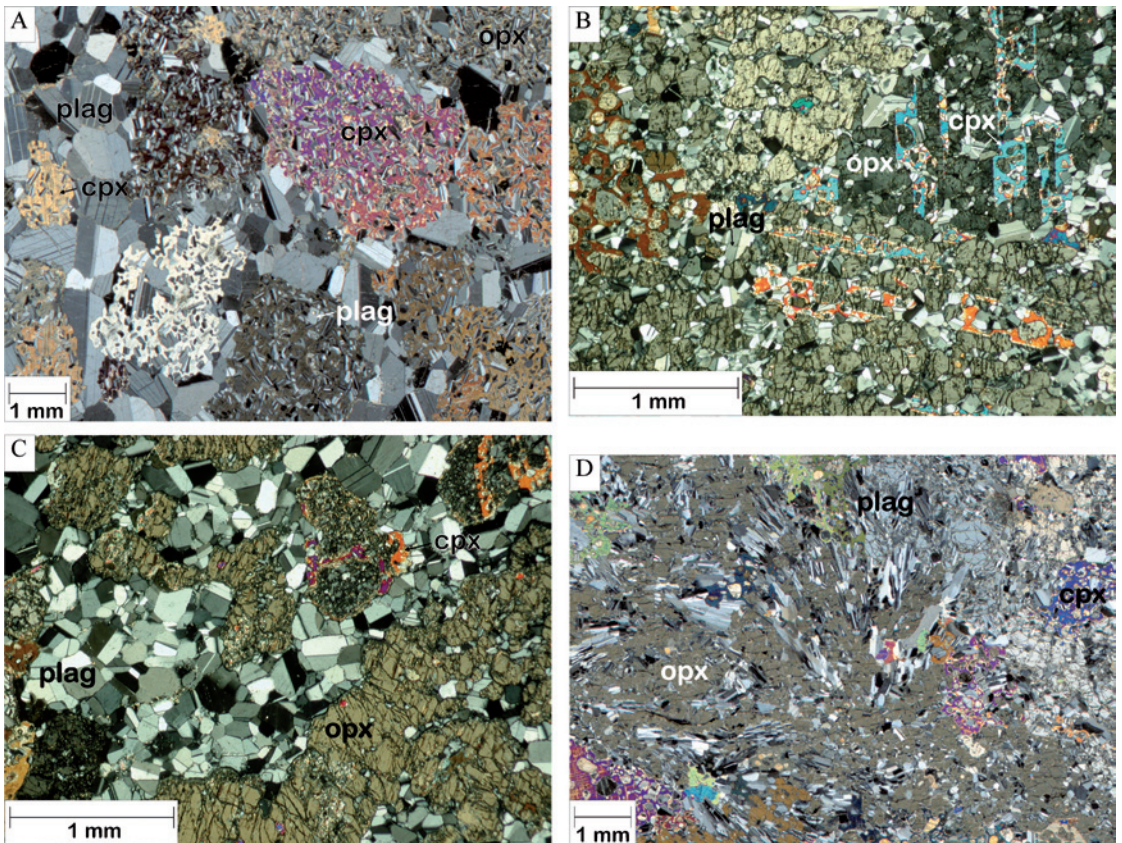


Fig. 5.11. Photomicrographs of textures in the noncumulate body of drill core B7. **A.** Oikocrystic bronzite and augite enclosing small plagioclase. Matrix plagioclase displays  $120^\circ$  triple junctions between crystals (B7 15.50, crossed nicols). **B.** Embayed and skeletal crystals of augite in megacrystic bronzite and a netted framework plagioclase (B7 13.00, crossed nicols). **C.** Megacrystic bronzite and mosaic-textured framework of plagioclase (B7 14.99, crossed nicols). **D.** Radiating plagioclase enclosed by oikocrystic orthopyroxene (B7 12.40, crossed nicols). Abbreviations: plag = plagioclase, cpx = clinopyroxene, opx = orthopyroxene.

Sulphides are located in the upper-central portion of the body (Fig. 5.10). The sulphides consist of chalcopyrite, pyrrhotite and pentlandite, and occur together with plagioclase, ortho- and clinopyroxene, greenish amphibole, chlorite, talc, quartz, orthoclase and apatite in cm-sized pockets or segregations that display a coarser grain size than their surroundings. In these pockets, the pyroxenes are mostly non-oikocrystic in contrast to the pyroxenes in the surrounding rocks. The pockets are also characterized by the presence of loveringite and brown igneous mica. However, the most sulphide-rich interval, around 11.50 m in the core, is free of loveringite. The

texture in the most sulphide-rich interval in the body is shown in the photomicrographs of Fig. 5.12.

In the lower part of the body occur two distinct, mm- to cm-wide layers of fine-grained gabbro. The upper one of the layers is a few cm thick and is located at the depth of 14.50 m in the drill core. The clinopyroxene in this layer is optically zoned, exsolution-free and occurs mostly as anhedral grains 2–4 mm in size, but also as drop-like up to 0.2 mm chadacrysts in oikocrystic plagioclase (Fig. 5.13.A). The lower layer is ~5 mm thick and is located at depth 15.25 m in the drill core. It has a granular texture (Fig. 5.13.B).

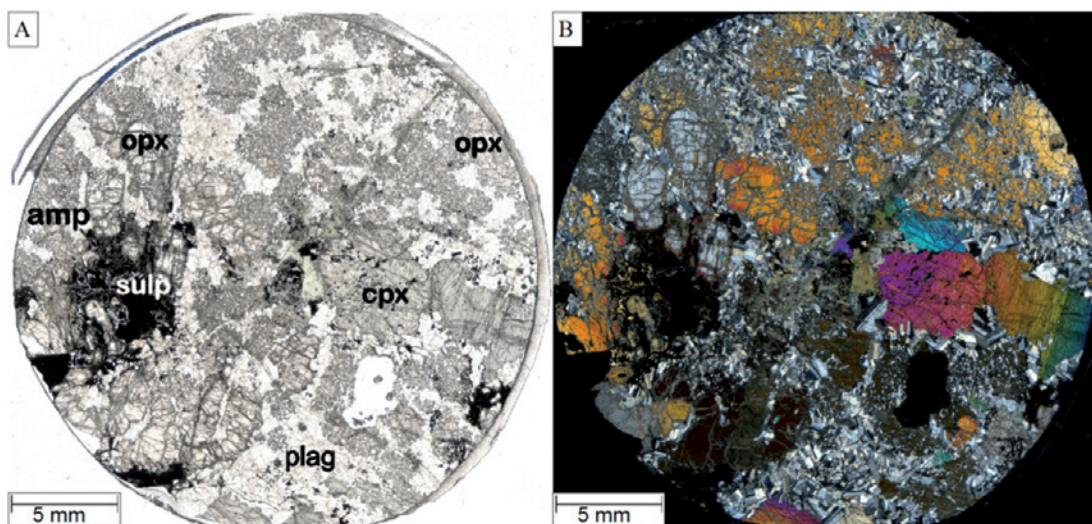


Fig. 5.12. Photomicrographs of a sulphide-rich area in the noncumulate body of drill core B7 (B7 11.65, **A** with parallel nicols and **B** with crossed nicols). Abbreviations: sulp = sulphides, amp = amphibole, plag = plagioclase, cpx = clinopyroxene, opx = orthopyroxene.

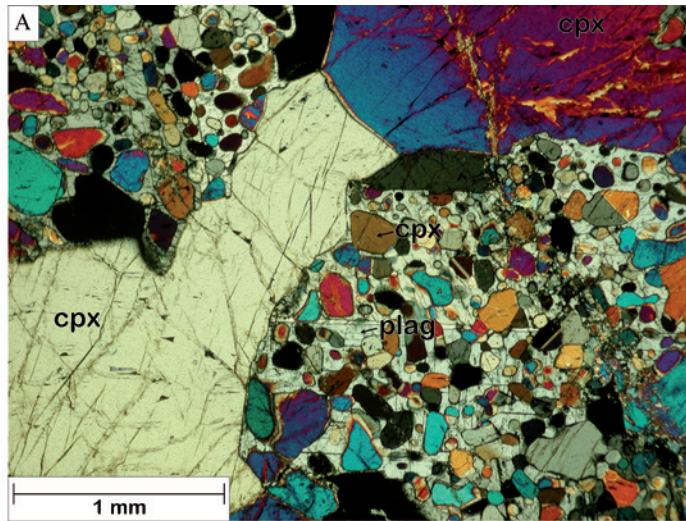


Fig. 5.13. Photomicrographs of textures in the noncumulate body of drill core B7. **A.** Unaltered gabbro layer containing anhedral clinopyroxene and oikocrystic plagioclase enclosing small drop-like diopside crystals (B7 14.50, crossed nicols). **B.** Granular layer in “Spotted-textured” section of the body (B7 15.25, parallel nicols). Abbreviations: plag = plagioclase, cpx = clinopyroxene.

### 5.8 Rometölväs Reef

As described in the previous chapter, the boundary between subzones MZb and MZc constitutes the stratigraphically highest and principal occurrence of the noncumulus-textured gabbronorite bodies. In many cases, this boundary is also Cu-Ni-PGE-enriched. The mineralization has been studied in the Rometölväs sampling site of the Syöte block and in the Baabelinälkky, Lanttioja, Väliavaara and Mustavaara sampling areas of the Porttivaara block. The same mineralized layer is also exposed in a few outcrops in the Pikku-Syöte and Aurinkokallio areas of the Syöte block (not investigated in detail) and has been intersected by drilling in the Kuusijoki area of the Kuusijärvi block. The locations of these areas are shown in Fig. 5.8.

The abovementioned sites can be regarded as representatives of the Cu-Ni-PGE-mineralized zone in the LS of the Koillismaa Intrusion, which is hereafter referred to as the Rometölväs Reef (RT Reef). All occurrences share a close association with the MZb-MZc border, the occurrence of noncumulate bodies and the association of pyrrhotite, chalcopyrite and pentlandite in cm-sized pockets of clus-

ters or mottles with relatively low-temperature minerals such as amphibole, clinozoisite-epidote, calcite, chlorite, biotite, quartz, apatite and scapolite.

Due to the clusters the mineralized rocks show a mottled appearance. Therefore, the Cu-Ni-PGE-mineralized rocks are subdivided into three types: weakly mottled, moderately mottled and highly mottled. In the weakly mottled type the mottles make up less than 10 vol. % of the rock. The moderately mottled type contains 10–30 vol. % mottles, whereas the highly mottled type contains more than 30 vol. % mottles.

The mottles have clearly replaced the intercumulus phases of cumulates. The central domains of the mottles include scapolite, pentlandite and pyrrhotite, whereas the margins contain fine-grained clinozoisite-epidote and chalcopyrite. Quartz is associated with chlorite and, in small fissures, with calcite and scapolite. Adjacent to sulphides in the mottles, the amphiboles display zonation from light-coloured central domains to darker coloured margins. Figure 5.14 shows a typical microtexture of a mottle.

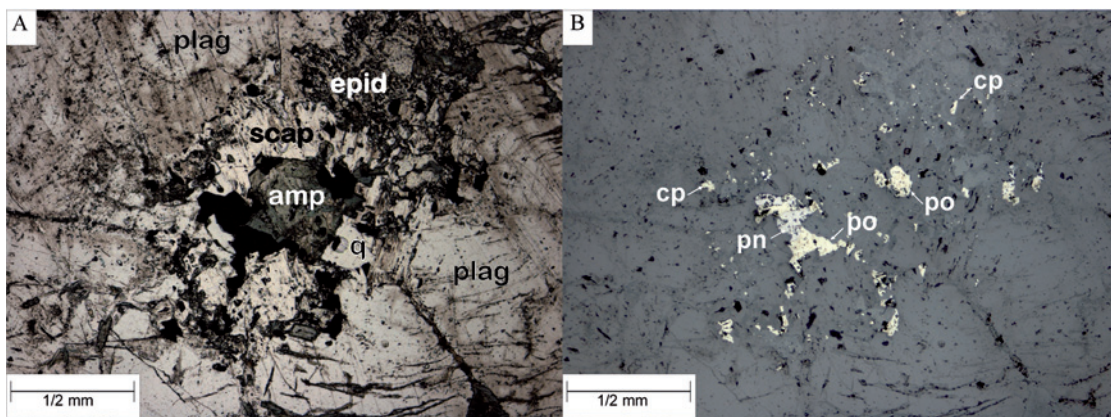


Fig. 5.14. Photomicrograph of a mottle: **A** is taken with parallel nicols and **B** is taken with reflected light and parallel nicols (B7 9.83, Rometölväs). Abbreviations: plag = plagioclase, scap = scapolite, epid = epidote, amp = amphibole, q = quartz, cp = chalcopyrite, pn = pentlandite, po = pyrrhotite.

### 5.8.1 Rometölväs

The Rometölväs area is located near the southern margin of the Syöte block. In the cumulates of the area, primary textures reveal as a weak plagioclase lamination, which is gently northwards dipping (30°) in the southern parts of the area, but in some northernmost outcrops, it dips with an angle of 65° towards the north. These cumulates belong to the MZc, since already in the stratigraphically lowermost outcrops of the area, augite is a cumulus phase. The Rometölväs contains a large number of discrete noncumulus-textured gabbro bodies.

Figure 5.15 shows a section of drill core B7. The most intensively mottled and most sulphide-enriched cumulates are located in the upper part of the drill core, in a 20 m thick interval that is overlain by adcumulates. These highly mottled rocks are gabbros and anorthosites and can be classified as poikilitic plagioclase orthocumulates (with oikocrystic augite) and plagioclase mesocumulates, in which the intercumulus material is mostly quartz. A distinct feature of the most intensively mottled cumulates is that they show more grain size variation in plagioclase than the other rocks. The highly mottled interval in the drill core includes the 6 m thick sulphide-bearing noncumulate body described in detail in Chapter 5.7.

### 5.8.2 Baabelinälkky

The Baabelinälkky area comprises variously mottled cumulates and a few noncumulus-textured gabbro bodies. As shown in Fig. 5.16, drilling has confirmed that the sul-

phide-bearing interval in the area is up to 20 m in thickness with a relatively gentle dip (35–40° NNW).

A section drill core B1 is shown in Fig. 5.17. The upper part of the drill core is composed of unaltered, weakly mottled gabbro-orthic adcumulate (pahC) belonging to the MZc. This rock hosts a noncumulate-textured gabbro body, at depth 2.40–2.70 m in the drill core. The highly mottled, Cu-Ni-PGE-enriched cumulates are anorthosites associated with the noncumulus-textured gabbro body located at depth 18.74–19.56 m in the drill core. The highly mottled cumulate surrounding the noncumulate body is anorthosites. The most intensively mottled cumulate can be found below the noncumulate body, where the rock is apatite-rich plagioclase cumulate (pC).

### 5.8.3 Lanttioja

The Lanttioja area comprises small gabbro and gabbro outcrops, which display a subtle and low-angle (40–45° NW) plagioclase lamination (Fig. 5.18). The stratigraphically lowest outcrops (135.1, 2, 3-TTK-99) consist of weakly mottled gabbro (pahC). The presence of cumulus augite suggests that the rock belongs to the MZc. In the Cu-Ni-PGE-enriched, more intensively mottled areas, such as represented by samples 135.4, 6, 7, 8, 10, 11, 12, 13 and 135.14-TTK-99, augite is usually oikocrystic. The sampling sites shown in the outcrop map of Fig. 5.18 do not contain noncumulate bodies, but one small noncumulate body was located 30 m to the west of the area.

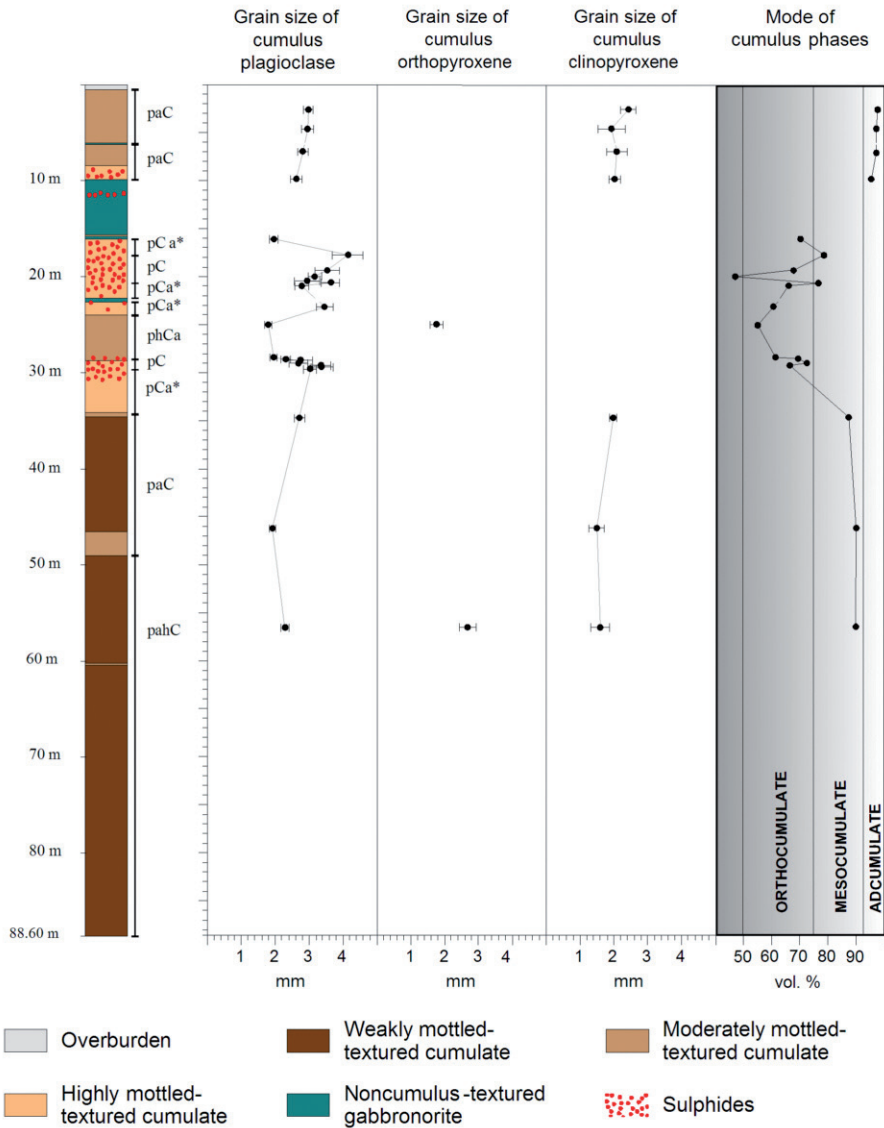


Fig. 5.15. Section of drill core B7 (Rometölväs) showing rocks, cumulus classification and grain size variation of major cumulus phases in the drill core. Pyroxene grain sizes are estimated from pseudomorphs. The error in the grain size is given as the standard error of mean ( $s/\sqrt{n}$ ).

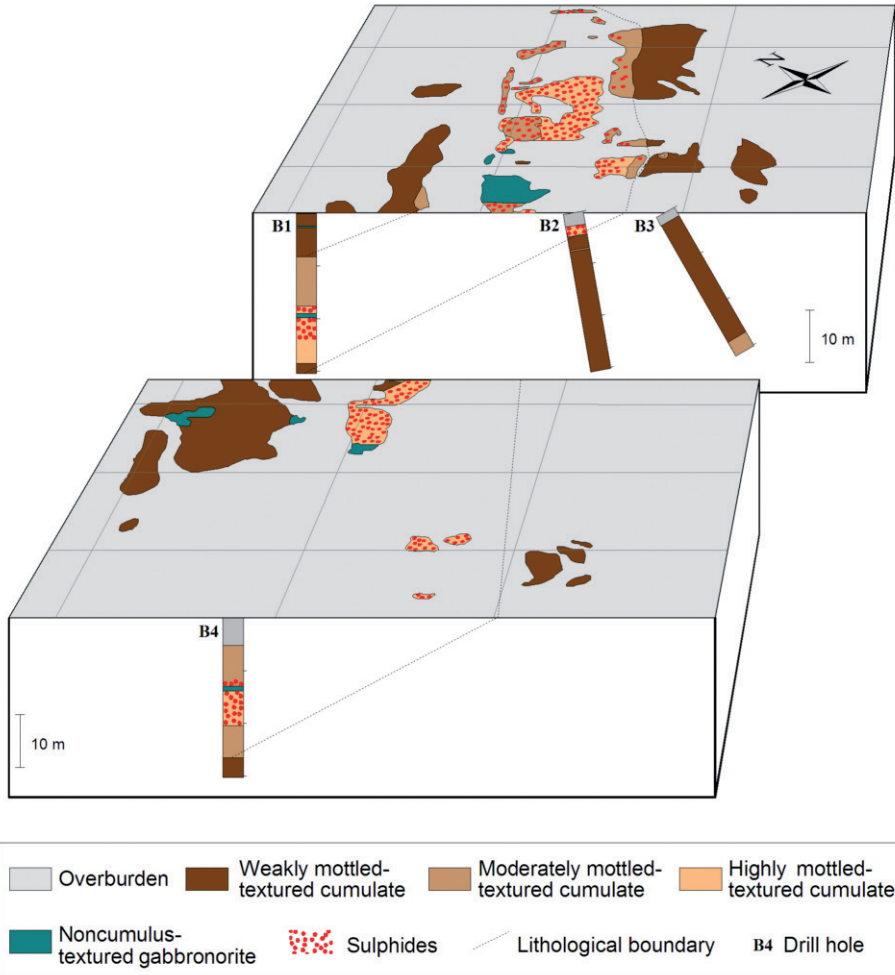


Fig. 5.16. Outcrop map of the Baabelinälkky area with drill hole cross sections. Modified from the map of Isohanni (1976).

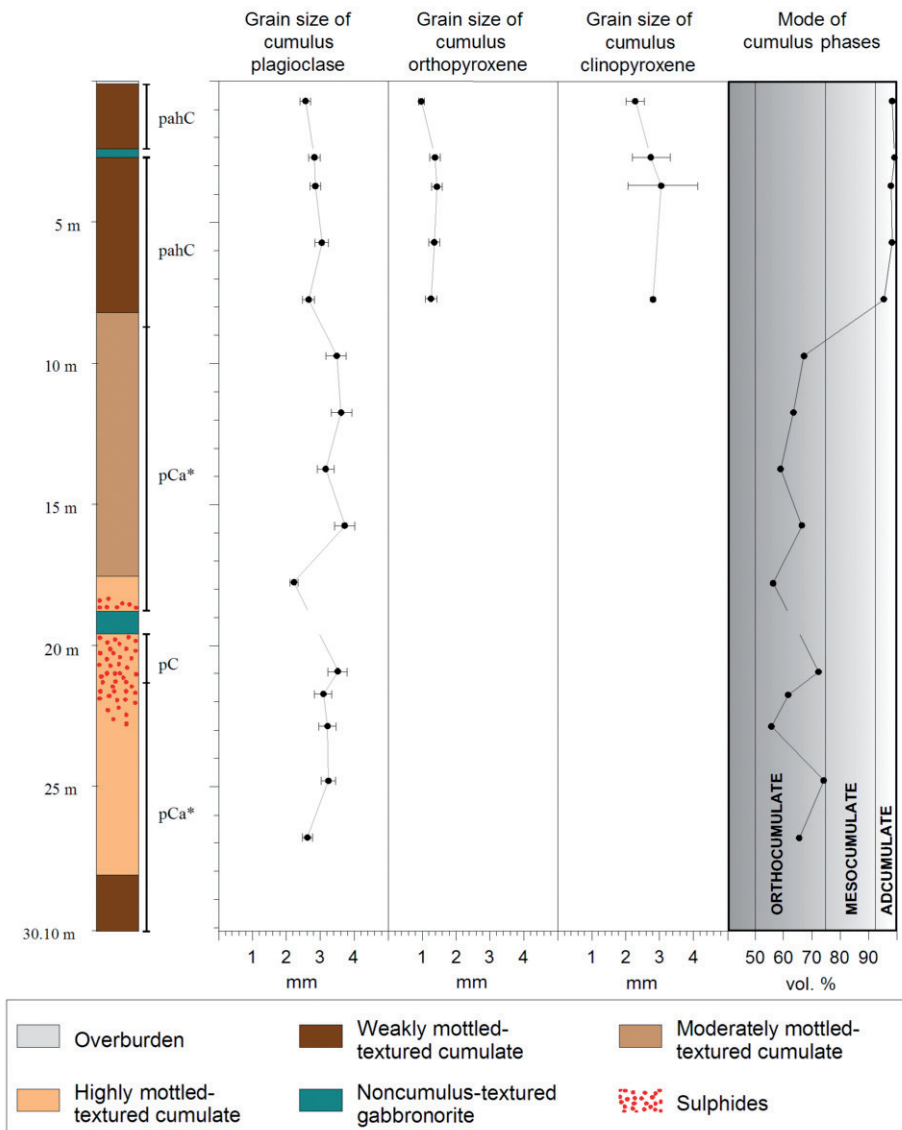


Fig. 5.17. Section of drill core B1 (Baabelinälkky) showing rocks, cumulus classification and grain size variation of major cumulus phases in the drill core. Pyroxene grain sizes are estimated from pseudomorphs. The error in grain size is given as the standard error of mean ( $s/\sqrt{n}$ ).

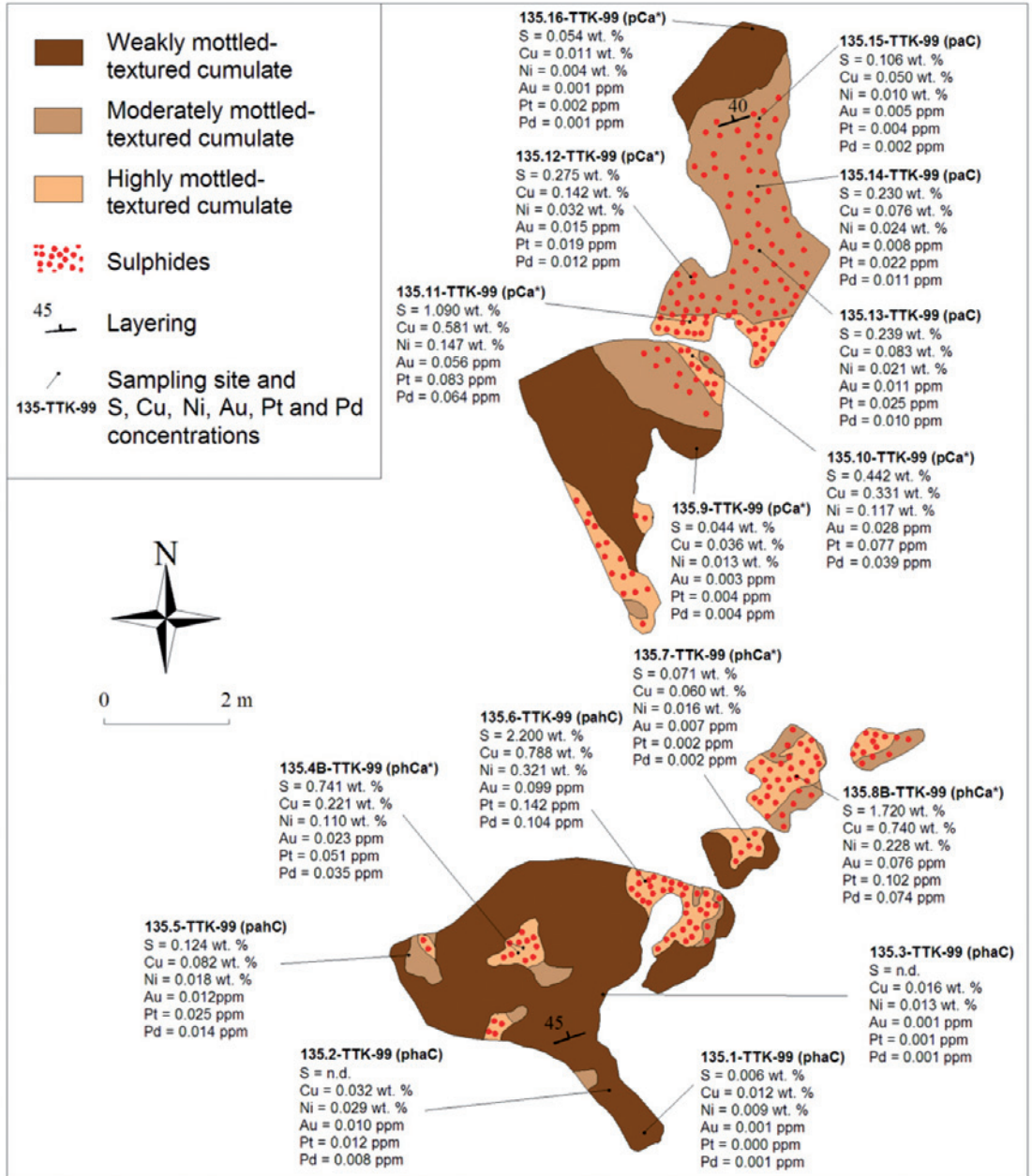


Fig. 5.18. Outcrop map of the Lantioja area showing the distribution of mottled cumulates.

## 5.8.4 Vällivaara and Mustavaara

The Vällivaara area forms part of the Porttivaara mapping profile, whilst the Mustavaara area is located a few hundred meters to the northeast of the profile. In the Vällivaara area, the reef occurs exactly at the MZb-MZc boundary, ca. 850 m above the base of the intrusion, since the Cu-Ni-PGE-mineralized sample (314-TTK-00) is the first to contain cumulus augite. In the Mustavaara area the mineralization is situated within the MZc cumulates. Both the Vällivaara and Mustavaara areas contain noncumulate bodies.

### 5.8.5 Distribution of variably mottled cumulates in the sampling sites

Although the RT Reef appears to be mostly situated close to the boundary between the MZb and MZc, detailed examination of the sampling areas reveals that the boundary does not strictly constrain the localization of the

mineralization. The sulphide-bearing mottles occur in several types of cumulates - gabbros, gabbroonorites and anorthosites, in which the distribution of the mottles is controlled by the amount of intercumulus material and also by the location of the noncumulus-textured gabbroonorite bodies.

Figure 5.19 illustrates mineral distributions in mineralized, variously mottled cumulates of the Rometölväs, Baabelinälkky, Lanttioja, Vällivaara and Mustavaara sampling sites. Regardless of the appearance of the mottled texture pyroxenes are usually altered. It is therefore difficult to determine the original modal proportions in the mottles. Nevertheless, when considering the three types (weakly, moderately and highly mottled), it is obvious that there is a positive correlation between the degree of alteration, the amount of sulphide minerals, and the abundance of scapolite, epidote and quartz+apatite+carbonate. The proportion of oxides and biotite+chlorite does not change distinctly between alteration types.

## 5.9 Summary

The 2500 m thick Koillismaa Intrusion is divided into two series, five zones and twelve subzones. The Marginal Series (MS), which hosts two subzones, is characterized by a reverse trend of differentiation where the rocks grade upwards from gabbroonorites through pyroxenites to peridotites. The rocks are sulphide-mineralized, with the sulphides being mostly concentrated in the upper part of the gabbroonorites and the lower part of the pyroxenites. The Layered Series (LS) comprises three subzones. The Lower Zone (LZ) is composed of olivine gabbroonorite in its lower part and gabbroonorite in its upper part. The Middle Zone (MZ) begins with a thin layer of olivine gabbroonorite, which is overlain by a thick package of gabbroonorite. The middle part of the gabbroonorite is marked by the first appearance of cumulus augite and inverted cumulus

pigeonite. This level is defined as the boundary between subzones MZb and MZc. The Upper Zone (UZ) is characterized by magnetite gabbro sandwiched with anorthosites and leucogabbros. The lower and upper chilled margins of the intrusion are locally exposed, with the latter separating the cumulates from a thick and homogenous layer of granophyre.

The cumulates along the boundary between subzones MZb and MZc of the Middle Zone are marked by an enrichment of sulphide- and PGE-mineralization referred to as the Rometölväs Reef. The reef forms a diffuse and laterally inconsistent zone up to 20 m in thickness. On the basis of alteration, the cumulates of the reef are subdivided into weakly, moderately and highly mottled-textured types. This subdivision correlates positively with the abundance of sulphides. Commonly,

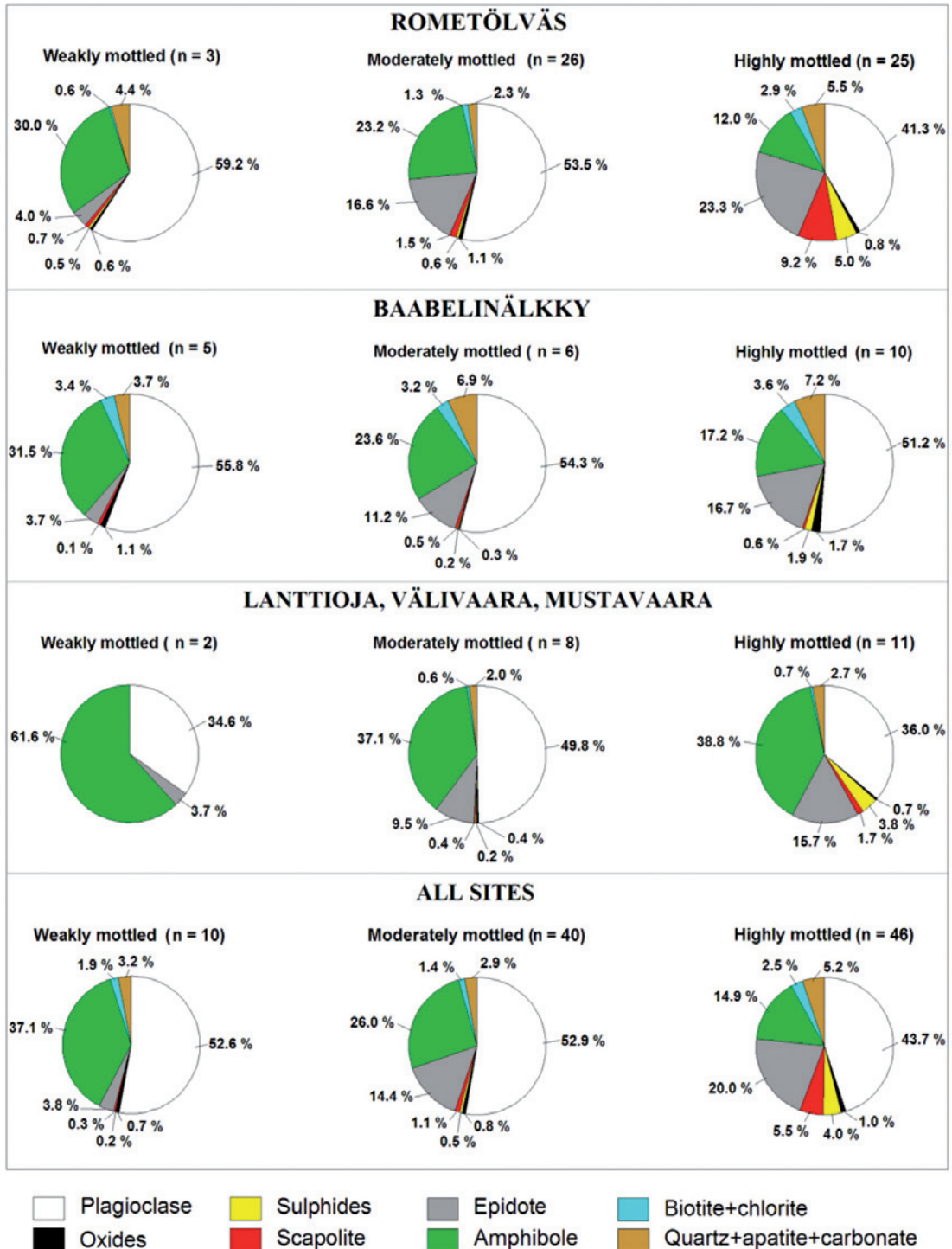


Fig. 5.19. Distribution of minerals in variously altered cumulates of the Rometölväs Reef sampling sites.

the most sulphide-rich and intensively mottled-textured cumulates are orthocumulates, whereas the less mottled cumulates are ad- to mesocumulates. A characteristic feature of the reef is the occurrence of lenticular, broadly concordant, meter-sized noncumulus-textured gabbronorite bodies that tend to be located within the altered, mottled, and mineralized zone. Some of the bodies are mineralized.

The Rometölväs Reef is the principal and uppermost level at which the noncumulate bodies have been found. They also occur at lower stratigraphic levels in the intrusion, but in these cases there are no sulphides associated with the bodies. Most of the noncumulus-textured bodies are texturally identical to the rocks of the Lotanvaara unit, which occurs at the base of the Koillismaa Intrusion.

## 6 MINERALS AND MINERAL CHEMISTRY

Mineral chemical investigations were focused on 1) cumulus, intercumulus and non-cumulus phases across the Koillismaa Intrusion, 2) minerals in the RT Reef and 3) sulphides and platinum-group minerals of the RT Reef and the MS. The principal aim of analysing cumulus, intercumulus and noncumulus phases was to study the compositional relations between minerals in the noncumulus-textured gabbronorite bodies and those

in the cumulates of the Koillismaa Intrusion, and accordingly their relations to the RT Reef. Therefore, the focus was placed on primary magmatic phases. Secondary phases were analysed when investigating the RT Reef, since the PGE mineralization occurs in the orthocumulate mottles. In the case of sulphides and precious metal phases, the purpose was to document and compare the mineral parageneses in the RT Reef and the MS.

### 6.1 Silicates

#### 6.1.1 Olivine

Electron microprobe analyses were usually conducted on the central parts of olivine crystals. Due to the general optical homogeneity of olivine, no traverses across individual grains were performed. The Fo mol. % in the olivine crystals ranges from 66.1-77.1, which corresponds to the results of Alapieti (1982) from the Porttivaara block. The most Fo-rich grains were found in olivine gabbronorite unit I of the LZa (22B-TTK-01), whereas the MZa hosts olivine crystals with the lowest Fo content (14-TTK-01). The NiO content in olivine ranges from 0.16 to 0.44 wt. % and correlates positively with Fo mol. %. All olivine analyses are given in Appendix 3.

#### 6.1.2 Pyroxenes

The pyroxenes of the study area consist of two types of Ca-poor phases; bronzite and inverted pigeonite, and two types of Ca-rich phases; augite and diopside. When analysing Ca-poor pyroxenes containing fine exsolution lamellae of augite parallel to {100} plane, a defocused beam on the plane {010} was used to obtain bulk composition of the original phase. The augites and inverted pigeonites which have coarse exsolution lamellae of orthopyroxene parallel to the {100} or {001} planes were analyzed using a focused beam on the {010} plane of the host phase, and as a consequence, only subsolidus compositions were obtained. In some cases, lamellae were

broad enough so that the composition of a single lamella could be determined using a focused beam. Selected pyroxene analyses are compiled in Appendices 4 and 5.

### 6.1.2.1 Noncumulate rocks

In Fig. 6.1.A pyroxenes from noncumulates are plotted into the En-Fs-Wo quadrilateral. Pyroxenes from the chilled margins are usually pervasively altered, but it was possible to analyse augite from two samples (10.2-TTK-98 and 38-TTK-00) of the upper chilled margin in the eastern Porttivaara block (“Kuusi-Pyhitys” in Fig. 4.1). In these samples, the composition of augite ranges from  $Wo_{40.5}En_{45.5}Fs_{14}$  to  $Wo_{40}En_{41}Fs_{19}$ . The augite and bronzite in the Lotanvaara mafic rock unit (“Lotanvaara” in Fig. 4.1) average  $Wo_{43}En_{45}Fs_{12}$  and  $Wo_3En_{74}Fs_{23}$ , respectively. In the noncumulus-textured gabbro-norite bodies the augite compositions range from  $Wo_{43}En_{47}Fs_{10}$  to  $Wo_{41}En_{38}Fs_{21}$  and the bronzite compositions from  $Wo_4En_{78}Fs_{18}$  to  $Wo_3En_{67}Fs_{30}$ . The noncumulate bodies of the Pirivaara block host the most Fe-rich pyroxenes, whereas the bodies of the Porttivaara and Kuusijärvi blocks host the most Mg-rich pyroxenes.

The clinopyroxene from the noncumulate body at 14.50 m in drill core B7 (Fig. 5.13.A, analysis 1 in Appendix 4) is of diopsidic composition in Morimoto’s (1988) classification. A microprobe traverse through a large (1350  $\mu\text{m}$  across), optically zoned and lamellae-free grain revealed reverse zoning: the composition varies smoothly from the border (36.5–37.6 mol. % En, 20.9–21.2 wt. % CaO, 0.3–0.5 wt. %  $TiO_2$  and 1.2–1.3 wt. %  $Al_2O_3$ ) to the core (35.2–35.4 mol. % En, 22.5–23.9 wt. % CaO, 0.2–0.3 wt. %  $TiO_2$  and 1.8–1.9 wt. %  $Al_2O_3$ ).

An electron microprobe traverse was also made across a large (600  $\mu\text{m}$  across) orthopyroxene grain within a pocket of coarse bronzite of sample 10-TTK-03 (Fig. 5.9.D) and across a small (32  $\mu\text{m}$  across) and opti-

cally zoned bronzite grain in the matrix of the pocket. The former is unzoned, whereas the latter shows normal zoning: 67 mol. % En component at the margin and 75 mol. % in the core. The skeletal augites in drill core B7 are unzoned when analysed with line traverses perpendicular to their elongation. Analysis 2 in Appendix 4 represents a composition of such augite.

Figures 6.2 and 6.3 depict pyroxene compositions across the noncumulus-textured body in drill core B7. The bronzites have Mg-numbers of 69.3–77.2, 0.2 wt. %  $Cr_2O_3$ , 0.1 wt. % NiO, 0.2 wt. %  $TiO_2$ , 0.8 wt. %  $Al_2O_3$  and 0.3 wt. % MnO. The augites have Mg-numbers of 74.4–83.3, 0.4 wt. %  $Cr_2O_3$ ,  $\leq 0.1$  wt. % NiO, 0.3 wt. %  $TiO_2$ , 1.4 wt. %  $Al_2O_3$ , 0.2 wt. % MnO and 0.2 wt. %  $Na_2O$ . As a result of zonation, the diopside grains at 14.50 m in the core show a large compositional variation, but otherwise, neither ortho- nor clinopyroxene grains show internal zonation or significant variations across the body.

### 6.1.2.2 Cumulate rocks

The composition of Ca-poor pyroxenes in the cumulates of the Koillismaa Intrusion ranges from  $Wo_3En_{77}Fs_{18}$  to  $Wo_4En_{58}Fs_{38}$  (Fig. 6.1.B). The grains of Ca-poor pyroxene in the cumulates have Mg-numbers of 62.5–81.3 and contain up to 0.6 wt. %  $Cr_2O_3$ , 0.1 wt. % NiO, 0.6 wt. %  $TiO_2$ , 0.8–2.0 wt. %  $Al_2O_3$  and 0.1–0.6 wt. % MnO.

The orthopyroxene in the lower part of the intrusion have fine exsolution lamellae parallel to the {100} plane, whereas in the MZc the orthopyroxene also contain coarser lamellae approximately parallel to the {001} plane (Fig. 6.4). This implies that orthopyroxene of the MZc originally crystallized as pigeonite above the orthorhombic-monoclinic inversion temperature and inverted to the orthorhombic form upon cooling. Hess (1960) named such orthopyroxenes the “Stillwater type”, and those orthopyroxenes that contains only fine

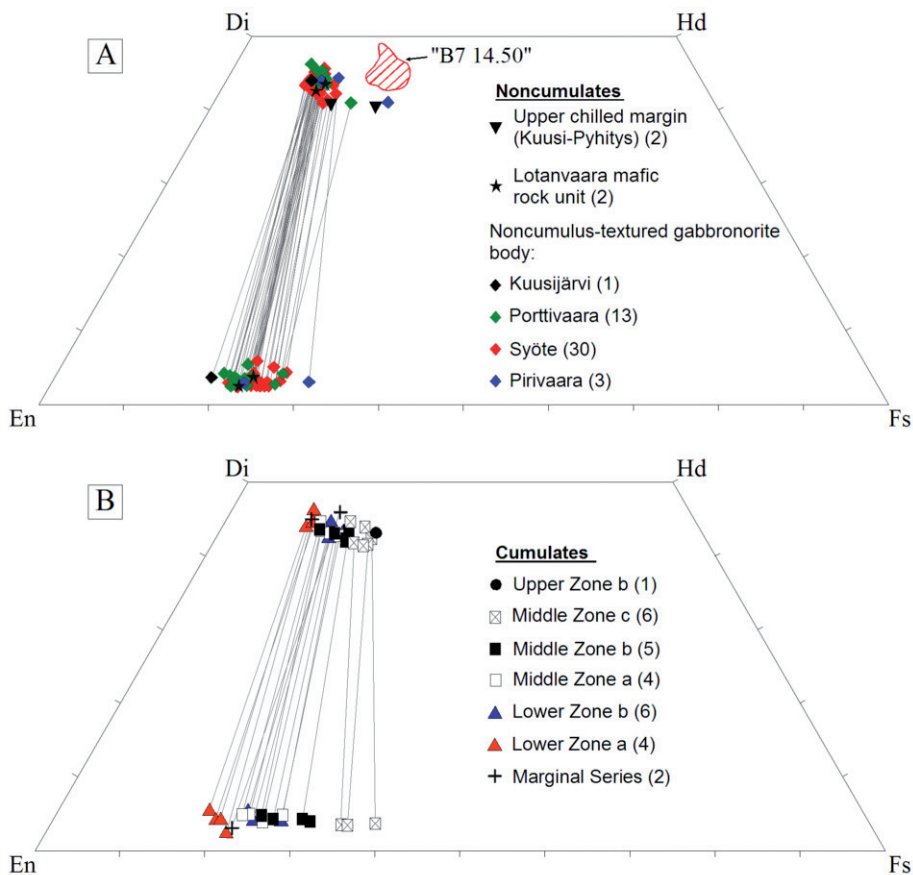


Fig. 6.1. Pyroxene compositions of noncumulates (A) and cumulates (B) in En-Wo-Fs quadrilaterals (mol. %). The symbols represent average compositions in a sample. The number of analysed samples are shown in parentheses. Pyroxene pairs are connected with tie lines. The red area in the quadrilateral of noncumulates represents clinopyroxene in a sample collected at a depth of 14.50 m in drill core B7 (see Figs 5.10 and 5.13.A).

lamellae parallel to {100} plane he named the "Bushveld type". In this research, the phases are referred to as primary orthopyroxene (Bushveld type) and inverted pigeonite (Stillwater type).

According to Hess (1941, 1960), Brown (1957) and Deer et al. (1995), the inverted pigeonite is stable at compositions more ferric than ca.  $En_{70}Fs_{30}$ . In primary orthopyroxenes the fine lamellae exsolve parallel to the {100} plane and crystallize as diopside, whereas the coarse lamellae in pigeonites are composed of augite, which exsolve on the {001} plane of pigeonite prior to inversion. After passing the monoclinic-orthorhombic inversion temper-

ature, pigeonite inverts to orthorhombic hypersthene, which itself exsolves a set of fine lamellae parallel to the {100} plane in a similar way as primary orthopyroxene does. Since these lamellae are extremely narrow (a few nanometers), their composition cannot be analysed accurately with an electron microprobe, but can be identified with the single crystal X-ray diffraction method or by optical determinations. In contrast, the coarse augite exsolutions parallel to the {001} plane of inverted pigeonite of the MZc are large enough to be analysed by microprobe (Fig. 6.4 and Analysis 9 in Appendix 4).

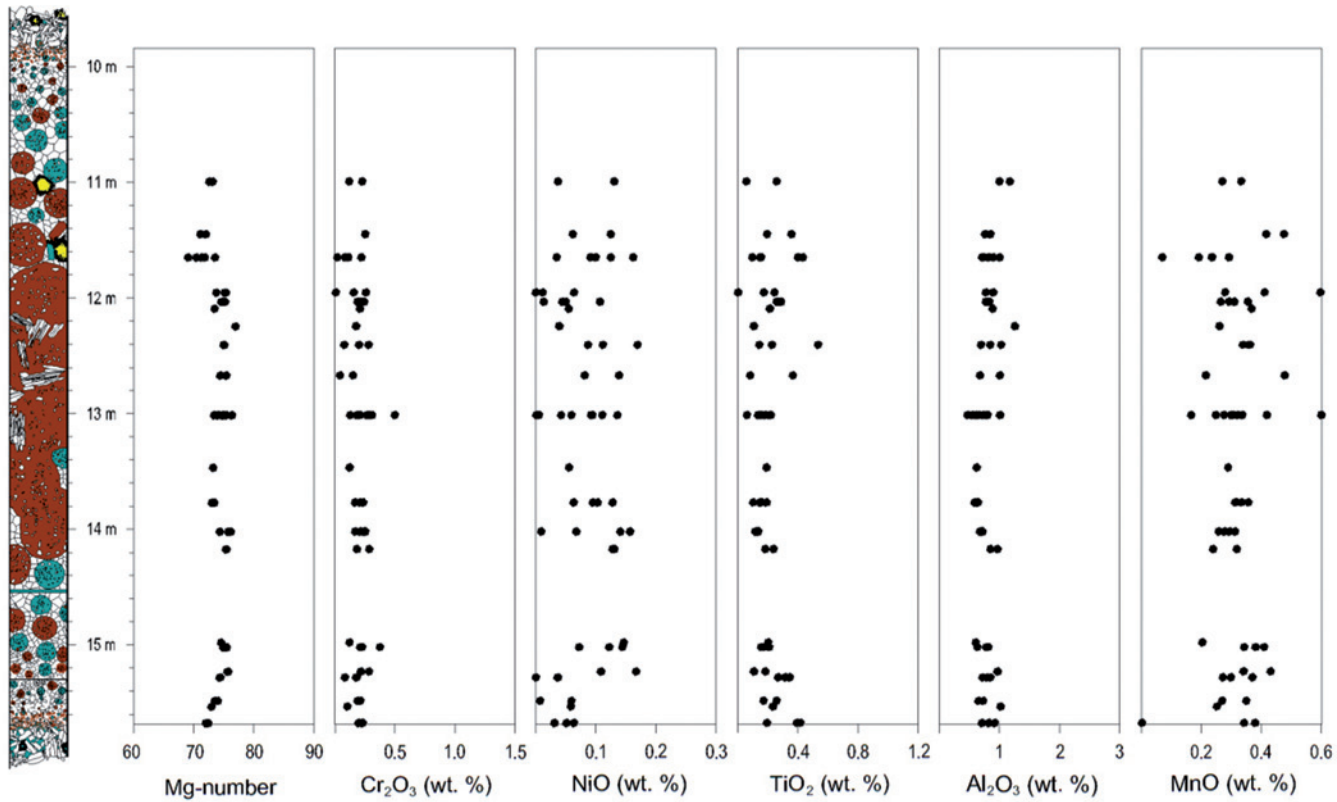


Fig. 6.2. Mg-number ( $100\text{Mg}/(\text{Mg}+\text{Fe}^{2+}+\text{Fe}^{3+}+\text{Mn})$ ) and concentrations of  $\text{Cr}_2\text{O}_3$ , NiO,  $\text{TiO}_2$ ,  $\text{Al}_2\text{O}_3$  and MnO in Ca-poor pyroxene of the noncumulate section in drill core B7. Mineral colours: brown = orthopyroxene, green = clinopyroxene, white = plagioclase, yellow = sulphides, black = amphibole+epidote+orthoclase+apatite+quartz. For textural description of the noncumulate, see Chapter 5.7.

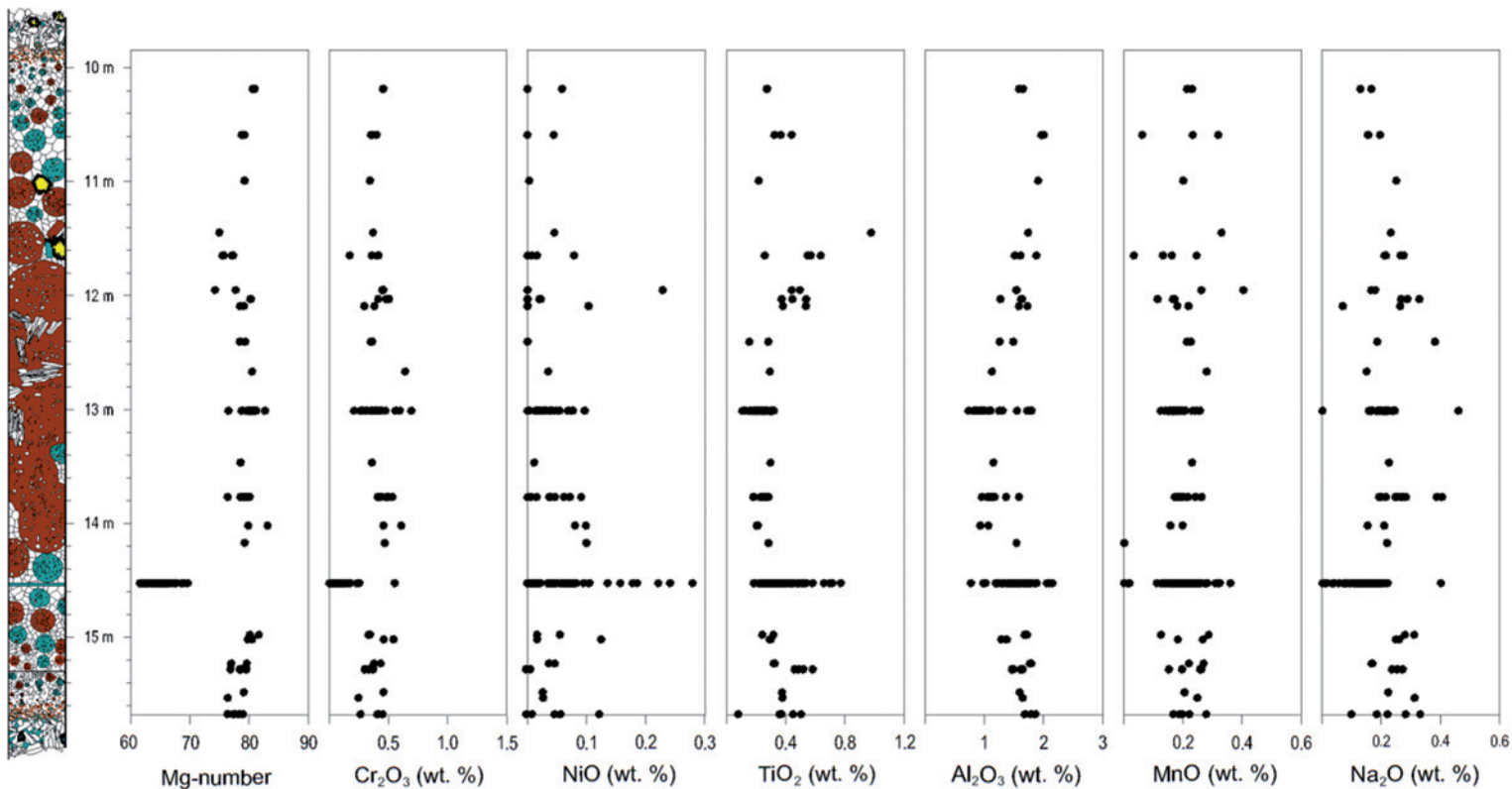


Fig. 6.3. Mg-number ( $100\text{Mg}/(\text{Mg}+\text{Fe}^{2+}+\text{Fe}^{3+}+\text{Mn})$ ) and concentrations of  $\text{Cr}_2\text{O}_3$ , NiO,  $\text{TiO}_2$ ,  $\text{Al}_2\text{O}_3$ , MnO and  $\text{Na}_2\text{O}$  in Ca-rich pyroxene of the noncumulate section in drill core B7. Mineral colours: brown = orthopyroxene, green = clinopyroxene, white = plagioclase, yellow = sulphides, black = amphibole+epidote +orthoclase+apatite+quartz. For textural description of the noncumulate, see Chapter 5.7.

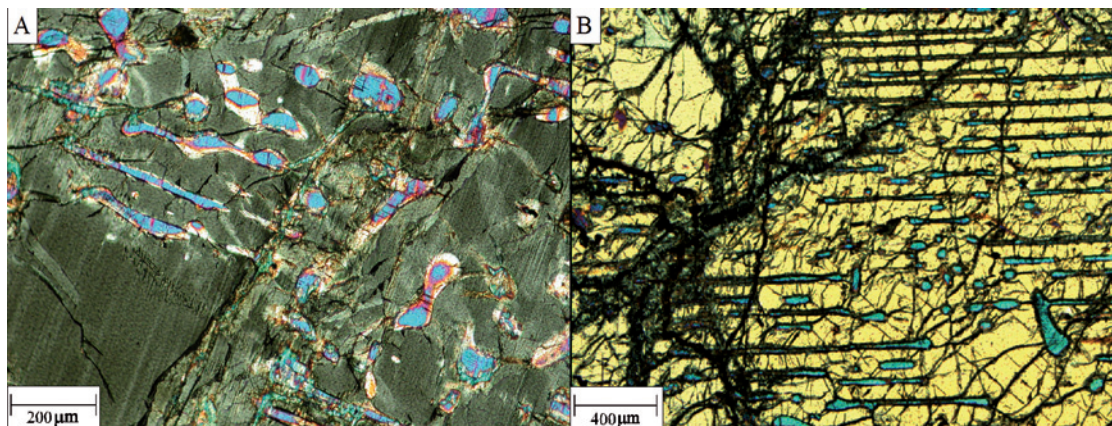


Fig. 6.4. Photomicrographs of exsolution textures in inverted pigeonite of the MZc. Figure A represents the  $\{010\}$  plane of the pigeonite which displays coarse augite lamellae parallel to the  $\{001\}$  plane and fine diopside lamellae parallel to the  $\{100\}$  plane in the pigeonite (6.1-TTK-03, crossed nicols). Figure B shows the  $\{100\}$  plane of the pigeonite where only the coarse lamellae are visible (9-TTK-03, crossed nicols).

The composition of Ca-rich pyroxene in the cumulates of the Koillismaa Intrusion ranges from  $Wo_{44}En_{45}Fs_{11}$  to  $Wo_{43}En_{38}Fs_{19}$  (Fig. 6.1.B). The clinopyroxene grains in the cumulates have Mg-numbers of 65.1–81.5 and contain up to 0.8 wt. %  $Cr_2O_3$ , 0.1 wt. % NiO, 0.2–1.2 wt. %  $TiO_2$ , 1.4–2.6 wt. %  $Al_2O_3$ , 0.1–0.4 wt. % MnO and 0.2–0.5 wt. %  $Na_2O$ .

The augites in the lower part of the intrusion have distinct lamellae oriented parallel to the  $\{100\}$  plane, but augites in the MZc, the UZa, and the UZb have lamellae oriented parallel to the  $\{001\}$  plane, indicating that these phases crystallized at temperatures above the pigeonite-orthopyroxene inversion curve. According to Hess (1960) and Deer et al. (1995) the augites that crystallize below the inversion temperature and coexist with primary orthopyroxene are commonly less Fe-rich than  $Wo_{41}En_{44}Fs_{15}$ . Lamellae in such augites exsolve parallel to the  $\{100\}$  plane and are of enstatitic or bronzitic composition. Upon crossing the inversion temperature, lamellae begin to exsolve approximately parallel to the  $\{001\}$  plane in augite and such lamellae crystallize as pigeonite. Since this pigeonite inverts to the orthorhombic form, a second set of lamellae in the host augites is formed. These lamel-

lae are composed of orthopyroxene and exsolve parallel to the  $\{100\}$  plane in augite, in a similar way as in Mg-bearing augite coexisting with primary orthopyroxene.

The cryptic variation in ortho- and clinopyroxene along the Porttivaara block profile is illustrated in Figs 6.5 and 6.6. Because of alteration, orthopyroxene compositions could only be determined in stratigraphic levels below the lower parts of the MZc, where compositional variation seems to be insignificant. Above the LZb the Mg-number and the  $Cr_2O_3$ ,  $Al_2O_3$  and MnO contents of orthopyroxene decrease. (Fig. 6.5) Clinopyroxene shows similar compositional variation with height as the Ca-poor pyroxene, but sample coverage is better. As seen in Fig. 6.6, the Mg-number of clinopyroxene decreases with height in the lower part of the intrusion but increases with height above the level of the upper LZb, at a stratigraphic height of ca. 500 m. In the centre of the MZb, at a stratigraphic height of ca. 750 m, the Mg-number of Ca-rich pyroxene begins to fall with height. Concentrations of  $Cr_2O_3$ , NiO, and  $Na_2O$  vary in a similar way as Mg-number but are decoupled from the trends of  $TiO_2$  and  $Al_2O_3$  content.

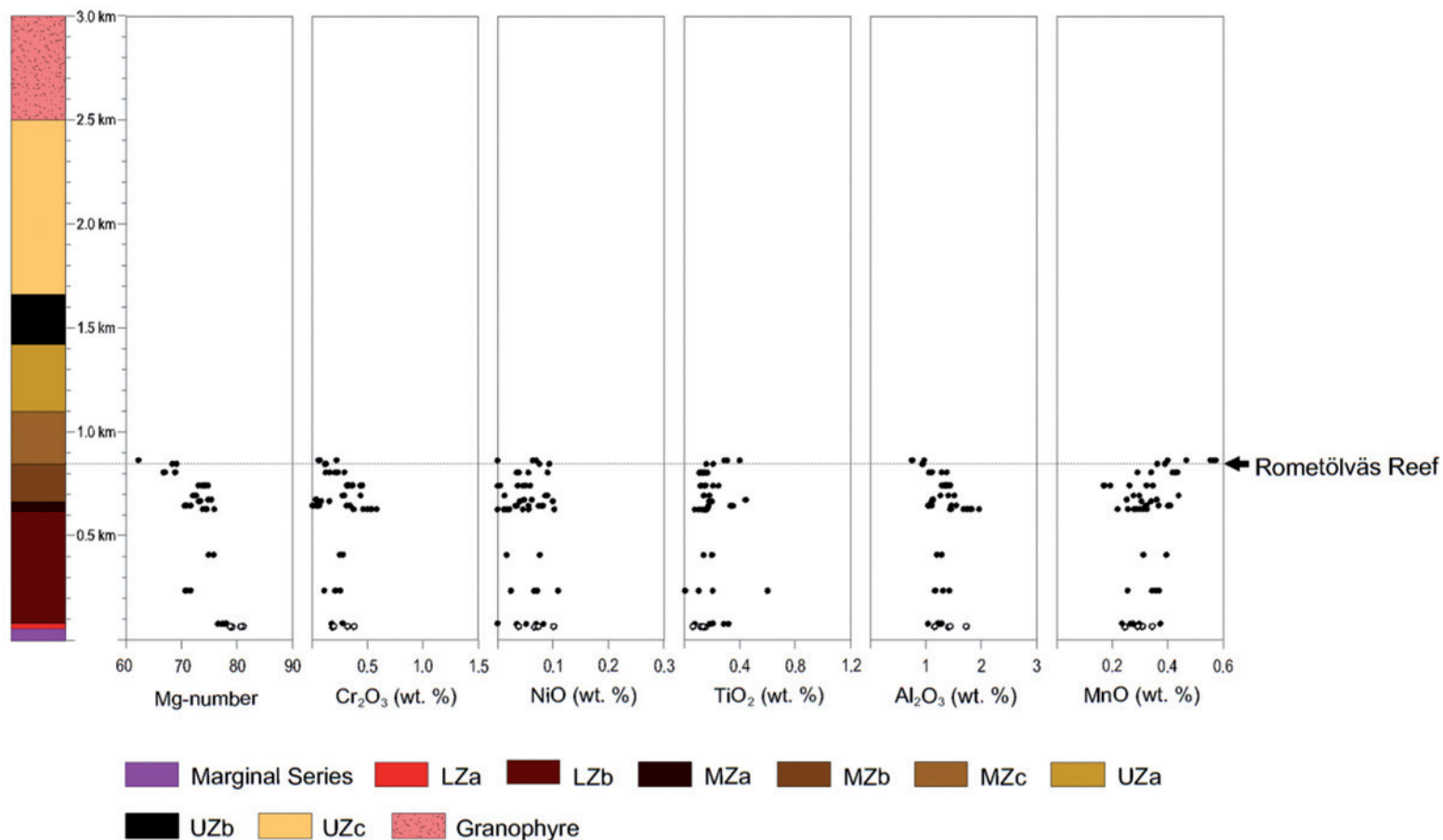


Fig. 6.5. Mg-number ( $100\text{Mg}/(\text{Mg}+\text{Fe}^{2+}+\text{Fe}^{3+}+\text{Mn})$ ) and concentrations of  $\text{Cr}_2\text{O}_3$ , NiO,  $\text{TiO}_2$ ,  $\text{Al}_2\text{O}_3$  and MnO in Ca-poor pyroxene across the stratigraphic sequence of the Porttivaara block (no lamellae compositions plotted, dots represent cumulus and circles represent intercumulus minerals).

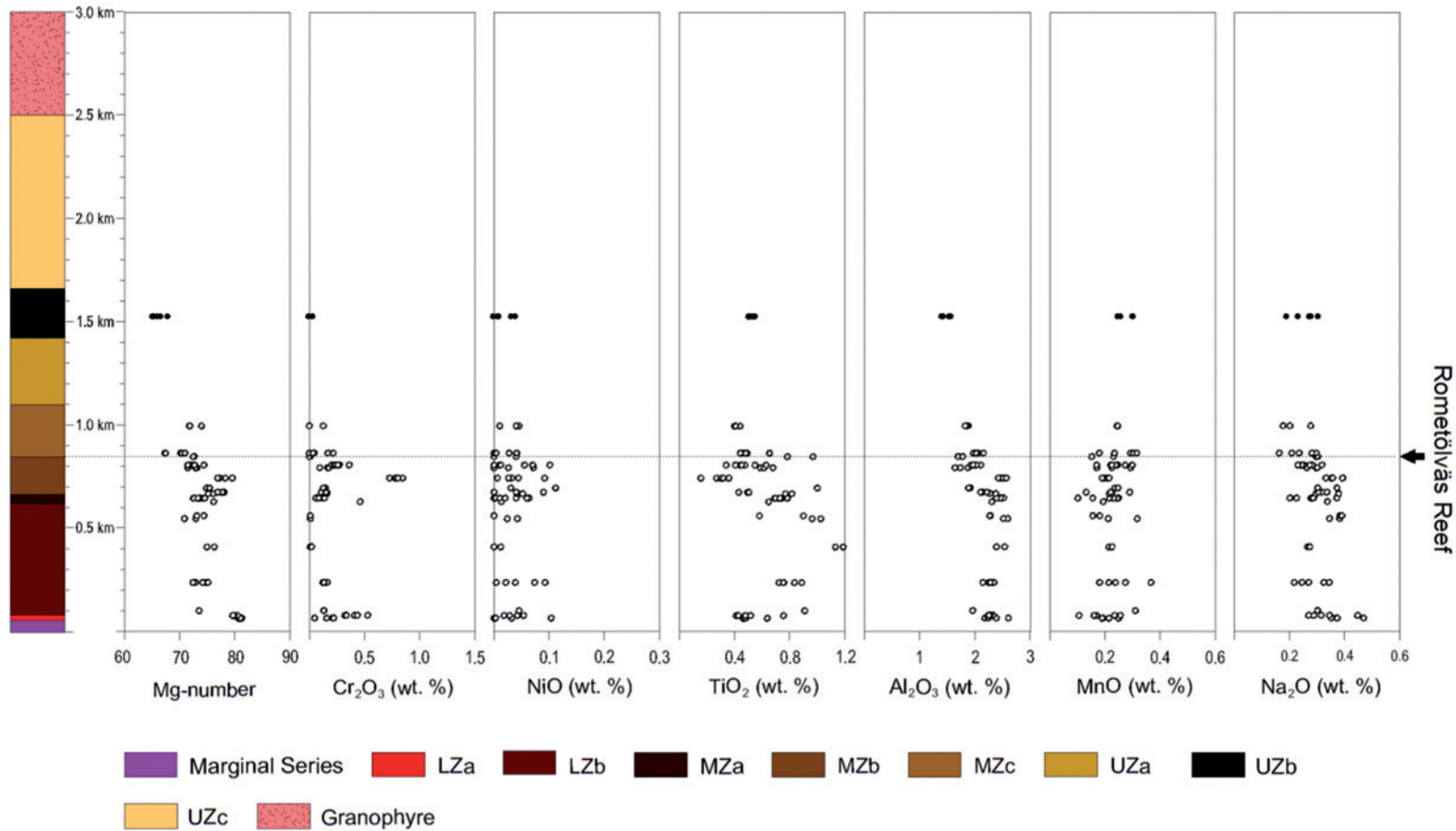


Fig. 6.6. Mg-number ( $100\text{Mg}/(\text{Mg}+\text{Fe}^{2+}+\text{Fe}^{3+}+\text{Mn})$ ) and concentrations of  $\text{Cr}_2\text{O}_3$ , NiO,  $\text{TiO}_2$ ,  $\text{Al}_2\text{O}_3$ , MnO and  $\text{Na}_2\text{O}$  in Ca-rich pyroxene across the stratigraphic sequence of the Porttivaara block (no lamellae compositions plotted, dots represent cumulus and circles represent intercumulus minerals).

### 6.1.2.3 Solidus compositions of the pyroxenes in cumulate rocks

The solidus compositions of augite and inverted pigeonite of the Koillismaa Intrusion were obtained using weighted average compositions of exolutions and their hosts. The relative proportions of lamellae and host were estimated using digital BE-images showing a typical unaltered lamellae texture. In the case of primary orthopyroxene grains, the microprobe analyses on {010} planes were taken as solidus compositions. The analytical data used in the estimation of solidus compositions is compiled in Table 6.1.

The quadrilateral of Fig. 6.7 illustrates the compositions of host and exsolution phases identified by sample numbers. There appears to be correlation between the lamellae and coexisting host compositions, which implies that the exsolution process began immediately below the solidus temperature. A noticeable feature

in the quadrilateral is that the Ca-poor lamellae exsolved from augites have lower Wo contents, but are richer in Fs component than the coexisting cumulus orthopyroxene.

In the Koillismaa Intrusion, the orthopyroxene-pigeonite transition took place at an orthopyroxene composition of  $En_{65}Fs_{35}$ , which compares closely to the estimate from the Bushveld Complex (Atkins 1969). The augite grains that crystallized above the inversion curve and coexisted with pigeonite were originally more Fe-rich than  $Wo_{35}En_{44}Fs_{21}$ . Following exsolution these augites are richer in iron than  $Wo_{42}En_{40}Fs_{18}$ , which compares well to the estimate given by Hess (1960) and Deer et al. (1995). The solidus trend of the Koillismaa Intrusion pyroxenes is shown in the quadrilateral of Fig. 6.7, where it is labelled as "K". This trend is short in comparison with the trends of the Bushveld Complex, the Skaergaard Intrusion and the Jimberlana Intrusion.

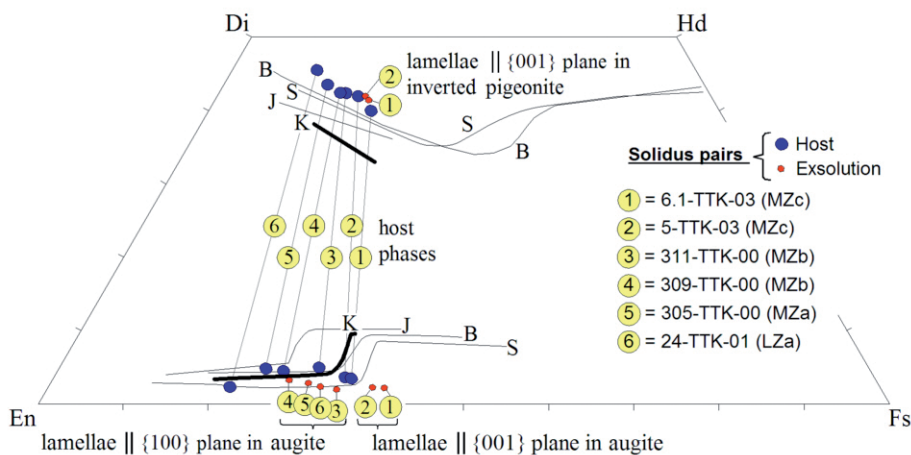


Fig. 6.7. The solidus trend of Koillismaa Intrusion (K) pyroxenes plotted in the En-Wo-Fs quadrilateral (mol. %). The solidus trends of the pyroxenes of the Bushveld Complex (B, data from Atkins 1969), the Skaergaard Intrusion (S, data from Brown & Vincent 1963) and the Jimberlana Intrusion (J, data from Campbell & Borley 1974) are also shown in the quadrilateral.

Table 6.1. Information on the grains used in the determination of solidus compositions and the fractionation trend of the pyroxenes of the Koillismaa Intrusion.

Sample	Phase	Phase description	Analytical key
24-TTK-01 (LZa)	Ca-rich	<u>Exsolution host</u> , 85.1 vol. % of the grain, intercumulus.	SILI 08.04/17, 18, 19
		<u>Lamellae</u> II {100} plane of the host, 14.9 vol. % of the grain.	SILI 08.04/13, 14, 15, 16
	Ca-poor	<u>Cumulus</u> .	SILI 08.04/20, 21, 22
305-TTK-00 (MZa)	Ca-rich	<u>Exsolution host</u> , 85.8 vol. % of the grain, intercumulus.	SILI 04.04.03/15, 35, 36, 42, 43
		<u>Lamellae</u> II {100} plane of the host, 14.2 vol. % of the grain.	SILI 04.04.03/32, 33, 34, 40, 41
	Ca-poor	<u>Cumulus</u> .	SILI 04.04.03/37, 38, 39
309-TTK-00 (MZb)	Ca-rich	<u>Exsolution host</u> , 82.7 vol. % of the grain, intercumulus.	SILI 08.04.03/5, 7
		<u>Lamellae</u> II {100} plane of the host, 17.3 vol. % of the grain.	SILI 08.04.03/1, 3, 4
	Ca-poor	<u>Cumulus</u> .	SILI 08.04.03/8, 9, 10
311-TTK-00 (MZb)	Ca-rich	<u>Exsolution host</u> , 82.0 vol. % of the grain, intercumulus.	SILI 04.04.03/18, 25, 26, 27, 28
		<u>Lamellae</u> II {100} plane of the host, 18.0 vol. % of the grain.	SILI 04.04.03/20, 21, 22, 23, 24
	Ca-poor	<u>Cumulus</u> .	SILI 04.04.03/29, 30, 31
5-TTK-03 (MZc)	Ca-rich	<u>Exsolution host</u> , 81.2 vol. % of the grain, cumulus.	SILI 03.09.03/3, 5
		<u>Lamellae</u> II {100} plane of the host, 18.8 vol. % of the grain.	SILI 03.09.03/4
	Ca-poor	<u>Exsolution host</u> , 84.0 vol. % of the grain, cumulus.	SILI 03.09.03/6
		<u>Lamellae</u> II {001} plane of the host, 16.0 vol. % of the grain.	SILI 03.09.03/7
6.1-TTK-03 (MZc)	Ca-rich	<u>Exsolution host</u> , 81.0 vol. % of the grain, cumulus.	SILI 06.10.03/6
		<u>Lamellae</u> II {001} plane of the host, 19.0 vol. % of the grain.	SILI 06.10.03/2/5
	Ca-poor	<u>Exsolution host</u> , 84.5 vol. % of the grain, cumulus.	SILI 03.09.03/19 & SILI 06.10.03/1
		<u>Exsolution</u> II {001} plane in the host, 14.5 vol. % of the grain.	SILI 03.09.03/18 & SILI 06.10.03/2

#### 6.1.2.4 Compositional differences between the pyroxenes in the noncumulate and cumulate rocks

The  $Mg/(Mg+Fe^{2+})$  value of pyroxene is used here as a measure of the degree of differentiation (Fig. 6.8), but since clinopyroxene commonly has greater  $Mg/Fe^{2+}$  than coexisting orthopyroxene and the analyses mostly represent subsolidus compositions, only general trends are described. The major emphasis is put on the comparison of pyroxene chemistry between cumulates and noncumulates, as this may provide insight to the relationship between these rocks.

In both cumulates and noncumulates, there is a trend towards lower Al (=  $Al^{IV}+Al^{VI}$ ), Cr and  $Fe^{3+}$  contents in both pyroxene phases with decreasing value of  $Mg/(Mg+Fe^{2+})$ . In both rock types Ti contents are higher in clinopyroxenes than in orthopyroxenes. The mode of occurrence of the pyroxenes in the cumulates, whether they occur as noncumulus, cumulus or intercumulus crystals, has generally no effect on the trends. The only exception is cumulus clinopyroxene which shows somewhat lower Si and higher  $Fe^{3+}$  contents at a given  $Mg/(Mg+Fe^{2+})$  than intercumulus grains.

The pyroxenes in the noncumulates generally have higher Si contents and lower Al contents than the pyroxenes in the cumulates. Clinopyroxenes of noncumulates are depleted in Ti but enriched in Cr at a given  $Mg/(Mg+Fe^{2+})$  relative to clinopyroxenes in cumulates. The pyroxenes in the Lotanvaara mafic rock unit and in the noncumulus-textured gabbro-noritic bodies have identical compositions.

### 6.1.3 Feldspars

In the case of optically zoned feldspar grains, a minimum of three spots from the unzoned inner portion of a grain were analyzed to determine composition. Appendix 6 includes selected feldspar analyses.

#### 6.1.3.1 Noncumulate rocks

The analyses of nine samples from the upper chilled margin in the eastern part of the Porttivaara block (“Kuusi-Pyhitys” in Fig. 4.1) show considerable variation in anorthite content, from  $An_{57}$  to  $An_{47}$ . The lower chilled margin (“259-TTK-00” in Fig. 4.1), whose plagioclase composition was determined from one sample yielded a more calcic composition ( $An_{64-60}$ ) than the upper chilled margin.

Plagioclase compositions of the noncumulate bodies are given in columns 3 and 4 of Appendix 6. In the Lotanvaara mafic rock unit (“Lotanvaara” in Fig. 4.1) the plagioclase compositions range from  $An_{68}$  to  $An_{62}$ , as determined from chadacrystic grains in two samples (Fig. 6.9.A). Among the noncumulate bodies, there is no significant variation between the different blocks of the intrusion (Fig. 6.9.B). The overall variation of the plagioclase composition in the noncumulate bodies is very wide, from  $An_{90}$  to  $An_{41}$ . The most calcic plagioclase ( $An_{90-82}$ ) is located in drill core B7 at Rometölväs (at a depth of 14.50 m), where plagioclase mostly forms oikocrysts that enclose diopside. These plagioclase grains are labeled in Fig. 6.9.B as “B7 14.50”.



Due to the large compositional variation in major components of plagioclase in the noncumulate bodies, altogether 20 plagioclase crystals were analysed with line traverses. Zonation in most of the crystals revealed to be normal.

Figure 6.10 illustrates the cryptic variation in plagioclase composition across the noncumulate section of drill core B7. Plagioclase in the upper part of the section mostly have ca.  $An_{75}$ , but towards the base of the body, there is a distinct decrease in the An content, from  $An_{70}$  to  $An_{65}$ . The FeO content in plagioclase in the noncumulate body is relatively homogenous and averages 0.4 wt. %. The maximum An content of plagioclase is similar in coexisting, morphologically different grains (radiating, chadacrystic, mosaic-textured or in sulphide-bearing pockets). Chadacrysts have  $An_{78-59}$  and mosaic-textured grains surrounding pyroxene oikocrysts have  $An_{77-53}$ . Plagioclase within the sulphide-bearing pockets represent the Ab-rich end of the compositional range, at  $An_{79}$  to  $An_{41}$ .

### 6.1.3.2 Cumulate rocks

The quadrilaterals in Fig. 6.11 illustrate the composition of plagioclase in the cumulate and granophyre samples. Analyses 5–8 in Appendix 6 represent cumulus plagioclase compositions and analysis 9 represent a plagioclase in granophyre. Three electron microprobe traverses through cumulus grains, one from each of the LZb, MZb and MZc, were performed to quantify the optically determined zonation in plagioclase crystals.

The reverse differentiation trend in the MS is reflected in the plagioclase compositions in the gabbro-noritic subzones (LZMSa and LZMSb, Fig. 6.11.D). Here plagioclase compositions cover a range from  $An_{73}$  to  $An_{45}$  and the most calcic grains occur in the stratigraphically uppermost subzone.

The variation of An and FeO contents in plagioclase of the Porttivaara block is shown in Fig. 6.12. The compositions of the most calcic phases cover a range from  $An_{77}$  to  $An_{52}$ .

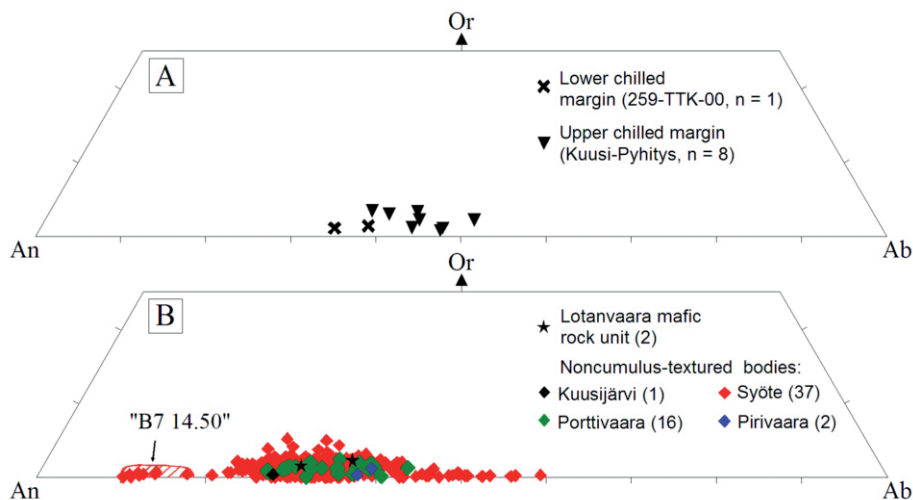


Fig. 6.9. Plagioclase compositions in the noncumulus-textured rocks plotted in the An-Or-Ab quadrilateral (mol. %). The number of analysed samples are shown in parentheses. The red striped area in the lower quadrilateral represents the plagioclase analyses of thin section B7 14.50 (drill core B7, Rometölväs).

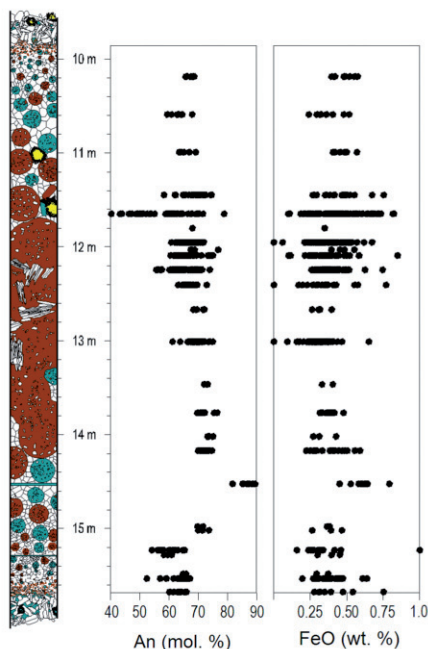


Fig. 6.10. Variation of An (mol. %) and FeO (wt. %) of plagioclase in a noncumulus-textured gabbro-norite body in drill core B7. All analysed compositions shown in the diagram. For textural description of the noncumulate body, see Chapter 5.7.

whereas FeO ranges mostly between 0.25 and 0.75 wt. %. In the lower part of the LS there is a steady decrease in An content in plagioclase with height, from An<sub>77</sub> to An<sub>64</sub>, but this trend turns reversed in the upper part of the LZb, at stratigraphic height of ca. 500 m. From there on the An content increases with height. In the MZa and the lower half of MZb (620–750 m stratigraphic height), it reaches values comparable to those in the lower portion of the in-

trusion (An<sub>75</sub>). Above this level, the An content decreases with height, upwards from the MZb and downwards from the middle part of the UZc to reach the lowest values (An<sub>52</sub>) at height of ca. 1500, in the UZb. Plagioclase in the upper part of the UZc (above height ca. 1900 m) displays a very uniform composition (ca. An<sub>66</sub>). In the granophyre, the An content of plagioclases is typically less than 10 mol. % (Fig. 6.11).

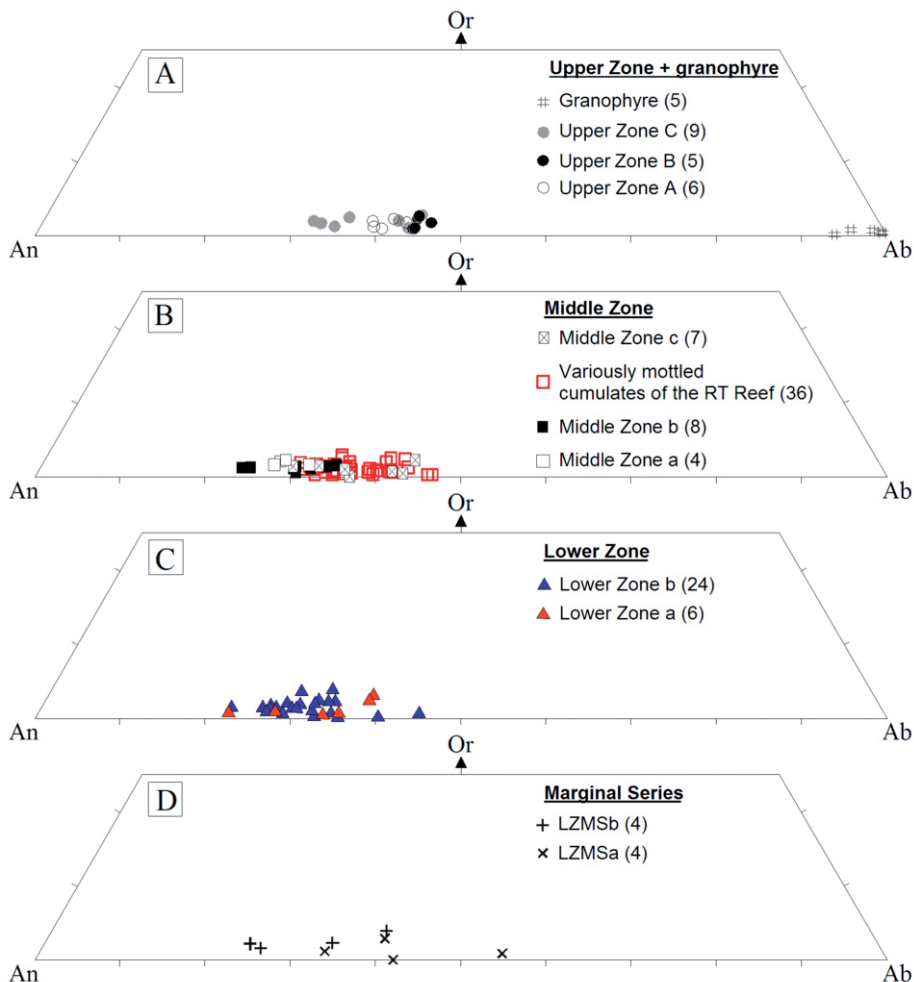


Fig. 6.11. Plagioclase compositions in the cumulate and granophyre samples of the study area in An-Or-Ab quadrilateral (mol. %). Only the most An-bearing composition in each sample is shown. The number of analysed samples is shown in parentheses.

## 6.1.4 Other silicate minerals

### 6.1.4.1 Amphibole group

According to the classification of Leake (1978) and Leake et al. (1997), all amphiboles analysed in this study can be defined as calcic amphiboles. They display significant within-grain compositional variation that is most

distinct in the grains of the mottled RT Reef cumulate samples (Fig. 6.13). The amphibole compositions analysed from the mottled cumulates cover the following ranges: 2.7–17.2 wt. % MgO, 8.5–25.4 wt. % FeO<sup>TOT</sup> and 35.6–54.7 SiO<sub>2</sub>. The pale green cores of amphiboles within mottles and pseudomorphic amphibole grains after clinopyroxene located adjacent to the mottles have the most Si- and Mg-

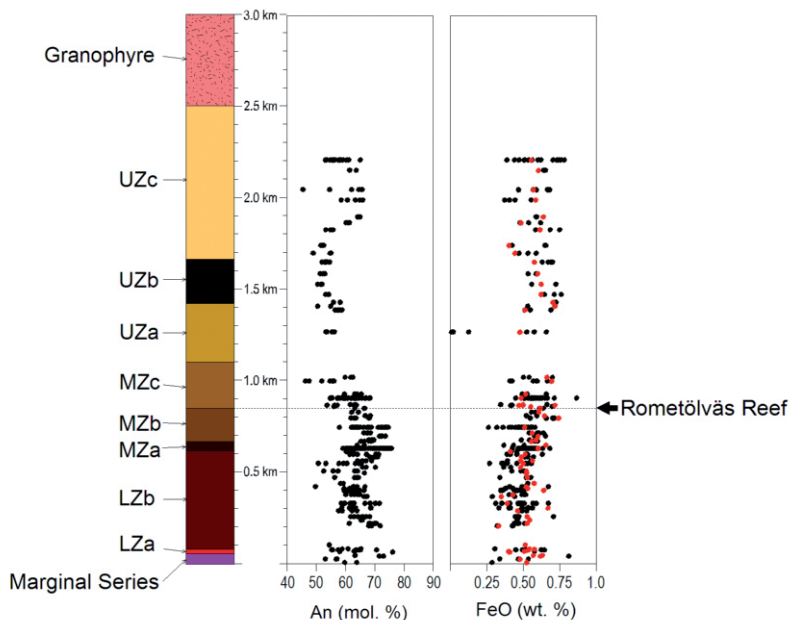


Fig. 6.12. Variation of An (mol. %) and FeO (wt. %) in plagioclase with height in the Porttivaara block. Red dots show the FeO in the most An-bearing plagioclase of individual thin sections.

rich compositions. Such phases can be defined as actinolites and hornblendes, whereas the darker green margins of amphibole within the mottles have the highest Fe, Na and K concentrations and can be defined as pargasites.

Actinolites and hornblendes contain less than 0.5 wt. % Na<sub>2</sub>O and K<sub>2</sub>O, but in pargasites, alkalic metal concentrations are higher, up to 2.2 wt. % Na<sub>2</sub>O and 2.8 wt. % K<sub>2</sub>O. Pargasites have also the highest concentrations of Cl (up to 4.1 wt. %) and Al<sub>2</sub>O<sub>3</sub> (up to 16.9 wt. %), whereas actinolites are the most water-bearing (0.8–2.1 wt. % H<sub>2</sub>O). Otherwise the amphiboles from mottled cumulates are compositionally similar: they have roughly constant CaO contents, 11.6–12.8 wt. % in actinolites and 11.2–12.0 wt. % in pargasites, and contain up to 0.6 wt. % Ti<sub>2</sub>O, 0.7 wt. % NiO and 0.6 wt. % MnO.

The amphibole grains in the sulphide-mineralized part of the noncumulate section in

drill core B7 (see Figs 5.10 and 5.12) consist of actinolites and hornblendes. The grains are richer in Mg than amphibole in the mottled cumulates but have otherwise similar compositions (Fig. 6.13). The grains in the non-cumulate body contain 9.7–18.3 wt. % MgO, 9.4–15.2 wt. % FeO<sup>TOT</sup>, 41.9–54.1 wt. % SiO<sub>2</sub>, 11.1–12.0 wt. % CaO, 3.0–16.3 wt. % Al<sub>2</sub>O<sub>3</sub> and 0.8–2.1 wt. % H<sub>2</sub>O. They also contain up to 0.3 wt. % Cl, 0.3 wt. % TiO<sub>2</sub>, 0.5 wt. % NiO and 0.6 wt. % MnO.

The amphibole grains of the MS are actinolites. They contain 17.5–18.6 wt. % MgO, 9.2–10.9 wt. % FeO<sup>TOT</sup>, 54.7–55.3 wt. % SiO<sub>2</sub>, 0.9–1.6 wt. % Al<sub>2</sub>O<sub>3</sub>, 0.18–2.1 wt. % H<sub>2</sub>O and 12.9 wt. % CaO.

#### 6.1.4.2 Epidote group

By means of optical determinations the crystals of the epidote group were classified

as members of the clinozoisite-epidote solid solution. According to Deer et al. (1995), the change from clinozoisite to epidote takes place at the pistacite (the name for the epidote end-member) molecule amount of 10 mol. %, which corresponds to ca. 6 wt. %  $\text{Fe}_2\text{O}_3$  in the mineral. The analysed phases contain 22.2–24.8 wt. %  $\text{CaO}$ , 23.1–31.9 wt. %  $\text{Al}_2\text{O}_3$ ,

36.4–41.0 wt. %  $\text{SiO}_2$  and 2.1–14.4 wt. %  $\text{Fe}_2\text{O}_3^{\text{TOT}}$ . The pistacite molecule amount in the analysed phases varies from 4.0 to 28.5 mol. %. Only one large grain appeared to contain a sufficient low pistacite component to be defined as clinozoisite. Ten selected analyses of epidote group minerals are shown in Appendix 8.

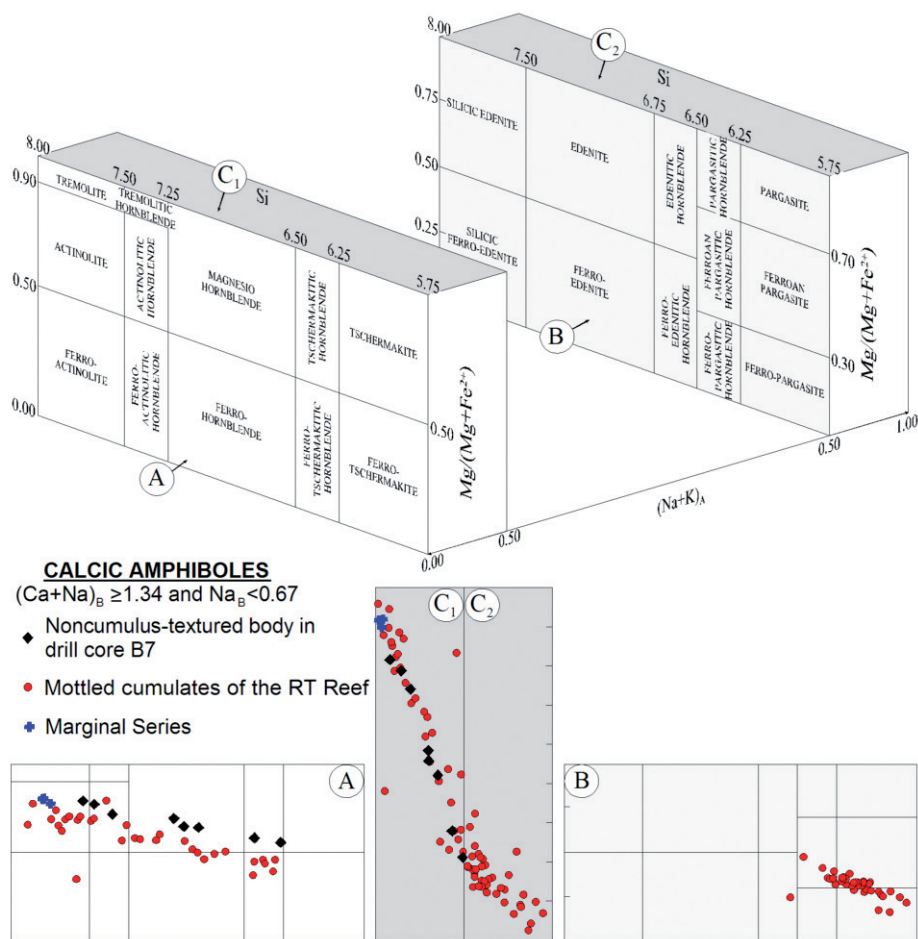


Fig. 6.13. Composition of amphibole in the Koillismaa Intrusion plotted in the classification for calcic amphiboles (Leake 1978; Leake et al. 1997). Mineral formulae are calculated on the basis of 23 oxygens ( $\text{H}_2\text{O}$ , Cl, F, S and P excluded) and  $\text{Fe}_2\text{O}_3/\text{FeO}$  is calculated using the method of Droop (1987). Ten selected analyses of amphibole group minerals are listed in Appendix 7.

#### 6.1.4.3 Scapolite group

All the scapolite group mineral analyses were performed on RT Reef cumulates and mostly from one drill core. According to the Commission on New Minerals and Mineral names of the International Mineralogical Association, the name of scapolite should be retained as a group name and the marialite-meionite series should be used as mineral names (Bayliss 1987). Based on the classification of Teertstra & Sherriff (1997), the analysed scapolite group minerals contain 51.3–68.7 mol. % marialite and are defined as calcian marialites ( $85 > Ma > 50$ ). They contain 50.5–58.5 wt. %  $\text{SiO}_2$ , 22.5–25.4 wt. %  $\text{Al}_2\text{O}_3$ , 6.8–11.5 wt. %  $\text{CaO}$ , 4.4–9.4 wt. %  $\text{Na}_2\text{O}$ , 0.2–0.5 wt. %  $\text{K}_2\text{O}$ , 2.1–3.3 wt. %  $\text{Cl}$ , 1.3–3.4 wt. %  $\text{CO}_3$  and low  $\text{SO}_4$  concentrations ( $< 0.8$  wt. %). The scapolite group minerals do not display a significant compositional variation across the RT Reef. Appendix 9 shows ten selected analyses of the scapolite group minerals.

#### 6.1.4.4 Phlogopite-biotite

Mica is present in two types: 1) biotite forms an alteration product in the mottled RT Reef cumulates and 2) primary magmatic phlogopite-biotite occurs as flakes in the olivine gabbronorites or adjacent to loweringite in the noncumulus-textured body studied in detail (see Chapter 5.7). Ten representative mica analyses are presented in Appendix 10.

According to Deer et al. (1995), the difference in chemistry of the solid solution se-

ries end-members phlogopite and biotite is not clearly defined. Phlogopite is the Mg-rich end-member whose octahedral site does not contain significant aluminium, whereas in biotite there is an appreciable degree of substitution of Al for octahedrally coordinated Mg and Fe. According to Bailey (1984), biotite compositions ideally are  $\text{K}(\text{Mg}_{0.6-1.8}\text{Fe}_{1.2-2.4}) (\text{Si}_3\text{Al})\text{O}_{10}(\text{OH},\text{F})_2$ , and on the basis of the most Mg-rich composition, the phlogopite-biotite boundary in this study is set at  $\text{Mg}/\text{Fe} = 1.5$ .

The analysed alteration biotites contain 35–36.5 wt. %  $\text{SiO}_2$ , 16.1–17.9 wt. %  $\text{Al}_2\text{O}_3$ , 6.8–8.6 wt. %  $\text{K}_2\text{O}$ , 8.4–11.5 wt. %  $\text{MgO}$ , 19.0–24.8 wt. %  $\text{FeO}^{\text{TOT}}$  and 0.2–1.8 wt. %  $\text{TiO}_2$ . They have a sufficient amount of aluminium in octahedrally coordinated sites ( $\text{Al}^{\text{VI}} = 0.5\text{--}0.8$ ) and  $\text{Mg}/\text{Fe}$  values close to 1.0.

Most of the igneous micas are phlogopites that contain 32.9–39.2 wt. %  $\text{SiO}_2$ , 12.5–15.0 wt. %  $\text{Al}_2\text{O}_3$ , 6.1–9.0 wt. %  $\text{K}_2\text{O}$ , 13.2–16.9 wt. %  $\text{MgO}$ , 12.0–17.0 wt. %  $\text{FeO}^{\text{TOT}}$  and 2.4–6.8 wt. %  $\text{TiO}_2$ . The Al substitution in the octahedrally coordinated cation sites is small ( $\text{Al}^{\text{VI}} < 0.4$ ) and  $\text{Mg}/\text{Fe}$  is mostly close to 2.0.

#### 6.1.4.5 Chlorite

The analysed chlorite grains contain 24.8–28.3 wt. %  $\text{SiO}_2$ , 16.9–22.0 wt. %  $\text{Al}_2\text{O}_3$ , 19.2–34.3 wt. %  $\text{FeO}^{\text{TOT}}$ , 8.2–19.9 wt. %  $\text{MgO}$ , 0.1–1.1 wt. %  $\text{MnO}$  and 11.1–11.9 wt. %  $\text{H}_2\text{O}$ . They contain also up to 1.3 wt. %  $\text{NiO}$ , 0.6 wt. %  $\text{Cl}$  and 2.1 wt. %  $\text{SO}_3$ . Ten selected chlorite analyses are presented in Appendix 11.

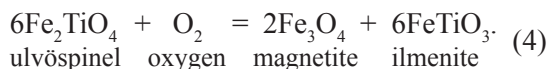
## 6.2 Oxides

### 6.2.1 Spinel group

The  $\text{Fe}_2\text{O}_3/\text{FeO}$  in the spinel minerals was calculated on the ulvöspinel and ilmenite basis as presented by Carmichael (1967) and on the stoichiometric basis as presented by Droop (1987). The stoichiometric  $\text{Fe}_2\text{O}_3/\text{FeO}$  was further used in mineral formulae calculations. Appendix 12 includes ten selected spinel analyses.

Selected oxide grains of the Koillismaa Intrusion are shown in Fig. 6.14. Chromite grains typically have alteration margins of magnetite (Fig. 6.14.A). To obtain the composition of the least altered part of the crystal microprobe analyses were performed on the central domains of grains. Spinel from the MS are lamellae-free, whereas ilmenomagnetites of the LS - and especially in the UZb - have variable textures of lamellae as shown in Fig. 6.14.B. Juopperi (1977) described three ilmenite lamellae generations of UZb ilmenomagnetites, 1) a coarse type exhibiting homogenous and granular lamellae, 2) long, thin lamellae occurring parallel to the  $\{111\}$  plane and 3) small splinter-like lamellae parallel to  $\{111\}$  which occur between the lamellae of the second type, but do not touch them. In noncumulates the spinels mostly have lamellae parallel to the  $\{111\}$  plane (Fig. 6.14.C), but these rocks contain also oxide grains that are free of lamellae or in which faint lamellae are confined to the centers of the grains (Fig. 6.14.D).

The exolutions form when titanomagnetite, which refers to any composition lying on the magnetite and ulvöspinel solid solution, undergoes subsolidus oxidation. The oxidation concerns the ulvöspinel component of the solid solution that reacts to magnetite and ilmenite, which begins to exsolve. Buddington & Lindsley (1964) expressed the exsolution with the following reaction:



Therefore, titanium ( $\text{Ti}^{4+}$ ) in spinels is largely controlled by subsolidus exsolution phenomena. This leaves  $\text{Al}^{3+}$ ,  $\text{Cr}^{3+}$ ,  $\text{Fe}^{3+}$ ,  $\text{Fe}^{2+}$ ,  $\text{Mg}^{2+}$ ,  $\text{Mn}^{2+}$ ,  $\text{Ni}^{2+}$  and  $\text{Zn}^{2+}$  as the principal elements in the analyses representing the exsolution hosts, and of these elements the trivalent ones have formed the basis of spinel subdivision into a chromite series ( $\text{Cr}^{3+}$ ), a magnetite series ( $\text{Fe}^{3+}$ ) and a spinel series ( $\text{Al}^{3+}$ ). The subdivision used here is a modification of the classification of Stevens (1944), which is illustrated in Fig. 6.15 and exemplified numerically in Appendix 13.

The spinels of the MS and LS differ markedly in their compositions. The spinels of the MS plot in the fields of ferrian and aluminian chromites, whereas the spinels of the LS are magnetites. In terms of the major components, the analysed MS spinels average 5.0 mol. % ulvöspinel, 24.4 mol. % inverted spinel, 46.6 mol. % Cr-spinel and 24.0 mol. % Al-spinel. These spinels contain on average 1.0 wt. %  $\text{V}_2\text{O}_3$ , 0.2 wt. % MgO, 0.1 wt. % NiO, 1.8 wt. % ZnO and 0.4 wt. % MnO. The LS spinels average 2.7 mol. % ulvöspinel, 90.8 mol. % inverted spinel, 4.2 mol. % Cr-spinel and 2.3 mol. % Al-spinel and contain up to 1.6 wt. %  $\text{V}_2\text{O}_3$ , 3.2 wt. % MgO, 0.6 wt. % NiO, 0.5 wt. % ZnO and 1.1 wt. % MnO. The most Cr-enriched spinel was found from the olivine cumulate body of Baabelinälkky (M-208B-71 in Fig. 6.15) with a composition of 2.6 mol. % ulvöspinel, 5.6 mol. % inverted spinel, 63.4 mol. % Cr-spinel and 28.4 mol. % Al-spinel and contains 0.5 wt. %  $\text{V}_2\text{O}_3$ , 1.3 wt. % MgO, 1.7 wt. % ZnO and 0.6 wt. % MnO. Ni was not detected in the phase.

The spinels of the Lotanvaara mafic rock unit cover a range from ferrian chromite to

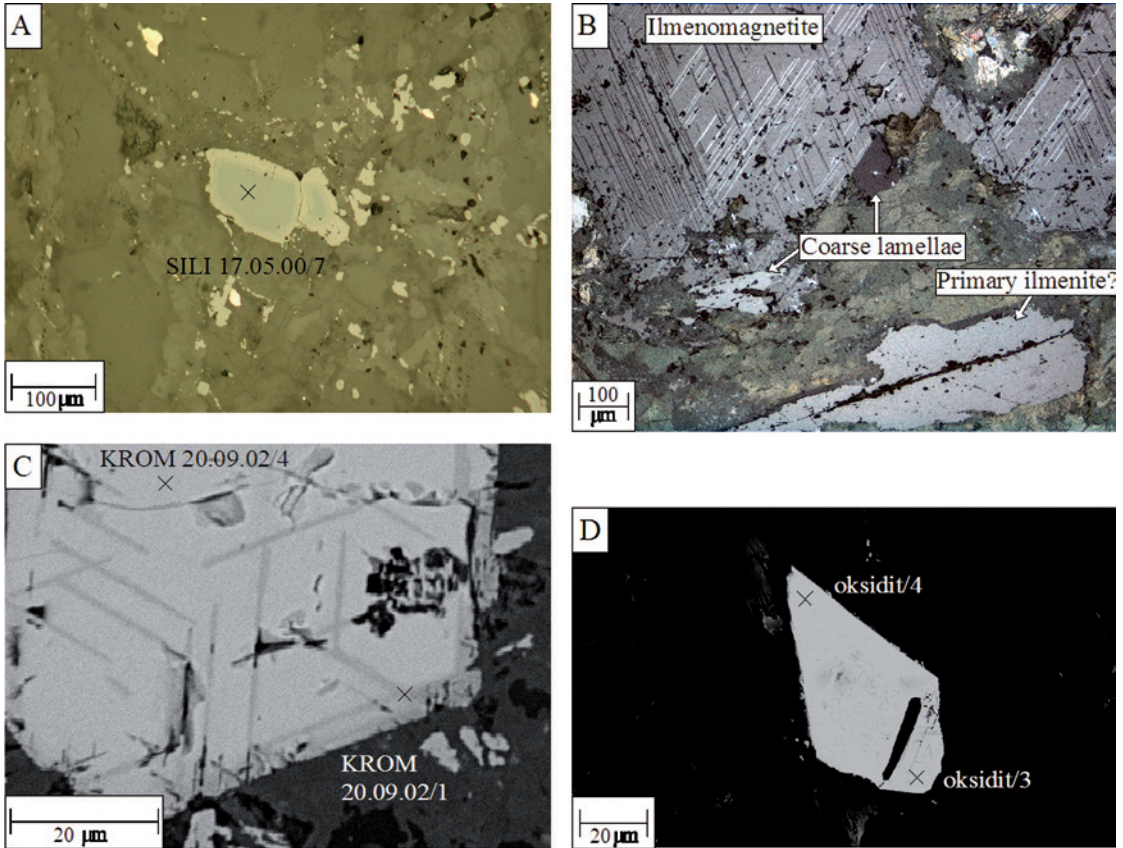


Fig. 6.14. Oxide minerals of the study area. **A.** Chromite in a cumulus-textured serpentinite body of Baabelinälkky area (M-208B-71, reflected light and crossed nicols), **B.** Ilmenomagnetite in magnetite gabbro (335-TTK-00, reflected light), **C.** Chromian magnetite with distinct lamellae in a rock of the Lotanvaara unit (72-TTK-99, BEI), **D.** Chromian magnetite with weak lamellae in a noncumulate body (10-TTK-03, BEI).

chromian magnetite (Fig. 6.15). These spinels contain 1.0–14.9 mol. % ulvöspinel, 22.8–61.6 mol. % inverted spinel, 28.1–45.4 mol. % Cr-spinel and 4.8–20.4 mol. % Al-spinel, and 0.8–1.9 wt. %  $V_2O_3$ , 0.5–2.1 wt. % ZnO, 0.6–1.7 wt. % MnO, and up to 0.2 wt. % MgO and 0.3 wt. % NiO.

The spinels in noncumulate bodies show significant variation from ferrian chromite through chromian magnetite to magnetite. Due to the small number of analyses per intrusion block, the compositions illustrated in Fig. 6.15 are divided into two groups according to the body size rather than their locations. Thus,

the first group comprises the analyses from small bodies, whereas the second group represent spinel grains in the large noncumulate body in drill core B7. The spinels in the large noncumulate body are richer in Fe than those in small bodies. In terms of major components the analysed grains in the noncumulate bodies have from 0.3–22.4 mol. % ulvöspinel, 11.5–97.5 mol. % inverted spinel, 2.2–61.4 mol. % Cr-spinel and up to 28.8 mol. % Al-spinel. These phases contain 0.4–4.0 wt. %  $V_2O_3$ , and up to 2.1 wt. % MgO, 0.3 wt. % NiO, 3.1 wt. % ZnO and 2.2 wt. % MnO.

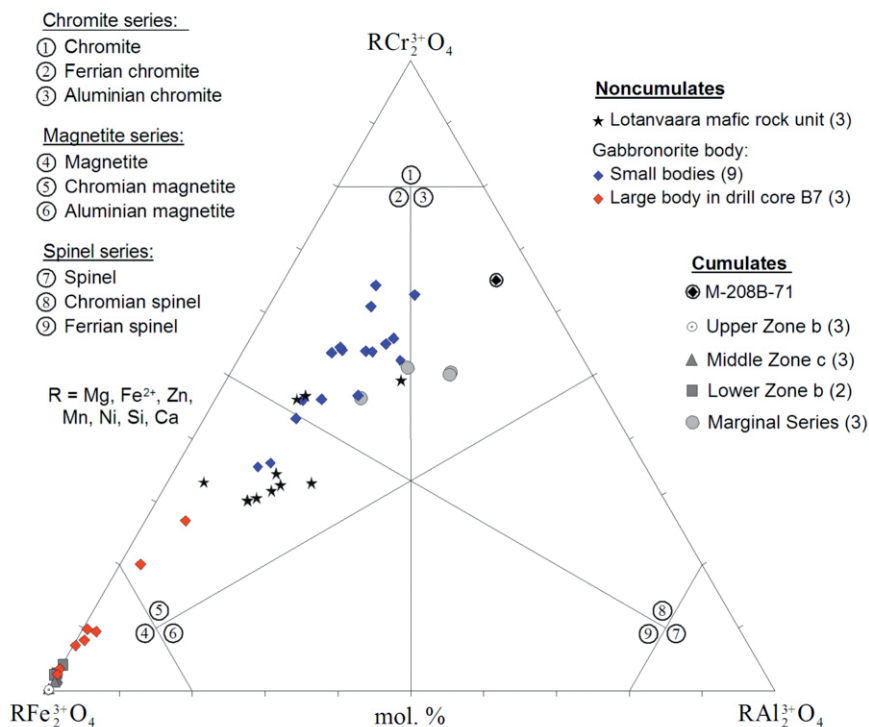


Fig. 6.15. Chromite-spinel-magnetite diagram illustrating spinel compositions in the study area. Number of analysed samples is shown in parentheses. Diagram is modified after Stevens (1944). See Appendix 13 for classification parameters.

## 6.2.2 Ilmenite

Two textural varieties of ilmenite can be distinguished: 1) discrete grains that occur independently from spinels and exhibit mostly elongate crystal forms and 2) exsolution products of the ulvöspinel-magnetite solid solution. Mathison (1975) called the first type primary ilmenite and the second type secondary ilmenite. Smith (1970) and Mathison (1975) noticed that the two types of ilmenite can be distinguished chemically, but the ilmenite grains analysed here were not systematically studied with regard to this question. Nevertheless, on a textural basis 17 analyses represent primary and 33 analyses represent secondary phases. Where grains are closely associated with spinels (Fig. 6.14.B), however, it is dif-

ficult to determine whether they are primary coprecipitates or the result of granular exsolution of earlier titanomagnetite.

The Fe<sub>2</sub>O<sub>3</sub>/FeO ratio in ilmenite was calculated on the ilmenite (Carmichael 1967) and stoichiometric basis (Droop 1987) and the ratio of the latter procedure was further used in mineral formulae calculations. Ten representative ilmenite analyses are listed in Appendix 14. Most of the analysed ilmenites can be defined as ferrian ilmenites, which according to Buddington et al. (1963), Anderson (1968) and Himmelberg & Ford (1977) is an optically homogenous rhombohedral Fe-Ti phase having an oxide stoichiometry of close to R<sub>2</sub>O<sub>3</sub> and Fe<sub>2</sub>O<sub>3</sub> less than 50 mol. %. However, the ilmenite occurring as rims around lovingite grains is called manganoan ilmenite in ac-

cordance with Tarkian & Mutanen (1987) and is described in Chapter 6.3.2.

The ferrian ilmenites in the cumulate rocks are mostly secondary phases. They contain 44.8–54.0 wt. %  $\text{TiO}_2$ , 40.5–51.4 wt. %  $\text{FeO}^{\text{TOT}}$ , 1.1–4.3 wt. %  $\text{MnO}$  and up to 0.5 wt. %  $\text{MgO}$ . Analyses 1 and 2 in Appendix 14 represent compositions of granular lamellae in the UZb ilmenomagnetite grains, and analyses 3 and 4 are compositions of thin lamellae in these ilmenomagnetite grains, conformable to their {111} planes. The highest  $\text{Fe}_2\text{O}_3$  con-

tent, ca. 14 wt. %, is observed in a primary ilmenite (analysis 5 of Appendix 14).

In noncumulates, ferrian ilmenite contains 45.3–55.5 wt. %  $\text{TiO}_2$ , 40.2–45.0 wt. %  $\text{FeO}^{\text{TOT}}$ , 1.2–3.4 wt. %  $\text{MnO}$  and up to 0.6 wt. %  $\text{MgO}$ . In Appendix 14 analysis 6 represents the composition of a {111} oriented lamella in spinel (the chromian magnetite of Fig. 6.14.C), and analysis 7 represents the composition of a primary ilmenite. Analogous to ilmenite in cumulates, the highest  $\text{Fe}_2\text{O}_3$  content, ca. 6 wt. %, occurs in primary ilmenite.

### 6.3 Accessory silicates and oxides

#### 6.3.1 Garnet

Small grains of garnet mostly occur as inclusions in plagioclase in the olivine gabbro-norite subzones of the Koillismaa Intru-

sion. The garnet grains are typically sieved with talc-rich inclusions and display compositional zonation (Fig. 6.16). Ten selected analyses are presented in Appendix 15.

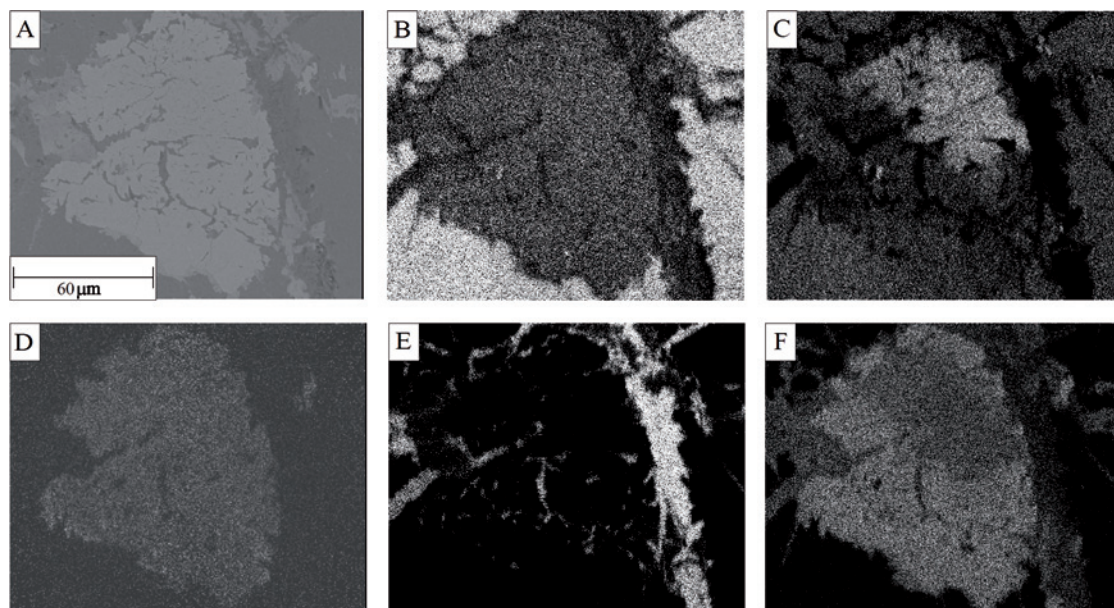
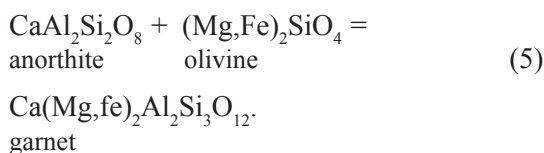


Fig. 6.16. A. BE-image of garnet in the LZa (24-TTK-01). B-F. X-ray scanning images illustrating the elements distribution of various elements in the grain: Al (B), Ca (C), Mn (D), Mg (E) and Fe (F).

The analysed garnets contain 8.4–26.5 wt. % FeO, up to 6.4 wt. % Fe<sub>2</sub>O<sub>3</sub>, up to 2.5 wt. % MgO, 8.1–23.9 wt. % CaO, 35.6–37.8 wt. % SiO<sub>2</sub>, 20.2–22.3 wt. % Al<sub>2</sub>O<sub>3</sub> and 1.8–6.9 wt. % MnO. They contain 18.7–60.7 mol. % almandine, 4.1–15.7 mol. % spessartine, 0.1–10.2 mol. % pyrope, 13.1–60.6 mol. % grossular and less than 0.2 mol. % uvarovite. The high manganese concentrations are probably due to the Mn-Fe diadochy, as these elements display a negative correlation in the analysed samples.

Mäkelä (1975) noted that the garnets of the Koillismaa Intrusion lie compositionally within the miscibility gap between pyralisites and ugrandite and proposed that the garnets formed as a result of olivine alteration. In accordance with Miller (1974) it is suggested here that the genesis of the garnets can be related to the following reaction:



where the garnet is composed of 2/3 of pyrope-almandine component and 1/3 of grossular component. The compositional zoning in the Koillismaa Intrusion garnets is related to these end-members with grain margins being pyrope- and almandine-enriched, and cores being grossular-rich.

### 6.3.2 Loveringite

Loveringite, first found and described by Gatehouse et al. (1978) and Campbell & Kelly (1978) in the Jemberlana Intrusion and by Cameron (1978) in the Bushveld Complex is a relatively rare phase belonging to the crichtonite group with the general formula AM<sub>21</sub>O<sub>38</sub>; A = large cations (Ca, REE, Y, Th, U, Pb) and M = small cations (Ti, Fe, Cr, Mg,

Zr, Al, V, Mn). At the time of its definition and description, Alapieti (1982) found loveringite in the Näränkävåara Intrusion during the microanalyses of spinel group minerals. As mentioned in Chapter 5.7, in the present study loveringite was found in the noncumulus-textured gabbro-norite body in drill core B7. The electron microprobe analyses were carried out on four thin sections that cover the 2 m thick loveringite-bearing interval in the noncumulate body, at a depth of 10.60–13.00 m in the drill core. Traverses were analysed across three grains to evaluate potential zoning. The Fe<sub>2</sub>O<sub>3</sub>/FeO in loveringite was calculated on the stoichiometric basis (Droop 1987). Ten representative analyses of loveringite are listed in Appendix 16.

The loveringite grains in the drill core are closely associated with phlogopite, orthoclase and apatite and form discrete grains up to 100×150 µm in size (Fig. 6.17.A). In one case loveringite occurs in a composite ilmenite-rutile-chromite-loveringite grain, which is 100×100 µm by size (Fig. 6.17.B). The discrete grains are typically mantled by manganoan ilmenite, which coat even the smallest fissures and holes (Fig. 6.17.A). Semi-quantitative X-ray scans (Fig. 6.18) revealed that such ilmenite in turn is associated with zircon, which occurs as a thin veneer over the ilmenite in a similar way as Koitelainen loveringite (Tarkian & Mutanen 1987). The ilmenite mantles commonly appear to be relatively thick when adjacent to quartz, and in such cases, there occurs a magnesium- and silica-rich phase between the quartz and the ilmenite (“talc?” in Fig. 6.18.B).

In addition to mafic-ultramafic intrusions, loveringite has been found in mantle xenoliths (Jones et al. 1982; Wang et al. 1999; Kalfoun et al. 2002; Săbău & Alberico 2003). The bivariate plots of Fig. 6.19 illustrate chemical differences between loveringites of these different geological environments.

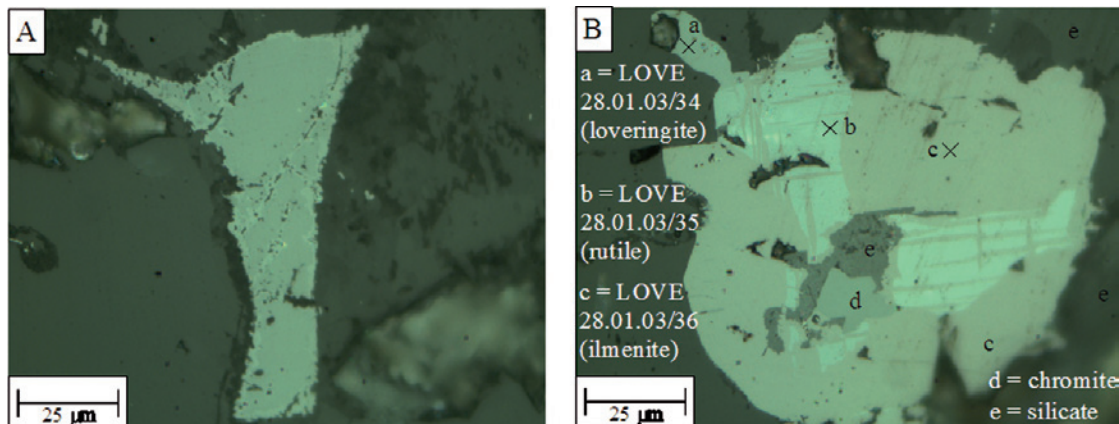


Fig. 6.17. **A.** Loveringite in a noncumulate body (B7 11.80, reflected light and parallel nicols), **B.** composite ilmenite-rutile-chromite-loveringite grain in a noncumulate body (B7 13.00, reflected light and parallel nicols). Analysis points are shown with crosses and identified by analytical keys.

Gatehouse et al. (1978) showed that loveringite has two types of isomorphous replacements, which include Fe-Cr and Ca-REE exchanges. The first type is distinct in the loveringites of this study: the most Cr-depleted and Fe-enriched grains occur in the sulphide-bearing area of the noncumulate body, at 10.60 m in the drill core, and the most Cr-enriched and Fe-depleted grains occur at 13.00 m, which is located furthest from the sulphides. The correlation between Ca and other large cations in the analysed loveringites is not so clear. (Fig. 6.19). However, the most distinctive feature in the compositional variation of loveringite of this research was re-

vealed in the line traverses: the phases have Mg-, Ti- and Ca-bearing cores and Cr- and Fe<sup>2+</sup>-bearing margins (Fig. 6.18A).

The loveringite grains are rimmed by manganian ilmenite (Figs 6.17.A and 6.18), which contain 49.7–50.9 wt. % TiO<sub>2</sub>, 28.3–33.3 wt. % FeO<sup>TOT</sup>, 14.8–16.6 wt. % MnO and up to 1.5 wt. % MgO. Full compositions of two such ilmenites are given in Appendix 14 (analyses 9 and 10). The ilmenite in the composite ilmenite-rutile-chromite-loveringite grain (Fig. 6.17.B) contains 54.0 wt. % TiO<sub>2</sub>, 44.2 wt. % FeO<sup>TOT</sup>, 1.2 wt. % MnO and 0.6 wt. % MgO (analysis 8 in Appendix 14).

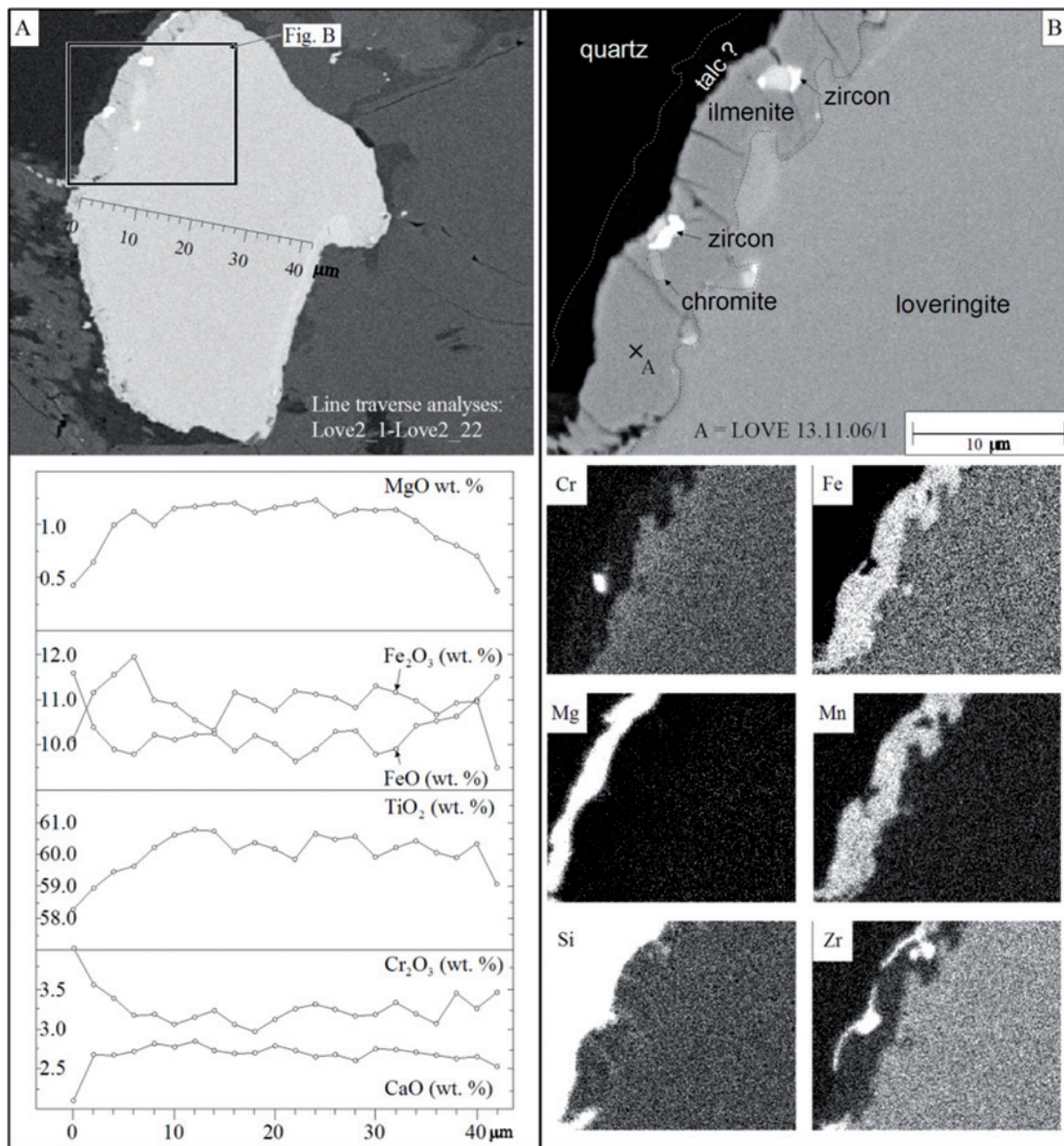


Fig. 6.18. **A.** BE-image of a lovingite grain (B7 11.80) showing the X-ray scanning area, line traverse location and selected compositions along the traverse: MgO, Fe<sub>2</sub>O<sub>3</sub>, FeO, TiO<sub>2</sub>, Cr<sub>2</sub>O<sub>3</sub> and CaO. **B.** BE-image and X-ray scanning images illustrating the distribution of phases and Cr, Fe, Mg, Mn, Si and Zr in the margin of the grain.

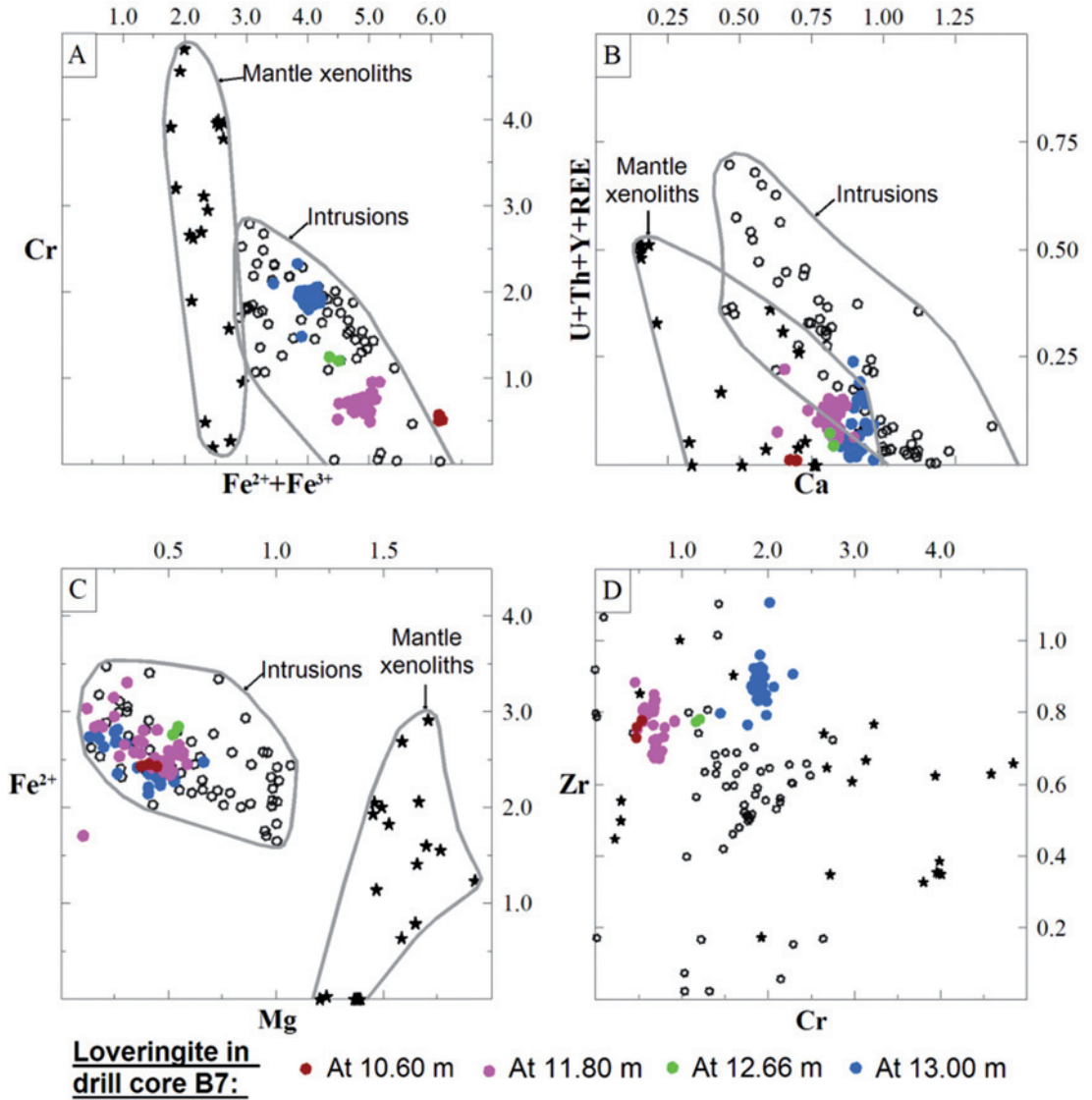


Fig. 6.19. The analysed loveringites (coloured dots) compared with loveringite analyses from mafic-ultramafic intrusions [black circles: the Jimberlana (Gatehouse et al. 1978; Campbell & Kelly 1978; Kelly et al. 1979), the Bushveld Complex (Cameron 1978), the Näränkäväära (Alapieti 1982), the Koitelainen (Tarkian & Mutanen 1987) the Western Laouni Layered Complex (Lorand et al. 1987), the Penikat (Halkoaho 1993), the Burakovski (Barkov et al. 1994), the Fedorova-Pana Tundra Complex (Barkov et al. 1996), the Akanvaara (Mutanen 1997) and the Bracco ophiolite Complex (Cabella et al. 1997)] and mantle xenoliths [starts: Bultfontein (Jones et al. 1982), the Garnet Ridge (Wang et al. 1999), the Barthatny (Kalfoun et al. 2002) and the Foltea ultramafic body (Săbău & Alberico 2003)]. Loveringite chemistry in the diagrams is expressed as atoms per formula unit.

### 6.3.3 Rutile, pseudobrookite, zircon and baddeleyite

Rutile was found in the noncumulus-textured gabbronorite of drill core B7 (Fig. 5.10) where it is closely associated with lovingite and apatite. Two grains were analysed. The first grain is  $100 \times 300 \mu\text{m}$  in size and contains lamellae that have a composition of pseudobrookite ( $\text{Fe}_2\text{TiO}_5\text{-FeTi}_2\text{O}_5\text{-Fe}_2\text{MgTi}_3\text{O}_{10}$ ) (Bowles 1988). The second rutile analysis was carried out on a composite ilmenite-rutile-chromite-lovingite grain shown in Fig. 6.17.B. This rutile crystal equally contains thin lamellae, but their composition was not determined. The composition of the first grain and its la-

mella are given as analyses 1, 2 and 4 of Appendix 17, whereas analysis 3 of the appendix represents rutile in the composite grain.

Most of the zirconium-rich phases were found during scanning of PGE-, gold- and silver-bearing phases, and therefore they are either from the MS or RT Reef. Some of the zircons occur as discrete grains, but more commonly zircon mantles anhedral up to  $20 \times 30 \mu\text{m}$  large baddeleyite grains (Fig. 6.20.A). Baddeleyite is present as anhedral composite grains mantled by zircon and as euhedral crystals up to  $50 \times 100 \mu\text{m}$  wide (Fig. 6.20.B). Appendix 17 includes selected zircon and baddeleyite analyses.

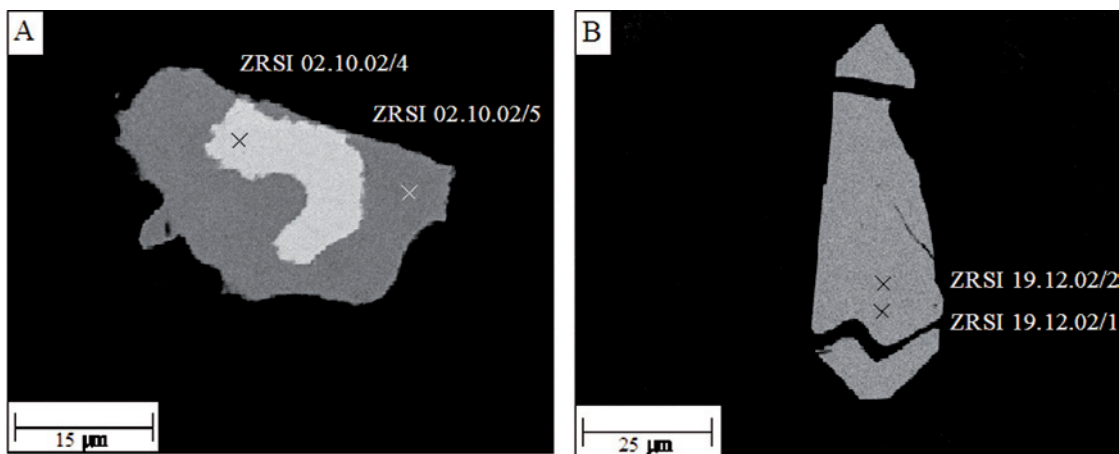


Fig. 6.20. Zircon and baddeleyite of the study area. **A.** Anhedral baddeleyite mantled by zircon in highly mottled gabbronorite (B4 14.70, BEI), **B.** Euhedral baddeleyite in olivine gabbronorite (25-TTK-01, BEI). Electron microprobe analysis points are shown with crosses and identified by analytical keys.

## 6.4 Phosphates

### 6.4.1 Apatite

Most of the apatite analyses were carried out on cumulates where the phase occurs as an intercumulus mineral together with granophyric intergrowths of quartz and albite. Individual grains are not compositionally zoned. Appendix 18 includes ten selected apatite analyses. The apatite compositions of the study area are presented in Fig. 6.21.

The apatites in the cumulate rocks are fluor- and hydroxy-apatites (Fig. 6.21). They contain 52.9–58.6 wt. % CaO, 40.1–44.1 wt. % P<sub>2</sub>O<sub>5</sub>, up to 3.1 wt. % Cl, 6.4 wt. % F and 1.7 wt. % H<sub>2</sub>O. The apatites from noncumulates contain 53.2–55.3 wt. % CaO, 40.1–43.7

wt. % P<sub>2</sub>O<sub>5</sub>, up to 5.2 wt. % Cl, 1.7 wt. % F and 1.1 wt. % H<sub>2</sub>O. The most Cl-rich apatite grains found in the bronzite segregations of noncumulate sample 10-TTK-03 (Figs 5.9.C and D). These grains are identified as “apatite in bronzite segregations“ in Fig. 6.21. The remainder of the apatites from noncumulates represent grains in the sulphide-bearing pockets of drill core B7. One grain is from the Lontanvaara mafic rock unit.

Figure 6.22 presents apatite compositions across the Porttivaara block stratigraphy. The most notable feature is a clear transition from Cl-rich to F-rich compositions in the RT Reef area.

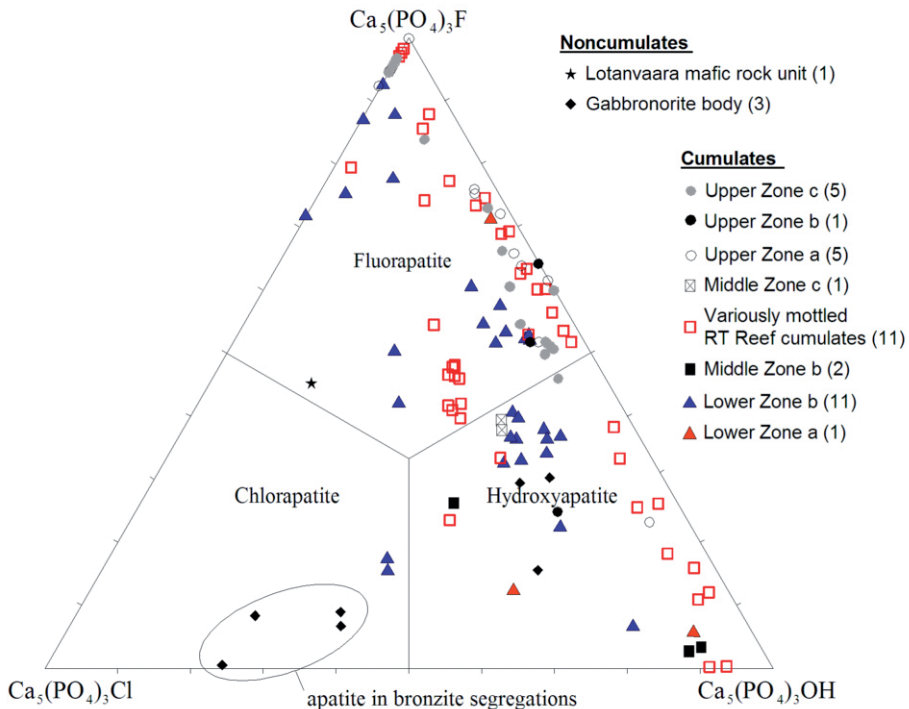


Fig. 6.21. Apatite compositions of the study area plotted in the fluor-, chlor- and hydroxyapatite triangle (mol. %). Number of analysed samples is shown in parentheses.

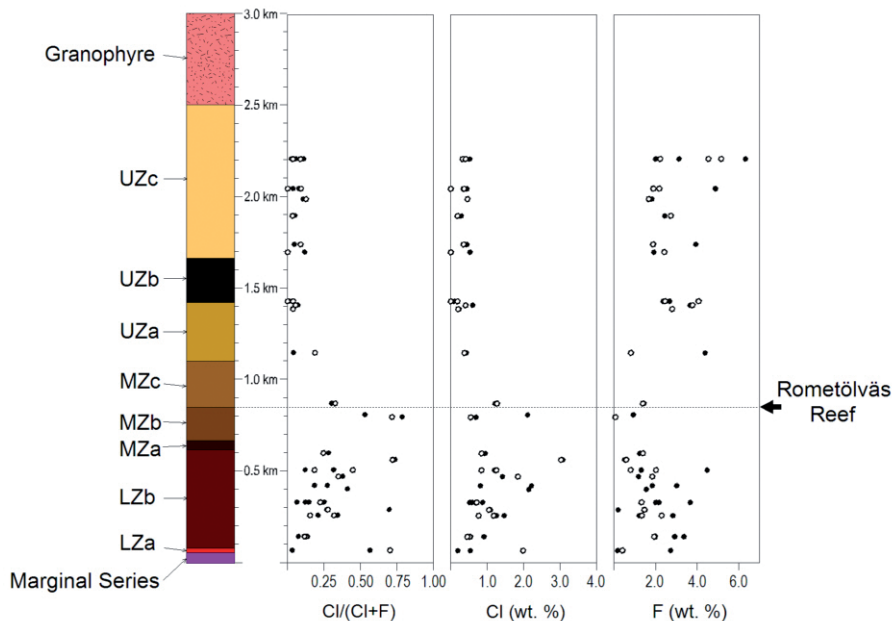


Fig. 6.22. Plot of the  $Cl/(Cl+F)$  and concentrations of Cl and F in apatite grains of the Porttivaara block. Black dots represent cores of crystals and circles represent crystal margins.

### 6.5 Sulphides

As mentioned in Chapter 5.4, the principal sulphide minerals of the MS comprise pyrrhotite, chalcopyrite, pentlandite, and in places pyrite. The analysed pyrrhotites ( $Fe_{1-x}S$ ) are relatively Ni-rich (up to 0.9 wt. %). According to Ramdohr (1980) the limit in composition between hexagonal and monoclinic form of pyrrhotite is reached when the iron deficit ( $x$ ) in the phase increases above 0.10. The analysed pyrrhotite grains are monoclinic on the basis of their iron deficit values (0.16-0.17). The pentlandites, or more precisely, the pentlandite-mackinawite series have Fe/Ni values in the range of 0.77-0.88. Idiomorphic pyrite contains up to 3.7 wt. % Co, whereas anhedral pyrite has a very low cobalt content. The analysed chalcopyrite compositions are close to stoichiometric. The compositions of pyrrhotite, chalcopyrite, pentlandite and pyrite are given in Appendix 19.

The accessory sulphides in the MS found during this research are millerite, members of the galena-clausthalite series, sphalerite and a blue mineral which is mantling chalcopyrite grains or occurs as tiny grains close to chalcopyrite. The blue mineral has a composition similar to geerite ( $Cu_8S_5$ ) (column 7 of Appendix 20). Millerite (analysis 1 of Appendix 20) was found to be present in one LZMSa sample. The analysed galena-clausthalites have  $S/(S+Se)$  values in the range of 0.4–1.0, which implies that most of the grains are galenas.

The appearance of sulphides in the noncumulate bodies and their host cumulates in the RT Reef are described in Chapters 5.7 and 5.8. Since the sulphide assemblages in both rocks are similar, their sulphide minerals are treated here together. In most of the reef sampling sites the typical sulphides are pyrrhotite, chalcopyrite and pentlandite. However, in one

Baabelinälkky cumulate sample bornite and millerite additionally occurs. Similar to the MS, the pyrrhotite of the noncumulate bodies and their host cumulates has a monoclinic structure: the iron deficits range from 0.12 to 0.20. These pyrrhotites are also relatively rich in Ni (up to 0.8 wt. %). The chalcopyrite compositions are close to stoichiometric and the pentlandites have Fe/Ni values of 0.78–0.91. Bornite was found to be closely associated with chalcopyrite, and in one sample it occurs with millerite, which in turn contains chalcopyrite lamellae. An analysis of millerite from the RT Reef is given in column 2 and bornite compositions are given in columns 3 and 4 of Appendix 20.

The accessory sulphides of the RT Reef comprise pyrite, sphalerite, galena-clausthalite, violarite, cobaltite and covellite. The pyrite grains show similar characteristics as in the MS, in that euhedral grains contain more

cobalt (up to 2.6 wt. % Co) than the anhedral ones. Sphalerite contain 2.8–9.5 wt. % Fe and up to 4.3 wt. % Cd. Most of the members of the galena-clausthalite series are galenas with up to 15.7 wt. % S, although some grains are pure clausthalites and contain up to 24.7 wt. % Se. Violarite is an alteration product of pentlandite and was found to be present in two samples collected from outcrops where the analysed violarite compositions display Fe/Ni values of 0.86–1.10. Two euhedral cobaltite grains were found in thin sections representing depths of 20.45 m and 29.40 m in drill core B7 from Rometölväs. The cobaltite of sample B7 20.45 m contains more cobalt than that in sample B7 29.40. The average formula of cobaltite in the former sample, as calculated on the basis of 1 S, is  $\text{Co}_{0.64}\text{Ni}_{0.31}\text{Fe}_{0.18}\text{As}_{0.97}\text{S}_{1.00}$  and in the latter sample  $\text{Co}_{0.50}\text{Ni}_{0.40}\text{Fe}_{0.18}\text{As}_{1.00}\text{S}_{1.00}$ . The cobaltite composition in sample B7 20.45 m is given in column 6 of Appendix 20.

## 6.6 Altaite, tellurobismutite and undefined Ni-Te-S mineral

Altaite (PbTe) and tellurobismuthite ( $\text{Bi}_2\text{Te}_3$ ) compositions were determined with EDS from the reef samples. Most of the analysed altaite grains are located at sulphide margins and are compositionally almost stoichiometric. However, some altaites contain up to 1.8 wt. % Se and 7.0 wt. % Ag. The grains of tellurobismuthite occur mostly at sulphide margins and contain up to 3.6 wt. % Fe, 1.6 wt. % Se and 1.7 % Ag. Appendix 21 includes selected altaite and tellurobismuthite analyses.

Ten grains of an undefined Ni-Te-S mineral were found in three thin sections collected from RT Reef cumulates at 20.85 m, 21.20 m and 21.65 m in drill core B1 from the Baabe-

linälkky area. Two selected analyses are given in columns 5 and 6 of Appendix 21. Most of the grains are discrete grains up to  $150\ \mu\text{m}^2$  in size, located within sulphides.

The undefined mineral contains Ni, Te, and S as major constituents, and has at least three ubiquitous minor constituents, Co, Fe, Cu. Some of the grains also contain small amounts of Pd and Sb. An empirical formula for the mineral can be calculated on the basis of 2 atoms per formula unit. This is exemplified using the analysis given in column 5 of Appendix 21 for which the calculated formula is  $(\text{Ni}_{0.81}\text{Co}_{0.10}\text{Fe}_{0.07}\text{Cu}_{0.02})_{1.00}(\text{Te}_{0.53}\text{S}_{0.47})_{1.00}$ .

## 6.7 PGE-, gold- and silver-bearing minerals

The PGE-, gold- and silver-bearing minerals of the MS can be subdivided into six groups. In decreasing order of abundance, these are 1) phases of the kotulskite-sobolevskite-sudburyite solid solution series (Fig. 6.23.A), 2) phases of the merenskyite-melonite-moncheite solid solution series (Fig. 6.23.B), 3) Au-Ag alloys (Fig. 6.23.C), 4) sperrylite (Fig. 6.23.D), 5) michenerite (Fig. 6.23.E) and 6) hessite. The three most abundant groups each make up 25–30 % of the total population. Approximately 90 % of the minerals are single-phase grains that occur in silicates, mostly as satellites around sulphides or at sulphide-silicate grain boundaries. (Table 6.2). The grain size distribution of the identified MS phases is shown in Fig. 6.24, which reveals that the smallest grains typically belong to the kotulskite-sobolevskite-sudburyite solid solution series, whereas sperrylite does not occur as grains smaller than ca. 1  $\mu\text{m}^2$ .

Similarly to the MS, the precious metal- and silver-bearing minerals of the RT Reef are mostly tellurides (Table 6.3), which can be classified into six groups: 1) members of the merenskyite-moncheite-melonite solid solution series (Fig. 6.23.F), 2) hessite (Figs 6.23.G and H), 3) sperrylite (Fig. 6.23.I), 4) volynskite (Fig. 6.23.J), 5) michenerite (Fig. 6.23.K) and 6) Au-Ag alloys (Fig. 6.23.L). Approximately 80 % of the grains are single-phase grains of which 50 % occur within silicates and the rest within sulphides or silicate-sulphide borders. The grain size distribution of the identified precious metal- and silver-bearing minerals of the reef is shown in Fig. 6.25. In contrast to the MS, the grains of the RT Reef are usually much larger in size.

Compositions of the kotulskite-sudburyite-sobolevskite series, michenerite and the merenskyite-moncheite-melonite series are illustrated in the Bi-PGE+Ni+Sb-Te diagram of Fig. 6.26. The grains of the kotulskite-sudburyite-sobolevskite series which were found only in the MS contain very low amounts of

Sb (< 2.5 wt. %) and can be defined as kotulskites that have 10-20 mol. % of sobolevskite component. Michenerite grains in both the MS and the RT Reef are somewhat richer in Te than the stoichiometric phase. Within the merenskyite-moncheite-melonite solid solution, the grains of the MS appear to contain more Bi (10.0 wt. % in average), than the ones from the RT Reef (2.6 wt. % in average). Compositions of the merenskyite-moncheite-melonite solid solution are further plotted in Fig. 6.27 where most of the MS grains are Pd-bearing and can be defined as merenskyites, while most of the RT Reef grains are Ni-bearing melonites.

The sperrylite grains of both the MS and the RT Reef are close to stoichiometric. They include also small amounts of Rh (up to 2.3 wt. %), Pd (up to 1.8 wt. %) and Fe (up to 1.3 wt. %).

Most of the Au-Ag alloys in the MS contain ca. 80 wt. % Au, but some of the grains are composed of almost pure gold. On the basis of three analyses the RT Reef Au-Ag alloys contain more Ag than Au and could be defined as aurian silver. Hessite both in the MS and the reef contains small amounts of thallium.

The identified PGE-, gold- and silver-bearing phases have similar compositions to those reported by Piirainen et al. (1977), Alapieti & Piirainen (1984), Piispanen & Tarkian (1984), Lahtinen (1985) and Kojonen & Iljina (2001). According to Kojonen & Iljina (2001), the PGE minerals in the MS are mostly melonite group phases, whereas the present study shows that the kotulskite-sobolevskite-sudburyite series phases are as abundant as the melonite group phases. Kojonen & Iljina (2001) collected their 60 samples from the Haukiaho area, but in this work only two samples represent that area and the remaining ten samples are from the Soukeli area of the Porttivaara block. Ten representative analyses of noble metal- and silver-bearing phases are shown in Appendix 22.

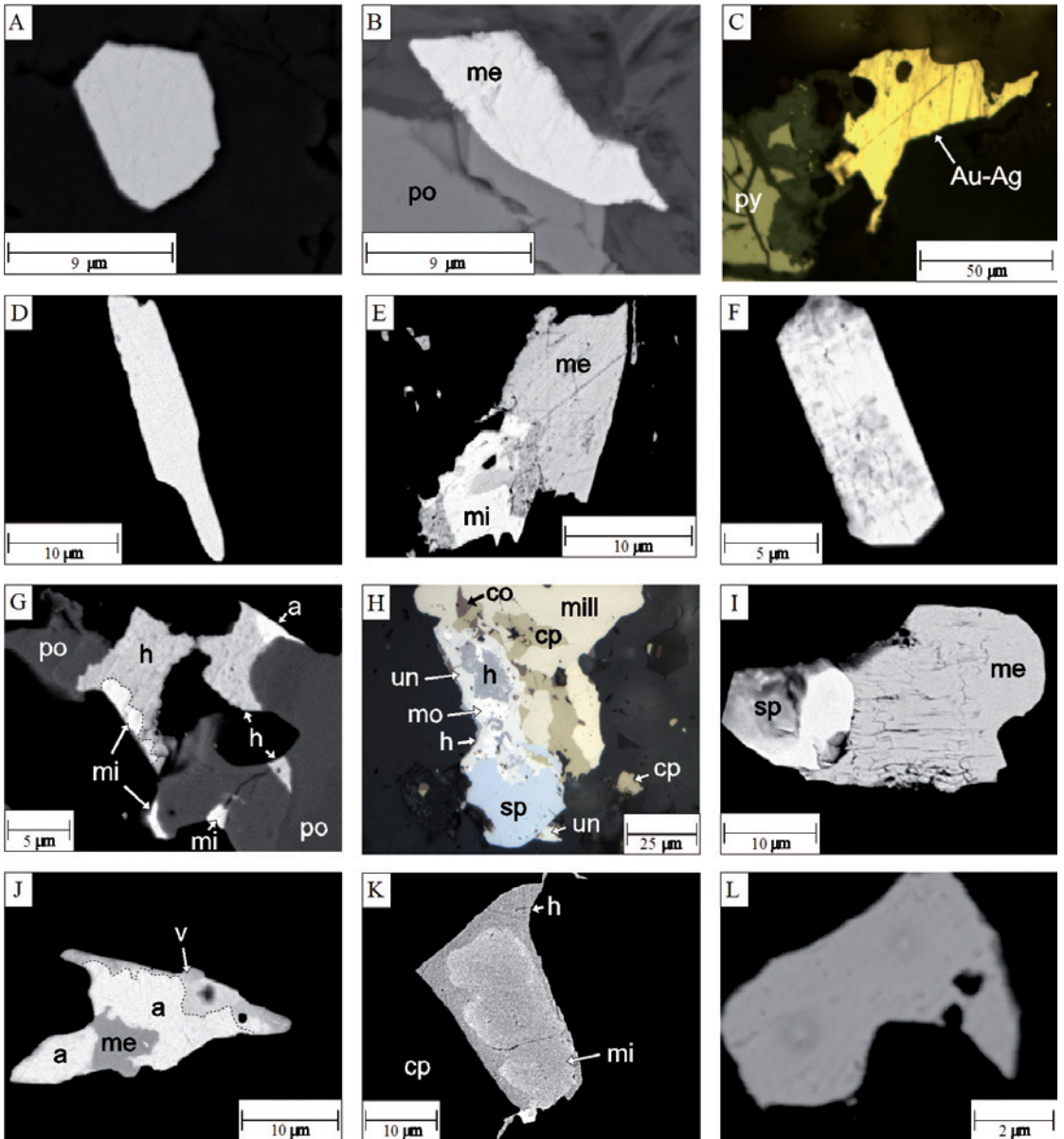


Fig. 6.23. PGE-, gold- and silver-bearing minerals of the study area. **A.** Kotulskite in silicate (R359 180.18, BEI), **B.** Merenskyite (me) at margin of pyrrhotite (po) (R359 180.18, BEI), **C.** Au-Ag alloy at margin of secondary pyrite (py) (264-TTK-00, reflected light and one nicol), **D.** Sperrylite in silicate (16-TTK-01, BEI), **E.** Composite grain of michenerite (mi) and merenskyite (me) at margin of pyrrhotite (400-TTK-00, BEI), **F.** Melonite in silicate (B4 14.70, BEI), **G.** Composite grain of hessite (h), michenerite (mi) and altaite (a) in pyrrhotite (po) (B7 11.65, BEI), **H.** Composite grain of sperrylite (sp), moncheite (mo), hessite (h), and undefined Ni-Te-S mineral (un) at margin of sulphide. Sulphide grain is composed of millerite (mill), chalcopyrite (cp) and covellite (co) (B1 21.65B, reflected light and one nicol), **I.** Composite grain of sperrylite (sp) and melonite (me) in silicate (20.95, BEI), **J.** Composite grain of altaite (a), melonite (me) and volynskite (v) at sulphide margin (B7 28.70, BEI), **K.** Composite grain of michenerite (mi) and hessite (h) at margin of chalcopyrite (cp) (B1 21.65, BEI), **L.** Au-Ag alloy in silicate (135.8B-TTK-99, BEI).

Table 6.2. Relative proportions and mode of occurrence of the PGE-, gold- and silver-bearing mineral grains of the Marginal Series.

PGE-, gold- and silver-bearing minerals (n = 251 from 12 samples):	
<i>Kotulskite-sobolevskite-sudburyite (PdTe-PdBi-PdSb)</i>	32.70 %
<i>Merenskyite-moncheite-melonite (PdTe<sub>2</sub>-PtTe<sub>2</sub>-NiTe<sub>2</sub>)</i>	29.80 %
<i>Electrum (AuAg)</i>	26.20 %
<i>Sperrylite (PtAs<sub>2</sub>)</i>	5.70 %
<i>Michenerite (PdBiTe)</i>	5.20 %
<i>Hessite (Ag<sub>2</sub>Te)</i>	0.40 %
Host phases:	
Composite grains (n = 16):	
<i>Silicate</i>	4.40 %
<i>Sulphide</i>	0.00 %
<i>Silicate-sulphide border</i>	2.00 %
Single grains (n = 235):	
<i>Silicate</i>	78.10 %
<i>Sulphide</i>	9.10 %
<i>Silicate-sulphide border</i>	6.40 %

Table 6.3. Relative proportions and mode of occurrence of the PGE-, gold- and silver-bearing mineral grains of the Rometölväs Reef.

PGE-, gold- and silver-bearing minerals (n = 290 from 31 samples):	
<i>Merenskyite-moncheite-melonite (PdTe<sub>2</sub>-PtTe<sub>2</sub>-NiTe<sub>2</sub>)</i>	51.80%
<i>Hessite (Ag<sub>2</sub>Te)</i>	34.20%
<i>Sperrylite (PtAs<sub>2</sub>)</i>	7.50%
<i>Volynskite (AgBiTe<sub>2</sub>)</i>	2.90%
<i>Michenerite (PdBiTe)</i>	2.50%
<i>Electrum (AuAg)</i>	1.10%
Host phases:	
Composite grains (n = 69):	
<i>Silicate</i>	3.10%
<i>Sulphide</i>	14.80%
<i>Silicate-sulphide border</i>	4.10%
Single grains (n = 221):	
<i>Silicate</i>	44.50%
<i>Sulphide</i>	22.80%
<i>Silicate-sulphide border</i>	10.70%

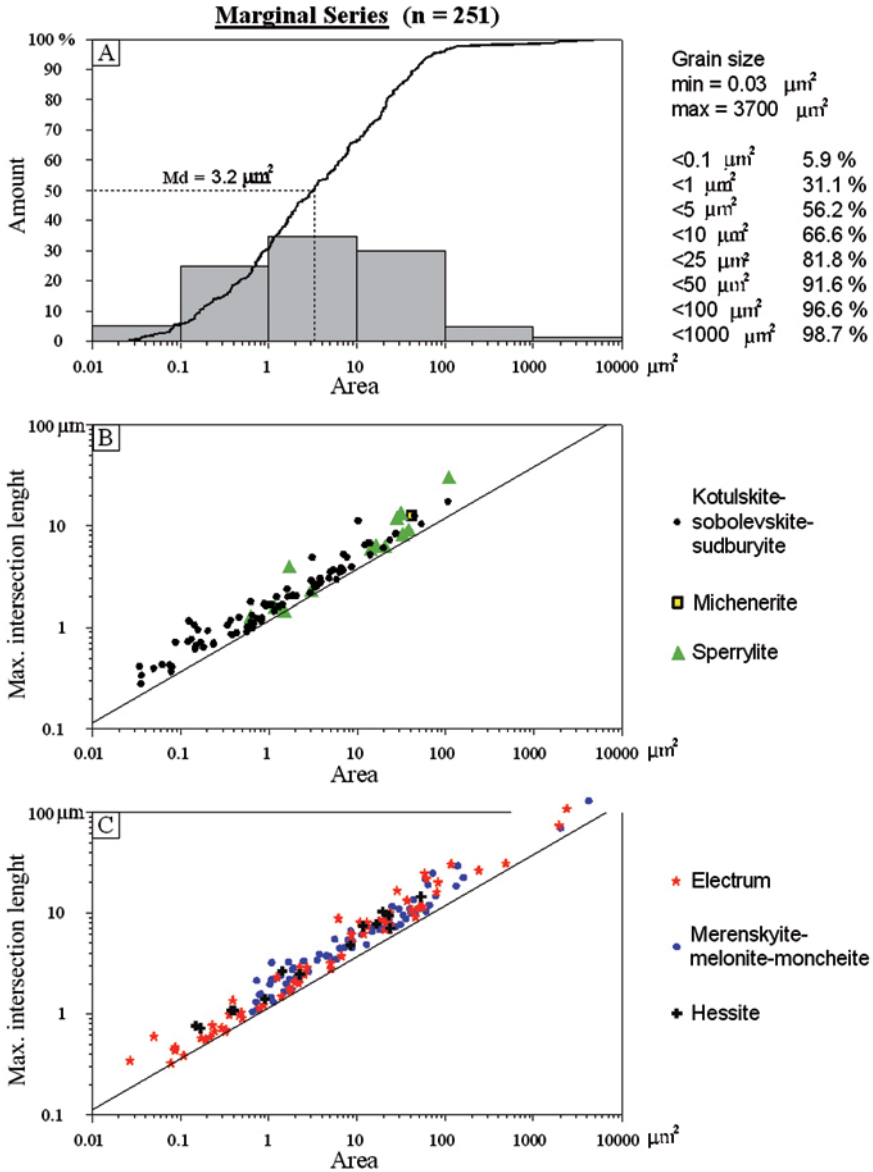


Fig. 6.24. **A.** Grain size distribution of the PGE-, gold- and silver-bearing grains of the Marginal Series. Md denotes the median of the grain size. **B** and **C.** Maximum intersection length vs. grain area -diagrams showing correlation between measured maximum intersection lengths (μm) and areas (μm<sup>2</sup>) of the grains. Upper limit of grain areas in B and C is described by the function  $A(r)=\pi r^2$ .

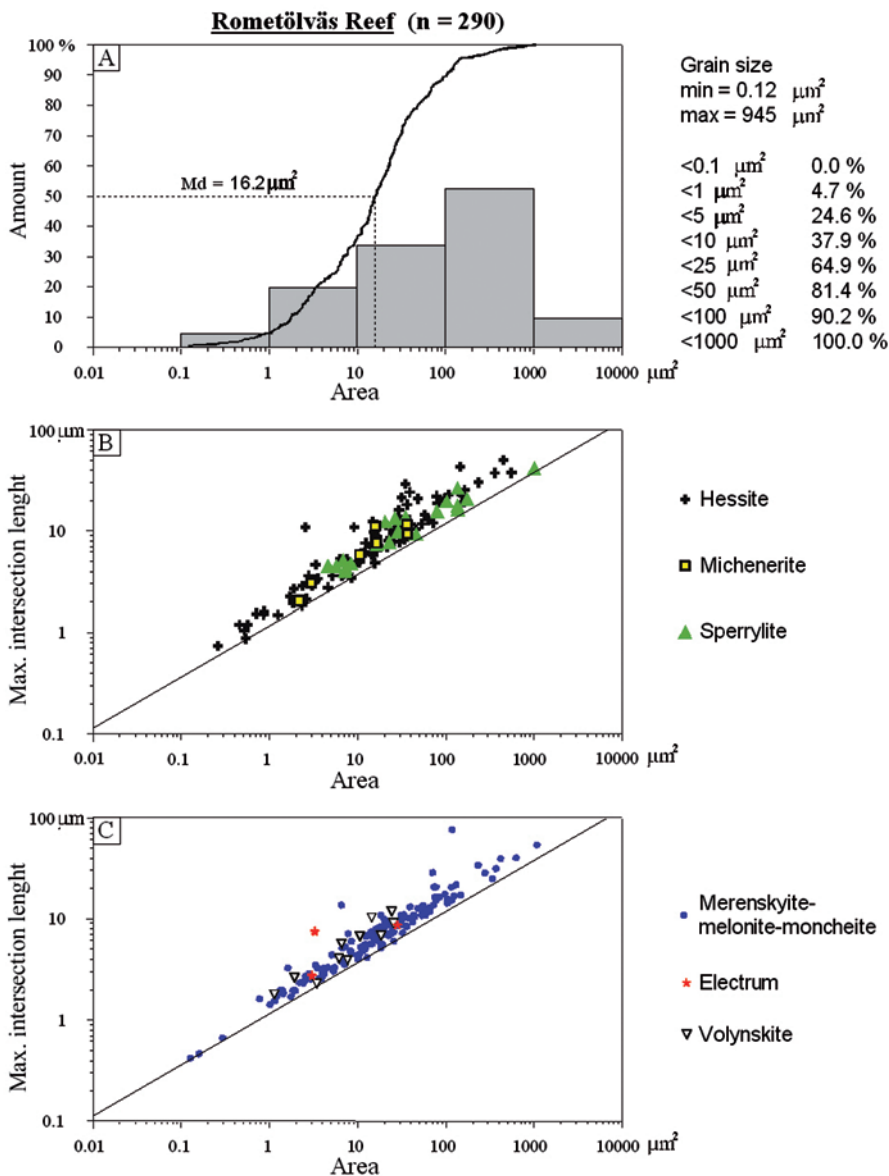


Fig. 6.25. **A.** Grain size distribution of the PGE-, gold- and silver-bearing grains of the Rometölväs Reef. Md denotes the median of the grain size. **B** and **C.** Maximum intersection length vs. grain area -diagrams showing correlation between measured maximum intersection lengths ( $\mu\text{m}$ ) and areas ( $\mu\text{m}^2$ ) of the grains. Upper limit of grain areas in B and C is described by the function  $A(r)=\pi r^2$ .

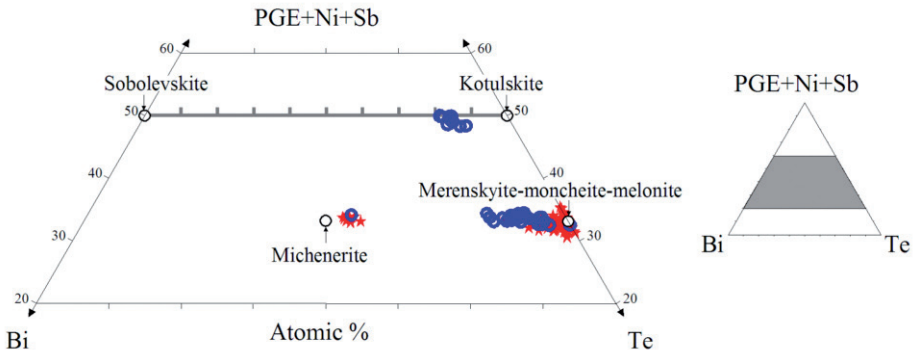


Fig. 6.26. PGE-Ni-Te-Bi-Sb phases of the study area plotted in Bi-PGE+Ni+Sb-Te space. Black circles denote the compositions of kotulskite, sobolevskite, michenerite and melonite-moncheite-merenskyite group. The ticked line denotes intermediate members in the sobolevskite-kotulskite solid solution series. Red stars represent grains from the Rometölväs grains and blue circles from the Marginal Series.

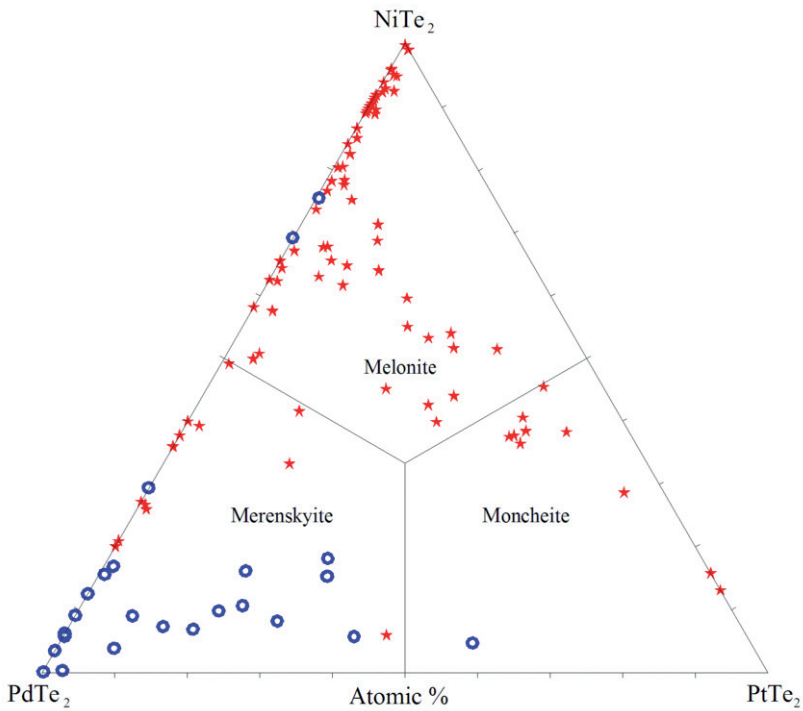


Fig. 6.27. Analysed grains of the merenskyite-melonite-moncheite series ( $\text{PdTe}_2\text{-NiTe}_2\text{-PtTe}_2$ ). Red stars represent grains from the Rometölväs Reef and blue circles grains from the Marginal Series.

## 6.8 Summary

The Koillismaa Intrusion shows only subdued variation in terms of silicate mineral compositions. The Marginal Series displays a reverse trend of differentiation, which is most evident in the composition of plagioclase. In most of the Layered Series the Mg-number and Cr<sub>2</sub>O<sub>3</sub> content of Ca-rich pyroxene and the An content of plagioclase decrease with height, *i.e.* they display a normal differentiation trend. However, in the upper part of the LZb and the lower part of the MZ, a further reversal towards more primitive values occurs. The most evolved, Ab-rich plagioclase in the Koillismaa Intrusion occurs in UZb. The plagioclase in the upper part of the UZc display very uniform compositions that are distinctly more primitive than those in the lower part of the subzone.

The Rometölväs Reef is not marked by a significant break in the compositions of silicate minerals, but apatite becomes relatively chlorine-poor above the reef. Within the reef,

the secondary phases in the sulphide-bearing mottles do not show compositional variation either across the reef or along the strike of the reef.

The sulphide mineral assemblages of the Marginal Series and the Rometölväs Reef are similar. In both environments, the principal sulphide minerals are chalcopyrite, pyrrhotite and pentlandite and the precious metal- and silver-bearing phases are usually tellurides. However, the PGE-, Au- and Ag-bearing phases in the reef display significantly smaller grain sizes than those in the Marginal Series.

Amongst the noncumulus-textured bodies, the Pirivaara bodies host the most Fe-rich pyroxenes whereas the Porttivaara and Kuusijärvi bodies host the most Mg-rich pyroxenes. The pyroxene compositions in the noncumulus-textured bodies and Lotanvaara rock unit are similar, and different from those in the cumulates of the Koillismaa Intrusion.

## 7 WHOLE-ROCK CHEMISTRY

### 7.1 Major and trace elements

#### 7.1.1 Chilled margins and the weighted average composition of the Koillismaa Intrusion

The compositions of the lower and upper chilled margins and the weighted average of the Koillismaa Intrusion are compared in Table 7.1. According to the classification of Le Maitre et al. (2002) most of the Koillismaa Intrusion chilled margins can be classified as boninite-like, since they tend to be characterized by SiO<sub>2</sub> > 52 wt. %, MgO > 8 wt. % and TiO<sub>2</sub> < 0.5 wt. %. The lower chilled margin appears to be more primitive than upper

chilled margin as the former has higher Mg-numbers than the latter. In view of the Mg-numbers in the lower and upper chilled margins, the chromium and nickel contents are surprisingly high in the upper chilled margin.

The lower and upper chilled margins of the Koillismaa Intrusion plot in the field of subalkaline basaltic andesite within the TAS diagram (Fig. 7.1.A). In the AFM diagram, the chilled margin analyses plot in an area covering the boundary between tholeiitic and calcalkalic fields. In Jensen's cation plot, however, they define a weak trend from the field of basaltic komatiite to that of high-Mg tholei-

itic basalts. (Figs 7.1.B and C). The weighted average composition of the intrusion was calculated using cumulate analyses of the Porttivaara block profile. This composition is basaltic (Figs 7.1.A and C) and is characterized by high  $Al_2O_3$  (18.6 wt. %), moderate  $TiO_2$  (0.8 wt. %) and relatively low  $MgO$  (6.3 wt. %).

The compositions of the chilled margins and the weighted average are plotted in  $[TiO_2]$  vs.  $[Al_2O_3]$  diagram (Fig. 7.2.A, Hanski et al.

2001b) and in ternary  $Al_2O_3$ - $10TiO_2$ - $100Cr$  plot (Fig. 7.2.B). These diagrams are used for classifying rocks derived from compositionally different primary magmas. It is noteworthy from Fig 7.2.B that in contrast to relatively primitive liquids which tend to have constant  $Al_2O_3/TiO_2$  ratios, the more evolved magmas, such as tholeiitic basalts, tend to plot close to along the  $Al_2O_3$ - $TiO_2$  side of the diagram. This is obviously due to the nature of crys-

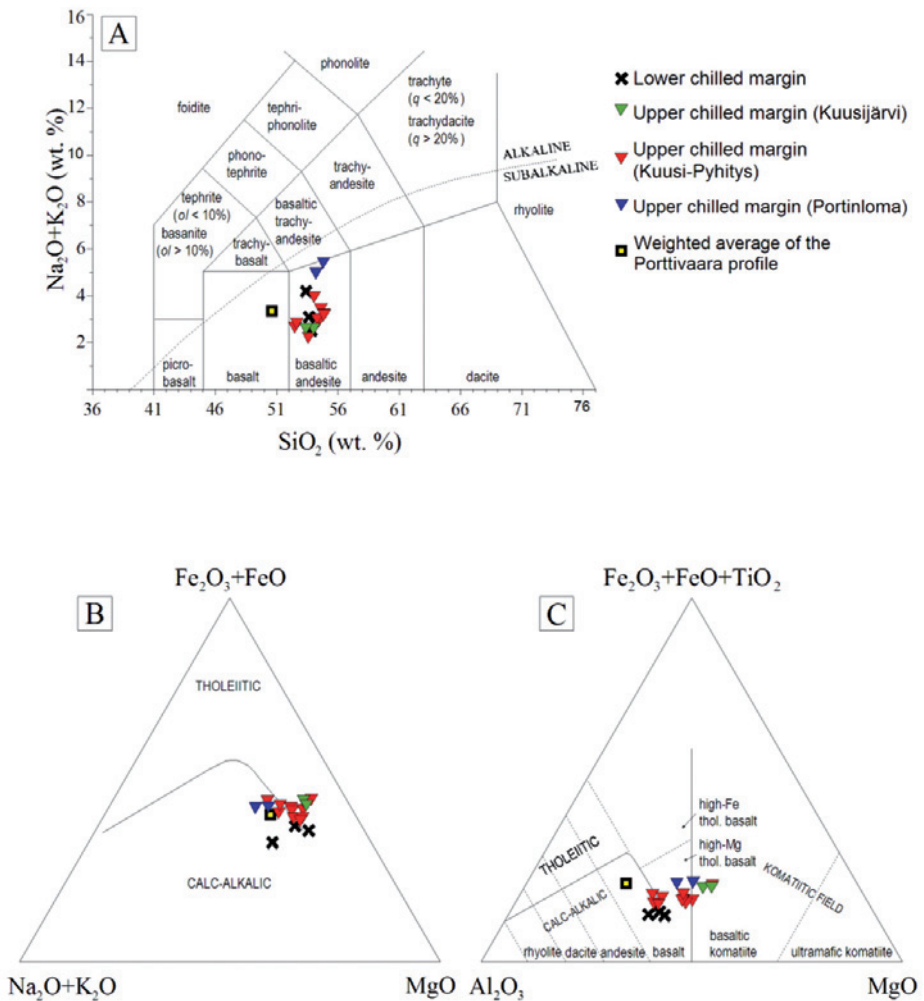


Fig. 7.1. TAS diagram (A) (Le Bas et al. 1986), AFM diagram (B) (Irvine & Baragar 1971) and Jensen's cation plot (C) (Jensen 1976) compiled for the Koillismaa Intrusion chilled margin analyses and the weighted average composition.

tallizing phases; in rocks derived from magmas of komatiitic, boninitic or other primitive lineage, the chemical difference in rock compositions is related to crystallization of olivine, pyroxene and chromite, whilst in the case of more evolved magmas the chemical difference of rocks is likely due to plagioclase-dominating crystallization.

In Fig. 7.2.A, the analyses of the chilled margins plot in the fields of boninites and Al-depleted komatiites and the weighted average plot in the field of Al-depleted komatiites. However, since many of the compositions of the chilled margins and the composition of the weighted average plot in the field of tholeiitic and calc-alkalic basalts of Fig. 7.2.B, they

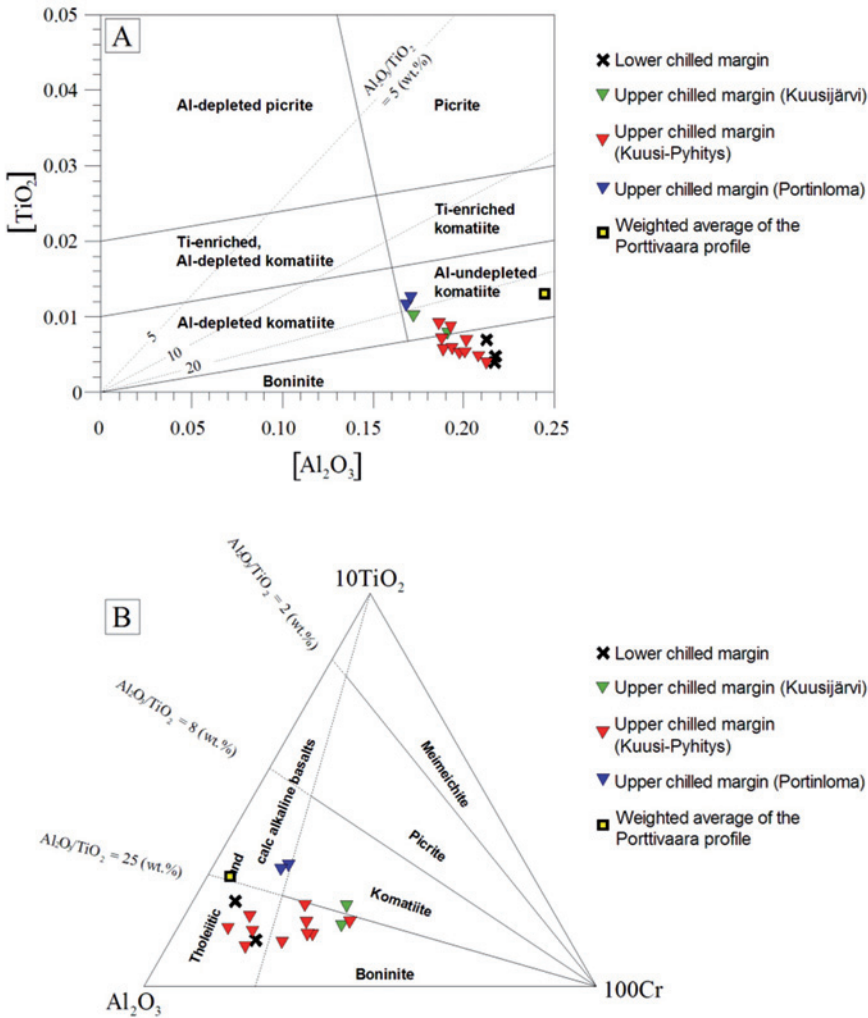


Fig. 7.2. [TiO<sub>2</sub>] versus [Al<sub>2</sub>O<sub>3</sub>] diagram (A) (Hanski et al. 2001b) and ternary Al<sub>2</sub>O<sub>3</sub>-10TiO<sub>2</sub>-100Cr (B) compiled for the Koillismaa Intrusion chilled margin analyses and the weighted average composition. The boundaries between the separate fields in B were drawn on the basis of 272 analyses of boninitic rocks, 544 analyses of komatiitic rocks, 39 analyses of picrites, 20 analyses of meimechites, 154 analyses of tholeiitic basalts and 52 analyses of calc-alkaline basalts (list of literature reference available from author upon request).

can be regarded as representatives of evolved rather than primitive magma.

Two samples from the lower chilled margin, 259-TTK-00 and U0144I-72 have similar chondrite- (Ch) and primitive mantle- (PM) normalized trace element patterns (A in Figs 7.3 and 7.4). Sample 259-TTK-00 has  $3.5\text{--}17.8 \times \text{Ch}$  of light rare earth elements (LREE: La-Sm),  $1.8\text{--}3.0 \times \text{Ch}$  of heavy rare earth elements (HREE: Gd-Lu) and the Ch-normalized composition shows a positive Eu-anomaly ( $\text{Eu}/\text{Eu}^* = 1.7$ ). The sample has  $(\text{La}/\text{Sm})_{\text{Ch}}$  of 5.2 and  $(\text{Gd}/\text{Lu})_{\text{Ch}}$  of 2.3. Sample 259-TTK-00 has  $(\text{La}/\text{Gd})_{\text{PM}}$  of 6.2 and  $(\text{Gd}/\text{Yb})_{\text{PM}}$  of 1.6, which results in a concave up pattern in the mantle-normalized diagram. In average, the upper chilled margin is richer in

REE, and particularly in HREE, than the lower chilled margin. The samples from different locations of the upper chilled margin (“Kuusijärvi”, “Portinloma” and “Kuusijärvi”, Fig. 4.1) form a coherent group in terms of their trace element compositions (B in Figs 7.3 and 7.4). The upper chilled margin analyses have  $(\text{La}/\text{Sm})_{\text{Ch}}$  values of 2.4–3.9,  $(\text{Gd}/\text{Lu})_{\text{Ch}}$  values of 1.4 to 2.5 and in the Ch-normalized diagram they show positive Eu-anomalies ( $\text{Eu}/\text{Eu}^* = 0.8\text{--}1.4$ ). In the PM-normalized diagram the patterns display distinct positive Sr and negative P anomalies. The values of  $(\text{La}/\text{Gd})_{\text{PM}}$  and  $(\text{Gd}/\text{Yb})_{\text{PM}}$  in the upper chilled margin analyses range from 2.8 to 4.9 and from 1.4 to 1.9, respectively.

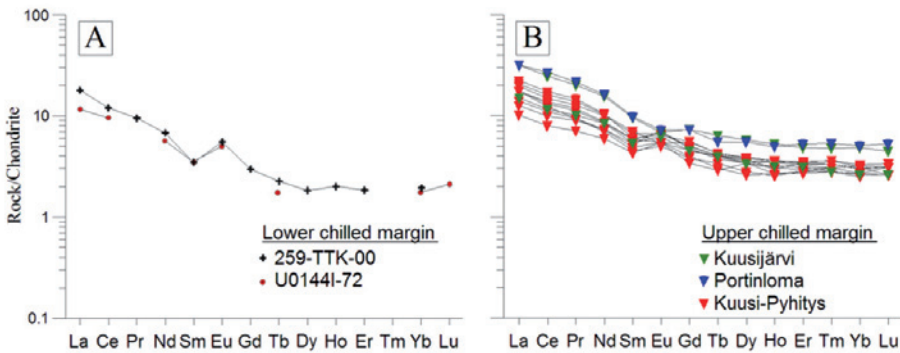


Fig. 7.3. Chondrite-normalized REE abundances of the chilled margins of the Koillismaa Intrusion. Normalizing values from Taylor & McLennan (1985). All elements analysed with ICP-MS.

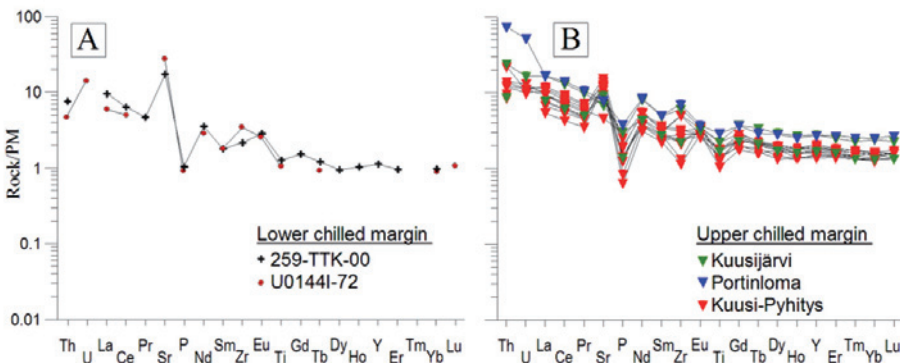


Fig. 7.4. Primitive Mantle-normalized trace element patterns of the Koillismaa Intrusion chilled margins. Normalizing values from Sun & McDonough (1989). Th, U, La, Ce, Pr, Nd, Sm, Eu, Gd, Tb, Dy, Ho, Y, Er, Tm, Yb and Lu analysed with ICP-MS. Sr, P, Zr and Ti analysed with XRF.

Table 7.1. Compositions of the chilled margins of the Koillismaa Intrusion (1–6) and the weighted average of the Porttivaara block (7) (full compositions of these rocks are given in Appendices 23 and 26).

<b>Sample</b>	<b>1</b>	<b>2</b>	<b>3</b>	<b>4</b>	<b>5</b>	<b>6</b>	<b>7</b>
wt. %							
SiO <sub>2</sub>	53.57	53.96	55.77	54.05	53.72	54.96	50.74
TiO <sub>2</sub>	0.28	0.23	0.42	0.34	0.46	0.69	0.78
Al <sub>2</sub> O <sub>3</sub>	16.61	16.54	16.76	14.42	12.19	12.26	18.64
Fe <sub>2</sub> O <sub>3</sub>	2.06	1.91	1.32	2.56	2.92	3.48	3.46
FeO	5.25	5.03	4.85	6.56	8.07	6.89	6.54
MnO	0.13	0.12	0.12	0.18	0.21	0.18	0.14
MgO	9.16	9.72	8.21	9.67	11.63	9.46	6.36
CaO	9.82	10.05	8.16	9.11	8.17	6.95	10.03
Na <sub>2</sub> O	2.55	2.44	3.90	2.54	1.77	5.00	2.85
K <sub>2</sub> O	0.54	0.10	0.50	0.54	0.82	0.05	0.41
P <sub>2</sub> O <sub>5</sub>	0.02	0.02	0.00	0.04	0.05	0.10	0.05
ppm							
Cr	464	310	-	582	936	376	144
Ni	218	160	200	176	291	163	192
V	102	98	10	150	177	211	323
Zr	24	39	-	38	47	96	37
Mg-number	75.7	77.5	75.1	72.3	72.0	70.9	63.4

1 = Lower chilled margin, 259-TTK-00 (Porttivaara block).

2 = Lower chilled margin, U0144I-72 (Kuusijärvi block, the composition is given by Juopperi 1976, Alapieti 1982 and Saini-Eidukat et al. 1997).

3 = Lower chilled margin, R0355-72 (Pirivaara block, the composition is given by Kerkkonen 1976).

4 = Upper chilled margin (Kuusi-Pyhitys, average composition of 10 samples).

5 = Upper chilled margin (Lake Kuusijärvi, average composition of 2 samples).

6 = Upper chilled margin (Portinloma, average composition of 2 samples).

7 = Weighted average of the Porttivaara block profile.

### 7.1.2 Lotanvaara mafic rock unit and noncumulus-textured gabbronorite bodies

The noncumulates of the Lotanvaara mafic rock unit and the noncumulate bodies can also be considered boninite-like according to the classification of Le Maitre et al. (2002). The compositions of the Lotanvaara rocks and the noncumulus-textured bodies are compared in Table 7.2.

In the TAS diagram, the analyses of the Lotanvaara mafic rock unit and the noncumulus-textured gabbronorite bodies display subalkaline compositions and plot in the fields of basalts and basaltic andesites (Fig. 7.5.A). In Jensen's cation plot (Fig. 7.5.C) the analyses project along a trend lying in the field of komatiites. The rocks of the Lotanvaara area are richest in MgO, whilst the noncumulus-textured bodies from the Pirivaara block record the most MgO-depleted compositions. The rock compositions are further illustrated with the  $\text{FeO}^{\text{TOT}}/\text{Al}_2\text{O}_3$  vs. MgO diagram of Fig. 7.6 and Mg-number vs. Ni diagram of Fig. 7.7.

The compositions of the Lotanvaara rocks and the noncumulus-textured bodies are plotted in  $[\text{TiO}_2]$  vs.  $[\text{Al}_2\text{O}_3]$  diagram (Fig. 7.8.A) and in ternary  $\text{Al}_2\text{O}_3$ -10 $\text{TiO}_2$ -100Cr plot (Fig. 7.8.B). In both diagrams, most of the analyses plot along a wide trend in the field of boninites. It is also obvious from the Fig 7.8.B that the rocks of Lotanvaara mafic unit record the most primitive compositions and the noncumulate bodies of the Pirivaara block are the most evolved.

The Ch-normalized trace element compositions of the samples collected from the Lotanvaara unit show slightly sloping LREE and flat

HREE patterns with subtle positive Eu-anomalies ( $\text{Eu}/\text{Eu}^* \sim 1.2$ ) (Fig. 7.9.A). The LREE concentrations in the rock range from 0.7 to  $7.7 \times \text{Ch}$  and HREE concentrations between 0.7 and  $3.3 \times \text{Ch}$ . The rock has  $(\text{La}/\text{Sm})_{\text{Ch}}$  values of 0.7–4.4 and  $(\text{Gd}/\text{Lu})_{\text{Ch}}$  values of 0.6–2.5. The REE patterns of noncumulus-textured gabbronorite bodies in different intrusion blocks are shown in Figs 7.9.B, C and D. The noncumulate bodies have  $(\text{La}/\text{Sm})_{\text{Ch}}$  values of 1.2–7.1 and  $(\text{Gd}/\text{Lu})_{\text{Ch}}$  values of 0.4–3.0. They have similar HREE concentrations as the rocks of the Lotanvaara unit, but contain more LREE ( $1$ – $19 \times \text{Ch}$ ), which results in steeper patterns in the diagrams. The Ch-normalized compositions of the noncumulate bodies have distinct positive Eu-anomalies ( $\text{Eu}/\text{Eu}^* \sim 1.6$ ) in the diagrams. The trace element concentrations of the Lotanvaara unit and the noncumulate bodies are very low, approaching the level of primitive mantle (Fig. 7.10). Both are characterized by distinct positive Sr anomalies in the PM-normalized diagram.

The variation in chemical components across the noncumulus-textured gabbronorite body at 9.85–15.64 m in drill core B7 was studied by continuous sampling, using approximately 30 cm long half-split core samples. The variation in the composition of major and selected trace elements is illustrated in Fig. 7.11. The body becomes progressively more evolved towards its interior as recorded *eg.* in the variation of Mg-number and the concentrations of incompatible elements  $\text{TiO}_2$ ,  $\text{K}_2\text{O}$ ,  $\text{P}_2\text{O}_5$ , Zr and Y. The most S-, Cu-, Ni-, Au-, Pd- and Pt- enriched samples are also the evolved ones. The weighted average concentration of the noncumulate body is listed in Appendix 23 (column 10).

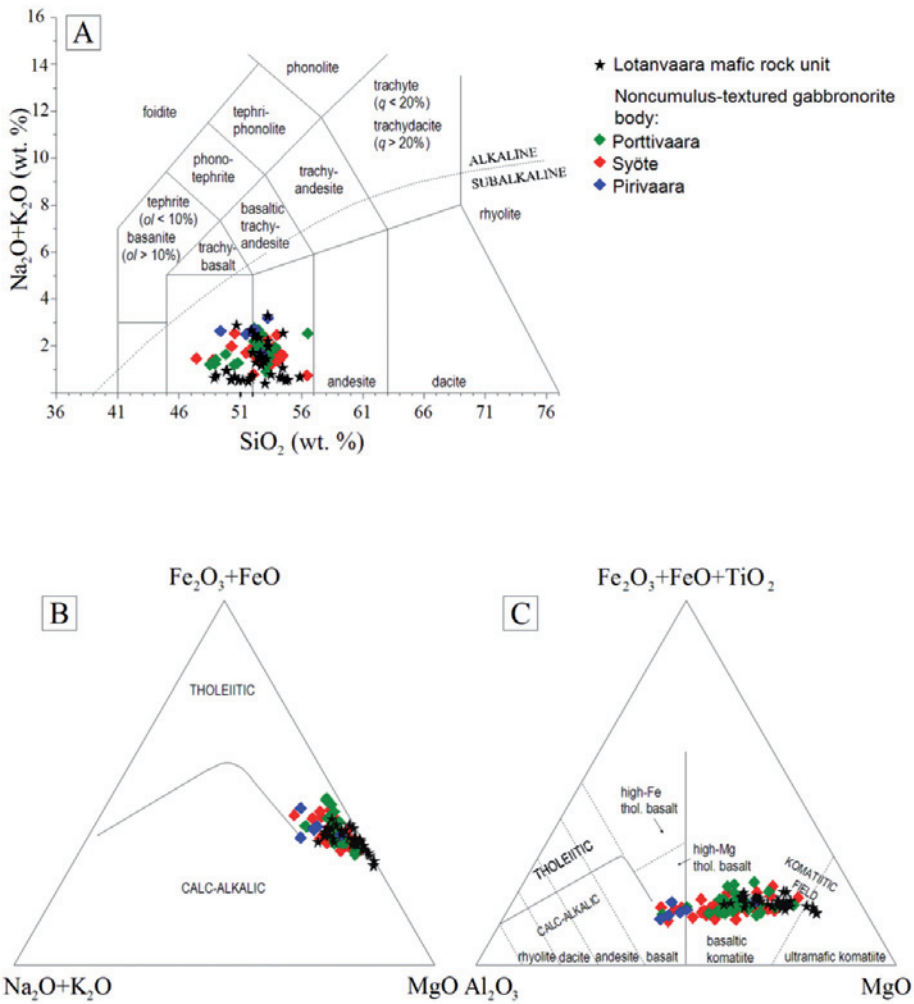


Fig. 7.5. TAS diagram (A) (Le Bas et al. 1986), AFM diagram (B) (Irvine & Baragar 1971) and Jensen's cation plot (C) (Jensen 1976) compiled for the Lotanvaara mafic rock unit and the noncumulus-textured gabbronorite bodies.

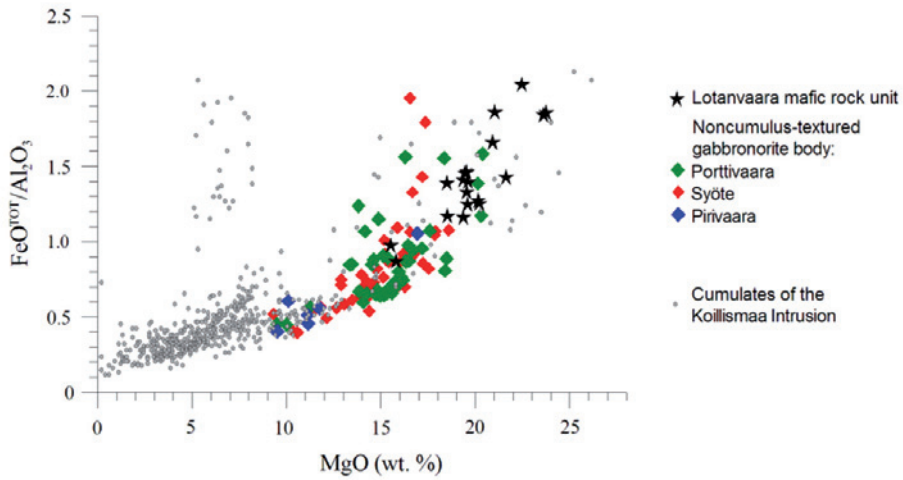


Fig. 7.6.  $\text{FeO}^{\text{TOT}}/\text{Al}_2\text{O}_3$  versus  $\text{MgO}$  diagram of the Lotanvaara mafic rock unit and the noncumulus-textured bodies. The compositions of the Koillismaa Intrusion cumulates are shown for comparison (these compositions are also shown in Fig. 7.13).

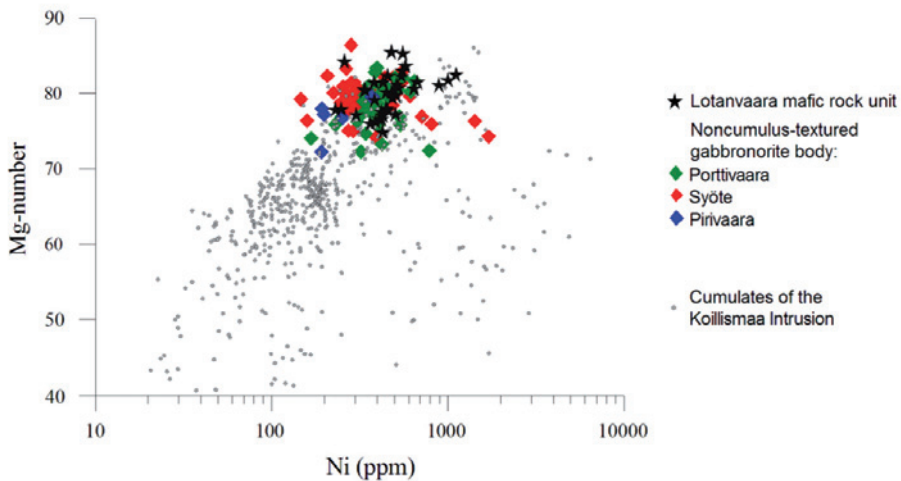


Fig. 7.7. Mg-number versus Ni diagram of the Lotanvaara mafic rock unit and the noncumulus-textured bodies. The compositions of the Koillismaa Intrusion cumulates are shown for comparison (these compositions are also shown in Fig. 7.14).

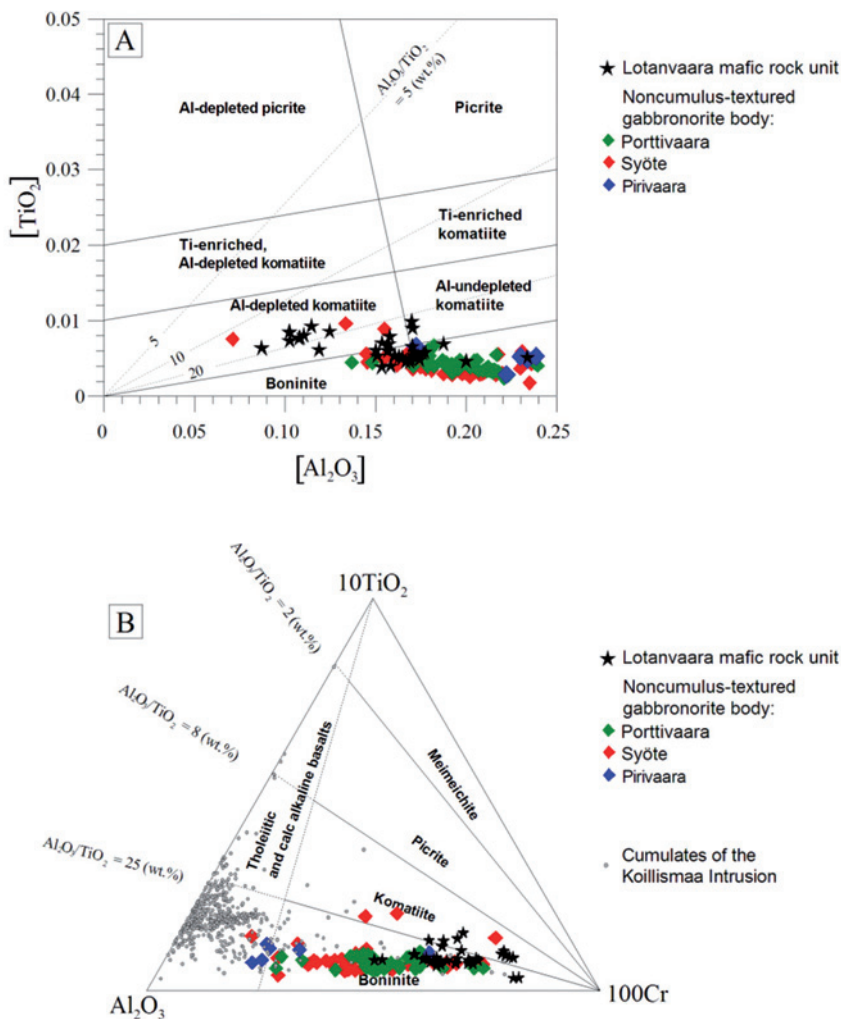


Fig. 7.8.  $[\text{TiO}_2]$  versus  $[\text{Al}_2\text{O}_3]$  diagram (A) (Hanski et al. 2001b) and ternary  $\text{Al}_2\text{O}_3$ - $10\text{TiO}_2$ - $100\text{Cr}$  (B) compiled for the Lotanvaara mafic rock unit and the noncumulus-textured bodies. The cumulate compositions of the Koillismaa Intrusion are shown for comparison. The boundaries between the separate fields in B were drawn on the basis of 272 analyses of boninitic rocks, 544 analyses of komatiitic rocks, 39 analyses of picrites, 20 analyses of meimechites, 154 analyses of tholeiitic basalts and 52 analyses of calc-alkaline basalts (list of literature reference available from author upon request).

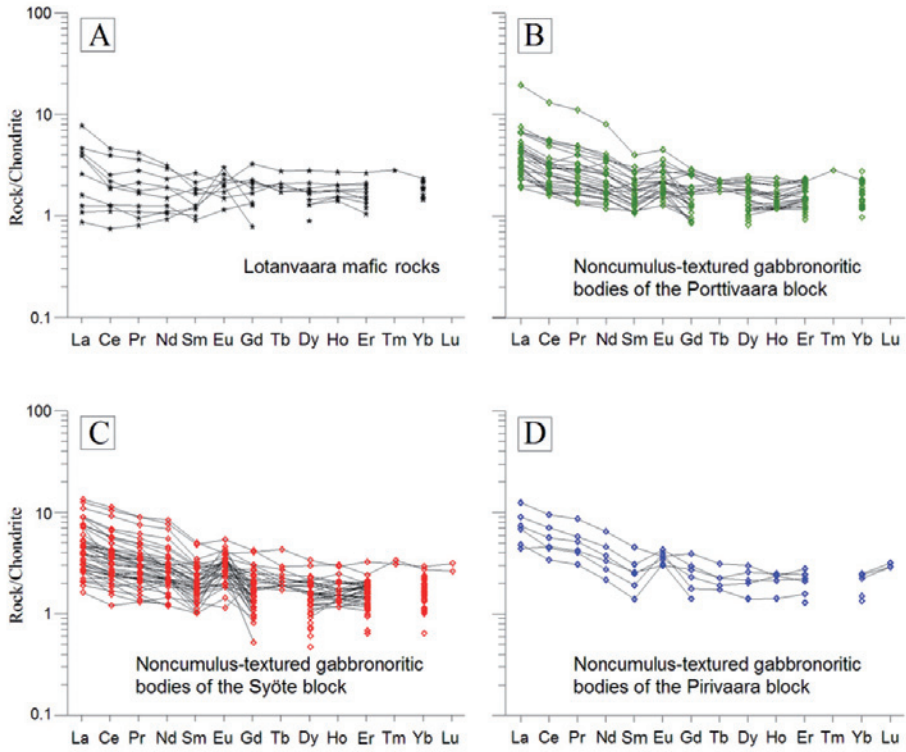


Fig. 7.9. Chondrite-normalized REE abundances of the Lotanvaara mafic rock unit and noncumulus-textured gabbro-norite bodies. Normalizing values are from Taylor & McLennan (1985). All elements analysed with ICP-MS.

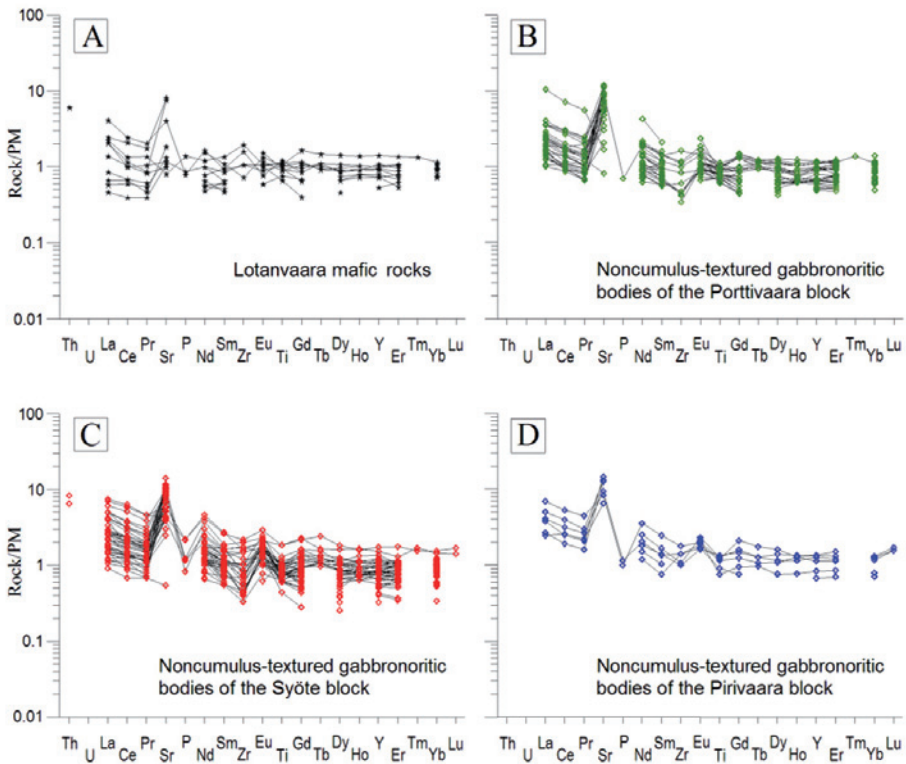


Fig. 7.10. Primitive Mantle-normalized trace element patterns of the Lotanvaara mafic rock unit and noncumulus-textured gabbronorite bodies. Normalizing values are from Sun & McDonough (1989). Th, U, La, Ce, Pr, Nd, Sm, Eu, Gd, Tb, Dy, Ho, Y, Er, Tm, Yb and Lu were analysed with ICP-MS. Sr, P, Zr and Ti analysed with XRF.

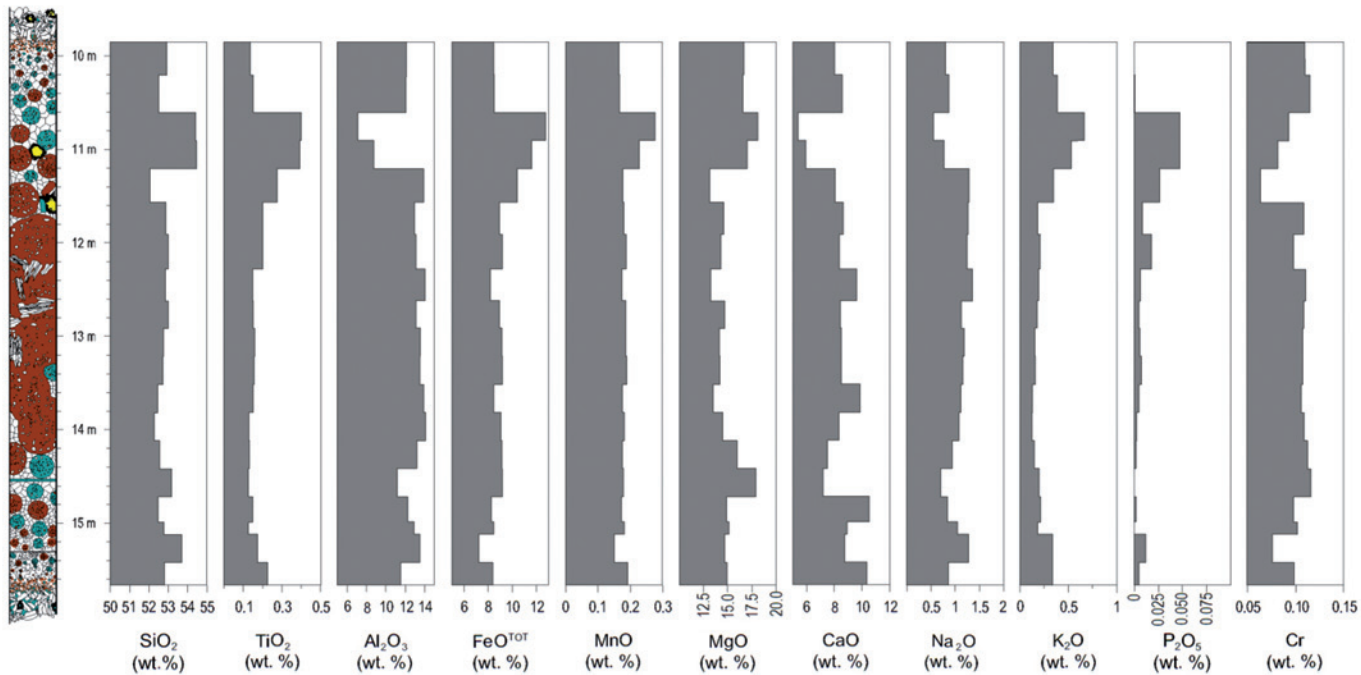


Fig. 7.11. Variation in the major and trace elements in the noncumulate of drill core B7, Rometölväs area. Major elements and the trace elements Cr, Cl and S analysed with XRF. Trace elements V, Zr and Y analysed with ICP-MS (10.20-10.60 m not analysed). Cu, Ni, Au, Pd and Pt analysed with FAAS and ICP-AES (9.85-10.60 m not analysed). For textural description of the noncumulate, see Chapter 5.7. Note that the noncumulate is also shown in Fig. 7.16.

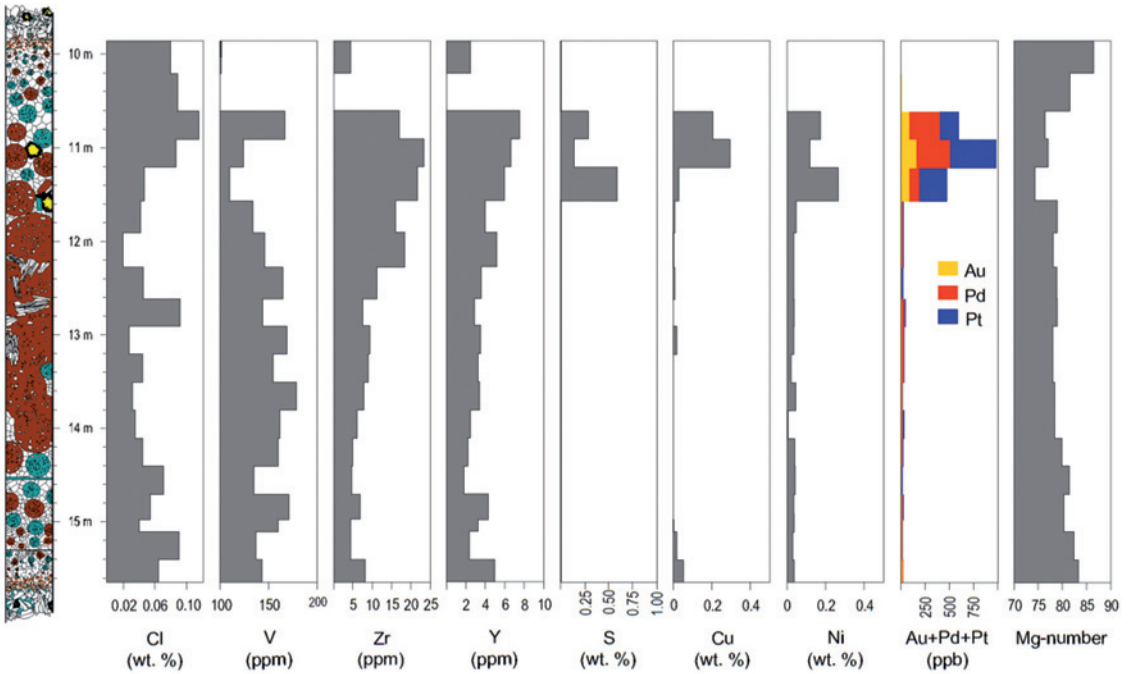


Fig. 7.11. Continued.

Table 7.2. Compositions of the Lotanvaara mafic rock unit and the noncumulus-textured gabbronorite bodies (full compositions of these rocks are given in Appendix 23).

Sample	1	2	3	4
wt. %				
SiO <sub>2</sub>	52.39	52.34	52.75	51.82
TiO <sub>2</sub>	0.27	0.19	0.19	0.24
Al <sub>2</sub> O <sub>3</sub>	8.37	11.94	12.05	15.48
Fe <sub>2</sub> O <sub>3</sub>	2.15	2.13	2.24	2.26
FeO	8.47	7.83	7.21	6.64
MnO	0.21	0.19	0.19	0.17
MgO	19.48	16.37	15.57	12.49
CaO	7.60	7.59	8.49	8.65
Na <sub>2</sub> O	0.67	1.20	0.98	1.93
K <sub>2</sub> O	0.34	0.22	0.32	0.31
P <sub>2</sub> O <sub>5</sub>	0.03	0.01	0.01	0.02
ppm				
Cr	2072	1318	1229	752
Ni	488	405	396	244
V	129	105	139	119
Zr	26	10	19	12
Mg-number	80.1	78.8	79.4	77.0

1 = Lotanvaara mafic rock unit (average composition of 36 samples).

2 = Noncumulus-textured bodies of the Porttivaara block (average composition of 45 samples).

3 = Noncumulus-textured bodies of the Syöte block (average composition of 47 samples).

4 = Noncumulus-textured bodies of the Pirivaara block (average composition of 6 samples).

### 7.1.3 Marginal Series, Layered Series and granophyre

Chemical (average and range) and normative rock compositions of the different Koillismaa Intrusion zones, subzones and units are presented in Appendices 24–26. The variation in major and selected trace element compositions across the intrusion height is presented in Fig. 7.12 on the basis of the data from the Porttivaara block profile and is considered briefly below.

*SiO<sub>2</sub>*: The pyroxenites and peridotites of the upper part of the MS and both olivine gabbro-norite units of the LZa contain relatively low SiO<sub>2</sub>, but above them, in the section from the LZb to the upper part of UZa, the SiO<sub>2</sub> content increases progressively with height. The oxide-rich bottom part of the UZb includes the least silica-bearing cumulates with 38.7 wt. % SiO<sub>2</sub>, but above this level, the concentration increases with height. The UZa and UZc, where the rocks typically are anorthosites and leucogabbros, have the highest SiO<sub>2</sub> concentrations. Granophyre contains ca. 70.0 wt. % SiO<sub>2</sub>.

*TiO<sub>2</sub>*: Most of the cumulates contain less than 1.0 wt. % TiO<sub>2</sub>. The pyroxenites and peridotites of the MS are most depleted in TiO<sub>2</sub>, as they contain less than 0.2 wt. % TiO<sub>2</sub>. The highest titanium concentration is reached in the lower part of the UZb (3.8 wt. % TiO<sub>2</sub>), in oxide-rich cumulates, from where the concentration smoothly decreases as a function of the intrusion height.

*Al<sub>2</sub>O<sub>3</sub>*: The lowest Al<sub>2</sub>O<sub>3</sub> contents are reached in the MS pyroxenites and peridot-

ites and in the LZa olivine gabbro-norites. The oxide-rich cumulates of the UZb are depleted in aluminium in comparison to adjacent subzones. The UZc rocks contain more than 20.0 wt. % Al<sub>2</sub>O<sub>3</sub> and have a sharp compositional boundary with the granophyre, which contains less than 13.0 wt. % Al<sub>2</sub>O<sub>3</sub>.

*Fe<sub>2</sub>O<sub>3</sub> and FeO*: The highest Fe<sub>2</sub>O<sub>3</sub> concentration of the profile, 17.4 wt. %, is found in the oxide-rich rocks in the basal part of the UZb from where the concentration smoothly decreases as a function of the intrusion height. In contrast to Fe<sub>2</sub>O<sub>3</sub>, FeO in the UZb does not differ much from the values in the surrounding subzones.

*MnO*: The cumulates contain typically 0.1–0.2 wt. % MnO. The highest MnO concentration is reached in the lower part of the profile, in the peridotites of the MS. The MZa and the whole UZb have a slightly elevated MnO contents. The granophyre layer contains less than 0.1 wt. % MnO.

*MgO*: The rocks below the RT Reef are more MgO-bearing than the rocks above it. With the exceptions of higher MgO contents in the MS, LZa and MZa, the cumulates below the reef contain typically ca. 10 wt. % MgO whereas the cumulates above the reef contain on average 6.0 wt. % MgO.

*CaO*: Most of the cumulates have relatively uniform CaO concentrations oscillating around 10 wt. %. In the ultramafic part of the MS and in the olivine-bearing cumulates of the LZa, the CaO content is lower. The CaO content of the granophyre is low (< 2.0 wt. %).

*Na<sub>2</sub>O and K<sub>2</sub>O*: The alkalic metal oxides show the lowest concentrations in the ultramafic cumulates of the MS. Between the LZa and UZa, Na<sub>2</sub>O content increases with height. The most Na<sub>2</sub>O-bearing cumulates belong to the plagioclase-rich subzones UZa and UZc, where the rocks contain up to 4.0 wt. % Na<sub>2</sub>O. In comparison to these values, the lower part of the UZb is depleted in Na<sub>2</sub>O. The K<sub>2</sub>O content of the profile oscillates around 0.5 wt. % whereas the granophyre contains 4.0–5.0 wt. % Na<sub>2</sub>O and 1.0–2.0 wt. % K<sub>2</sub>O.

*P<sub>2</sub>O<sub>5</sub>*: The cumulates contain typically less than 0.1 wt. % P<sub>2</sub>O<sub>5</sub>, but in the granophyre the content is significantly higher, at ca. 0.3 wt. %.

*Cr*: The key observation is the dramatic change in Cr content at about the level of the RT Reef, from relatively high values (ca. 100–1000 ppm) below the reef to very low values above the reef; there Cr content is mostly below the detection limit of XRF technique (30 ppm). The variation of the Cr content in the lower part of the intrusion is characterized by two maximas. The lower one is located in the lower part of the intrusion, where the MS pyroxenites and the lower part of the LZb contain almost 0.1 wt. % Cr. The upper maximum is found in the lower part of the MZb, at ca. 700 m of the stratigraphic sequence of Fig. 7.12, which includes the most Cr-rich cumulates of the profile (0.1 wt. % Cr).

*Cl*: As in the case of Cr, the most notable change occurs at the level of the RT Reef where Cl values decrease significantly. In many places below the reef, the rocks contain up to 0.4 wt. % Cl, whereas above the reef most of the rocks contain less than 0.2 wt. % Cl.

*V*: The variation of vanadium in the profile is similar to that of TiO<sub>2</sub>. Thus the highest V content, ca. 0.2 wt. %, is reached in the oxide-rich rocks of the lower part of the UZb.

*Zn, Sr and Zr*: These trace elements do not show significant variations. The cumulates typically contain 50–100 ppm Zn, 200–300 ppm Sr and less than 75 ppm Zr. The granophyre has lower Zn and Sr contents than the cumulates but significantly higher Zr contents (up to 300 ppm).

*Chalcophile elements (S, Cu, Ni and Au+Pd+Pt)*: The MS contains up to 1.9 wt. % S, 0.8 wt. % Cu and 0.5 wt. % Ni and the RT Reef contains up to 1.0 wt. % S, 0.6 wt. % Cu and 0.2 wt. % Ni. The MS contains up to 1.3 ppm Au+Pd+Pt, while in the reef the corresponding value is distinctly lower, 0.2 ppm. The chalcophile element chemistry of both mineralized occurrences is dealt with in detail in Chapter 7.2.

*Modified differentiation index (MDI), modified crystallization index (MCI) and Mg-number*: The MDI, MCI and Mg-number remain roughly constant below the RT Reef where MDI is usually ~ 30, MCI is ~ 50 and Mg-number is ~ 75. Above the reef, these differentiation indexes have a trend towards evolved values as a function of the intrusion height: MDI increases up to 40, MCI decreases down to 40 and Mg-number falls below 60.

In the LS sequence the most distinct feature is the difference between the compositions of the cumulates below and above the RT Reef. This feature is further illustrated with the diagrams of Fig. 7.13 where the FeO<sup>TOT</sup>/Al<sub>2</sub>O<sub>3</sub> with a given MgO is usually higher in the rocks above the reef than in those below it. The samples collected from the reef define two trends indicating that the reef can be located in cumulates from both zones. The rock compositions are also shown with the Mg-number vs. Ni diagram of Fig. 7.14, but in this representation the samples do not define as distinct separate compositional trends as seen in Fig. 7.13.

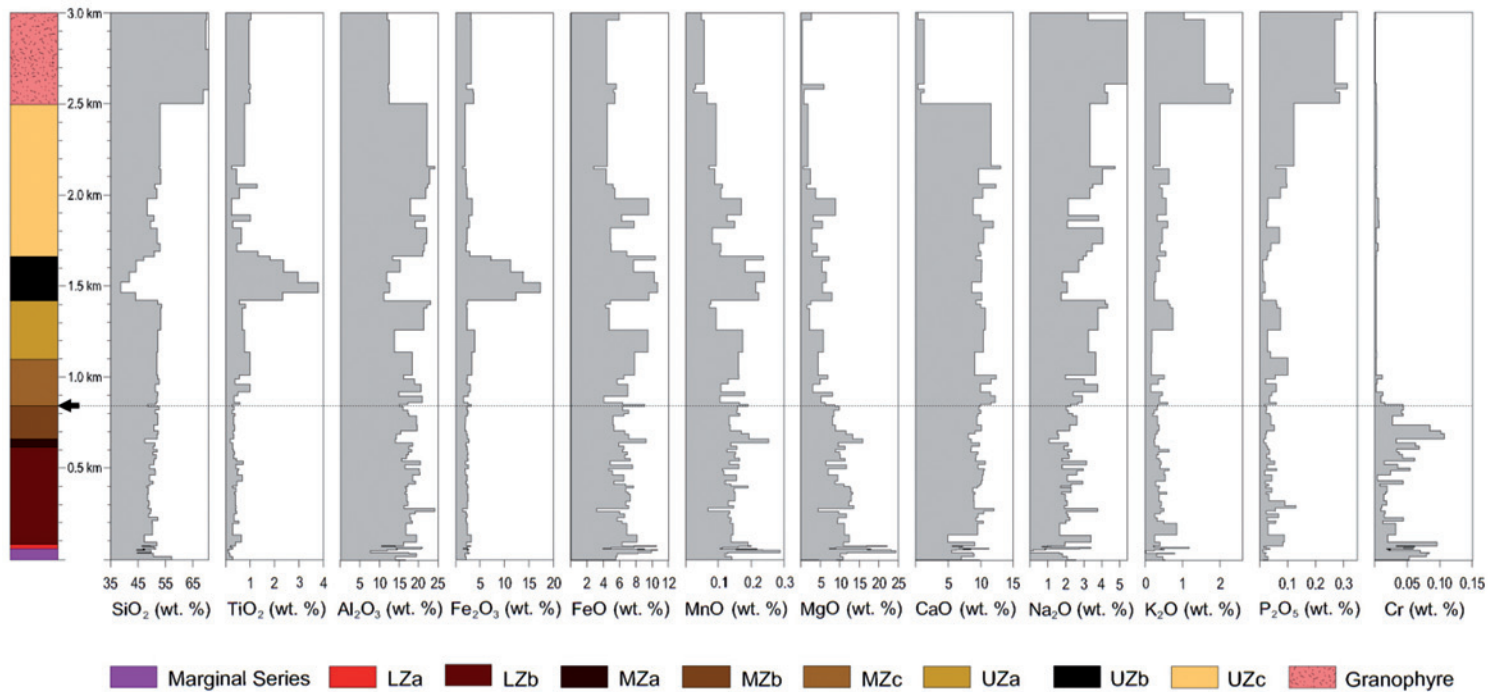


Fig. 7.12. Variation of the major and trace element compositions, MDI, MCI and Mg-number along the Porttivaara block stratigraphic sequence. All elements except precious metals were analysed by XRF. Au, Pd and Pt were analysed by ICP-AES and GFAAS. The location of the Rometölväs Reef in the stratigraphy is indicated by an arrow and a dotted line.

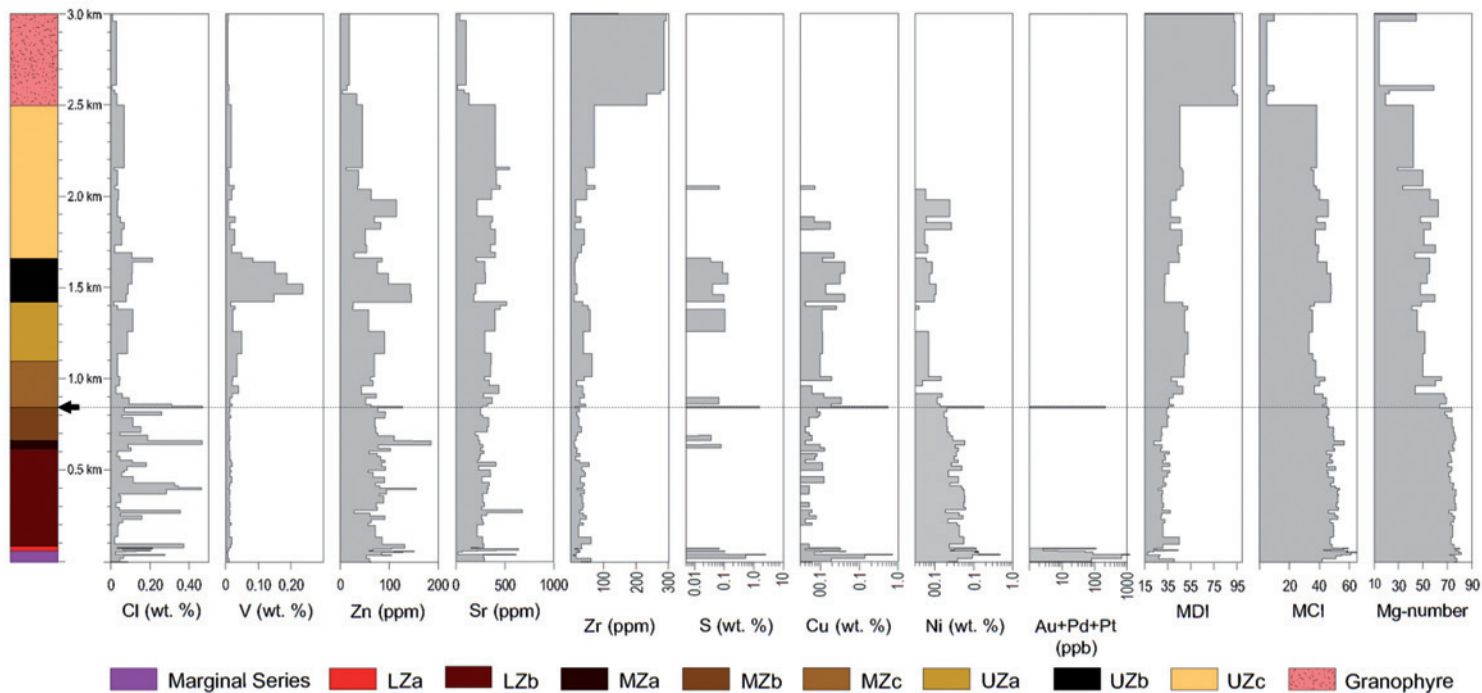


Fig. 7.12. Continued (Note logarithmic scales in the concentrations of S, Cu, Ni and Au+Pd+Pt).

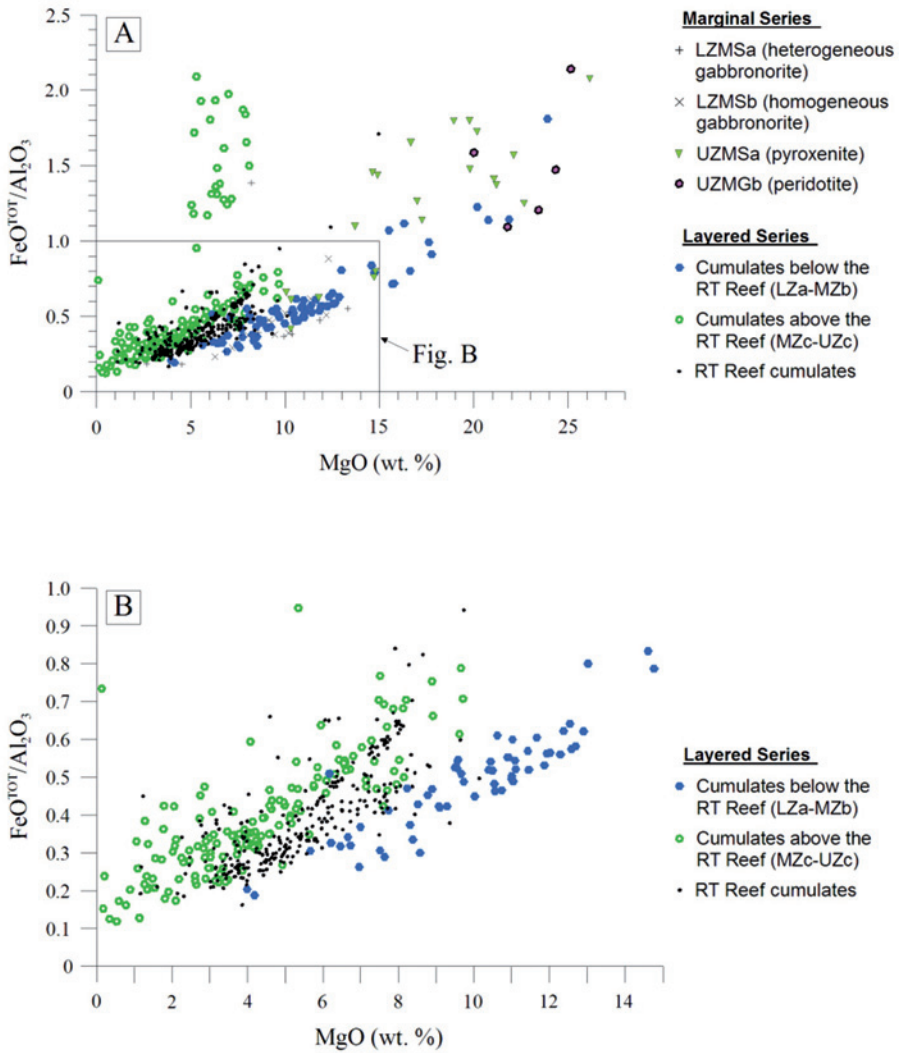


Fig. 7.13. **A** and **B**.  $\text{FeO}^{\text{TOT}}/\text{Al}_2\text{O}_3$  versus MgO diagram illustrating the compositions of the cumulates that are located below and above the Rometölväs Reef.

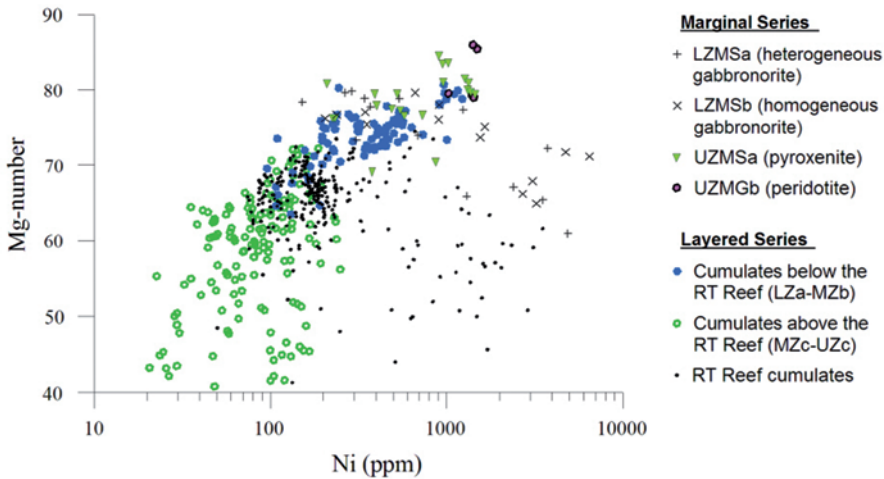


Fig. 7.14. Mg-number versus Ni diagram illustrating the compositions of the cumulates that are located below and above the Rometölväs Reef.

As seen in the chemical profiles of Fig. 7.12 and the diagrams of Figs 7.13 and 7.14 the level of the Rometölväs Reef is marked by a significant change in Mg-number,  $\text{FeO}^{\text{TOT}}/\text{Al}_2\text{O}_3$  and MgO, Cl, Ni and Cr contents of cumulates. Detailed compositional profiles across the reef in drill cores B1 of the Baabelinälkky and B7 of the Rometölväs are illustrated in Figs 7.15 and 7.16. It becomes apparent that the texture rather than the distribution of cumulates controls the concentrations of the ore components. It is obvious that alteration types, from weakly to highly mottled-textured cumulates, show a close relationship with chalcophile element enrichment.

As shown in Figs 7.15 and 7.16, the highly mottled cumulates have higher concentrations

of  $\text{SiO}_2$ ,  $\text{Al}_2\text{O}_3$ , FeO,  $\text{Na}_2\text{O}$ ,  $\text{K}_2\text{O}$ , S, Cu, Ni, Sr, Zr, Au, Pd and Pt and lower concentrations of MgO, MnO, Cr and V than the less altered types. In drill core B7, the highly mottled cumulates are richer in chlorine than the less altered types, but in drill core B1, there is no variation in chlorine. In both drill cores,  $\text{TiO}_2$ ,  $\text{Fe}_2\text{O}_3$ , CaO,  $\text{P}_2\text{O}_5$  and Zn appear to vary more in the highly mottled cumulates than in less altered types. Furthermore, in both drill cores, the noncumulate bodies hosted by the highly mottled cumulates are more enriched in ore components than the bodies that are associated with the less altered cumulates.

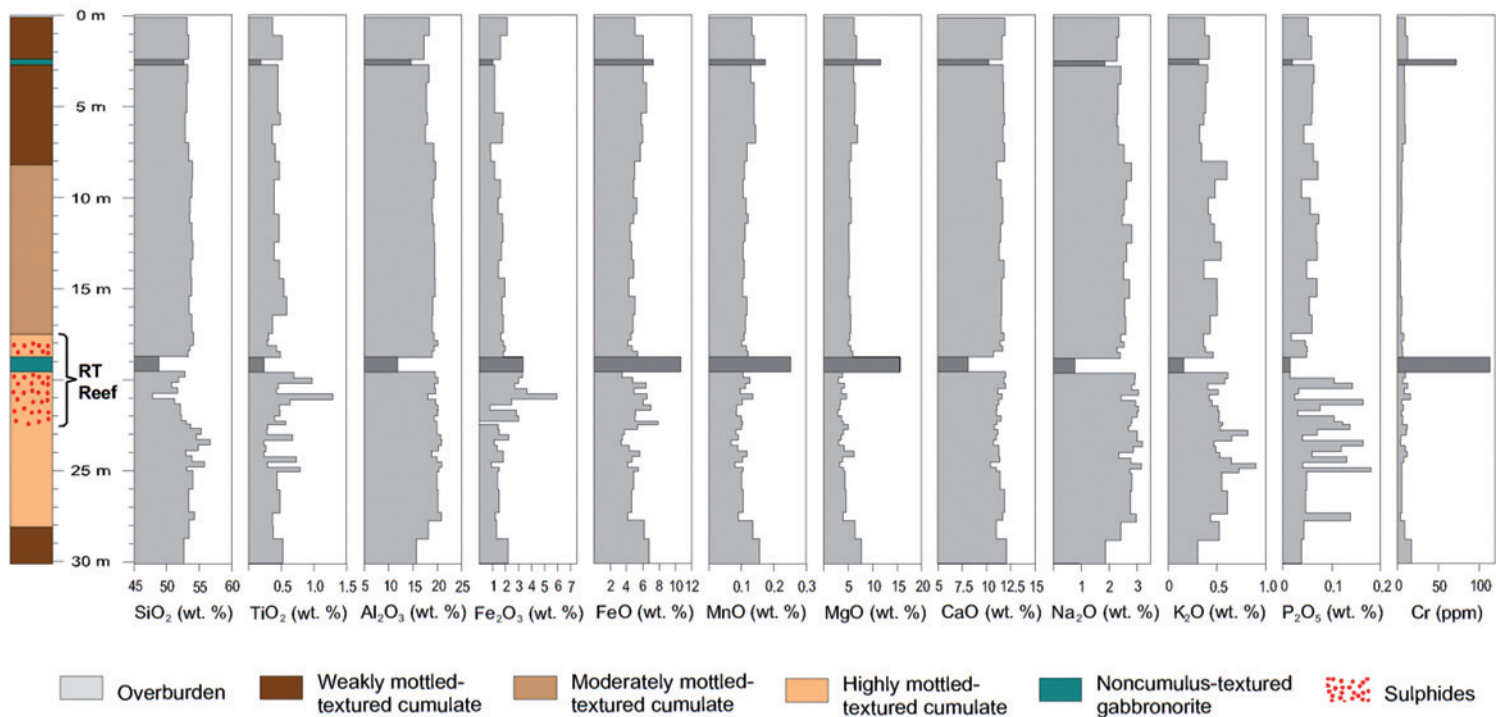


Fig. 7.15. Variation in the major and trace element compositions in drill core B1 (Baabelinälkky). All elements except precious metals were analysed by XRF. Au, Pd and Pt analysed by FAAS.

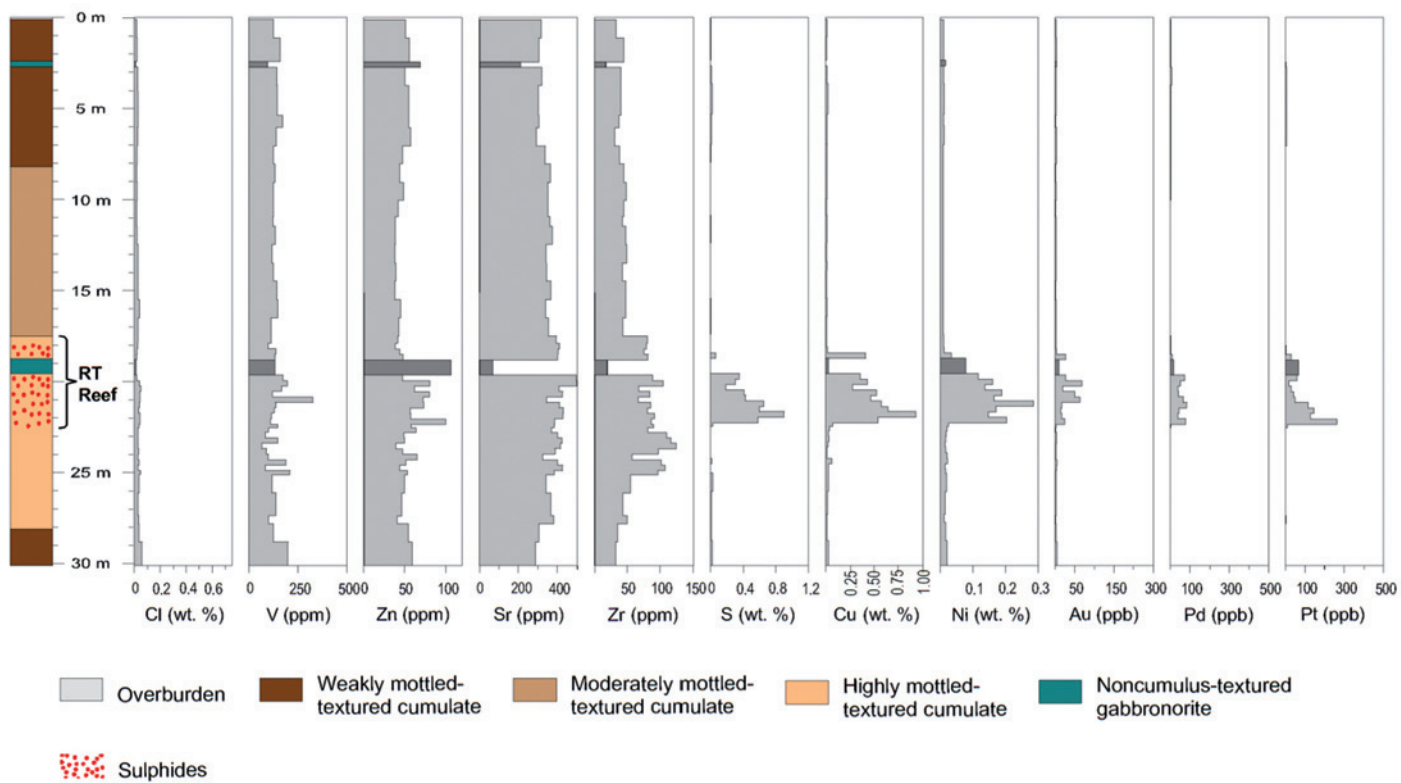


Fig. 7.15. Continued.

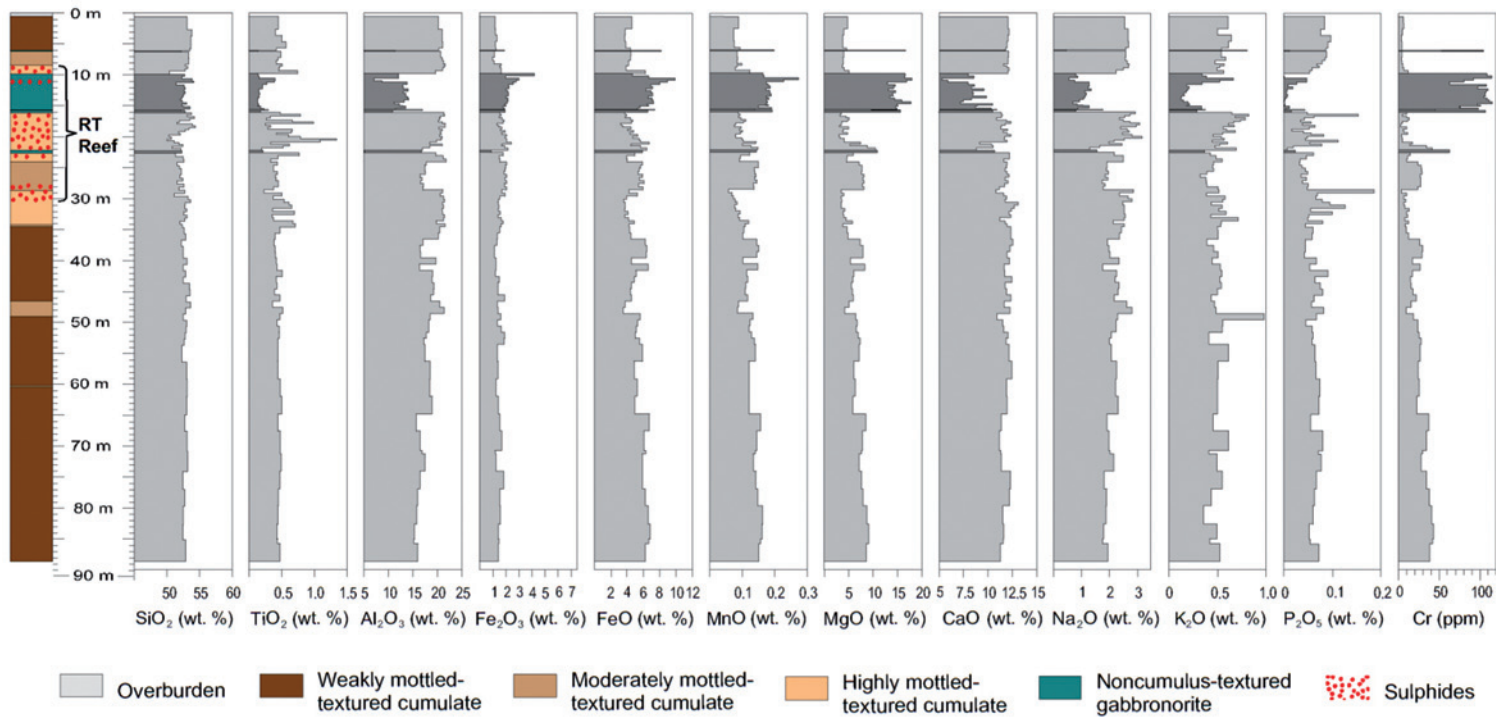


Fig. 7.16. Variation in the major and trace element concentrations in drill core B7 (Rometölväs). All elements except precious metals were analysed by XRF. Au, Pd and Pt were analysed by FAAS. Note that the noncumulate section between 9.85 and 15.64 m in the drill core is also shown in Fig. 7.11.

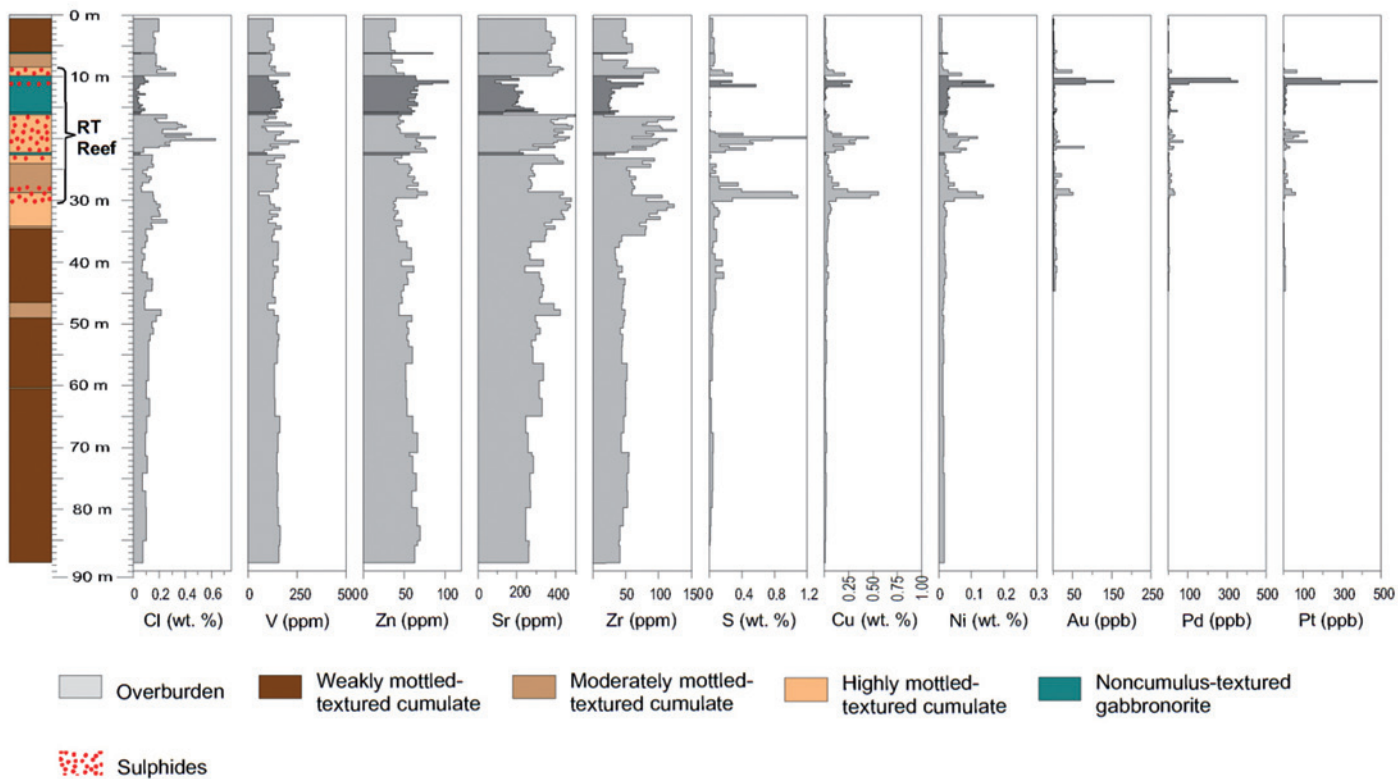


Fig. 7.16. Continued.

## 7.2 Chalcophile elements

The compositions of the MS and the RT Reef are illustrated within the molar ternary Cu-S-Ni diagrams of Fig. 7.17 where the samples are grouped on the basis of sulphur concentration (Fig. 7.17.A) and rock type (Fig. 7.17.B). The diagram illustrates the effect of silicate and sulphide hosted base metals (Ni and Cu) on the rock compositions, and is used for the determination of the sulphide fraction in both the MS and RT Reef.

On the basis of the observed sulphide mineral assemblages, the bulk compositions of the sulphide fraction in both the MS and the RT Reef should plot within the triangle outlined by the tie lines between chalcopyrite, pentlandite and pyrrhotite. The stoichiometric compositions of common sulphide minerals and the electron microprobe data of sulphides analysed during this research are shown in Fig. 7.17.A. Assuming that most sulphur in the samples is bonded to sulphide minerals, the effect of Cu and Ni hosted in silicates becomes more dominating with decreasing amounts of sulphide minerals.

In both the MS and the RT Reef the effect is related to Ni in silicates, since the samples with low sulphur concentration ( $S < 500$  ppm) tend to plot outside the field of sulphide mineral assemblages towards the Ni apex of the diagram. In the MS the effect of Ni hosted in silicates is more dominating, because the rocks of the RT Reef are typically plagioclase-rich cumulates while in the MS they include more Ni-bearing mafic silicates, such as olivine and pyroxene. Therefore, to produce a reliable estimate of the sulphide fraction composition of the MS and RT Reef, Cu/Ni of both mineralized occurrences is determined using the analyses containing more than 500 ppm S.

### 7.2.1 Marginal Series

In the MS, sulphur and chalcophile elements are typically concentrated in the gabbro-noritic

rocks, which contain up to 3.9 wt. % S, 0.9 wt. % Cu, 1.1 wt. % Ni, 790 ppb Au, 2650 ppb Pd and 846 ppb Pt. The diagrams of Fig. 7.18 illustrate chalcophile element contents and ratios in the different rock types of the MS.

The average Cu/Ni ratio in the sulphide fraction of the MS is 1.3 (Fig. 7.18.A). The concentrations of PGE and sulphur in the MS show a positive correlation (Table 7.3). The PGE geochemistry of the MS is characterized by the predominance of Pd over Pt with an average Pd/Pt value of 2.8 (Fig. 7.18.C). Table 7.4 includes average precious metal ratios for separate MS sites, including Soukeli (Fig. 5.5) of the Porttivaara block and Haukiaho of the Kuusijärvi block. The average Pd/Pt values range from 2.3 to 2.8 and, on the basis of the samples collected from Soukeli, the MS has Pd/Ir of 37.0 and  $(Pt+Pd)/(Os+Ir+Ru)$  of 11.3.

### 7.2.2 Rometölväs Reef

The concentrations of the chalcophile metals in the RT Reef show a distinct relationship with textures of the cumulates in that the highly mottled rocks display the highest metal grades (Fig. 7.19). There appears to be no systematic variation in metal contents between different sampling sites (Fig. 7.20). The mottled cumulates contain up to 2.2 wt. % S, 0.9 wt. % Cu and 0.3 wt. % Ni, whereas their PGE grades are usually low, reaching 103 ppb Au, 241 ppb Pd and 263 ppb Pt. The highest PGE grades are found in the sulphide-bearing portion of the noncumulate of drill core B7. This rock contains up to 1 ppm Au+Pd+Pt (155 ppb Au, 355 ppb Pd and 480 ppb Pt) and up to 0.6 wt. % S, 0.3 wt. % Cu and 0.3 wt. % Ni (Figs 7.11 and 7.16). The sulphur and chalcophile element concentrations and ratios in the noncumulus-textured bodies are shown in Fig. 7.21. Metal concentrations are lowest in samples distally located relative to the reef, and in this respect, the noncumulate body in drill

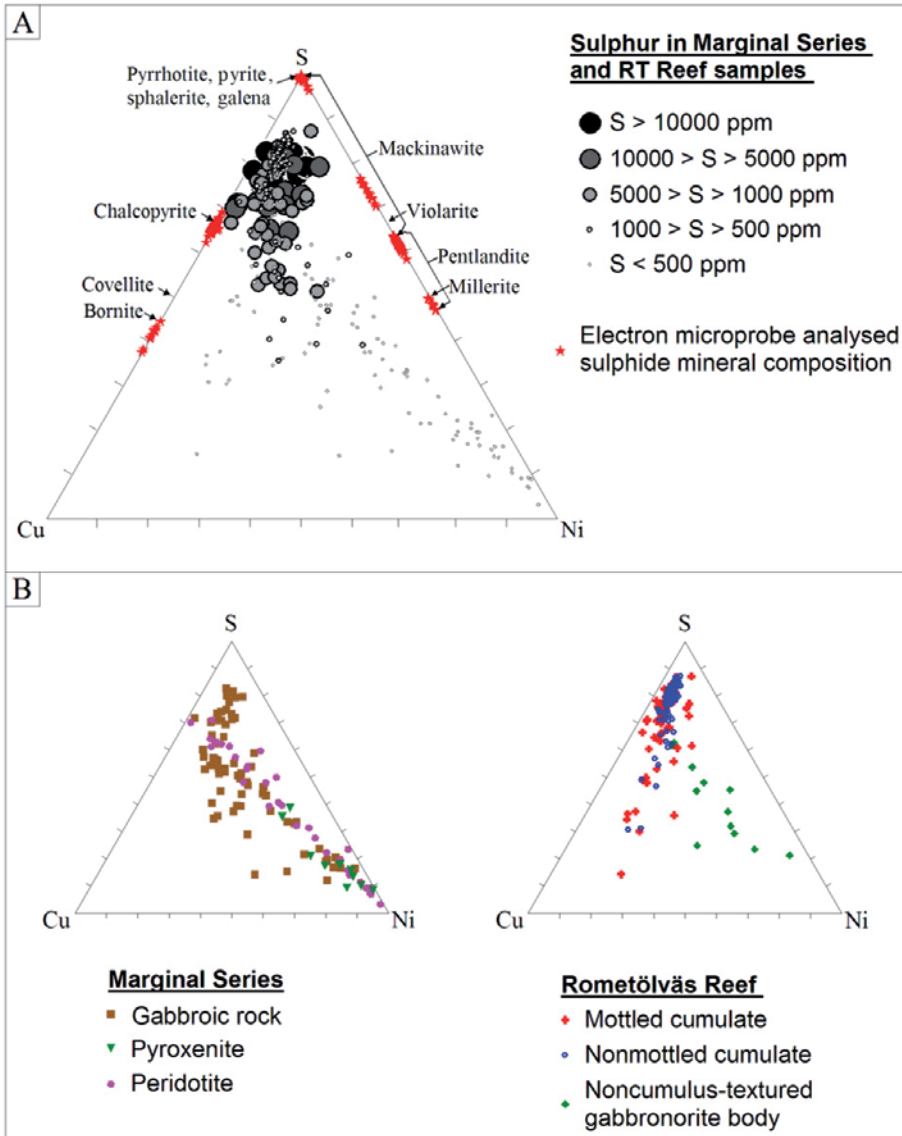


Fig. 7.17. Ternary Cu-S-Ni (in mole proportions) illustrating the effect of silicate and sulphide hosted copper and nickel on the whole-rock compositions of the Marginal Series and the Rometölväs Reef.

core B7 is exceptional among the analysed noncumulate bodies.

The average Cu/Ni ratio in the sulphide fraction of the mottled cumulates of the RT Reef is 4.1 (Fig. 7.19.A). For the noncumulates, the average ratio cannot be defined precisely due

to significant compositional variation (Fig. 7.21.A). The best estimate is that Cu/Ni is less than 3.0. The effect of silicate Ni appears to be less obvious in the cumulates than in the noncumulates, as seen in the Cu/Ni vs. S diagram (Figs 7.19.B, 7.20.B and 7.21.B).

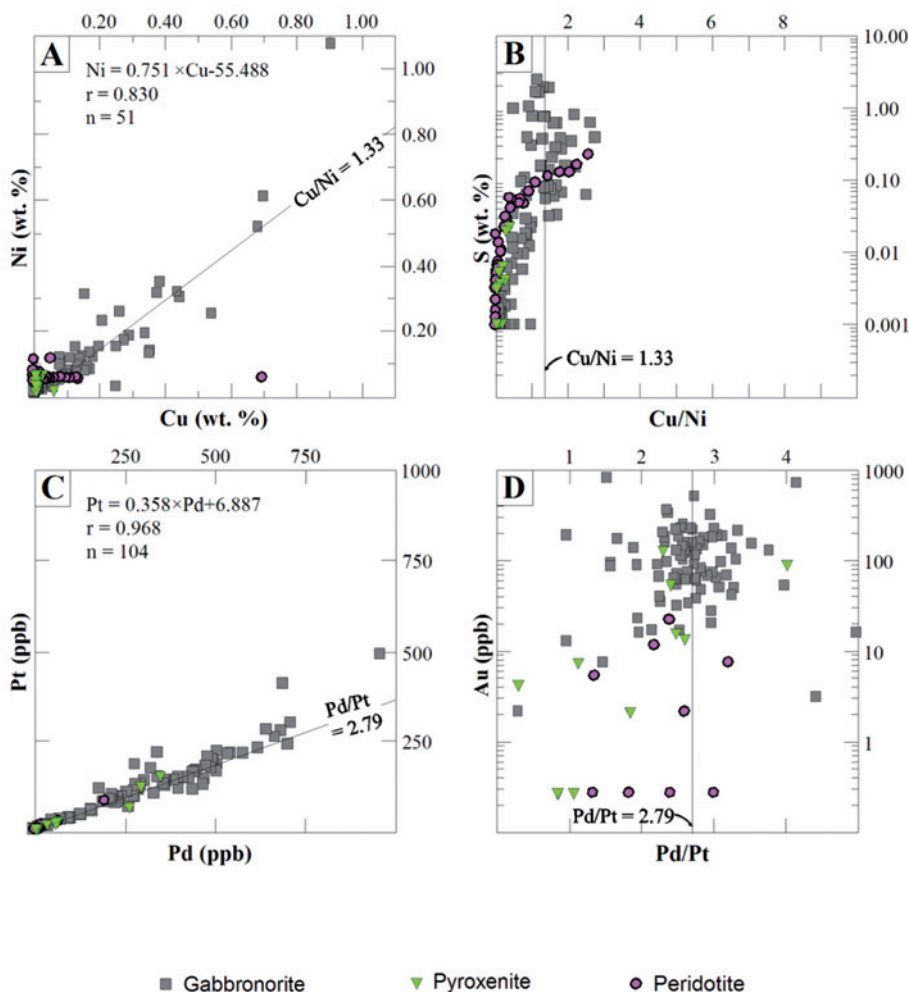


Fig. 7.18. Chalcophile element abundances in the rocks of the Marginal Series. The copper-nickel ratio was determined using best fitting linear correlation of analyses that contain more than 500 ppm sulphur. The palladium-platinum ratio was determined using detected concentrations. Concentrations below the detection limit are set to half of the detection limit in order to illustrate their low values (see Appendix 27 for detection limits).

Analogous to the MS, the correlations listed in Table 7.3 suggest a positive correlation between precious metal concentrations and abundance of sulphides. The average Pd/Pt in both cumulates and noncumulates is close to 1.0, and this value is generally independent of the analytical method used (Table 7.5,

Figs 7.19.C, 7.20.C and 7.21.C). The Pd/Ir and (Pt+Pd)/(Os+Ir+Ru) ratios in the reef cumulates are 17.9–27.8 and 15.0–23.0, respectively. In the noncumulates located close to the reef, Pd/Ir averages 8.7 and (Pt+Pd)/(Os+Ir+Ru) 16.3.

Table 7.3. Correlation matrix (Pearson's correlation coefficient) for base metals and precious metals in the Marginal Series, mottled cumulates of the Rometölväs Reef and noncumulus-textured gabbronorite bodies. Sulphur, Cu and Ni were analysed by ICP-AES and FAAS (no XRF sulphur used in calculation). In cases where precious metal concentrations in a sample were determined using several methods, a priority order of ICP-MS → ICP-AES and GFAAS (GTK methods 704U/705U and 704P/705P over 521) → FAAS was used.

<b>Marginal Series, n = 180</b>							
	S	Cu	Ni	Co	Pd	Pt	Au
Cu	0.887	1.000					
Ni	0.956	0.855	1.000				
Co	0.868	0.689	0.915	1.000			
Pd	0.842	0.800	0.914	0.755	1.000		
Pt	0.803	0.851	0.879	0.758	0.968	1.000	
Au	0.463	0.547	0.380	0.279	0.443	0.379	1.000
<b>Rometölväs Reef cumulates, n = 296</b>							
	S	Cu	Ni	Co	Pd	Pt	Au
Cu	0.959	1.000					
Ni	0.929	0.853	1.000				
Co	0.912	0.825	0.953	1.000			
Pd	0.800	0.707	0.746	0.810	1.000		
Pt	0.833	0.731	0.759	0.816	0.833	1.000	
Au	0.903	0.781	0.717	0.794	0.699	0.668	1.000
<b>Noncumulus-textured gabbronorite bodies, n = 84</b>							
	S	Cu	Ni	Co	Pd	Pt	Au
Cu	0.995	1.000					
Ni	0.853	0.564	1.000				
Co	0.691	0.357	0.764	1.000			
Pd	0.370	0.939	0.664	0.425	1.000		
Pt	0.520	0.847	0.770	0.416	0.847	1.000	
Au	0.561	0.899	0.754	0.129	0.919	0.982	1.000

Table 7.4. Average (A), limits of variation (B) and standard deviation (C) of precious metal ratios of the Marginal Series samples calculated for different analytical methods. Cu/Ni calculated using samples containing more than 500 ppm sulphur. Standard deviation is not shown for prospects whose sample number (n) is less than 10.

	<b>Pd/Pt</b>	<b>Pd/Pt</b>	<b>Pd/Pt</b>	<b>Pd/Pt</b>	<b>Pd/Ir</b>	<b>(Pt+Pd)/ (Os+Ir+Ru)</b>
	FAAS	GFAAS (521U)*	ICP-AES & GFAAS (704P/U & 705P/U)*	ICP-MS (714M)*	ICP-MS (714M)*	ICP-MS (714M)*
A	2.3		2.8	2.43	36.95	11.26
1 B	(2.0–2.5)		(2.0–4.2)	(1.92–2.98)	(16.96–51.01)	(5.14–13.68)
C			0.72			
n	2		15	5	5	5
A		2.5	2.8			
2 B		(1.3–5.6)	(1.7–4.0)			
C		0.74	0.35			
n		38	64			

1 = Porttivaara block: Soukeli, 2 = Kuusijärvi block: Haukiahö.

\*Analytical code of the GTK, see detailed description of the methods from Rasilainen et al. (2007).

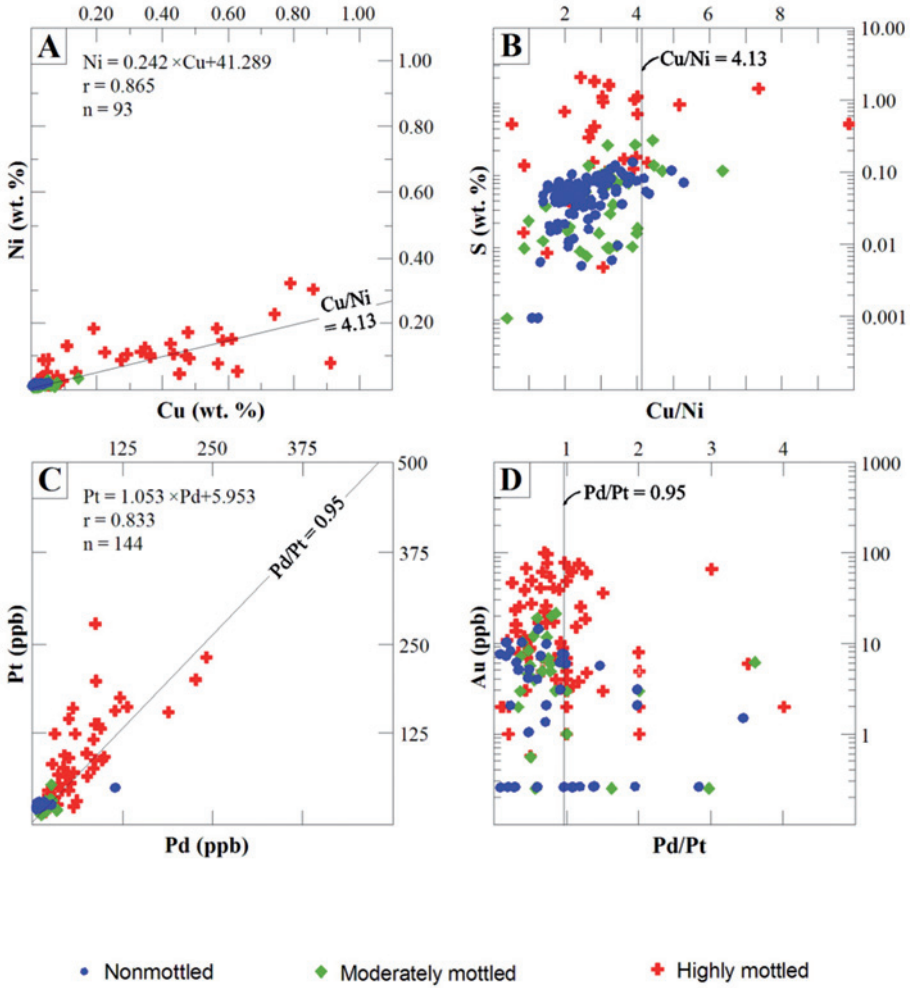


Fig. 7.19. Chalcophile element abundances in the cumulates of the Rometölväs Reef subdivided on the basis of alteration type (nonmottled, moderately mottled and highly mottled). The copper-nickel ratio was determined using best fitting linear correlation of analyses that contain more than 500 ppm sulphur. The palladium-platinum ratio was determined using detected concentrations. Concentrations below the detection limit are set to half of the detection limit in order to illustrate their low values (see Appendix 27 for detection limits).

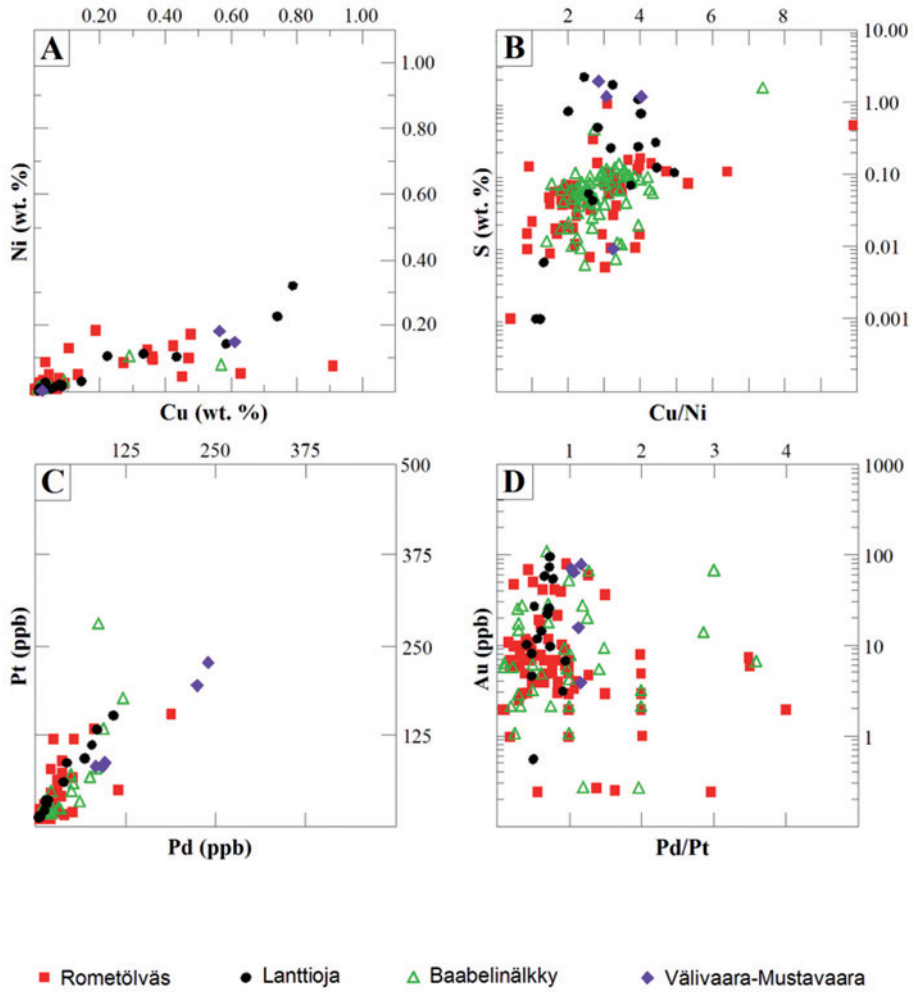


Fig. 7.20. Chalcophile element abundances in the cumulates of the Rometölväs Reef subdivided on the basis of sampling site (Rometölväs, Lanttioja, Baabelinälkky and Väliavaara-Mustavaara). The copper-nickel ratio was determined using best fitting linear correlation of analyses that contain more than 500 ppm sulphur. The palladium-platinum ratio was determined using detected concentrations. Concentrations below the detection limit are set to half of the detection limit in order to illustrate their low values (see Appendix 27 for detection limits).

The Koillismaa Intrusion, northeastern Finland – evidence for PGE reef forming processes in the layered series

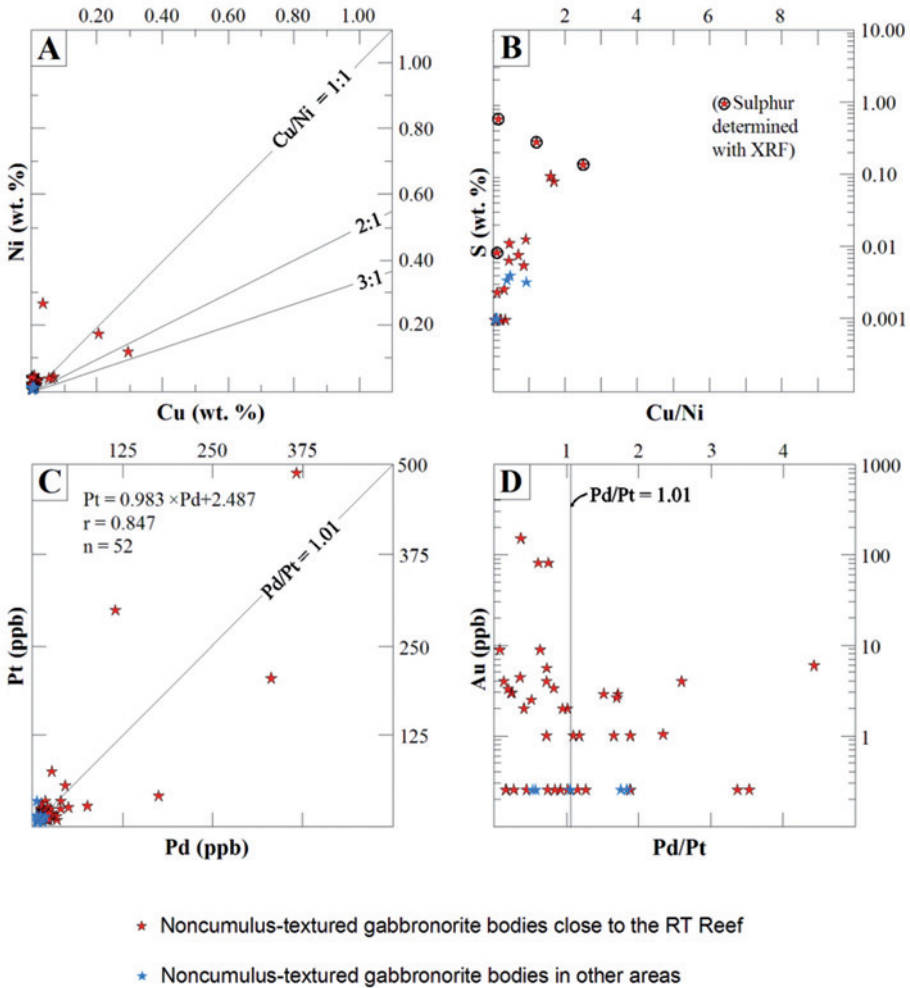


Fig. 7.21. Chalcophile element abundances in the noncumulus-textured gabbronorite bodies subdivided on the basis of their location in the intrusion (close to the RT Reef and in other areas). The copper-nickel ratio was determined using best fitting linear correlation of analyses that contain more than 500 ppm sulphur. The palladium-platinum ratio was determined using detected concentrations. Concentrations below the detection limit are set to half of the detection limit in order to illustrate their low values (see Appendix 27 for detection limits).

Table 7.5. Average (A), limits of variation (B) and standard deviation (C) of precious metal ratios in the Rometölväs Reef samples calculated for different analytical methods. Cu/Ni was calculated using samples containing more than 500 ppm sulphur. Standard deviation is not shown for prospects where sample number (n) is less than 10. (\*Analytical code of the GTK, see Table 3.1. for explanation).

	Pd/Pt	Pd/Pt	Pd/Pt	Pd/Pt	Pd/Ir	(Pt+Pd)/ (Os+Ir+Ru)
	FAAS	GFAAS	ICP-AES/GFAAS	ICP-MS	ICP-MS	ICP-MS
		(521U)	(704P/U or 705P/U)	(714M)	(714M)	(714M)
<b>Mottled cumulates of the Rometölväs Reef:</b>						
1	A	1	1.7	0.9	26.38	16.99
	B	(0.1–5.1)	(0.3–6.8)	(0.44–1.99)	(11.51–38.44)	(12.21–22.82)
	C	0.91	1.79	0.43	7.48	
	n	59	13	13	12	5
2	A			0.62	22.04	17.6
	B			(0.42–0.82)	(19.59–24.49)	(13.95–21.24)
	n			2	2	2
3	A	1	1,1	0.5	26.6	22.95
	B	(0.2–3.0)	(0.1–3.6)	(0.30–0.72)	(16.77–38.14)	(15.68–33.52)
	C	0.64	0.99			
	n	25	16	4	4	4
	A			0.65	17.85	16.22
	B			(0.41–0.95)	(8.62–24.95)	(14.57–17.55)
4	C			0.16	5.48	
	n			15	15	5
	A		1	1.11	27.82	15.03
5	B		(0.9–1.0)	(1.03–1.17)	(23.92–32.72)	(13.42–17.30)
	n		3	5	5	5
<b>Noncumulus-textured gabbronorite bodies of the Rometölväs Reef:</b>						
6	A	1.4	1.3	1.02	8.68	16.33
	B	(0.1–5.5)	(0.2–4.9)	(0.07–1.69)	(0.87–16.86)	(5.42–32.49)
	C	1.42	1.14			
	n	19	27	5	5	5

1 = Syöte block: Rometölväs,

2 = Syöte block: Pikku-Syöte & Aurinkokallio,

3 = Porttivaara block: Baabelinälkky,

4 = Porttivaara block: Lanttioja,

5 = Porttivaara block: Väливаара & Mustavaara.

6 = All the noncumulus-textured gabbronorite bodies of the RT Reef.

### 7.2.3 Compositions of the sulphide fractions of the Marginal Series and the Rometölväs Reef

The concentrations of sulphur, base metals and noble metals in selected samples of the MS and RT Reef samples (row A) and their values when recalculated to 100 % sulphides (rows B and C) are presented in Tables 7.6, 7.7 and 7.8. The recalculation to 100 % sulphide, *i.e.* the estimate of the composition of the sulphide fraction was made by assuming 37.0 wt. % sulphur in the sulphide fraction (row B in the tables) and using the method of Hoffman et al. (1979) and Wilson (1988) (row C in the tables). According to these methods, the proportion of sulphide minerals in the sulphide fraction is adjusted by the relative proportions of Ni, Cu and S in analysis. Chalcopyrite, pentlandite and pyrrhotite were assumed to be the sulphide phases in both the MS and RT Reef, and the phase compositions were taken from the average electron microprobe analyses of the sulphides in the prospects. The proportions of the phases in the sulphide fraction were calculated by converting analysed Cu to chalcopyrite, Ni to pentlandite and the remaining sulphur to pyrrhotite.

The data presented in Table 7.6 for the sulphide fraction of the MS averages 36.0 wt. % S, 10.9 wt. % Cu, 9.5 wt. % Ni, 0.4 wt. % Co, 0.5 ppm Os, 0.4 ppm Ir, 1.1 ppm Ru, 0.3 ppm Rh, 19.1 ppm Pd, 7.3 ppm Pt, 5.4 ppm Au and 0.4 ppm Re. The average values for Cu/Ni and Pd/Pt are 1.1 and 2.6, respectively.

In the mottled cumulates of the RT Reef (Table 7.7), the average sulphide fraction has 36.3 wt. % S, 17.8 wt. % Cu, 5.2 wt. % Ni, 0.3 wt. % Co, 0.1 ppm Os, 0.1 ppm Ir, 0.2 ppm Ru, 0.3 ppm Rh, 2.7 ppm Pd, 4.1 ppm Pt, 1.8 ppm Au and 2.1 ppm Re. The average values of Cu/Ni and Pd/Pt for the compositions shown in Table 7.7 are 4.0 and 0.7, respec-

tively. The second composition in Table 7.8 displays the sulphide fraction of the sulphide-rich interval in the noncumulus-textured gabbro-norite body in drill core B7 (see Fig. 5.10).

There are no published estimates for the sulphide fraction contents of the RT Reef, but for the MS several estimates have been published. On the basis of the data given by Lahtinen (1985) for drill cores in the Kuusijärvi and Porttivaara blocks, the mineralized layer in the MS averages Cu/Ni of 1.8 and Pd/Pt of 2.7. Alapieti & Piirainen (1984) estimated that in the ore-bearing interval of the MS in the Kuusijärvi block, the sulphide fraction averages are 17.7 wt. % Cu, 8.9 wt. % Ni, 10.7 ppm Pt, 24.4 ppm Pd and 7.1 ppm Au, and that the Cu/Ni and Pd/Pt are 2.0 and 2.3, respectively. Iljina (2004) used the average of 290 analyses to calculate an sulphide fraction of the MS, at Cu/Ni and Pd/Pt values of 1.7 and 2.5, respectively. A metallurgical test with a 50 kg sample taken by North Atlantic Natural Resources from the Haukiahö area resulted in a sulphide fraction composition of 9.7 wt. % Cu and 5.0 wt. % Ni with recoveries of 89 % and 64 %, respectively, and a bulk rock composition of 0.31 ppm Au, 0.23 ppm Pt and 0.57 ppm Pd (Posey 2001, Iljina et al. 2005). When the recoveries are converted to 100 % to obtain the *in situ* sulphide fraction composition of the MS, the Cu and Ni contents of 10.9 wt. % and 7.8 wt. % are obtained, respectively, and Cu/Ni and Pd/Pt of the MS are 1.4 and 2.5, respectively. These values are very close to the ones estimated in this study

Barnes et al. (1988) showed that primary mantle derived magmas show a trend of increasing Pd/Ir and Cu/Ni at progressively lower degrees of partial melting (Fig. 7.22). The Koillismaa data plot close to the field of flood basalts, consistent with their relatively Cu- and Pd-rich nature.

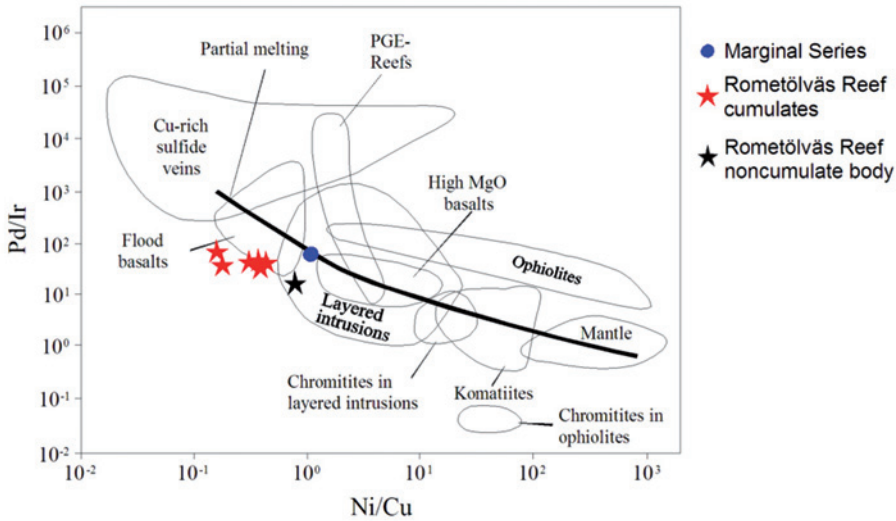


Fig. 7.22. Metal ratio diagram of Pd/Ir versus Ni/Cu (Barnes et al. 1988) for the Marginal Series and the Rometölväs Reef. The data of the Koillismaa Intrusion are from Tables 7.6, 7.7 and 7.8.

Table 7.6. Chalcophile element concentrations in representative samples from the Marginal Series. A = whole-rock content, B = composition of the sulphide fraction, assuming 37.0 wt. % S and C = composition of the sulphide fraction estimated by the method of Hoffman et al. (1979) and Wilson (1988). Where the analysed concentration is below the detection limit, a value of 50 % of the detection limit was used as concentration in the calculation of the average (n.a. = not analysed, see Appendix 27 for detection limits).

	S	Cu	Ni	Co	Os	Ir	Ru	Rh	Pd	Pt	Au	Re
	wt. %	wt. %	wt. %	wt. %	ppb	ppb	ppb	ppb	ppb	ppb	ppb	ppb
1 A	1.072	0.318	0.268	0.012	n.a.	n.a.	n.a.	n.a.	420	166	200	n.a.
1 B	37.00	10.98	9.25	0.41					14496	5729	6903	
1 C	35.99	10.68	9.00	0.40					14101	5573	6715	
2 A	1.680	0.494	0.414	0.015	24.7	20.5	50.2	15.5	674.5	265.3	204.7	22.5
2 B	37.00	10.88	9.12	0.33	544	451	1106	341	14855	5843	4508	496
2 C	36.66	10.78	9.03	0.33	539	447	1095	338	14719	5789	4467	491
3 A	0.887	0.283	0.264	0.009	n.a.	n.a.	n.a.	n.a.	714	268	130	n.a.
3 B	37.00	11.80	11.01	0.38					29784	11179	5423	
3 C	35.25	11.25	10.49	0.36					28375	10651	5166	

1 = Soukeli, Porttivaara block: average of 11-TTK-00, 53-TTK-00, 261-TTK-00, 400-TTK-00 and 401-TTK-00. S, Cu and Ni analysed with ICP-AES, Au+PGE with ICP-AES and GFAAS.  
 2 = Soukeli, Porttivaara block: average of 257-TTK-00, 402-TTK-00, 16-TTK-01 and 33-TTK-01. S, Cu and Ni analysed with ICP-AES, Au+PGE with ICP-MS.  
 3 = Haukiahö, Kuusijärvi block: average of 8 drill core samples from 3543/98R359 (179.06-182.71 = 3.65 m of the MS). S, Cu and Ni analysed with ICP-AES, Au+PGE with GFAAS.

Table 7.7. Chalcophile element concentrations in representative samples from the Rometölväs Reef cumulates. A = whole-rock content, B = composition of the sulphide fraction, assuming 37.0 wt. % S and C = composition of the sulphide fraction estimated by the method of Hoffman et al. (1979) and Wilson (1988). Where the analysed concentration is below the detection limit, a value of 50 % of the detection limit was used as concentration in the calculation of the average (n.a. = not analysed, n.d. = not detected, see Appendix 27 for detection limits).

	S	Cu	Ni	Co	Os	Ir	Ru	Rh	Pd	Pt	Au	Re
	wt. %	wt. %	wt. %	wt. %	ppb	ppb	ppb	ppb	ppb	ppb	ppb	ppb
1 A	0.542	0.385	0.056	0.003	1.2	1.2	2.6	n.d.	29.2	46.6	31.6	31.6
1 B	37.00	26.28	3.82	0.20	82	82	177		1993	3181	2157	2157
1 C	35.48	25.20	3.67	0.20	79	79	170		1911	3050	2069	2069
2 A	0.555	0.360	0.097	n.a.	1.7	3.1	3.9	4.7	76.0	123.0	17.2	n.a.
2 B	37.00	24.00	6.47		113	207	313	316	5067	8200	1147	
2 C	35.21	22.84	6.15		108	198	298	301	4822	7803	1091	
3 A	0.822	0.232	0.148	n.a.	n.a.	n.a.	n.a.	n.a.	26.0	81.0	11.0	n.a.
3 B	37.00	10.44	6.66						1170	3646	495	
3 C	37.17	10.49	6.69						1176	3663	497	
4 A	1.540	0.567	0.077	0.004	3.5	2.9	5.4	14.5	111.0	160.0	103.0	n.a.
4 B	37.00	13.62	1.84	0.10	84	70	129	348	2667	3844	2475	
4 C	37.71	13.88	1.88	0.10	85	71	131	355	2718	3918	2522	
5 A	0.401	0.289	0.105	0.004	1.4	1.5	3.0	2.5	38.5	53.7	26.7	n.d.
5 B	37.00	26.67	9.69	0.35	130	138	274	232	3552	4955	2464	
5 C	34.16	24.62	8.94	0.32	120	128	253	214	3280	4574	2774	
6 A	0.104	0.033	0.010	0.002	n.a.	n.a.	n.a.	n.a.	6.0	10.0	7.0	n.a.
6 B	37.00	11.74	3.56	0.71					2135	3558	2490	
6 C	37.55	11.91	3.61	0.72					2166	3611	2527	
7 A	0.847	0.377	0.123	0.006	1.6	2.1	3.3	6.2	47.8	71.5	42	n.a.
7 B	37.00	16.47	5.37	0.26	70	92	144	271	2088	3123	1835	
7 C	36.54	16.26	5.31	0.26	69	90	142	267	2062	3085	1812	
8 A	1.440	0.677	0.212	0.007	4.0	4.8	7.6	16.3	126.7	112.1	53.9	n.d.
8 B	37.00	17.40	5.45	0.18	103	123	195	419	3255	2880	1385	
8 C	36.72	17.26	5.41	0.18	102	122	194	416	3231	2859	1374	

1 = Rometölväs, Syöte block: average of 74.1-TTK-00, 77.1-TTK-00, 77.2-TTK-00 and B6 28.51-31.23. S, Cu and Ni analysed with ICP-AES, Au+PGE with ICP-MS.

2 = Rometölväs, Syöte block: B7 20.57-20.87. S, Cu and Ni analysed with FAAS, Au+PGE with ICP-MS.

3 = Rometölväs, Syöte block: average of B7 19.07-19.37, B7 19.67-19.97 and B7 19.97-20.27. All elements analysed with FAAS.

4 = Baabelinälkky, Porttivaara block: 80-TTK-99. S, Cu and Ni analysed with ICP-AES, Au+PGE with ICP-MS.

5 = Baabelinälkky, Porttivaara block: B4 13.90-18.46. S, Cu and Ni analysed with ICP-AES, Au+PGE with ICP-MS.

6 = Baabelinälkky, Porttivaara block: average of B2 11.66-12.36 and B2 12.36-13.36. S, Cu and Ni analysed with ICP-AES, Au+PGE with ICP-AES.

7 = Lanttioja, Porttivaara block: average of 4B, 6, 8A, 8B, 10, 11, 12, 13 and 14 of 135-TTK-99. S, Cu and Ni analysed with ICP-AES, Au+PGE with ICP-MS.

8 = Välivaara, Porttivaara block: average of 137.1-TTK-99, 314-TTK-00 and 320.1-TTK-00. S, Cu and Ni analysed with ICP-AES, Au+PGE with ICP-MS.

Table 7.8. Chalcophile element concentrations in representative samples from the noncumulus-textured gabbro-norite bodies associated with the Rometölväs Reef. A = whole-rock content, B = composition of the sulphide fraction, assuming 37.0 wt. % S and C = composition of the sulphide fraction estimated by the method of Hoffman et al. (1979) and Wilson (1988). Where the analysed concentration is below the detection limit, a value of 50 % of the detection limit was used as concentration in the calculation of the average. (n.a. = not analysed, n.d. = not detected, see Appendix 27 for detection limits).

	<b>S</b>	<b>Cu</b>	<b>Ni</b>	<b>Co</b>	<b>Os</b>	<b>Ir</b>	<b>Ru</b>	<b>Rh</b>	<b>Pd</b>	<b>Pt</b>	<b>Au</b>	<b>Re</b>
	<b>wt. %</b>	<b>wt. %</b>	<b>wt. %</b>	<b>wt. %</b>	<b>ppb</b>							
A	0.097	0.068	0.043	0.004	n.d.	1.5	3.0	n.d.	15.1	9.0	5.9	10.2
1 B	37.00	25.94	16.40	1.53		572	1144		5760	3433	2251	3891
C	32.83	23.01	14.55	1.35		508	1016		5111	3046	1997	3452
A	0.337	0.177	0.186	n.a.	n.a.	n.a.	n.a.	n.a.	260	322	107	n.a.
2 B	37.00	19.43	20.42						28546	35353	11748	
C	30.73	16.14	16.96						23709	29362	9757	

1 = Rometölväs, Syöte block: 74.2-TTK-00. S, Cu and Ni analysed with ICP-AES, Au+PGE with ICP-MS.

2 = Rometölväs, Syöte block: average of B7 10.60–10.90, B7 10.90–11.20, B7 11.20–11.56. Sulphur analysed with XRF, rest of the elements with FAAS.

#### 7.2.4 Chondrite- and mantle-normalized multi element patterns of the sulphide fraction of the Marginal Series and the Rometölväs Reef

Both the MS and the RT Reef have fractionated chondrite-normalized PGE patterns (Fig. 7.23), but the slopes of the MS are more gradual than those of the RT Reef. In general, the patterns are flat from Os to Ru, but while the MS shows a progressive increase from Ir to Au, the RT Reef shows a sharp increase from Ru to Rh, followed by a more gentle increase from Rh to Au. The patterns of the base metal-enriched noncumulate bodies resemble those of the MS. The legend in the diagram for the RT Reef includes estimates of the distance of

the sampling sites from the basal contact of the Koillismaa Intrusion. The reef appears to be coherent in its chalcophile element contents along the strike of layering of the Koillismaa Intrusion.

Mantle-normalized diagrams are used to compare the compositions of the MS and the RT Reef with domestic and foreign PGE deposits hosted by mafic-ultramafic intrusions (Fig. 7.24). Naldrett (2004) classified PGE deposits on the basis of morphology and mineralized occurrences into 1) stratiform-strat-abound, 2) stratabound and 3) discordant to strata.

The Merensky Reef and UG-2 chromitite of the Bushveld (Cawthorn et al. 2002) and the J-M Reef of the Stillwater Complex (Todd

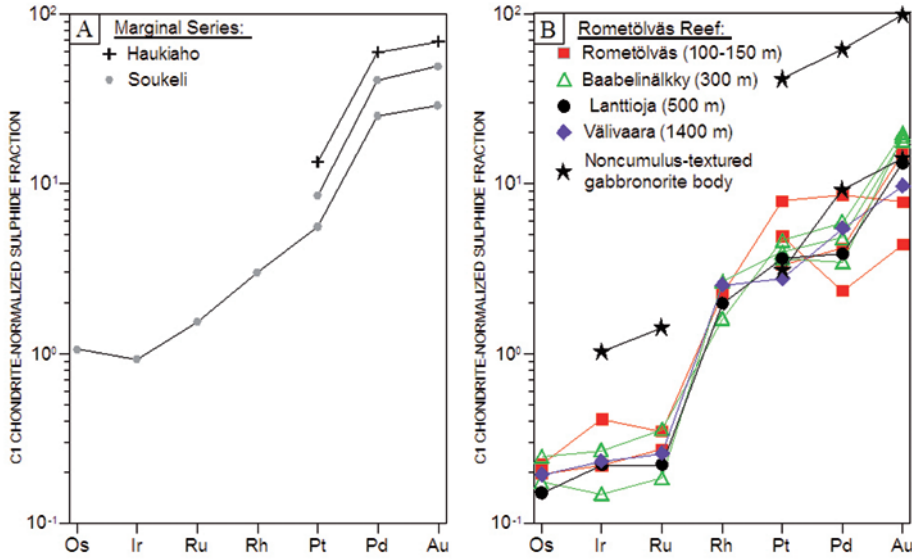


Fig. 7.23. Chondrite-normalized metal patterns of the sulphide fractions of the Marginal Series and the Rometölväs Reef presented in Tables 7.6, 7.7 and 7.8. The legend of the Rometölväs Reef includes the distances from the basal part of the Koillismaa Intrusion to the sampling sites, measured perpendicular to the igneous layering without dip correction. Normalizing values are from Barnes & Maier (1999).

et al. 1982; Zientek et al. 2002) are the best-known deposits of the stratiform-stratabound type. In the Fennoscandian Shield, similar deposits include the Sompujärvi (SJ), Paa-sivaara (PV) and Ala-Penikka (AP) Reefs of the Penikat Intrusion (Alapieti & Lahtinen 1986, 2002; Halkoaho et al. 1989a, b, 1990a, b, 2005; Huhtelin et al. 1989a, 1990; Halko-aho 1993) and the Siika-Kämä (SK) Reef of the Portimo Complex (Huhtelin et al. 1989b, 1990; Alapieti & Lahtinen 2002; Iljina 2005). The patterns of these deposits, denoted here as the reef-type, are shown in Figs 7.24.B and C.

Peck et al. (2001) proposed the term “contact-type” to describe the stratabound deposits, since in layered intrusions most of these deposits are located within a couple of hun-

dreds of meters of the basal contact of the intrusions, as accumulations of magmatic sulphides. The patterns of this type of deposits, from Finland and elsewhere, are shown in Figs 7.24.B and D. Examples of such deposits are the PGE-Cu-Ni occurrences in the lower part of the East Bull Lake intrusion (Peck et al. 2001; James et al. 2002) and the Two Duck Lake intrusion (Watkinson & Ohnenstetter 1992; Barrie et al. 2002), the Dunka Road deposits of the Partridge River intrusion of the Duluth Complex (Thériault & Barnes 1998; Thériault et al. 2000) and the Platreef (Cawthorn et al. 2002). In the Fennoscandian Shield similar deposits include the basal disseminated ores of the Monchegorsk pluton (Dedeev et al. 2002) and the basal PGE miner-

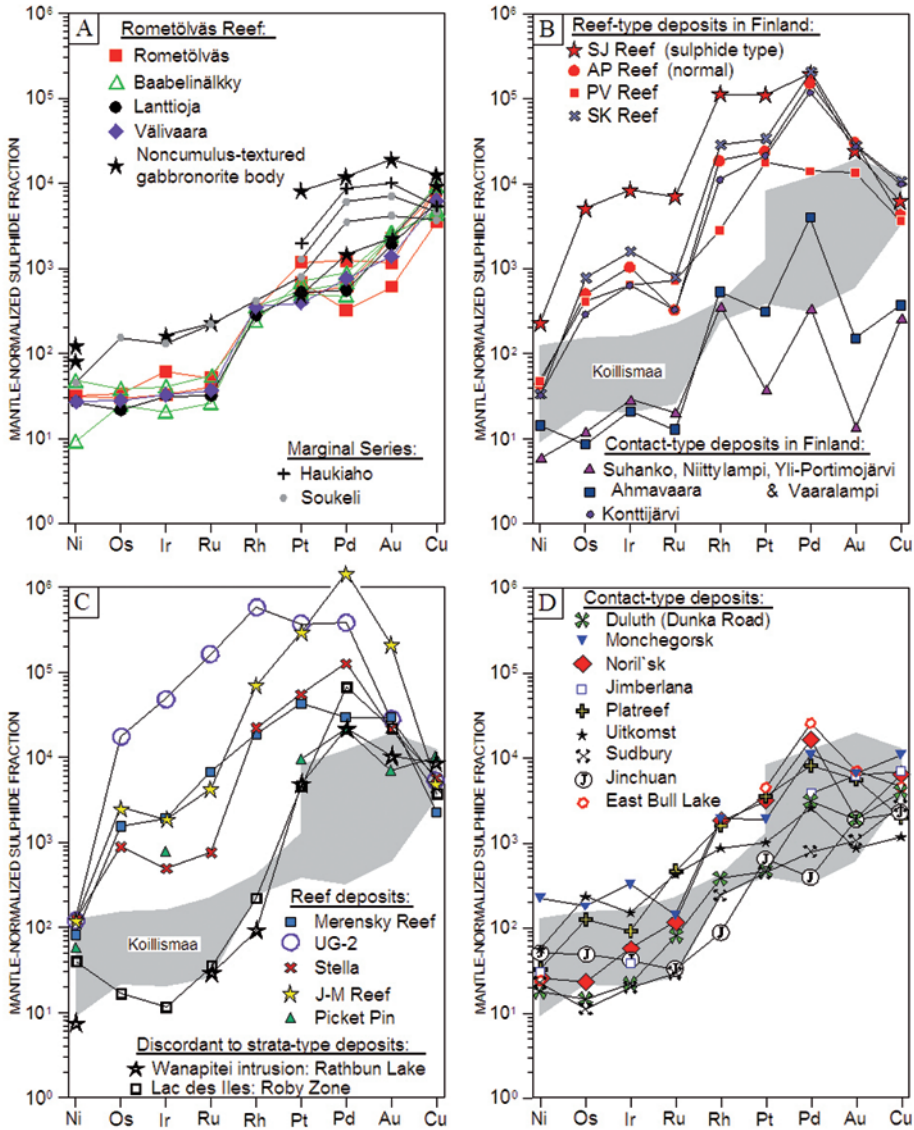


Fig. 7.24. Mantle-normalized patterns of the sulphide fractions of the Marginal Series and the Rometölväs Reef (A) compared to PGE deposits in other mafic-ultramafic intrusions: reef- and contact-type deposits in Finland (B), reefs and discordant to strata-type deposits (C) and contact-type deposits (D). The Koillismaa Intrusion patterns are drawn on the basis of the compositions presented in Tables 7.6, 7.7 and 7.8. Data source of the compared mineralizations is compiled in Appendix 28. Conversion to 100 % sulphides is made on the basis 37 wt. % S in sulphide fraction. Mantle-normalizing values are from Barnes & Maier (1999).

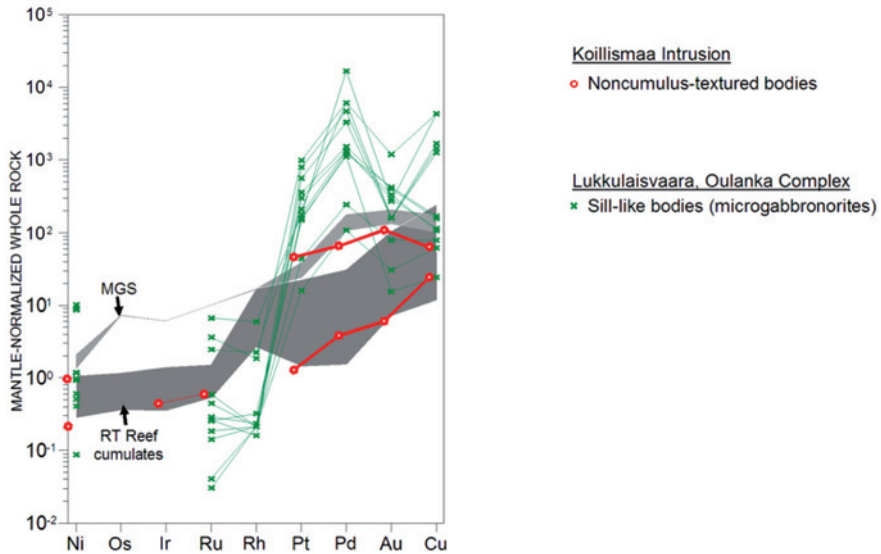


Fig. 7.25. Mantle-normalized whole-rock patterns of the noncumulate bodies and cumulates of the Marginal Series and the Rometölväs Reef (shaded) compared to the PGE occurrence associated with sill-like bodies (microgabbro-norites) of the Lukkulaisvaara intrusion. The Koillismaa Intrusion patterns are drawn on the basis of the data presented in Tables 7.6, 7.7 and 7.8. Data source of the Lukkulaisvaara is compiled in Appendix 28.

alizations in the Fedorova-Pana Tundra intrusion (Schissel et al. 2002) and the Suhanko-Konttijärvi intrusion of the Portimo Complex (Alapieti et al. 1989). By morphology the deposits of Jinchuan (Chai & Naldrett 1992a, b) Sudbury (Naldrett 2004) and Uitkomst Intrusion (Maier et al. 2004) belong to the contact-type, although they are principally exploited for Ni and Cu.

Examples of the deposits that are discordant to strata include the Rathbun Lake deposit of the Wanapitei intrusion (Rowell & Edgar 1986), the Roby Zone of the Lac des Iles intrusion (Hinchey et al. 2005) and the PGE-rich dunite pipes of the Bushveld Complex (Schiffries 1982; Stumpf & Rudlicke 1982). Shown in Fig. 7.24.C are the mantle-normalized patterns of the two first mentioned examples.

The PGE mineralization of the MS of the Koillismaa Intrusion is of the contact-type.

The mantle-normalized composition of the sulphide fraction of the MS is similar to that of the other contact-type deposits. The mantle-normalized pattern of the sulphide fraction of the RT Reef is also comparable to those of other contact-type deposits, even though it does not structurally belong to the type. (Fig. 7.24.A).

The compositions of the noncumulus-textured gabbro-norite bodies and their host cumulates of the RT Reef are compared with the Lukkulaisvaara PGE mineralization of the Oulanka Complex, Russia (Fig. 7.25), as the latter is hosted by sill-like gabbro-norite bodies that resemble the noncumulus-textured bodies of the Koillismaa Intrusion.

The patterns shown in Fig. 7.25 represent whole-rock compositions instead of the sulphide fractions, because the available Lukkulaisvaara data (Semenov et al. 1998) do

not include the concentrations of sulphur. Recently Latypov et al. (2008b) published new analyses from Lukkulaivaara that include concentrations of sulphur, but not those of Os, Ir, Ru and Rh. As shown in Fig. 7.25, the metal

patterns of the Koillismaa Intrusion noncumulus-textured bodies are different from those of the sill-like bodies of the Lukkulaivaara intrusion. The Lukkulaivaara bodies have patterns similar to those of reef-type deposits.

### 7.3 Summary

The upper chilled margins of the Koillismaa Intrusion are compositionally systematically more evolved than the lower chilled margins. The compositions of the chilled margins resemble bonites by their major element compositions. The chilled margins are more primitive than the weighted average composition of the Koillismaa Intrusion, which is basaltic and is characterized by relatively high  $\text{Al}_2\text{O}_3$ , moderate  $\text{TiO}_2$  and low MgO.

Among the noncumulate bodies, those from the Pirivaara display the most evolved compositions and those from the Porttivaara display the most primitive compositions. The noncumulate body in drill core B7 shows evidence of internal chemical fractionation: the body margins display the most primitive composition and towards the upper sulphide-bearing third of the body, the composition becomes more evolved. The rocks of the Lotanvaara unit resemble the noncumulate bodies, but they are richer in MgO and Cr contents and poorer in  $\text{Al}_2\text{O}_3$  content than the noncumulate bodies.

The stratigraphic position of the Rometölväs Reef is marked by changes in major element chemistry of rocks. The cumulates below the reef are distinctly richer in chlorine, nickel, chromium and in MgO compared to the cumulates above the reef. The cumulates below and above the reef define separate and distinct compositional trends in  $\text{FeO}^{\text{TOT}}/\text{Al}_2\text{O}_3$  versus

MgO space. The samples collected from the reef define two trends implying that the reef rocks contain components from cumulates below and above the reef. However, at a smaller scale, such as individual drill cores and outcrops, the chalcophile element concentrations of the reef are controlled by rock texture: highly mottled rocks display the highest grades of ore components.

The gabbronorites of the Marginal Series contain up to 3.9 wt. % S, 0.9 wt. % Cu, 1.1 wt. % Ni, 790 ppb Au, 2650 ppb Pd and 846 ppb Pt, whilst the mottled cumulates of the reef contain up to 2.2 wt. % S, 0.9 wt. % Cu, 0.3 wt. % Ni and up to 103 ppb Au, 241 ppb Pd and 263 ppb Pt. The richest portion of the Rometölväs Reef consist of sulphide-bearing rock in the noncumulus-textured gabbronorite body in drill core B7. This rock contains up to 1 ppm Au+Pd+Pt and up to 0.6 wt. % S, 0.3 wt. % Cu and 0.3 wt. % Ni. The average values of Cu/Ni and Pd/Pt of the Marginal Series are 1.3 and 2.8, respectively, and in the mineralized cumulates of the Rometölväs Reef the corresponding values are 4.1 and 1.0 respectively. The Pd/Pt value in the mineralized noncumulate bodies is similar to that in the reef cumulates.

The sulphide fraction of both the Marginal Series and the Rometölväs Reef display compositions similar to those observed in contact-type deposits elsewhere.

## 8 Sm-Nd ISOTOPE CHEMISTRY

### 8.1 General features of the Sm-Nd isotopic systematics

Sm-Nd isotopes were measured for a granodioritic sample from the Archaean basement, a sample representing Lotanvaara mafic rock unit, four upper chilled margin samples, 19 cumulate samples and five samples from noncumulate bodies. The isotopic data are presented in Tables 8.1 and 8.2, including the  $\epsilon_{\text{Nd}}$  values calculated assuming an age of 2440 Ma.

The  $\epsilon_{\text{Nd}}$  values and  $^{143}\text{Nd}/^{144}\text{Nd}$  evolution lines of the whole-rock samples are shown in Fig. 8.1, which also includes the evolution envelope of Archaean samples close to the Koillismaa Intrusion. The  $^{143}\text{Nd}/^{144}\text{Nd}$  evolution line of the granodioritic basement sample (29-TTK-99) is shown in Fig. 8.1.C. This line corresponds to the other Archaean samples from the area. The granodiorite is also similar in its Sm (1.43 ppm) and Nd (9.24 ppm) concentrations to the Archaean granitoid compositions given by Lauri et al. (2006). On the basis of the envelope, the Archaean upper crust at the time of the magmatism of the Koillismaa Complex, had  $\epsilon_{\text{Nd}}$  values in the range of -8.5 to -5.0.

Data from the noncumulus-textured igneous rocks are plotted in Fig. 8.1.A. The upper chilled margin samples have the lowest initial  $^{143}\text{Nd}/^{144}\text{Nd}$  values. Their  $\epsilon_{\text{Nd}}$ (2440 Ma) values range from -2.8 to -4.0 and their evolution lines intersect with the line of depleted mantle at a model age of 2925–3400 Ma. The isotopic compositions of the sample (79-TTK-99) at 2440 Ma is questionable, since its evolution line does not intersect the line of depleted mantle. Therefore the isotopic composition was probably disturbed in a post-crystallization stage. In the noncumulate bodies the  $\epsilon_{\text{Nd}}$ (2440 Ma) values range from -0.9 to -3.3 and  $T_{\text{DM}}$  ages from 2845 to 3130 Ma. The Lotanvaara mafic rock unit displays the  $\epsilon_{\text{Nd}}$ (2440 Ma) value of -3.0 and  $T_{\text{DM}}$  age of 3085 Ma.

The upper chilled margin samples have less radiogenic initial Nd compositions than the

cumulates (Fig. 8.2). This may imply local contamination of the magma that formed the upper chilled margin, but the components of assimilation could not have been derived from the granophyre above the chilled margin, because the granophyre has similar initial  $^{143}\text{Nd}/^{144}\text{Nd}$  ratios as the cumulates.

The isotopic data on cumulate samples collected from the Porttivaara block profile are shown in Fig. 8.1.B. The samples are relatively uniform in their compositions, having  $\epsilon_{\text{Nd}}$ (2440 Ma) in the range of -0.8 to -2.1 and  $T_{\text{DM}}$  ages from 2805 to 3020.

As shown in Fig. 8.1.C, the variability of the initial  $^{143}\text{Nd}/^{144}\text{Nd}$  ratio in cumulates of drill core B7 is larger than in the Porttivaara profile. Even though this feature may partly be due to the fact that these analyses were conducted in different laboratories, the data suggest that the reef cumulates were not contaminated *in situ* by Archaean upper crust during their crystallization.

This conclusion is based on the fact that the degree of alteration in cumulates does not correlate with isotope compositions. On the basis of the available data, the mottled, sulphide-bearing cumulates record somewhat larger variation in their  $\epsilon_{\text{Nd}}$ (2440 Ma) values than the nonmottled cumulates but do not show any trend towards more depleted or more enriched isotope compositions. The samples from drill core B7 have  $\epsilon_{\text{Nd}}$ (2440 Ma) values in the range of -1.8 to 1.8 and model ages of 2520–2870 Ma. Four out of the ten whole-rock samples analysed from the drill core turned out to be more radiogenic than the contemporaneous CHUR and also show the youngest  $T_{\text{DM}}$  ages.

Further indication of that the Koillismaa Intrusion was not substantially contaminated *in situ* by Archaean upper crust after emplacement is the isotopic homogeneity of the cumulate samples across the LS.

Table 8.1. Sm-Nd isotopic data for noncumulus-textured igneous rocks and Archaean basement.

Sample	Rock, area	Sm (ppm)	Nd (ppm)	$^{147}\text{Sm}/^{144}\text{Nd}$	$^{143}\text{Nd}/^{144}\text{Nd}$	$\epsilon_{\text{Nd}}(2440 \text{ Ma})$	$T_{\text{DM}}(\text{Ma})$
<b>Upper chilled margin</b>							
391-TTK-00, wr <sup>A)</sup>	Gabbronorite Kuusijärvi.	2.53	12.55	0.1217	0.511289±4	-2.9±0.2	2925
10.1-TTK-98, wr	Gabbronorite, Kuusi-Pyhitys.	0.88	3.36	0.1579	0.511831±8	-3.7±0.4	3400
31-TTK-99, wr	Gabbronorite, Kuusi-Pyhitys.	1.92	8.65	0.1344	0.511435±11	-4.0±0.4	3125
103.3-TTK-99, wr	Gabbronorite, Portinloma.	2.43	12.43	0.1183	0.511222±9	-3.1±0.3	2925
<b>Lotanvaara mafic rock unit</b>							
72-TTK-99, wr	Noncumulus-textured gabbronorite, Lotanvaara.	0.72	3.10	0.1419	0.511608±22	-3.0±0.6	3085
72-TTK-99, plag	—”—	0.26	2.44	0.0639	0.510486±15	-0.4±0.4	
72-TTK-99, cpx	—”—	2.25	8.19	0.1659	0.511950±16	-3.9±0.5	
72-TTK-99, opx (2)	—”—	0.50	1.69	0.1784	0.512266±50	-1.6±1.2	
<b>Noncumulus-textured gabbronorite bodies</b>							
70-HAP-99, wr (1)	Noncumulus-textured gabbronorite, Porttivaara.	0.54	2.19	0.1498	0.511776±11	-2.2±0.4	3065
70-HAP-99, wr (2)	—”—	0.81	3.46	0.1417	0.511589±17	-3.3±0.5	3120
70-HAP-99, plag	—”—	0.23	2.25	0.0604	0.510317±17	-2.6±0.4	
70-HAP-99, cpx	—”—	2.68	10.44	0.1550	0.511783±14	-3.7±0.5	
70-HAP-99, opx	—”—	0.67	2.50	0.1633	0.511935±10	-3.3±0.4	
79-TTK-99, wr	Noncumulus-textured gabbronorite, Baabelinälkky.	0.39	1.14	0.2062	0.512517±15	-5.4±0.6	-
87-TTK-99, wr	Noncumulus-textured gabbronorite, Rometölväs.	0.87	4.86	0.1080	0.511077±14	-2.7±0.4	2845
138-TTK-99, wr	Noncumulus-textured gabbronorite, Lanttioja.	0.56	2.11	0.1604	0.512013±12	-0.9±0.4	2995
159-TTK-99, wr (1)	Noncumulus-textured gabbronorite, Pirivaara.	0.86	3.32	0.1559	0.511878±12	-2.1±0.4	3130
159-TTK-99, wr (2)	—”—	0.65	2.54	0.1551	0.511907±11	-1.3±0.4	3000
262.2-TTK-00, wr	Noncumulus-textured gabbronorite, Porttivaara.	0.34	1.25	0.1660	0.512090±34	-1.1±0.9	3115
<b>Archaean basement</b>							
29-TTK-99, wr <sup>A)</sup>	Granodiorite gneiss	1.43	9.24	0.0937	0.510709±4	-5.4±0.2	2975

<sup>A)</sup> Analysed by VSEGEI.

$^{147}\text{Sm}/^{144}\text{Nd}$  determined to a precision of 0.4 % at the  $2\sigma$  level.

$^{143}\text{Nd}/^{144}\text{Nd}$  normalized to  $^{146}\text{Nd}/^{144}\text{Nd} = 0.7219$ . Errors are  $2\sigma$  in last significant unit.

Average  $^{143}\text{Nd}/^{144}\text{Nd}$  value for LaJolla standard was  $0.511851\pm 11$ .

$T_{\text{DM}}$  calculated according to DePaolo (1981).

Abbreviations: wr = whole-rock, opx = orthopyroxene, cpx = clinopyroxene, plag = plagioclase.

Table 8.2. Sm-Nd isotopic data for cumulates.

Sample	Rock, area, subzone, structural height	Sm (ppm)	Nd (ppm)	$^{147}\text{Sm}/^{144}\text{Nd}$	$^{143}\text{Nd}/^{144}\text{Nd}$	$\epsilon_{\text{Nd}}(2440 \text{ Ma})$	$T_{\text{DM}}(\text{Ma})$
22B-TTK-01, wr	Olivine gabbronorite, Porttivaara, LZa, ~ 60 m.	0.66	3.12	0.1281	0.511474±10	-1.3±0.4	2810
22B-TTK-01, plag	—”—	0.20	1.43	0.0865	0.510828±15	-0.8±0.4	
22B-TTK-01, opx (1)	—”—	0.70	2.24	0.1890	0.512407±13	-2.2±0.5	
22B-TTK-01, opx (2)	—”—	0.70	2.20	0.1910	0.512459±10	-1.8±0.4	
265-TTK-00, wr	Olivine gabbronorite, Porttivaara, LZa, ~ 70.	0.54	2.46	0.1315	0.511514±16	-1.5±0.5	2855
277-TTK-00, wr	Gabbronorite, Porttivaara, LZb, ~ 80 m.	2.34	11.10	0.1273	0.511419±9	-2.1±0.3	2885
300-TTK-00, wr	Gabbronorite, Porttivaara, LZb, ~ 540 m.	2.19	10.38	0.1274	0.511423±9	-2.0±0.3	2880
59-W-73, wr	Olivine gabbronorite Porttivaara, MZa, ~ 670 m.	0.91	4.30	0.1275	0.511464±10	-1.3±0.4	2805
59-W-73, plag	—”—	0.36	2.52	0.0867	0.510752±50	-2.4±1.1	
59-W-73, cpx	—”—	3.76	12.61	0.1803	0.512288±10	-1.8±0.4	
59-W-73, opx	—”—	1.55	4.93	0.1896	0.512433±41	-1.9±1.0	
14-TTK-01, wr	—”—	0.66	2.85	0.1394	0.511630±8	-1.8±0.3	2925
309-TTK-00, wr	Gabbronorite, Porttivaara, MZb, ~ 740 m.	1.18	5.46	0.1302	0.511502±12	-1.4±0.4	2830
320.1-TTK-00, wr (1)	Gabbronorite, Porttivaara, MZb/MZc, ~ 850 m.	1.65	7.13	0.1401	0.511629±11	-2.0±0.4	2955
320.1-TTK-00, wr (2)	—”—	1.64	7.07	0.1400	0.511652±9	-1.5±0.4	2900
335-TTK-00, wr	Magnetite gabbro, Porttivaara, UZb, ~ 1520 m.	0.86	3.19	0.1633	0.512063±10	-0.8±0.4	3020
B7 8.26-8.55,wr <sup>A)</sup>	Gabbro (highly mottled), Rometölväs, MZb/MZc.	1.77	8.46	0.1265	0.511420±12	-1.8±0.4	2850
B7 23.60-24.10,wr <sup>A)</sup>	Gabbro (highly mottled), —”—, —”—.	1.27	6.28	0.1221	0.511528±9	+1.7±0.3	2525
B7 27.10-27.60,wr <sup>A)</sup>	Gabbronorite (moderately mottled), —”—, —”—.	1.64	6.98	0.1422	0.511776±10	+0.2±0.4	2720
B7 28.10-28.60,wr <sup>A)</sup>	Gabbronorite (moderately mottled), —”—, —”—.	1.40	6.27	0.1348	0.511579±8	-1.3±0.3	2850
B7 30.10-30.60,wr <sup>A)</sup>	Gabbro (highly mottled), —”—, —”—.	1.84	9.17	0.1215	0.511404±7	-0.5±0.3	2720
B7 34.10-34.58,wr <sup>A)</sup>	Gabbro (highly mottled), —”—, —”—.	1.52	7.00	0.1311	0.511679±9	+1.8±0.3	2520
B7 35.60-36.60,wr <sup>A)</sup>	Gabbro (nonmottled), —”—, —”—.	1.58	7.25	0.1317	0.511545±6	-1.0±0.3	2800
B7 38.60-39.60,wr <sup>A)</sup>	Gabbro (nonmottled), —”—, —”—.	1.44	6.32	0.1380	0.511629±4	-1.3±0.3	2870
B7 53.60-56.32,wr <sup>A)</sup>	Gabbronorite (nonmottled), —”—, —”—.	1.49	6.72	0.1337	0.511666±4	+0.7±0.2	2635
B7 67.55-70.73,wr <sup>A)</sup>	Gabbronorite (nonmottled), —”—, —”—.	1.66	7.57	0.1324	0.511595±11	-0.3±0.4	2730

<sup>A)</sup> Analysed by VSEGEI.

$^{147}\text{Sm}/^{144}\text{Nd}$  determined to a precision of 0.4 % at the 2 $\sigma$  level.

$^{143}\text{Nd}/^{144}\text{Nd}$  normalized to  $^{146}\text{Nd}/^{144}\text{Nd} = 0.7219$ . Errors are 2 $\sigma$  in last significant unit.

Average  $^{143}\text{Nd}/^{144}\text{Nd}$  value for LaJolla standard was 0.511851±11.

$T_{\text{DM}}$  calculated according to DePaolo (1981).

Abbreviations: wr = whole-rock, opx = orthopyroxene, cpx = clinopyroxene, plag = plagioclase.

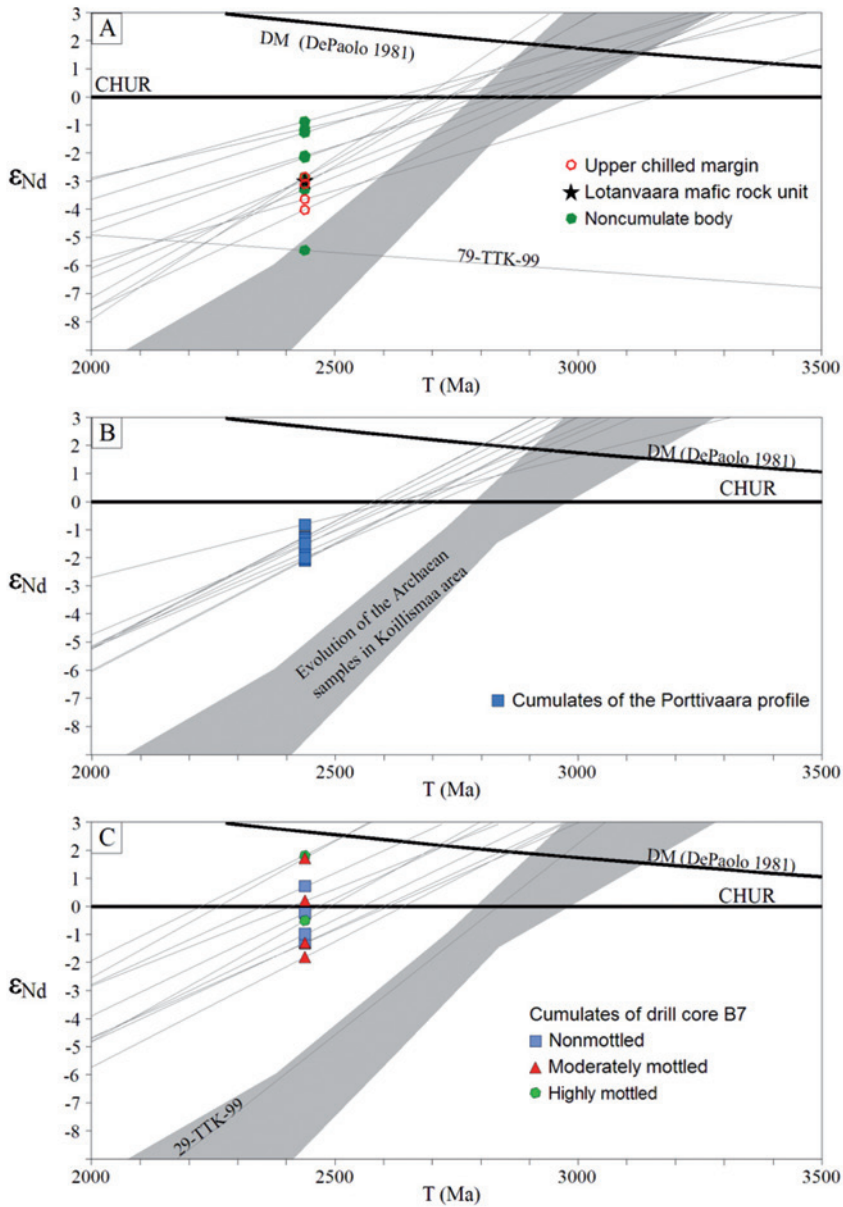


Fig. 8.1.  $\epsilon_{Nd}$ -age diagrams for whole-rock isotopic compositions of Tables 8.1 and 8.2. DM is the evolution of the depleted mantle by DePaolo (1981) and CHUR denotes the chondritic uniform reservoir (DePaolo & Wasserburg 1976). The grey shaded area shows the evolution of the Archaean samples of the Koillismaa area on the basis of the data from Lauri et al. (2006).

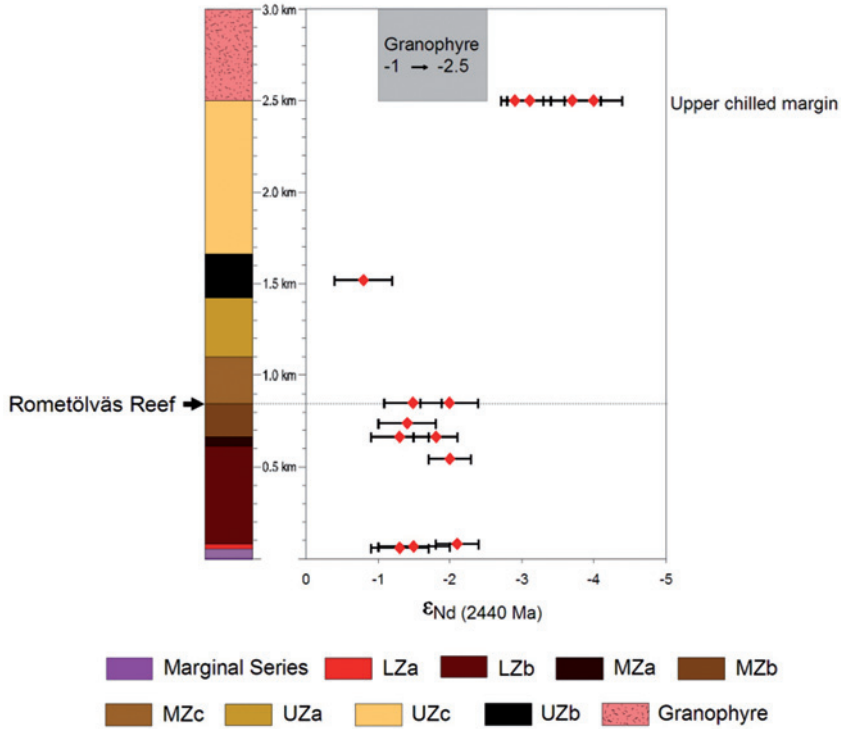


Fig. 8.2. Variation of  $\epsilon_{Nd}(2440 \text{ Ma})$  values in whole-rock samples along the stratigraphic sequence of the Portti-vaara block. Red symbols in the figure are  $\epsilon_{Nd}$  values and bars indicate error estimates. The gray shaded area shows the range of  $\epsilon_{Nd}(2440 \text{ Ma})$  values in granophyre (data from Lauri et al. 2006).

### 8.2 Age determinations

The Sm-Nd isotope data for minerals and their host rocks are plotted in  $^{143}\text{Nd}/^{144}\text{Nd}$ - $^{147}\text{Sm}/^{144}\text{Nd}$  diagrams of Figs 8.3 and 8.4. Mineral fractions were analysed from two fresh noncumulate samples, one from the Lotanvaara rock (72-TTK-99) and the other from a large noncumulate body (70-HAP-00) that is located at the MZa-MZb boundary in the Port-

tivaara block. The cumulate rocks are represented by fresh olivine gabbronorite samples from the LZa (22B-TTK-01) and MZa (59-W-73 and 14-TTK-01). The whole-rock data of sample 14-TTK-01 are combined with those of sample 59-W-73, since the distance between their sampling sites in the field is only ca. 10 m.

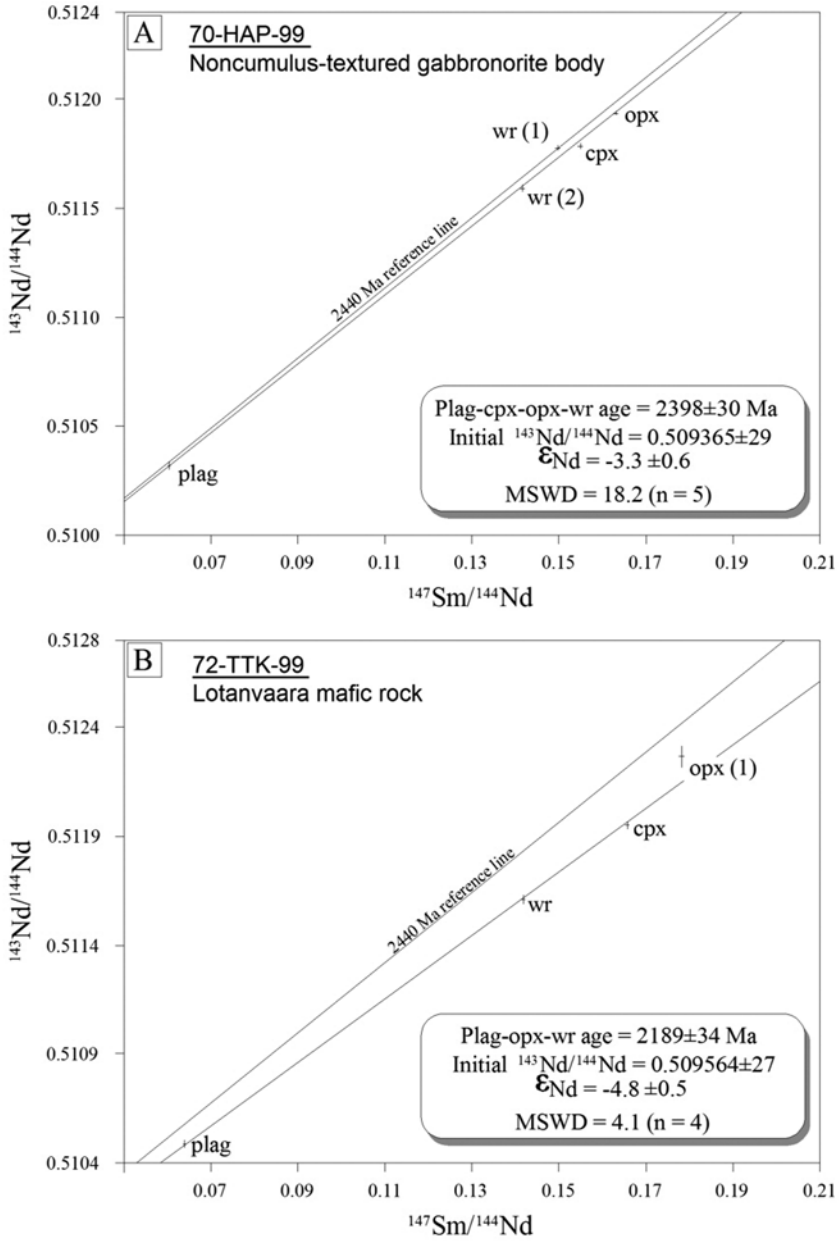


Fig. 8.3.  $^{143}\text{Nd}/^{144}\text{Nd}$ - $^{147}\text{Sm}/^{144}\text{Nd}$  diagrams for mineral fractions and whole-rocks of noncumulate body (70-HAP-99) and Lotaanvaara mafic rock unit (72-TK-99). The 2440 Ma reference line is derived from the initial  $^{143}\text{Nd}/^{144}\text{Nd}$  values determined from the samples.

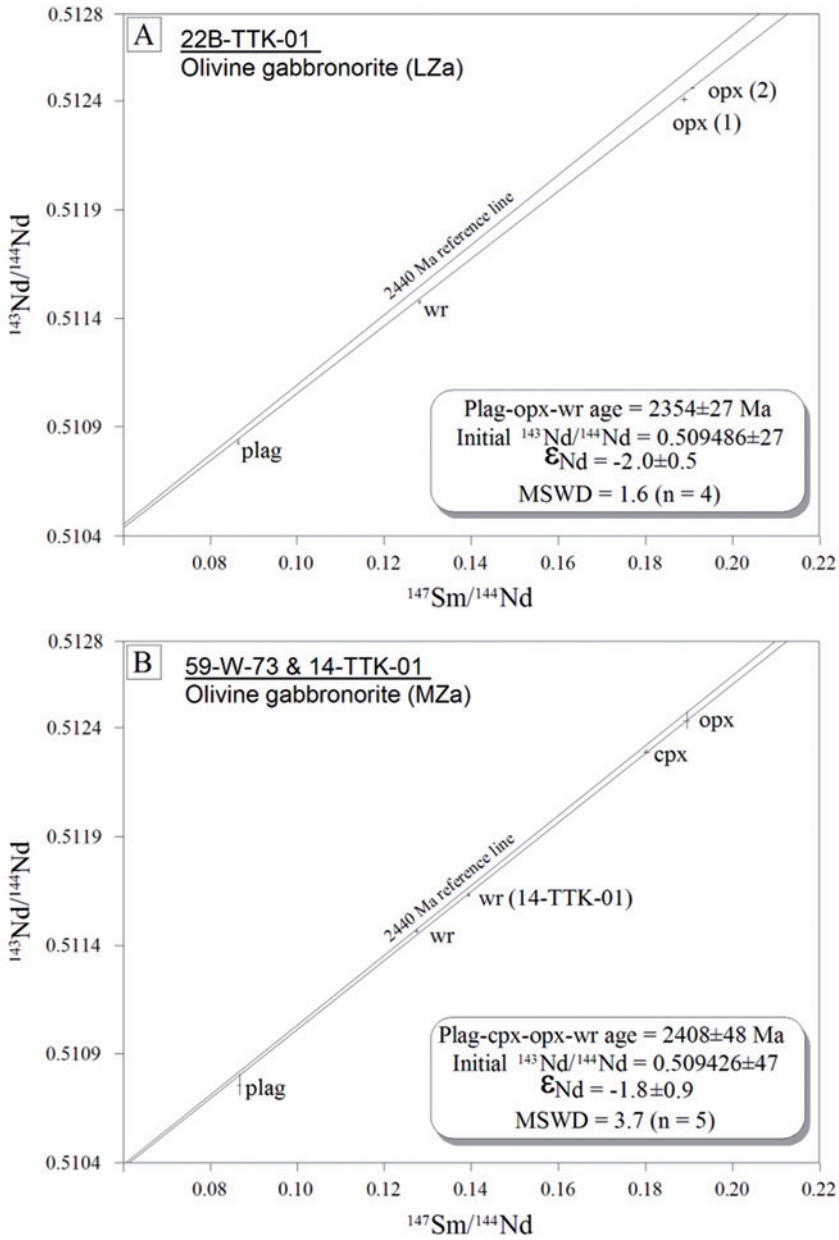


Fig. 8.4.  $^{143}\text{Nd}/^{144}\text{Nd}$ - $^{147}\text{Sm}/^{144}\text{Nd}$  diagrams for mineral fractions and whole-rocks of LZa (22B-TTK-01) and MZa (59-W-73 & 14-TTK-01) olivine gabbronorites. The 2440 Ma reference line is derived from the initial  $^{143}\text{Nd}/^{144}\text{Nd}$  values determined from the samples.

Even though both of the noncumulate samples display a fairly wide spread in their  $^{147}\text{Sm}/^{144}\text{Nd}$  ratios, neither of them defines isochrons since their values of mean squared weighted deviation (MSWD) are higher than 2.5 (Fig. 8.3). Nevertheless, the Sm-Nd data for plagioclase, pyroxenes and two whole-rock analyses of 70-HAP-99 from the noncumulate body yield an errorchron age of  $2398 \pm 30$  Ma, which is close to the U-Pb age of the Koillismaa Complex ( $2436 \pm 5$  Ma, Alapieti 1982). If the more radiogenic whole-rock analysis (wr 1) is excluded, the subpopulation defines an isochron (MSWD = 2.0,  $n = 4$ ) age of  $2374 \pm 31$  Ma (initial  $^{143}\text{Nd}/^{144}\text{Nd} = 0.509371 \pm 29$ ,  $\epsilon_{\text{Nd}} = -3.8 \pm 0.6$ ). The plagioclase, pyroxenes and whole-rock analyses of sample 72-TTK-99 representing the Lotanvaara mafic rock yield an errorchron age of  $2189 \pm 34$  Ma.

The  $^{143}\text{Nd}/^{144}\text{Nd}$ - $^{147}\text{Sm}/^{144}\text{Nd}$  isotope data for cumulates and their minerals are shown in Fig. 8.4 where the sample 22B-TTK-01 from the LZa yields an isochron age of  $2354 \pm 27$  Ma (Fig. 8.4.A). The mineral fractions and

whole-rocks from the MZa (59-W-73 & 14-TTK-01) define an errorchron age of  $2408 \pm 48$  Ma (Fig. 8.4.B). The result is the same even if the 14-TTK-01 whole-rock analysis is omitted:  $2398 \pm 49$  Ma, initial  $^{143}\text{Nd}/^{144}\text{Nd} = 0.509442 \pm 50$ ,  $\epsilon_{\text{Nd}} = -1.8 \pm 1.0$ , MSWD = 3.6.

Although these Sm-Nd ages are somewhat younger than the U-Pb ages from the Koillismaa Complex, the Sm-Nd isotopic results are compatible with those from other coeval layered intrusions and mafic dykes in the Fennoscandian Shield whose initial  $\epsilon_{\text{Nd}}$  values are slightly below zero (Appendices 1 and 2). The narrow spread of the slightly negative initial  $\epsilon_{\text{Nd}}$  values of the early Palaeoproterozoic layered intrusions, coeval mafic dykes and volcanic rocks in the Fennoscandian Shield has been attributed to a primary LREE-enriched mantle source and/or assimilation by crustal material during magma ascent (Balashov et al. 1990a; Turchenko 1992; Balashov et al. 1993; Amelin & Semenov 1996; Puchtel et al. 1996, 1997; Hanski et al. 2001a; Alapieti & Lahtinen 2002).

### 8.3 Summary

The noncumulus-textured gabbro-norite bodies, the Lotanvaara mafic rock unit and cumulates of the Koillismaa Intrusion have similar initial Nd isotope compositions. In these rocks the  $\epsilon_{\text{Nd}}$ (2440 Ma) values are negative, ranging from ca. -1 to -3. The upper chilled margin shows somewhat less radiogenic initial Nd isotope compositions, since the analysed samples collected from different locations of the upper chilled margin have the  $\epsilon_{\text{Nd}}$ (2440 Ma) values in the range of ca. -3 to -4. The Archaean upper crust at the time of the magmatism of

the Koillismaa Complex had the least radiogenic Nd isotope composition, at  $\epsilon_{\text{Nd}}$  approximately -5 to -8.5.

The Koillismaa Intrusion magma chamber did not assimilate the Archaean country rock material after emplacement, because the cumulate samples have relatively uniform Nd isotope compositions. It is therefore more likely that the initial Nd isotope compositions reflect the composition of the parental magma of the Koillismaa Intrusion.

## 9 CONDITIONS OF CRYSTALLIZATION IN THE KOILLISMAA INTRUSION

Because the stratigraphic position of the Rometölväs Reef in the Koillismaa Intrusion is marked by changes in major element chemistry of the rocks, it is possible that the genesis

of the reef is related to the magma dynamics in the intrusion. Therefore, it is of importance to examine the conditions of the crystallization of the Koillismaa Intrusion.

### 9.1 Pyroxene thermometer

A successful application of the pyroxene thermometer requires knowledge of the composition of a primary phase, *i.e.* the composition prior to exsolution. The primary pyroxene compositions of the Koillismaa Intrusion have been estimated in Chapter 6.1.2.3 (Table 6.1). For the use of two-pyroxene thermometers of Wood & Banno (1973) and Wells (1977), another requirement is that the coexisting ortho- and clinopyroxene should have crystallized contemporaneously. Generally it is thought that the requirement is met when both of the phases exhibit similar textural status, for instance as cumulus crystals. Therefore, some of the pyroxene pairs do not meet the second requirement, as their augite grains show an intercumulus habit whereas coexisting orthopyroxene is a cumulus phase.

The small variation in equilibrium temperatures of coexisting pyroxene phases reflects the variation in chemical fractionation of the Koillismaa Intrusion. The thermometer of Wood & Banno (1973) gives solidus temperatures in the range of 1056 to 1092 °C for six pyroxene pairs in cumulus-textured rocks of the Koillismaa Intrusion, whereas the thermometer of Wells (1977) yields temperatures of 1110–1176 °C (Table 9.1). The tem-

peratures determined for the MZc where both ortho- and clinopyroxene occur as cumulus crystals provide the most reliable estimates of solidus temperatures.

Several pyroxene pairs of the gabbro-noritic noncumulate bodies were used to determine their crystallization temperatures and one of these estimates, ca. 985 °C with both calibrations, is given in Table 9.1. The temperature is obviously too low to represent the temperature of crystallization of pyroxenes in the noncumulate bodies.

The subsolidus temperatures were determined using mostly exsolution lamellae in augites of the LZa, MZa and MZb. However, for the MZc temperatures were also estimated using granular lamellae of inverted pigeonite. Depending on the thermometric calibration, the estimation of the temperature of lamellar exsolution is 930–970 °C (using the thermometer of Wood & Banno 1973) or 970–1020 °C (using the thermometer of Wells 1977). The granular lamellae in inverted pigeonite appear to have formed a few tens of degrees lower than the fine lamellae of augite. For the inversion temperature the model of Wood & Banno (1973) gives ca. 930 °C and the model of Wells (1977) ca. 980 °C.

Table 9.1. Calculated equilibrium temperatures (°C) of coexisting ortho- and clinopyroxenes of the Koillismaa Intrusion. WB-73 = calculated using the method of Wood & Banno (1973), W-77 = calculated using the method of Wells (1977).

<b>Sample</b>	<b>Description</b>	<b>WB-73:</b>	<b>W-77:</b>
24-TTK-01 (LZa)	Solidus temperature	1083	1110
	Exsolution of Ca-poor phase from augite	935	969
305-TTK-00 (MZa)	Solidus temperature	1061	1127
	Exsolution of Ca-poor phase from augite	962	998
309-TTK-00 (MZb)	Solidus temperature	1092	1156
	Exsolution of Ca-poor phase from augite	970	996
311-TTK-00 (MZb)	Solidus temperature	1056	1153
	Exsolution of Ca-poor phase from augite	945	994
5-TTK-03 (MZc)	Solidus temperature	1057	1172
	Exsolution of Ca-poor phase from augite	931	995
	Exsolution of Ca-rich phase from pigeonite = inversion temperature	929	975
6.1-TTK-03(MZc)	Solidus temperature	1056	1176
	Exsolution of Ca-poor phase from augite	943	1021
	Exsolution of Ca-rich phase from pigeonite = inversion temperature	930	980
B7 13.00 (Noncumulate)	Skeletal augite and megacrystic host	985	984

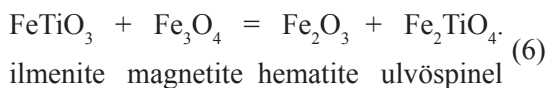
Table 9.2. Information on the oxide grains used for determination of the T- $fO_2$ -relations of the magnetite gabbro of the Koillismaa Intrusion.

<b>Sample</b>	<b>Phase</b>	<b>Phase description</b>	<b>Analytical key</b>
335-TTK-00 (UZb)	Spinel	<u>Exsolution host</u> 72.3 vol. % of oxide grains	SILI 22.04.03/8 and SILI 10.10.03/10
		<u>Lamellae</u> Il{111} plane 19.4 vol. % of oxide grains	SILI 10.10.03/7, 8, 9
	Ilmenite	<u>Granular exsolution</u> 8.3 vol. % of oxide grains (Granular lamellae contain 1.9 vol. % of hematite exsolutions)	SILI 10.10.03/4, 5, 6
		<u>Separate crystal</u> , see Fig. 6.14.B: "Primary ilmenite?"	SILI 10.10.03/1, 2
337-TTK-00 (UZb)	Spinel	<u>Exsolution host</u> 70.4 vol. % of oxide grains	SILI 03.03.03/21, 22
		<u>Lamellae</u> Il{111} plane 19.7 vol. % of oxide grains	SILI 03.03.03/20, 23, 25
	Ilmenite	<u>Granular exsolution</u> 9.9 vol. % of oxide grains (Granular lamellae contain 2.0 vol. % of hematite exsolutions)	SILI 03.03.03/18, 19

## 9.2 Magnetite-ilmenite equilibrium

Magnetite-ilmenite equilibrium permits determination of the oxygen fugacity and temperature of formation of coexisting oxides if they crystallized in equilibrium and retained their original compositions. If these requirements were maintained since the crystallization, it is possible to estimate the conditions at which the phases formed, using the  $T$ - $fO_2$ -composition relationship described by Buddington and Lindsley (1964).

The oxidation of ulvöspinel component in reaction 4 (see Chapter 6.2.1) is dependent on the partial pressure of oxygen. Another pertinent reaction is the one between coexisting ilmenite-hematite and magnetite-ulvöspinel solid solution, where the cation exchange is dependent on temperature so that at high temperatures both ulvöspinel and ilmenite are the dominant phases (Buddington & Lindsley 1964):



Two model redox reactions in magmatic systems that involve oxygen in equilibrium with the silicate melt include the oxidation of magnetite to hematite (HM buffer) and fayalite to magnetite and quartz (QFM buffer). Depending on the conditions along the buffer line in the  $T$ - $fO_2$ -space, the buffer balances the magnetite production or consumption according to reactions 4 and 6. The  $T$ - $fO_2$ -relation can be established by the components of coexisting cubic and rhombohedral phases.

Although the technique of Buddington & Lindsley (1964) has originally been restricted to magmas that have precipitated separate ilmenite-hematite and magnetite-ulvöspinel solid solutions during cooling, the approach

has been used in estimation of the subsolidus conditions of exsolution in single titanomagnetite grains (Himmelberg & Ford 1977; Pang et al. 2008). According to Buddington & Lindsley (1964) the increasing degrees of diffusion and oxidation result in a systematic range from single, homogenous titanomagnetite grains through ferrian ilmenite lamellae in magnetite. It is likely that diffusion decreases as cooling proceeds and therefore, the coarse segregations of ilmenite forming composite grains with ilmenomagnetites probably exsolve at higher temperature than the long and thin lamellae conformable to  $\{111\}$  plane of the host oxide grains. Hence, the existing iron-titanium oxides in the magnetite gabbro of the Koillismaa Intrusion are interpreted to be a result of a minimum of three stages of crystallization: crystallization of primary oxides (stage A), exsolution of granular lamellae (stage B) and exsolution of fine lamellae oriented parallel to the  $\{111\}$  plane oriented lamellae (stage C).

The composition of primary titanomagnetite, *i.e.* the composition prior to the development of exsolution lamellae, was reconstructed from analytical and modal data of ilmenomagnetite grains from two magnetite gabbro (UZb) samples (335-TTK-00 and 337-TTK-00). The modal proportions of host and lamellae were estimated using digital BE-images or photomicrographs showing typical lamellar texture in these samples. The primary oxide compositions of these samples were estimated using the method of Bowles (1977). The information on phase relations and analyses of the samples is compiled in Table 9.2, whilst Tables 9.3 and 9.4 show the analysed and calculated compositions.

Table 9.3. Compositions and modal data used in the calculation of primary oxide compositions (stage A) and the conditions during lamellae formation (stage B and C) of sample 335-TTK-00.

Sample 335-TTK-00	Vol. %	Average
Ilmenomagnetite components (stage C): <u>Exsolution host:</u> Mt <sub>96.4</sub> Usp <sub>3.6</sub> <u>Lamellae Il{111} plane:</u> Ilm <sub>98.3</sub> Hem <sub>1.7</sub>	78.8 21.2	Titanomagnetite prior to exsolution Il{111} plane (stage B): Mt <sub>67.4</sub> Usp <sub>32.6</sub>
Granular ilmenite components (stage C): <u>Exsolution host:</u> Ilm <sub>98.9</sub> Hem <sub>1.1</sub> <u>Hematite lamellae:</u> Hem <sub>100.0</sub> *	98.1 1.9	Granular ilmenite prior to exsolution of hematite (stage B): Ilm <sub>97.2</sub> Hem <sub>2.8</sub>
Titanomagnetite components (stage B): <u>Exsolution host:</u> Mt <sub>67.4</sub> Usp <sub>32.6</sub> <u>Granular exsolution:</u> Ilm <sub>97.2</sub> Hem <sub>2.8</sub>	91.7 8.3	Titanomagnetite prior to granular exsolution (stage A): Mt <sub>58.4</sub> Usp <sub>41.6</sub>
Separate ilmenite grain components (stage C): <u>Exsolution host:</u> Ilm <sub>99.0</sub> Hem <sub>1.0</sub> <u>Hematite lamellae:</u> Hem <sub>100.0</sub> *	93.8 6.2	Separate ilmenite grain prior to exolutions (stage A): Ilm <sub>92.6</sub> Hem <sub>7.4</sub>

\*composition assumed.

Table 9.4. Compositions and modal data used in the calculation of the primary oxide compositions (stage A) and the conditions during lamellae formation (stage B and C) of sample 337-TTK-00.

Sample 337-TTK-00	Vol. %	Weighted average
Ilmenomagnetite components (stage C): <u>Exsolution host:</u> Mt <sub>96.7</sub> Usp <sub>3.3</sub> <u>Lamellae Il{111} plane:</u> Ilm <sub>98.8</sub> Hem <sub>1.2</sub>	78.1 21.9	Titanomagnetite prior to exsolution Il{111} plane (stage B): Mt <sub>66.4</sub> Usp <sub>33.6</sub>
Granular ilmenite components (stage C): <u>Exsolution host:</u> Ilm <sub>97.8</sub> Hem <sub>2.2</sub> <u>Hematite lamellae:</u> Hem <sub>100.0</sub> *	98.0 2.0	Granular ilmenite prior to exsolution of hematite (stage B): Ilm <sub>95.8</sub> Hem <sub>4.2</sub>
Titanomagnetite components (stage B): <u>Exsolution host:</u> Mt <sub>66.4</sub> Usp <sub>33.6</sub> <u>Granular exsolution:</u> Ilm <sub>95.8</sub> Hem <sub>4.2</sub>	90.1 9.9	Titanomagnetite prior to granular exsolution (stage A): Mt <sub>56.0</sub> Usp <sub>44.0</sub>

\*composition assumed.

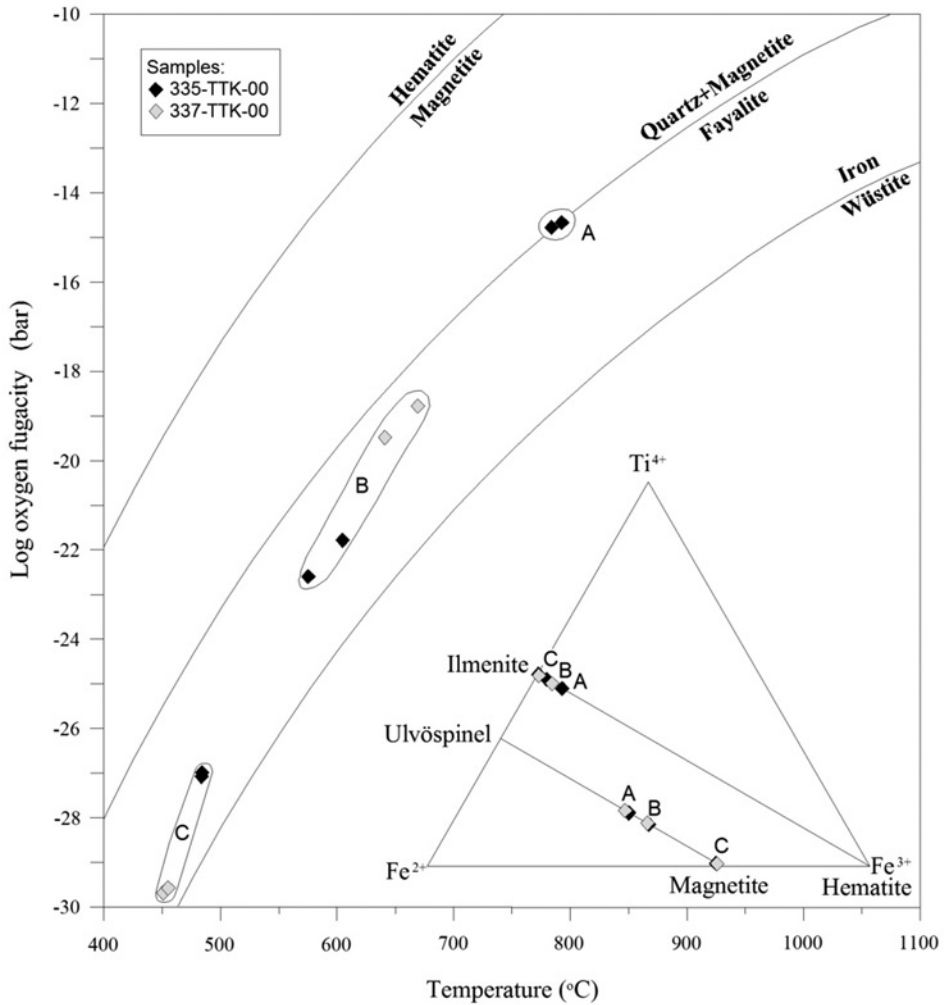


Fig. 9.1. T-fO<sub>2</sub> conditions indicated by the compositions of iron titanium oxide minerals from two magnetite gabbro samples of the Koillismaa Intrusion: A = conditions for primary oxides (ulvöspinel-magnetite and ilmenite-hematite solid solutions) B = conditions for granular exsolution and C = conditions for thin lamellae oriented parallel to the {111} plane. Conditions were estimated with calibrations of Spencer & Lindsley (1981) and Andersen & Lindsley (1985). Buffer lines are from Myers & Eugster (1983). The triangle illustrates the TiO<sub>2</sub>-FeO-Fe<sub>2</sub>O<sub>3</sub> system, in which the compositions are plotted and identified by the stages A, B and C.

Table 9.5. Calculated equilibrium temperatures (°C) and oxygen fugacities (bar) of coexisting oxides. SL-81 = calculated using the method of Spencer & Lindsley (1981), AL-85 = calculated using the method of Andersen & Lindsley (1985).

Sample	Description	SL-81:		AL-85:	
		T	log $f_{O_2}$	T	log $f_{O_2}$
335-TTK-00 (UZb)	Solidus temperature*	785	-14.8	794	-14.7
	Exosolution of granular lamellae	576	-22.6	606	-21.8
	Exsolution of {111} plane oriented lamellae	485	-27.1	485	-27
337-TTK-00 (UZb)	Exosolution of granular lamellae	642	-19.5	670	-18.8
	Exsolution of {111} plane oriented lamellae	456	-29.6	452	-29.7

\* too low to represent conditions of the crystallization of primary titanomagnetite.

The calculated solid solution composition of the primary oxides in the samples is 56 and 58 mol. %  $Fe_3O_4$  (stage A in Tables 9.3 and 9.4), whereas the average composition of the oxide phases after granular exsolution is approximately 67 mol. % of  $Fe_3O_4$  (stage B in Tables 9.3 and 9.4). The latter composition corresponds very closely to the estimation of Juopperi (1977) for the highest possible magnetite amount in the solid solution of the primary titanomagnetite of the UZb. The estimate was made using the Fe and Ti contents of the magnetic concentrate of the Mustavaara Vanadium Mine. This indicates that during the production of the magnetic concentrate, the fine ilmenite lamellae oriented parallel to the {111} plane were not succeeded to collect to the non-magnetic fraction.

The compositions shown in Tables 9.3 and 9.4 were used to estimate the temperatures and oxygen fugacities during the cessation of granular and {111} plane oriented lamellae. In addition, for sample 335-TTK-00, the separate ilmenite grain shown in Fig. 6.14.B was used to estimate the conditions of formation of primary phases in ilmenite-hematite and magnetite-ulvöspinel solid solutions. The conditions were estimated with calibrations of Spencer & Lindsley (1981) and Andersen &

Lindsley (1985). The calculated temperature and oxygen fugacity values are shown in Table 9.5.

The temperature and oxygen fugacity values during the crystallization of primary titanomagnetite are 790 °C and  $10^{-15}$  bar, respectively. These values are obtained from sample 335-TTK-00. The values are obviously too low to represent the crystallization conditions of primary titanomagnetite. Therefore, it is likely that the separate ilmenite used in the calculation does not actually represent a separate phase of ilmenite-hematite solid solution, but is a product of granular exsolutions of titanomagnetite. In both samples, the calibrations yield temperatures and oxygen fugacities ranging from 580 to 670 °C and from  $10^{-19}$  to  $10^{-23}$  bar for the granular exsolution. The conditions for the formation of {111} plane-oriented lamellae (stage C) are 450–485°C and  $10^{-27}$ – $10^{-30}$  bar of oxygen pressure. (Table 9.5).

The temperature and oxygen fugacity values determined for crystallization (stage A), formation of the granule exsolution (stage B) and {111} plane oriented lamellae (stage C) are plotted in the  $f_{O_2}$ -T grid of Fig. 9.1. The figure shows also the lines for QFM (quartz-fayalite-magnetite), HM (hematite-magnetite)

and IW (iron-wüstite) buffers. The calculated values fall near the QFM buffer. At magmatic temperatures ( $> 1000\text{ }^{\circ}\text{C}$ ) along the isopleth, one can thereby obtain an  $f\text{O}_2$  of ca. QFM+1 log units. In these redox conditions the spinel solid solution composition, as represent-

ed by Buddington & Lindsley (1964), Spencer & Lindsley (1981) and Andersen & Lindsley (1985) is  $\text{Mt}_{60}\text{Usp}_{40}$ . This composition is very similar to the estimated primary ulvöspinel-magnetite solid solution composition of the UZb of the Koillismaa Intrusion.

### 9.3 Summary

Pyroxene equilibrium has been used to estimate the crystallization temperatures of the cumulates of the Koillismaa Intrusion. The estimated temperatures do not vary along the stratigraphic section of the intrusion and give 1050–1175  $^{\circ}\text{C}$  for the solidus temperatures of pyroxenes in the LS.

Magnetite-ilmenite equilibrium has been used to estimate the redox conditions during crystallization in the magma chamber of the Koillismaa Intrusion. In  $T$ - $f\text{O}_2$  space, the oxidation state of the magma can be characterized by conditions of one log unit above the QFM buffer.

## 10 PARENTAL MAGMA OF THE KOILLISMAA INTRUSION

### 10.1 Methods to estimate parental magma composition

Many past studies have used chilled margins of intrusions to estimate the composition of their parental magmas because the chilled margins are assumed to represent liquid quenched against cold wall rocks. Similar approaches include estimation of the compositions of extrusive equivalents of the intrusive rocks or dykes associated with the intrusions. (Hess 1960; Wager 1960; Wadsworth 1961; Wager & Brown 1967; Donaldson 1974; McBirney & Noyes 1979; Page 1979; Irvine 1982; Wilson 1982; Naslund 1984; Nolan & Morse 1986; Emeleus 1987; Hoover 1989; Prendergast & Keays 1989; Emeleus et al. 1996).

However, Huppert & Sparks (1989) have shown that the compositions of chilled margins to intrusions may not represent that of the primary parental magma. An initial chilled margin, *i.e.* the chill whose composition cor-

responds to the parental magma, forms when heat conduction from the magma towards the wall rocks exceeds the conduction from the wall rocks towards the magma. As the thermal convection commences in the magma chamber, the heat flux from the magma toward wall rocks begins to increase. Consequently, the initial chilled margins may be completely melted. When the thermal convection in the chamber wanes and heat conduction from the magma to the wall rocks decreases, a secondary chilled margin develops. If the melt composition has changed prior to secondary chilling, for instance by reactions with country rocks, thermomigration or compositional convection in the magma, the chilled margin composition will not correspond to the parental magma composition.

Another approach in defining parental magma composition is based on the stratigraphic

ic summation of chemical analyses of the rocks of the intrusive body. This is made on the assumption of closed system crystallization without magma addition or eruption. The major potential error involved in this method arises from the choice of the sampling profile to provide involvement of all correct layers in their right relative volume proportions into the calculation. Another problem is that if some parts of the intrusion have been eroded the bulk composition of the intrusion can obviously not be determined. The approach works well with vertical sections for tabular intrusions, but for intrusions with more complex geometries, these calculations do not provide reliable estimations.

A further method to estimate the composition of parental magma of an intrusion is geochemical thermometry, which is based on experimentally determined mineral-melt partition data for phase equilibria (Frenkel et al. 1988; Ariskin 1999; Ariskin & Barmina 2004). This approach is independent of the compositions of chilled margin or weighted averages, because it makes use of the chemical composition of cumulus-textured rocks near the contact of intrusions that have been crystallized in the early stages of the intrusion. Two principal assumptions underlie this approach. The most important is that the original liquid and crystals are assumed to be in chemical equilibri-

um. The second assumption is that the samples have different compositions as a result of the modal proportions of cumulus minerals only. If both of these assumptions are valid, one can state that during equilibrium melting of cumulate samples having the same liquidus temperature, the modelled composition of residual liquid will converge with increasing temperature and intersect at a point in the temperature-composition space that represents the conditions under which the cumulate assemblage was formed. Because equilibrium melting is reversible with respect to equilibrium crystallization, the constructed “melting” lines can be understood as crystallization trajectories for starting compositions to those of the cumulates under consideration.

The benefit of the geochemical thermometry is that it provides an independent estimate of the parental magma composition, which can be used to test the validity of the other estimates, such as the compositions of chilled margins and weighted average compositions. Moreover, the technique generates additional petrological information by providing an estimate of the liquidus temperature of the magma. Thus, the method can be used to test the validity of other temperature estimates, such as pyroxene thermometry. The potential drawbacks of the method are the same as in the method of chilled margin compositions.

## 10.2 Estimation of the Koillismaa Intrusion parental magma composition

As shown in Chapter 7.1, the compositions of the chilled margins differ from that of the weighted average. The method of geochemical thermometry is used to test the validity of these compositionally different estimates for the parental magma. In geochemical thermometry, cumulus-textured rocks are treated as liquids. Their compositions are used to define the liquidus minerals (cumulus crystals) and evolution lines of residual liquid com-

position (liquid lines of descent) as function of temperature. With two or more chemically contrasting rock compositions with differences caused by variations in proportions of cumulus crystals, the trajectories of the liquid lines of descents will result in compositional lines intersecting in the T-X spacing. The intersections provide the temperature (T) and composition (X) of the magma during initial crystallization. With a single sam-

ple, if the temperature of the equilibrium was known independently, it is possible to define the trapped liquid composition as a function of the temperature. The locations of the cumulate samples used for the test are shown in Fig. 5.5. These samples belong to the subzone LZa, which is located less than 100 m from the basal contact of the intrusion. The samples are unaltered and provide compositionally contrasting compositions as shown in Table 10.1.

The geochemical thermometry was performed with the COMAGMAT computer program, which according to Ariskin (1999) and Ariskin & Barmina (2004) works best for tholeiitic systems with an accuracy of modelled crystallization temperatures of 10–15 °C and major element compositions of modelled minerals and liquids within a range of 0.5 to 1 wt. %.

The supposed physical parameters were an oxygen buffer of QFM+1 log units and a pres-

sure of 0.5 Kbar. These initial conditions were determined by the assumed emplacement depth of the Koillismaa Intrusion (~ 1.5 km) and by the magnetite-ilmenite equilibria of Chapter 9.2. Judging from the absence of igneous amphibole and mica in the cumulus assemblage, the magma of the intrusion was undersaturated with respect to H<sub>2</sub>O. Therefore, the modellings were conducted in anhydrous conditions.

The trajectories of liquid lines of descent of SiO<sub>2</sub>, TiO<sub>2</sub>, Al<sub>2</sub>O<sub>3</sub>, FeO<sup>TOT</sup>, MnO and MgO simulated for the compositions of the selected samples during equilibrium crystallization are depicted in Fig. 10.1. The trajectories intersect at 1200±25 °C, which suggest a common trapped liquid for the samples. The model composition of trapped liquid defined near 1200 °C for the samples is compiled in Table 10.2 (“Average of 1–6”). The liquid line of descent calculated for equilibrium crystallization of the model composition is shown by

Table 10.1. Compositions of cumulus-textured rocks of the Koillismaa Intrusion (1–6) used in geochemical thermometry.

Sample	1	2	3	4	5	6
SiO <sub>2</sub>	48.30	47.62	51.74	52.48	51.09	47.82
TiO <sub>2</sub>	0.16	0.15	0.28	0.24	0.29	0.21
Al <sub>2</sub> O <sub>3</sub>	12.20	14.63	20.65	16.78	15.89	10.96
FeO <sup>TOT</sup>	11.99	10.38	5.35	7.71	9.19	12.38
MnO	0.20	0.15	0.10	0.15	0.15	0.18
MgO	19.19	17.09	7.27	10.94	13.20	22.08
CaO	6.86	8.55	11.36	9.41	8.15	5.46
Na <sub>2</sub> O	0.72	0.89	2.77	2.03	1.66	0.66
K <sub>2</sub> O	0.37	0.52	0.44	0.23	0.32	0.22
P <sub>2</sub> O <sub>5</sub>	0.02	0.02	0.03	0.03	0.06	0.03

Compositions are presented on the basis of normalization to 100 wt. % on a volatile-free basis.

1 = 16-TTK-01, olivine gabbro-norite/poCb\*a\*, LZa (lowermost unit).

2 = 23-TTK-01, olivine gabbro-norite/poCb\*a\*, LZa (lowermost unit).

3 = 17.1-TTK-00, gabbro-norite/pbCa\*, LZa (middlemost unit).

4 = KOIL112/3, gabbro-norite/pbCa\*, LZa (middlemost unit).

5 = KOIL112/21, gabbro-norite/pbCa\*, LZa (middlemost unit).

6 = 24-TTK-01, olivine gabbro-norite/pboCa\*, LZa (uppermost unit).

a thick red line in Fig. 10.1. It is noteworthy that the magma of this composition begins to crystallize at a temperature of 1200°C, inferring that the estimated liquidus temperature is correct.

The compositions of the chilled margins of the Koillismaa Intrusion and the weighted average of the Porttivaara block profile are presented in Table 7.1. The model composition resembles that of the chilled margins in terms of its SiO<sub>2</sub> and TiO<sub>2</sub> contents, but is more similar to the weighted average in terms of its FeO<sup>TOT</sup> contents. The Al<sub>2</sub>O<sub>3</sub> and MgO contents of the model composition are between those of the chilled margins and the weighted average.

Fractional crystallization of the compositions of the lower chilled margin sample 259-TTK-00 (column 1 in Table 7.1) and the

weighted average (column 7 in Table 7.1) were modelled with the COMAGMAT assuming the same conditions as described above (oxygen buffer of QFM+1 and pressure of 0.5 Kbar). The crystallization sequences of these compositions using COMAGMAT are shown in Fig. 10.2.

According to the COMAGMAT, fractional crystallization of a melt of the composition of the lower chilled margin produces a crystallization sequence similar to that in the Koillismaa Intrusion. Olivine is the first phase to crystallize with a liquidus temperature of 1245 °C. At 1212 °C and after only 2 % crystallization plagioclase appears on the liquidus. Olivine and plagioclase crystallize together until orthopyroxene appears on the liquidus and replaces olivine at a temperature of 1174 °C. Clinopyroxene begins to crystallize at 1155 °C,

Table 10.2. Compositions of trapped liquid defined near 1200 °C for the Koillismaa Intrusion cumulates by means of geochemical thermometry.

Sample	1	2	3	4	5	6	Average of 1-6
T °C	1197 °C	1201 °C	1200 °C	1200 °C	1201 °C	1200 °C	1200 °C
SiO <sub>2</sub>	51.87	51.34	53.82	54.69	53.70	52.54	52.99±0.52
TiO <sub>2</sub>	0.23	0.25	0.44	0.31	0.38	0.34	0.32±0.03
Al <sub>2</sub> O <sub>3</sub>	17.35	16.77	16.43	16.61	17.35	17.53	17.01±0.19
FeO <sup>TOT</sup>	10.94	10.93	7.52	8.20	9.22	11.13	9.66±0.64
MnO	0.19	0.16	0.14	0.16	0.16	0.17	0.16±0.01
MgO	8.08	8.16	7.62	7.77	7.78	8.11	7.92±0.09
CaO	9.76	10.32	10.36	9.68	8.96	8.73	9.64±0.28
Na <sub>2</sub> O	1.03	1.21	2.96	2.25	1.97	1.06	1.75±0.32
K <sub>2</sub> O	0.53	0.83	0.65	0.29	0.41	0.35	0.51±0.08
P <sub>2</sub> O <sub>5</sub>	0.03	0.03	0.05	0.04	0.08	0.05	0.05±0.01

Compositions are presented on the basis of normalization to 100 wt. % on a volatile-free basis.

The error in the average given as the standard error of mean (s/√n).

1 = 16-TTK-01, olivine gabbro-norite/poCb\*a\*, LZa (lowermost unit).

2 = 23-TTK-01, olivine gabbro-norite/poCb\*a\*, LZa (lowermost unit).

3 = 17.1-TTK-00, gabbro-norite/pbCa\*, LZa (middlemost unit).

4 = KOIL112/3, gabbro-norite/pbCa\*, LZa (middlemost unit).

5 = KOIL112/21, gabbro-norite/pbCa\*, LZa (middlemost unit).

6 = 24-TTK-01, olivine gabbro-norite/pboCa\*, LZa (uppermost unit).

and soon thereafter, at 1127 °C, magnetite appears on the liquidus and orthopyroxene crystallization diminishes. Magnetite is the last phase to crystallize together with augite and plagioclase. The modelled crystallization was calculated to end at a temperature of 921 °C with a F. % value of 13. (Fig. 10.2.A).

The modelled crystallization sequence of the weighted average composition begins with crystallization of plagioclase at the temperature of 1253 °C. After 13 % crystallization, olivine appears on the liquidus at a temperature of 1193 °C. At 1150 °C, olivine is replaced by orthopyroxene and magnetite. At 1131 °C clinopyroxene appears on the liquidus. Plagioclase, magnetite and clinopyroxene are the last phases to crystallize. The modelled solidus temperature produced by a melt composition of the weighted average is 995 °C at a F. % value of 12. (Fig. 10.2.B).

Using the composition of the lower chilled margin, COMAGMAT predicts a crystallization sequence similar to that observed in the Koillismaa Intrusion: ol+plag → plag+opx → plag+opx+cpx → plag+cpx+magn. In this respect, the chilled margin composition appears to be a better candidate for the parental magma than the weighted average.

COMAGMAT predicts similar liquidus temperatures of ortho- and clinopyroxene for both the lower chilled margin and the weighted average compositions as obtained by pyroxene thermometry described in Chapter 9.1. The liquidus temperatures for both the compositions of the lower chilled margin and the weighted average are 40–50 °C higher than that obtained by geochemical thermometry. The possible reason for this may be the small amount of cotectic phases (olivine and plagioclase) suspended in the parental magma.

For a liquid representing the lower chilled margin composition and assuming redox conditions between QFM+0 and QFM+2, 2.5 Kbar can be taken as the maximum pressure of crystallization. This is because at pressures higher than 2.5 Kbar, the crystallization sequence predicted by COMAGMAT diverges significantly from that of the Koillismaa Intrusion. The precipitation of spinel group phases in the lower part of the LS (see Chapter 6.2.1) indicates that already at an early stage the partial pressure of oxygen in the Koillismaa magma was similar or slightly more oxidizing than conditions indicated by the QFM buffer in T- $fO_2$  space.

### 10.3 Summary

The COMAGMAT computer program was used to determine the composition of the Koillismaa Intrusion parental magma and its crystallization sequence. The model magma

has a similar crystallization sequence as the lower chilled margin of the intrusion, indicating that it represents a suitable approximation of the parental magma of the intrusion.

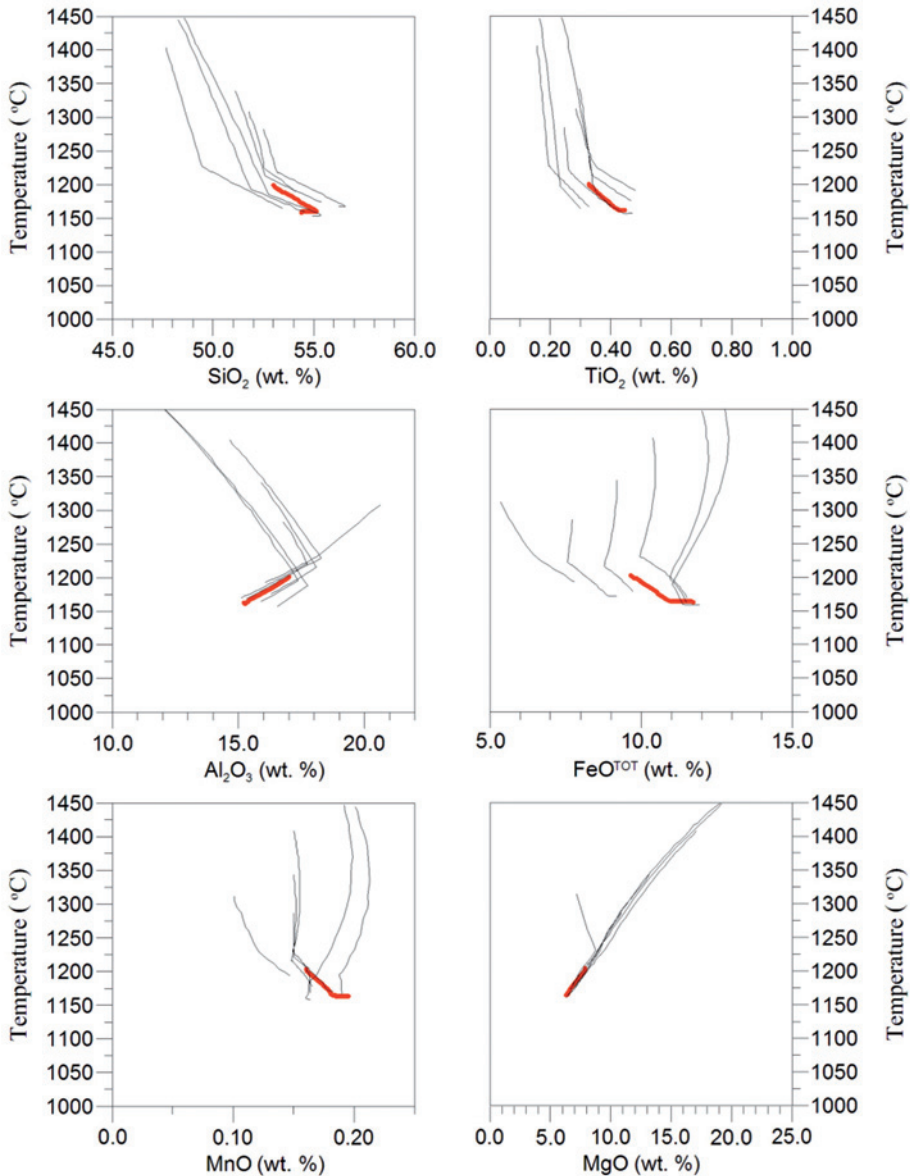


Fig. 10.1. Liquid lines of descent of  $\text{SiO}_2$ ,  $\text{TiO}_2$ ,  $\text{Al}_2\text{O}_3$ ,  $\text{FeO}^{\text{TOT}}$ ,  $\text{MnO}$  and  $\text{MgO}$  during equilibrium crystallization simulated for the cumulus-textured rocks of the LZa of the Koillismaa Intrusion. The rock compositions used in the simulation are given in table 10.1. The thick red line shows the liquid line of descent of the model composition given in the last column of Table 10.2. Simulations were conducted with the COMAGMAT program, assuming anhydrous magma at 0.5 Kbar and oxygen buffer QFM+1 log units.

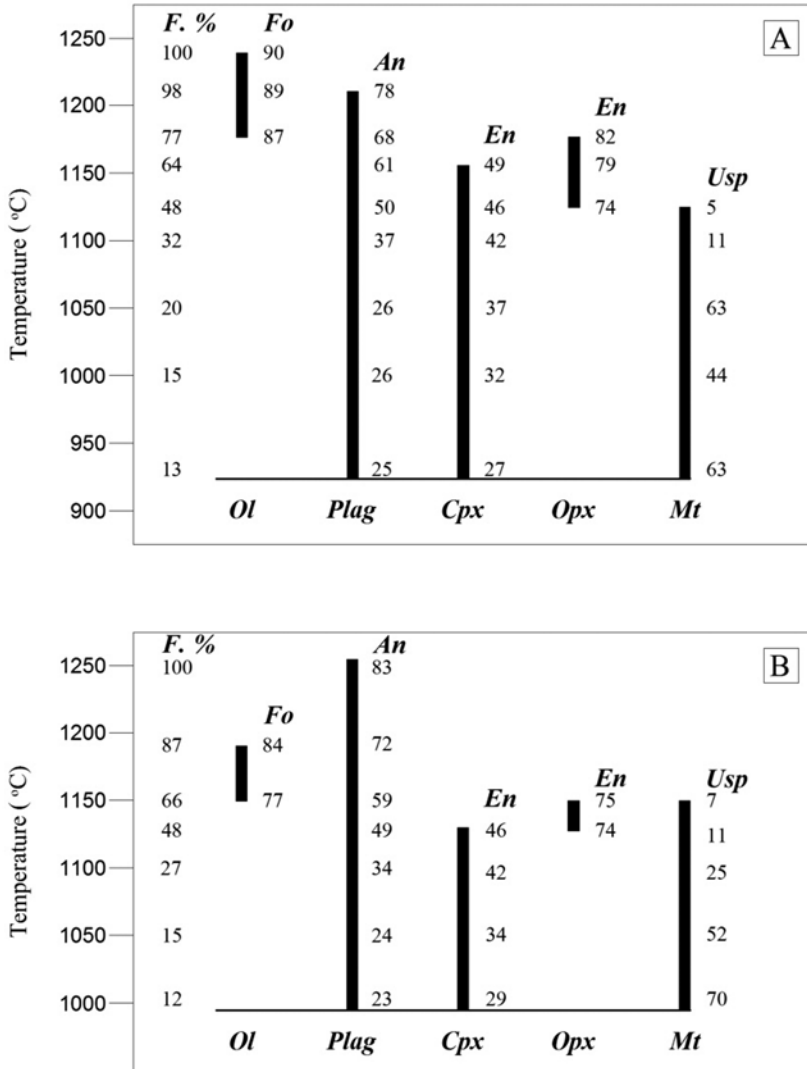


Fig. 10.2. Mineral crystallization sequences produced by fractional crystallization of the lower chilled margin (A) and the weighted average of the Porttivaara block of the Koillismaa Intrusion (B). Simulations were conducted with the COMAGMAT program, assuming anhydrous magma at 0.5 Kbar and oxygen buffer QFM+1 log units. Abbreviations: *F. %* = Fractionation index, *Fo* = forsterite content, *An* = Anorthite content, *En* = Enstatite content, *Usp* = ulvöspinel content, *Ol* = olivine, *Plag* = plagioclase, *Cpx* = clinopyroxene, *Opx* = orthopyroxene, *Mt* = Magnetite.

## 11 DISCUSSION AND CONCLUSIONS

### 11.1 Differentiation in the Koillismaa Intrusion

Alapieti (1982) was the first to note that the lower portion of the Koillismaa Intrusion shows only subdued chemical fractionation. He attributed the feature to periodic replenishing and magma mixing and went on to argue that the magma chamber had been filled prior to complete consolidation of the lower part of it. He designated this period the Integration Stage of the Koillismaa Intrusion in accordance with the terminology of Wager & Brown (1967).

The Integration Stage of the Koillismaa Intrusion correlates to the stratigraphic sequence below the Rometölväs Reef. These rocks include at least two distinct compositional reversals which may be interpreted to reflect replenishments of the chamber with primitive magma. The lower reversal is located in the LZb, ca. 500 m above the base of the intrusion where clinopyroxene becomes more magnesian and plagioclase more calcic (Figs 6.6 and 6.12). The upper reversal is located in the MZa, which is an olivine-rich subzone 620–670 m above the base of the intrusion. This subzone contains Cr-poor pyroxene and plagioclase that show almost as primitive compositions as the rocks in the lowermost parts of the intrusion, and it overlies LZb which is mostly lacking olivine.

The level of the RT Reef marks a significant change in *e.g.* Cr, Ni and MgO content of the cumulates. Therefore, the rocks above the RT Reef are interpreted to have formed from relatively differentiated residual magma in the chamber. It is likely that the more evolved and therefore lighter magma convected upwards

due to the crystallization in the lower part of the magma chamber that became replenished by a denser undifferentiated parental magma.

In the middle part of the UZ (Fig. 6.12: between 1600 and 1900 m in the stratigraphy of the Porttivaara block), the plagioclase grains show reverse trend to what would be expected in cumulate layers produced by fractional crystallization. Above this level, the plagioclase grains show relatively uniform compositions being distinctly An-richer than the grains in the lower part of the subzone. The magnetite gabbro (UZb), which is located below the UZc, hosts the most evolved, *i.e.* the most Ab-rich plagioclase grains. This compositional variation in plagioclase indicates that the UZc crystallized prior to the magnetite gabbro, either by roof crystallization or by plagioclase flotation. This is in accordance with the idea of Juopperi (1977) who concluded from the fragments of anorthosite in the upper part of the magnetite gabbro that at time of its crystallization, the UZb was already overlain by cumulates that underwent episodes of collapse. Therefore, the magnetite gabbro is interpreted to be the sandwich layer of the Koillismaa Intrusion.

The COMAGMAT modelling shows that the chilled margin is a better candidate for the parental magma of the Koillismaa Intrusion than the weighted average. The compositions of the chilled margins can be attributed to the Cr-poor parental magma type suggested to the Fennoscandian early Palaeoproterozoic layered intrusions (Lahtinen *et al.* 1989; Hanski *et al.* 2001b; Alapieti & Lahtinen 2002).

## 11.2 Noncumulus-textured bodies of the Koillismaa Intrusion

### 11.2.1 Review of the origin of noncumulus-textured igneous rocks

Noncumulus-textured igneous rocks are traditionally viewed as products of a rapid increase in the degree of supersaturation caused by a sudden change in physicochemical conditions (composition, T, P) of the magma.

The margins of magma chambers are the most suitable places for the development of noncumulus textures, because at these sites, the magma may quench against cooler country rocks. Supercooling has been proposed to explain noncumulus textures in intraplutonic zones, layers or bodies (Berg 1980; Chapman & Rhodes 1992; Tegner et al. 1993; Wiebe & Snyder 1993; Tegner & Wilson 1995), but in many of these cases the textures can alternatively be attributed to degassing or devolatilization (Grokhovskaya et al. 1992; Barkov et al. 1995; Semenov et al. 1998, 2000; Kazanov & Zaytseva 1999; Glebovitsky et al. 2001; Latypov & Chistyakova 2001; Kazanov et al. 2005; Latypov et al. 2008a, b) *i.e.* a sudden reduction in volatile pressure of a magma causing an increase in liquidus and solidus temperatures.

Textures and minerals identical to those of noncumulus-textured igneous rocks are also characteristic of hornfels. For instance, in the Fongen-Hyllingen Complex, Norway, the raft-like, fine-grained and granoblastic mafic bodies that can be more than 100 m thick and nearly 1500 m long have been interpreted to represent country rock inclusions (Wilson & Larsen 1985; Habekost & Wilson 1989; Wilson & Sørensen 1996). A similar model has been proposed by Matthes & Schubert (1971) for the “beerbachites” of the Odenwald area in Germany, which are fine- to medium-grained mafic bodies within gabbroic intrusions. Dokuchaeva & Yakovlev (1994) and Dedeev et al. (2002) reported numerous plagi-

oclase-hypersthene (and spinel-cordierite-hypersthene) hornfels fragments in the sulphide- and PGE-enriched “Critical Horizon” of the Monchegorsk Pluton. They suggested that the fragments represent assimilated xenoliths from the host gneisses. A purely sedimentary source for fragments showing textures and minerals similar to those of noncumulus-textured igneous rocks has been proposed for the granular and banded xenoliths of the Skjækerdal Intrusion in Norway (Carstens 1958).

### 11.2.2 The origin of noncumulus-textured bodies of the Koillismaa Intrusion

There are two main mechanisms to produce noncumulus-textured igneous rocks: (1) rapid supersaturation of magma and (2) thermally induced recrystallization. Furthermore, these rocks can also be subdivided based on whether they are internally and externally derived with respect to their host intrusion. The various models are schematically shown in Fig. 11.1.

Hypotheses A-C consider the bodies as small intrusions of supersaturated magma. Under these circumstances, the bodies can be products of interstitial liquid of the cumulates (Fig. 11.1.A), of residual magma derived from the supernatant liquid column and intruded into partially consolidated cumulates (Fig. 11.1.B) or of magma derived from a different magma chamber (Fig. 11.1.C). Alternatively, the noncumulus-textured bodies could represent metamorphosed mafic fragments, derived either from within the intrusion (in which case they are autholiths, Fig. 11.1.D) or from the country rocks (in which case they are xenoliths, Fig. 11.1.E).

The most important argument against a co-genetic source of the noncumulus-textured bodies and the Koillismaa Intrusion are their

different compositions. The pyroxene compositions of noncumulus-textured bodies are different from those in chilled margins and cumulus-textured rocks (Fig. 6.8). By their major and trace element compositions the noncumulus-textured bodies are usually different being more primitive than most of the cumulates and the chilled margins of the Koillismaa Intrusion (compare  $[\text{TiO}_2]$  vs.  $[\text{Al}_2\text{O}_3]$  diagrams and ternary  $\text{Al}_2\text{O}_3$ - $10\text{TiO}_2$ - $100\text{Cr}$  plots of Figs 7.2 and 7.8, TAS and AFM diagrams and Jensen's cation plots of Figs 7.1 and 7.5,  $\text{FeO}^{\text{TOT}}/\text{Al}_2\text{O}_3$  vs. MgO diagrams of Figs 7.6 and 7.13, Mg-number vs. Ni diagrams of Figs 7.7 and 7.14, Ch-normalized patterns of Figs 7.3 and 7.9, and PM-normalized patterns of Figs 7.4 and 7.10).

This leaves two models to consider, *i.e.* the bodies could represent the crystallized products of externally derived magmas intruding into the cumulates of the Koillismaa Intrusion (Fig. 11.1.C) or they could be mafic xenoliths (Fig. 11.1.E). Of these alternatives the former one is the more plausible to explain the origin of the noncumulus-textured bodies, because:

1) The Sm-Nd isotope compositions of the variably altered, mottled-textured rocks of the Rometölväs Reef do not indicate *in situ* contamination during the crystallization of the Koillismaa Intrusion. If the noncumulate bodies were fragments derived from country rock, *i.e.* from the Lotanvaara unit, then it is likely that a great amount of fragments would be derived from the Archaean basement, which represents the most typical country rock of Koillismaa Intrusion area. In this case, the basement fragments could have assimilated into the magma to become vague remnants represented by the altered cumulates of the reef. This would be marked in the Sm-Nd isotope compositions of the reef cumulates, because in the Archaean basement the  $\epsilon_{\text{Nd}}(2440 \text{ Ma})$  differ significantly from the correspond-

ing values determined from the rocks of the intrusion. (Fig. 8.1).

2) The inward-directed chemical trend in the noncumulate body studied in detail is similar to the compositional variation in intrusive bodies (*cf.* Jaupart & Tait 1995). In the body, the whole-rock compositions show increase in incompatible elements ( $\text{TiO}_2$ ,  $\text{K}_2\text{O}$ ,  $\text{P}_2\text{O}_5$ , Zr and Y) from the margins to the middle of the upper third of the body, where the rock contains sulphide-rich pockets (Fig. 7.11). This trend is also consistent with the chemical variation of loiveringite grains in the body, since the most Fe-rich grains are located closest to the areas of the most incompatible element-rich whole-rock compositions of the body (Fig. 6.19). Also, the compositional variation in plagioclase grains of the body reflects differentiation, in that the most sodic plagioclases occur in the centre of the body, associated with the sulphide-rich pockets.

The textural and compositional similarities of the noncumulate bodies and the Lotanvaara mafic rock unit suggest that these rocks represent the same magma where the Lotanvaara unit represents the most primitive end, whilst the noncumulate bodies found in the Pirivaara block represent the most evolved end-members of this magma (compare textures shown in photomicrographs of Figs 5.3B and 5.9B, pyroxene compositions shown in Figs 6.1 and 6.8, whole-rock compositions shown in Figs 7.5, 7.6, 7.7, 7.8, 7.9 and 7.10).

3) The gradation from the quenched margins to the poikilitic center of the noncumulus-textured body studied in detail (Fig. 5.10) can be explained by crystal nucleation and growth in a small intrusion or dyke where the margins represent the places of the most intense supersaturation. This is illustrated in Fig. 11.2, which schematically shows the textural development of a rock in response to variable growth and nucleation rates of two phases.

### MECHANISM

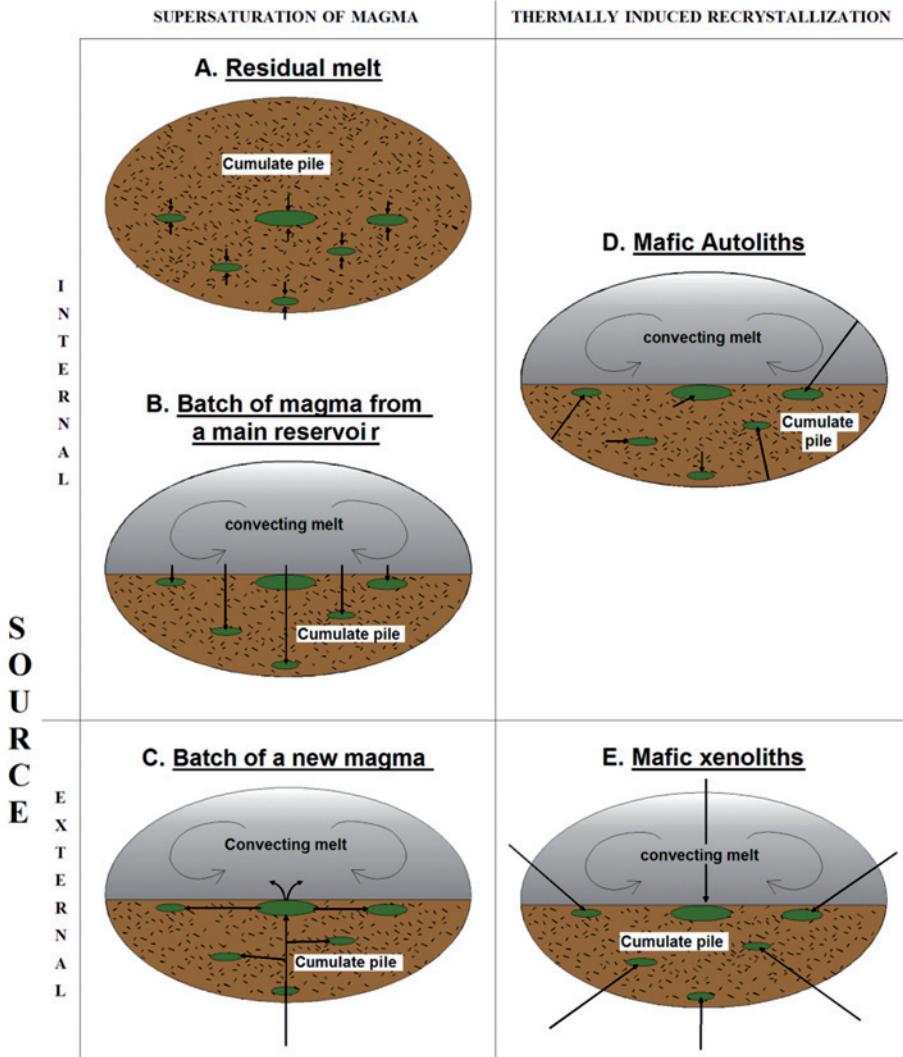


Fig. 11.1. Sketch diagram summarizing hypotheses for the origin of noncumulus-textured bodies in the Koillismaa Intrusion. Process-based and source-based models may be distinguished. A, B and C assume magma supersaturation where the source of the magma can be the interstitial liquid of the cumulates (A), residual magma from the main reservoir (B) or new magma (C). D and E assume that the bodies are chilled autoliths (D) or xenoliths (E).

According to Campbell (1987), nucleation and growth of crystals in silicate melt are contemporaneous processes under most conditions, and when shown as function of supersaturation, their rates have bell-shaped curves as illustrated schematically for two phases in Fig. 11.2.A. Importantly, the maximum rate in the growth of a phase occurs at a lower degree of supersaturation than its maximum nucleation rate. Furthermore, before nucleation of a phase can begin, the system has to be slightly supersaturated, which is indicated by  $\delta T$  in the figure. Thus, there is a window where only crystal growth is possible, but on the other hand, crystals cannot grow unless they first nucleate.

Kirkpatrick (1983) has shown that plagioclase requires larger degrees of supersaturation to nucleate than pyroxene, olivine and spinel. In addition, experimental studies have shown that the polymerization of crystals and melts control growth and nucleation rates. For instance, Kirkpatrick et al. (1979) has demonstrated with quenching experiments of several synthetic plagioclase compositions that the growth rates of plagioclases increase with increasing An content. Therefore, in addition to the degree of supersaturation, the liquidus phase equilibria play significant role in the development of rock textures.

- If the degree of supersaturation is high enough, such as in case 1 of Fig. 11.2, there will be no crystal nucleation and growth, and as a consequence, the liquid will be quenched to glass. In the noncumulate body studied in detail, this texture

is found at the margins of the body, which in Fig. 5.10 is referred to as Quenched area.

- At a lower supersaturation level, as represented by case 2 of Fig. 11.2, the nucleation rate of the red phase is at maximum, but the conditions do not allow the crystals to grow much as indicated by the growth rate function of the phase. At this level of supersaturation, a new phase, the grey one, begins to nucleate.
- At a still lower degree of supersaturation, as shown by case 3 of Fig. 11.2, the maximum growth rate of the red phase is reached. The grey phase shows its maximum nucleation rate, but has a limited capacity to grow as indicated by the growth rate function of it.
- At the lowest degree of supersaturation, as shown in case 4 of Fig. 11.2, the red phase does not nucleate and thus undergoes limited growth cannot really grow it there are no nuclei. In contrast, the grey phase grows at its maximum rate, but there are few nuclei. This texture is found in the central parts of the body and is referred to as Spotted or Megacyclic area in Fig. 5.10.

Figure 11.2 provides also an explanation as to why in the Lotanvaara rocks and the noncumulate bodies the chadacrysts located close to the edges of oikocrysts are relatively large and why a phase can simultaneously occur both as chadacrystic and within the matrix of oikocrysts.

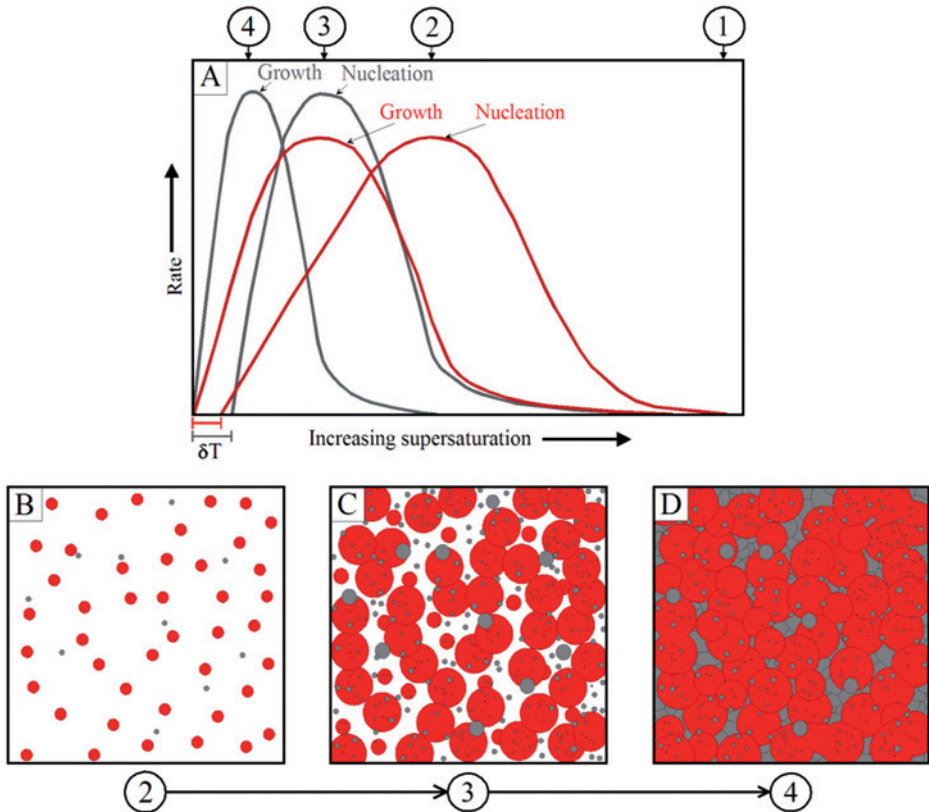


Fig. 11.2. Schematic diagram illustrating the variation in nucleation and growth rates of two phases (red and grey) as a function of supersaturation (A, modified from Kirkpatrick et al. 1979, Brandeis et al. 1984 and Campbell 1987). Cartoons B-D explain the formation of poikilitic texture in relation to various nucleation and growth rates (compare D to photomicrographs of Figs 5.11, 5.12 and 5.13. In text, the red coloured phase is referred to as red phase and grey coloured to as grey phase).

### 11.3 Genetic aspects on the Rometölväs Reef

PGE reefs tend to be located at stratigraphic discontinuities that record major petrological changes in layered intrusions. Such changes can be marked by reversals in crystallization sequences indicated by mineral and whole-rock compositions or compositional difference between the rocks and minerals below and above the reef. This is well illustrated by such well-known reefs as the Merensky Reef, UG-2, J-M Reef and the SJ-, AP- and PV-Reefs of the Penikat Intrusion and the SK Reef in the Portimo Complex in Finland (Alapieti & Lahtinen 2002; Cawthorn et al. 2002;

Zientek et al. 2002; Naldrett 2004; Iljina & Hanski 2005).

The RT Reef of the Koillismaa Intrusion is equally situated at such a compositional break within its host intrusion, defined by the appearance of clinopyroxene and inverted pigeonite and the disappearance of primary orthopyroxene. The cumulates that are located below the reef are enriched in MgO, Cl, Cr and Ni relatively to those above it. (Figs 7.12, 7.13 and 7.14). The rocks located below and above the reef show distinct compositional trends in terms of  $FeO^{TOT}/Al_2O_3$  ratio at a

given MgO content (Fig. 7.13). Apatites from below the reef show higher Cl/(Cl+F) values than those located above the reef (Fig. 6.22).

These observations could indicate that the mineralization of the RT Reef formed in response to mixing of compositionally contrasting magmas, as has been proposed for other reef type deposits (Campbell et al. 1983). For example, the magma chamber could have been replenished by relatively differentiated magma, and the mixing between differentiated and primitive magma triggered sulphide saturation.

The Koillismaa Intrusion contains several stratigraphic discontinuities and compositional reversals, but PGE mineralization occurs only associated with one of these reversals, namely the RT Reef. Therefore, in view of orthomagmatic model, the boundary between MZb and MZc is not the most plausible place of a reef as there are even more distinct indications of magma replenishments in the stratigraphy below the RT Reef (see Chapter 11.1).

A further feature of the RT Reef that has been observed in other reefs elsewhere is that the most metal-rich rocks are typically highly altered. The PGE grade correlates positively with the degree of hydrothermal alteration; the ore components are concentrated in motles of hydrous phases, indicating that these "secondary" phases are related to mineralizing rather than to any postmagmatic events (Figs 5.14 and 7.19).

Lauder (1970) suggested that the upward percolating ore-bearing fluids trapped by an impervious layer could explain the stratigraphic break in the Cl content of apatite and whole-rocks. In the Stillwater and Bushveld Complexes the PGE mineralized reefs equally mark a transition in the composition of apatite from Cl-rich to more F-rich. Boudreau & McCallum (1989) used this as an evidence supporting hydrothermal origin of the reefs and attributed the compositional variation of apatite to fluid migration. Accordingly, the noncumulate bodies could represent impermeable fluid traps,

which would account for the occurrence of mottled textured and ore-enriched cumulates mainly below the bodies. The ore components could have been derived from the Marginal Series. This model could explain the elevated Cu/Ni ratios of the RT Reef in comparison to the Marginal Series, but one would also expect to see an enrichment in Pt and Pd relative to the Os, Ir and Ru in the reef, which is not observed. In addition, if the PGE were derived from upward migrating fluids one would expect some variation in chalcophile element contents and ratios along the strike of the reef because the reef is located at various stratigraphic height above the base of the intrusion. Regarding the variations in the apatite composition, one could argue that they reflect an elevated proportion of intercumulus melt, (the Cl-rich cumulates below the RT Reef are typically orthocumulates). Cawthorn (1994) showed that equilibration of apatite grains with intercumulus melt could explain the variations in the apatite composition with stratigraphic height. This process is analogous to that in which cumulus minerals become more Fe-rich on cooling and react with the interstitial melt.

However, the RT Reef shows some important differences to other PGE reefs, namely the close association of the mineralization with noncumulus-textured bodies. This association is unlikely to be coincidental. The reef is the stratigraphically uppermost level in the Koillismaa Intrusion where the noncumulus-textured bodies have been found. The bodies associated with the reef horizon show a relatively larger size and are more abundant than the bodies at lower stratigraphic levels in the intrusion. Furthermore, those bodies associated with the reef horizon are the only ones that include sulphides or are associated with sulphide-mineralized cumulates. These observations have to be taken into account when proposing a genetic model for the origin of the RT Reef.

In the present work it is argued that the ore components in the RT Reef are sourced from

the magma that formed the noncumulus-textured bodies. The body that was studied in detail contains a sulphide-rich area containing ca. 1 ppm Au+Pd+Pt, whilst in the surrounding mottled-textured cumulates the concentrations are typically lower, less than 250 ppm Au+Pd+Pt (Figs 7.11 and 7.16). The sulphides are located in pocket-like segregations which differ by their texture and mineralogy from the surrounding sulphide-poor areas of the body. The pockets have coarser grain sizes, contain different phases (amphibole, chlorite, talc, quartz, orthoclase and Cl-rich apatite) and mineral morphologies (non-oikocrystic pyroxenes) than in their surroundings. Isohanni (1976) concluded that the pockets represent melts derived from the partially crystallized cumulates surrounding the noncumulate bodies. However, it is demonstrated by this research that this cannot be the case. The segregations are genetically related to the noncumulate body, because their pyroxene and plagioclase compositions resemble more closely the compositions elsewhere in the body than in the surrounding cumulates. For example, in the pockets and elsewhere in the body, the Mg-number in the bronzites and augites is always higher than 70 and 75, respectively, whilst in the surrounding Koillismaa Intrusion cumulates bronzites have Mg-numbers < 70 and augites < 75 (Figs 6.2 and 6.3). The sulphide-rich pockets are located in the most incompatible element-enriched portion of the body (Figs 5.10 and 7.11), suggesting that they represent segregations of residual liquid produced by differentiation in the noncumulate body.

If a magma intrudes into hot cumulates, it would be expected that the crystallization rate of the new injection is relatively slow. This would favour the development of cumulus rather than noncumulus texture. Therefore, it is likely that there was some other process than supercooling that evoked rapid crystallization in the bodies. It is suggested here that the magma that formed the noncumulus-textured

bodies was volatile-rich and underwent degassing during ascent and upon intrusion and related depressurization, consistent with the occurrence of vesicle-like bronzite segregations including hydrous phases (Figs 5.9.C and D).

It is proposed that degassing-induced crystallization responsible for the textures of the noncumulate bodies also led to the migration of PGE-rich fluids into the surrounding cumulates. This would explain the very close spatial relationship of the chalcophile element-enriched cumulates and the noncumulate bodies. It is noteworthy that the ore-rich cumulates of the RT Reef are located mainly below the noncumulate bodies (Figs 5.15, 5.16, 5.17, 7.15 and 7.16). This can also be explained degassing: due to sudden loss of volatiles the fluid phase enriched in ore components would have escaped into the surrounding cumulates, after which the bodies acted as impervious traps for these metal-enriched fluids percolating upwards.

The Lotanvaara mafic unit represents the most primitive end and the noncumulate bodies of the Pirivaara block represent the most evolved end of the same magma. Since the Lotanvaara mafic rock unit is situated proximal and the bodies of the Pirivaara block are located distal to the connecting gravity anomaly, it is probable that the anomaly represents - in addition to the magma of the Koillismaa Intrusion - the feeder channel for the magma of the Lotanvaara unit and the noncumulate bodies.

It is argued that the magma that formed the noncumulate bodies intruded laterally along the layering in the partially consolidated magma chamber of the Koillismaa Intrusion. During the injection of this magma, the upper part of the crystalline sequence of the magma chamber of the Koillismaa Intrusion was semi-consolidated. This area would have served as a rheologically suitable place for the magma of the noncumulate bodies with the least competent rocks in the cumulate pile of

the magma chamber of Koillismaa Intrusion. This explains the voluminous distribution of the bodies in the stratigraphic level of the RT Reef.

It is notable that among the noncumulus-textured bodies which are located in the Layered Series of the Koillismaa Intrusion, only those that are located in the RT Reef are associated with chalcophile element-enrichment. If the magma from which the noncumulate bodies crystallized was the source of the ore components, all bodies should be associ-

ated with PGE mineralization. As mentioned, the occurrence of vesicle-like bronzite segregations including hydrous phases (Figs 5.9.C and D) indicates that the magma of the noncumulate bodies was already fluid-saturated during injection. Therefore, it is possible that the fluids were already separated to the upper part of the magma prior or during the injection to form the noncumulate bodies. This would explain the absence of mineralization in noncumulate bodies located below the RT Reef.

#### 11.4 Genetic model of the Rometölväs Reef

The genetic model for the Rometölväs Reef proposed here attributes the magma of the noncumulate bodies as the source of the ore-components, whereas the cumulates of the Koillismaa Intrusion merely control the location of the bodies. The development of the mineralization is illustrated in Figs 11.3, 4, 5 and 6.

Phase 1) The magma of the Koillismaa Intrusion was emplaced between the supracrustal rocks and the Archaean basement gneiss. The connecting zone represents the feeder conduit, presently located at the eastern side of the intrusion. (Fig. 11.3).

Phase 2) During the crystallization of the LZ the magma chamber is periodically replenished, and the final dimension of the Koillismaa Intrusion is reached. The upper portion of the cumulate pile is semi-consolidated. The granophyre formed in response to heating of the acid volcanic roof rocks by the heat of the convecting and crystallizing magma. The plagioclase grains belong to the upper part of the UZc in the stratigraphy of the intrusion. (Fig. 11.4).

Phase 3) New primitive and volatile-bearing magma injects to form the rocks of the Lotanvaara unit and the noncumulus-textured bodies in the partially crystallized magma cham-

ber of the Koillismaa Intrusion (Fig. 11.5). This new magma is under high fluid pressure and most of the fluids are concentrated in the upper part of its injection. Decompression-induced abrupt loss of volatiles causes the magma to become rapidly supersaturated and distribute the volatiles rich in ore components to the surrounding cumulates which are altered. In the larger bodies, a portion of the volatiles remain inside the rapidly crystallizing bodies resulting in some PGE enrichment in the centre of these bodies. Fluids expelled from the bodies are subsequently trapped below the bodies.

Phase 4) After the formation of the Rometölväs Reef, the Koillismaa Intrusion continues to crystallize. The magnetite gabbro (UZb) represents one of the most differentiated residual liquid to crystallize. During the crystallization of the magnetite gabbro, some fragments collapse to it from the overlying anorthosite. (Fig. 11.6).

The proposed genetic model of the Rometölväs Reef can be applied in PGE exploration in the Koillismaa Intrusion and also in other mafic-ultramafic layered intrusions. According to the model the noncumulate bodies play a critical role as the source of PGE.

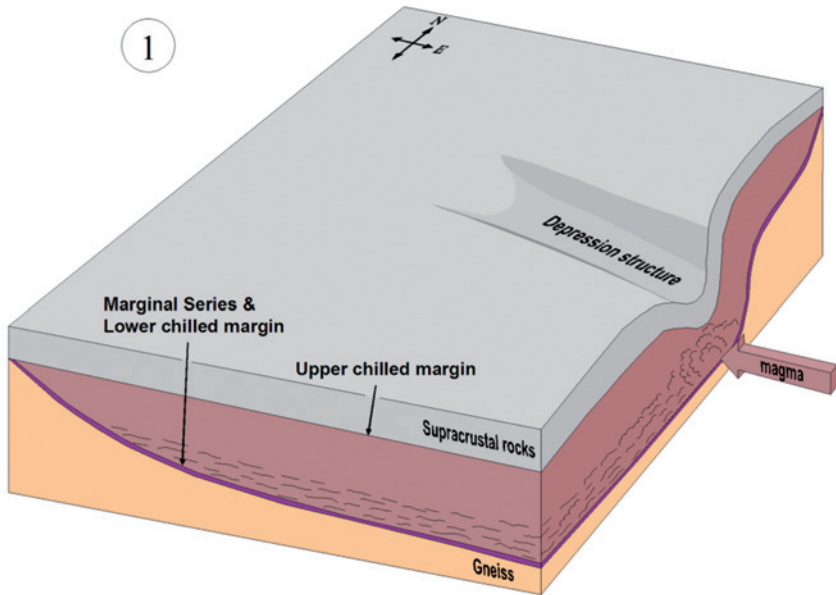


Fig. 11.3. Generalized diagrammatic sketch illustrating the cross sections of the sheet-like magma chamber of the Koillismaa Intrusion located in between the supracrustal rocks and the Archaean basement gneiss. The area in the chamber marked by wavy lines indicates the magma currents during periodic replenishments.

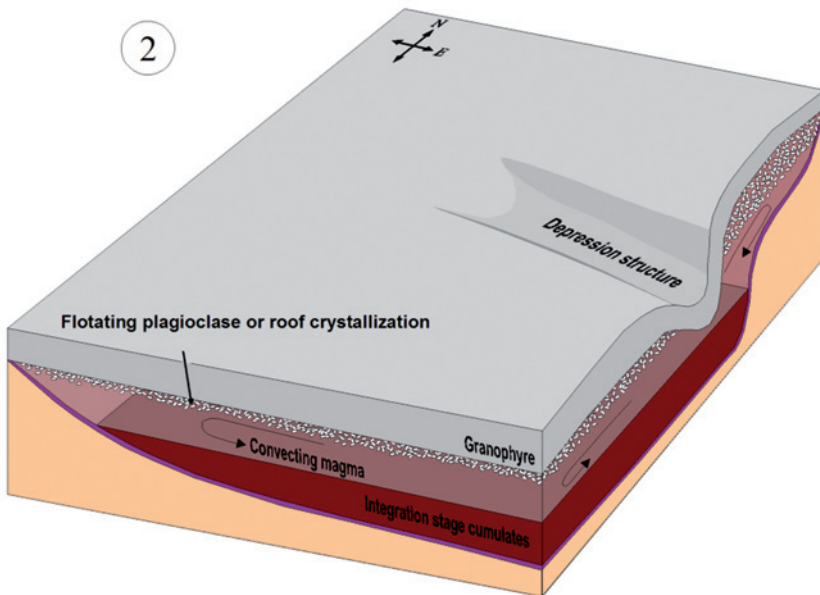


Fig. 11.4. Generalized diagrammatic sketch illustrating the cross sections of the Koillismaa Intrusion during the stage when the lower part of the magma chamber was consolidated and the upper part of the chamber contained floating grains of plagioclase.

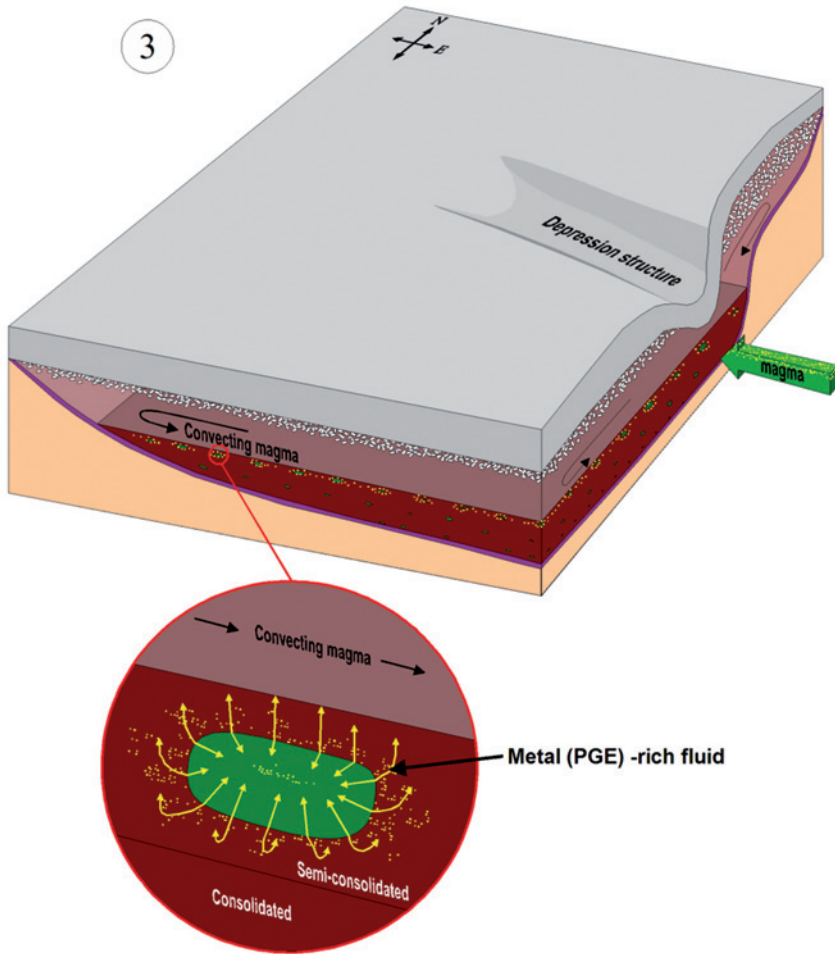


Fig. 11.5. Generalized diagrammatic sketch illustrating the cross sections of the Koillismaa Intrusion where the magma of noncumulate bodies injects to the semi-consolidated magma chamber of the Koillismaa Intrusion. This new magma introduces chalcophile elements to form the mineralization during rapid supersaturation caused by decompression induced abrupt loss of volatiles.

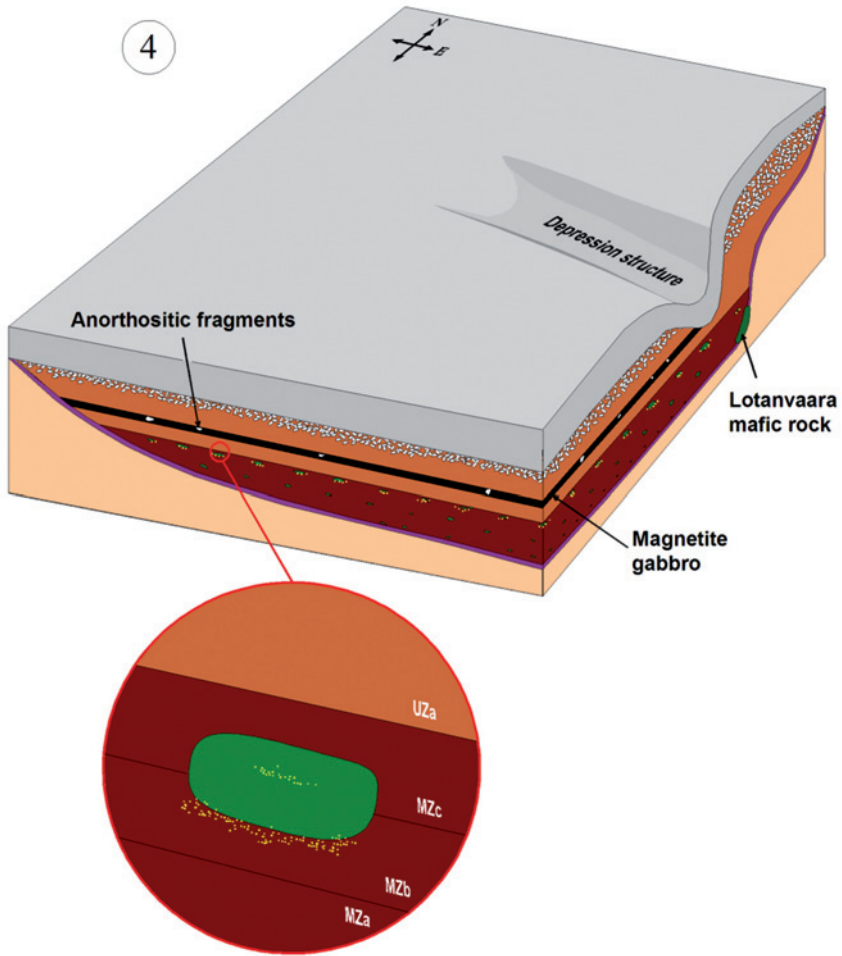


Fig. 11.6. Generalized diagrammatic sketch illustrating the cross sections of the Koillismaa Intrusion with the location of the Rometölväs Reef and the noncumulate bodies.

## 12 ACKNOWLEDGEMENTS

On 6<sup>th</sup> August 2007, Prof. Tuomo Alapieti died suddenly at the age of 60. The study of layered intrusions and associated ore deposits had been his primary geological interest for about 30 years. He suggested the topic of the present thesis and it is largely due to his enthusiasm and critical guidance that the thesis was completed.

After the death of Prof. Alapieti my work was supervised by Prof. Seppo Gehör and Dr. Rais Latypov to whom I wish to express my sincerest gratitude for their effort. The suggestions and contributions of Dr. Tapio Halkoaho and Dr. Hannu Makkonen, the official reviewers of the manuscript, are acknowledged with sincere gratitude. I am also very thankful to Dr. Markku Iljina for being a great team leader during my time in the Geological Survey of Finland's (GTK) project in the Koillismaa area. Prof. Wolfgang Maier, who proof-checked the English and made considerable amount of very usefull comments, is acknowledged with special mention. Further, I wish to sincerely acknowledge Prof. Eero Hanski for his interest in my work. Without the aforementioned persons this book would not be in your hands!

I have greatly benefited from help, reviews and stimulating discussions with many colleagues and friends including Jan Akkerman, Dr. Alexei Ariskin, Dr. Pasi Eilu, Dr. Pentti Hölttä, Dr. Aarre Juopperi, Oleg Kazanov, Asko Kontinen, Dr. Esko Korhikoski, Dr. Aulis Kärki, Markus Kyläkoski, Prof. Emeritus Kauko Laajoki, Jarmo Lahtinen, Dr. Pertti Lamberg, Dr. Laura Lauri, Dr. Vesa Nykänen, Risto Pietilä, Heikki Salmirinne, Dr. Pertti Sarala, Dr. Peter Sorjonen-Ward, Dr. Pekka Tuisku, Dr. Tuomo Törmänen and Dr. Jouni Vuollo. I would also like to express my appreciation to Jukka Konnunaho for many constructive comments on the work. I am pleased to thank Dr. Risto Kaukonen for helping with

the noble metal phase identifications. Special thanks to Dr. Tapani Mutanen for advising me to search loveringite.

Special thanks are also due to Erkki Eijärvi, Sari Forss, Riitta Kontio, Taimi Nousiainen, Larissa Tuomisto from the Department of Geosciences and Johanna Rautio from the Department of Chemistry at the University of Oulu for the high quality whole-rock analyses and thin sections. Elvi Hiltula, Päivi Huhtala, Jouko Paaso, Raija Peura, Seppo Sivonen and Olli Taikina-aho are thanked for help and guidance with the equipment in the Institute of Electron Optics of the University of Oulu. Many thanks also go to Kai Hietala and Dr. Jussi Liipo of the Outotec Research Oy, Pori, for conducting high quality electron microprobe analyses of loveringite.

For advices during the isotope analytical work and data interpretation I am greatly indebted to Dr. Hannu Huhma, Dr. Irmeli Mänttari and Tuula Hokkanen of the GTK's Southern Finland Office, Espoo. I also warmly thank Pentti Kouri for collecting pure mineral fractions for isotope analyses, using the electric pulse disaggregator at the GTK's Northern Finland Office, Rovaniemi. I wish to thank Dr. Sergei Sergeev for the Sm-Nd isotopic results of the Centre for Isotopic Research at the A. P. Karpinsky All Russian Geological Research Institute (VSEGEI), St. Petersburg. In addition, I wish to express my gratitude to Dr. Arto Karinen, not only because of brotherhood, but also for assisting with the statistical error estimation of the data.

The layout of this thesis was made by Päivi Kuikka-Niemi and Tiina Vaahtera to whom I wish to express special thanks for excellent work.

This work would not have been possible without the generous financial assistance provided by the Outokumpu Foundation, the K. H. Renlund Foundation, the Tauno Tönning

Foundation, the Foundation for Research of Natural Resources in Finland, the Finnish Graduate School of Geology and the Faculty of Science of the University of Oulu. I also wish to acknowledge the Geological Survey of Finland for providing data and material for the thesis.

I wish to thank my parents, Tuulikki and Matti Karinen, and my sister, Saila Karinen,

for their interest in my work and their always positive attitude.

Finally – and not least – I wish to express my warmest gratitude to my wife Tarja, my children Aapo, Unna, Vikke and Minni and Elsa-dog for patience and love during my research work.

### 13 REFERENCES

- Airo, M.-L. 1999.** Aeromagnetic and petrophysical investigations applied to tectonic analysis in the northern Fennoscandian shield. Geological Survey of Finland, Report of Investigation 145. 51 p.
- Alapieti, T., Hugg, R. & Piirainen, T. 1979.** Structure, mineralogy and chemistry of the Syöte section in the Early Proterozoic Koillismaa layered intrusion, northeastern Finland. Geological Survey of Finland, Bulletin 299. 43 p.
- Alapieti, T. 1982.** The Koillismaa layered igneous complex, Finland - its structure, mineralogy and geochemistry, with emphasis on the distribution of chromium. Geological Survey of Finland, Bulletin 319. 116 p.
- Alapieti, T. & Piirainen, T. 1984.** Cu-Ni-PGE mineralization in the marginal series of the Early Proterozoic Koillismaa layered igneous complex, northeastern Finland. In: Buchanan, D. L. & Jones, M. J. (eds) Sulphide Deposits in Mafic and Ultramafic Rocks. London: The Institution of Mining and Metallurgy, 123–131.
- Alapieti, T. T. & Lahtinen, J. J. 1986.** Stratigraphy, Petrology and Platinum-Group Element Mineralization of the Early Proterozoic Penikat Layered Intrusion, Northern Finland. Economic Geology 81, 1126–1136.
- Alapieti, T. T., Lahtinen, J. J., Huhma, H., Hänninen, E., Piirainen, T. A. & Sivonen, S. J. 1989.** Platinum-group element bearing Cu-Ni mineralization in the marginal series of the early Proterozoic Suhanko-Konttijärvi layered intrusion, northern Finland. In: Prendergast, M. D. & Jones, M. J. (eds) Magmatic sulphides – Zimbabwe Volume. London: The Institution of Mining and Metallurgy, 177–187.
- Alapieti, T. T., Filén, B. A., Lahtinen, J. J., Lavrov, M. M., Smolkin, V. F. & Voitshekovsky, S. N. 1990.** Early Proterozoic Layered Intrusions in the Northeastern Part of the Fennoscandian Shield. Mineralogy and Petrology 42, 1–22.
- Alapieti, T. T. & Lahtinen, J. J. 2002.** Platinum-Group Element Mineralization in the Layered Intrusions of Northern Finland and the Kola Peninsula, Russia. In: Cabri, L. J. (ed.) The Geology, Geochemistry, Mineralogy and Mineral Beneficiation of Platinum-Group Elements. Canadian Institute of Mining, Metallurgy and Petroleum, Special Volume 54, 507–546.
- Amelin, Yu. V. & Semenov, V. S. 1990.** On the age and sources of magmas of Early Proterozoic layered intrusions of Karelia. The Isotopic Dating of the Endogenic Ore formations. Kiev, 40–42. (in Russian)
- Amelin, Y. V., Heaman, L. M. & Semenov, V. S. 1995.** U-Pb geochronology of layered mafic intrusions in the eastern Baltic Shield: implications for the timing and duration of Paleoproterozoic continental rifting. Precambrian Research 75, 31–46.
- Amelin, Yu. V. & Semenov, V. S. 1996.** Nd and Sr isotopic geochemistry of mafic layered intrusions in the eastern Baltic shield: implications for the evolution of Paleoproterozoic continental mafic magmas. Contributions to Mineralogy and Petrology 124, 255–272.
- Andersen, D. J. & Lindsley, D. H. 1985.** New (and Final!) Models for the Ti-magnetite/Ilmenite Geothermometer and Oxygen Barometer. In: AGU 1985 Spring Meeting EOS, Transaction, American Geophysical Union, p. 416.
- Anderson, A. T. 1968.** The oxygen fugacity of alkaline basalt and related magmas, Tristan da Cunha. American Journal of Sciences 266, 704–727.
- Ariskin, A. A. 1999.** Phase equilibria modeling in igneous petrology: use of COMAGMAT model for

- simulating fractionation of ferro-basaltic magmas and genesis of high-alumina basalt. *Journal of Volcanology and Geothermal Research* 90, 115–162.
- Ariskin, B. B. & Barmina, G. S. 2004.** COMAGMAT: Development of a Magma Crystallization Model and Its Petrological Applications. *Geochemistry International* 42, (Suppl. 1). 157 p.
- Atkins, F. B. 1969.** Pyroxenes of the Bushveld Intrusion, South Africa. *Journal of Petrology* 10, 222–249.
- Bailey, S. W. 1984.** Classification and structures of the micas. In: Bailey, S. W. (ed.) *Micas*. Mineralogical Society of America, *Reviews in Mineralogy* 13, 1–12.
- Bakushkin, Ye. M., Zhuavlev, D. Z., Bayanova, T. B. & Balashov, Yu. A. 1990.** Mountain Generalskaya. In: Mitrofanov, F. P. & Balashov, Yu. A. (eds) *Geochronology and genesis of layered basic intrusions, volcanites and granite-gneisses of the Kola Peninsula*. The U.S.S.R Academy of Sciences, Kola Science Centre, 14–15.
- Balagansky, V. V., Kudryashov, N. M., Balashov, Yu. A., Apanasevich, E. A., Gannibal, L. F. & Levkovich, N. V. 1997.** The age of the Zhemchuznyi drusite massif, Northwestern White Sea area: U-Pb isotope data and geological implication. *Geochimiya* 2, 158–168. (in Russian)
- Balagansky, V. V., Timmerman, M. J., Kislitsyn, R. V., Daly, J. S., Balashov, Yu. A., Gannibal, L. F., Sherstennikova, O. G. & Ryungen, G. I. 1998.** Isotopic age of rocks from the Kolvitsa Belt and the Umba block (the south-eastern extension of the Lapland Granulite Belt), Kola Peninsula. *Proceedings of the Murmansk State Technical University* 3, 19–32. (in Russian)
- Balagansky, V. V., Timmerman, M. J., Kozlova, N. Ye. & Kislitsyn, R. V. 2001.** A 2.44 Ga syn-tectonic mafic dyke swarm in the Kolvitsa Belt, Kola Peninsula, Russia: implications for early Palaeoproterozoic tectonics in the north-eastern Fennoscandian Shield. *Precambrian Research* 105, 269–287.
- Balashov, Yu. A., Bayanova, T. B. & Mitrofanov, F. P. 1990a.** Sources of layered intrusions. In: Mitrofanov, F. P. & Balashov, Yu. A. (eds) *Geochronology and genesis of layered basic intrusions, volcanites and granite-gneisses of the Kola Peninsula*. The U.S.S.R Academy of Sciences, Kola Science Centre, 24–30.
- Balashov, Yu. A., Bayanova, T. B., Amelin, Yu. V., Gannibal, L. F., Zhangurov, A. A., Koshcheev, O. A., Ryungenen, G. I., Fedotov, Zh. A., Sharkov, I. V. & Sherstennikova, O. G. 1990b.** Imandra lopolith. In: Mitrofanov, F. P. & Balashov, Yu. A. (eds) *Geochronology and genesis of layered basic intrusions, volcanites and granite-gneisses of the Kola Peninsula*. The U.S.S.R Academy of Sciences, Kola Science Centre, 10–14.
- Balashov, Yu. A., Bayanova, T. B. & Mitrofanov, F. P. 1993.** Isotope data on the age and genesis of the layered basic-ultrabasic intrusions in the Kola Peninsula and northern Karelia, northeastern Baltic Shield. *Precambrian Research* 64, 197–205.
- Ballhaus, C. G. & Stumpfl, E. F. 1986.** Sulfide and platinum mineralization in the Merensky Reef: evidence from hydrous silicates and fluid inclusions. *Contributions to Mineralogy and Petrology* 94, 193–204.
- Ballhaus, C. G., Cornelius, M. & Stumpfl, E. F. 1988.** The Upper Critical Zone of the Bushveld Complex and the Origin of Merensky-type Ores – A Discussion. *Economic Geology* 83, 1082–1091.
- Barkov, A. Y. 1991.** A U-Pb dating of zircons from the Kivakka layered intrusion, North Karelia. In: *All-Union Seminar, St Petersburg*, 21–23. (in Russian) Referred by Glebovitsky, V. A., Semenov, V. S. & Belyatsky, B. V. 2001. The Structure of the Lukkulaivaara intrusions, Oulanka Group, northern Karelia: Petrological implications. *Canadian Mineralogist* 39, 607–637.
- Barkov, A. Y. 1992.** Aspects of Petrology and Geochemistry of the Lukkulaivaara and Kivakka Layered Intrusions, northern Karelia. Ph. D. thesis, Russian Academy of Sciences, IGEM, Moscow, Russia. (in Russian) Referred by Barkov, A. Y., Martin, R. F., Tarkian, M., Poirier, G. & Thibault, Y. 2001. Pd-Ag tellurides from a Cl-rich environment in the Lukkulaivaara layered intrusion, northern Russian Karelia. *Canadian Mineralogist* 39, 639–653.
- Barkov, A. Y., Pakhomovskii, Y. A., Trofimov, N. N. & Lavrov, M. M. 1994.** Loveringite, a first occurrence in Russia, from the Burakovsky layered intrusion, Karelia. *Neues Jahrbuch für Mineralogie* 3, 101–111.
- Barkov, A. Yu., Savchenko, Ye. E. & Zhangurov, A. A. 1995.** Fluid migration and its role in the formation of platinum-group minerals: evidence from the Imandrovsky and Lukkulaivaara layered intrusions, Russia. *Mineralogy and Petrology* 54, 249–260.
- Barkov, A. Y., Savchenko, Y. E., Men'shikov, Y. P. & Barkova, L. P. 1996.** Loveringite from the Last-Yavr mafic-ultramafic intrusion, Kola Peninsula; a second occurrence in Russia. *Norsk Geologisk Tidsskrift* 76, 115–120.
- Barnes, S.-J., Boyd, R., Korneliussen, A., Nilsson, L.-P., Often, M., Pedersen, R. B. & Robins, B. 1988.** The use of mantle normalization and metal ratios in discriminating between the effects of par-

- tial melting, crystal fractionation and sulphide segregation on platinum group element, gold, nickel and copper: Examples from Norway. In: Prichard, H. M., Potts, P. J., Bowles, J. F. W. & Cribb, S. J. (eds) *Geo-platinum '87 symposium*. London: Elsevier Applied Science, 113–143.
- Barnes, S.-J., Zientek, M. L. & Severson, M. J. 1997.** Ni, Cu, Au, and platinum-group element contents of sulphides associated with intraplate magmatism: a synthesis. *Canadian Journal of Earth Sciences* 34, 337–351.
- Barnes, S.-J. & Maier, W. D. 1999.** The fractionation of Ni, Cu and the noble metals in silicate and sulfide liquids. In: Keays, R. R., Leshner, C. M., Lightfoot, P. C. & Farrow, C. E. G. (eds) *Magmatic Ore Deposits and their application in mineral exploration*. Geological Association of Canada, Short Course Volume 13, 69–106.
- Barnes, S.-J. & Maier, W. D. 2002.** Platinum-Group Element Distributions in the Rustenburg Layered Suite of the Bushveld Complex, South Africa. In: Cabri, L. J. (ed.) *The Geology, Geochemistry, Mineralogy and Mineral Beneficiation of Platinum-Group Elements*. Canadian Institute of Mining, Metallurgy and Petroleum, Special Volume 54, 431–458.
- Barnes, S. J. & Naldrett, A. J. 1985.** Geochemistry of the J-M (Howland) Reef of the Stillwater Complex, Minneapolis Adit Area. I. Sulfide Chemistry and Sulfide-Olivine Equilibrium. *Economic Geology* 80, 627–645.
- Barrie, C. T., MacTavish, A. D., Walford, P. C., Chataway, R. & Middaugh, R. 2002.** Contact-type and Magnetite Reef-type Pd-Cu Mineralization in Ferroan olivine Gabbros of the Coldwell Complex, Ontario. In: Cabri, L. J. (ed.) *The Geology, Geochemistry, Mineralogy and Mineral Beneficiation of Platinum-Group Elements*. Canadian Institute of Mining, Metallurgy and Petroleum, Special Volume 54, 321–337.
- Barth, T. F. W. 1955.** Presentation of rock analyses. *The Journal of Geology* 63, 348–363.
- Barth, T. F. W. 1962.** *Theoretical Petrology*. Second Edition. New York - London – Sydney: Wiley and Sons. 416 p.
- Bayanova, T. B. & Smolkin, V. F. 1996.** U-Pb isotopic study of the layered intrusions of the northern Pechenga area, Kola Peninsula. IGCP project 336 symposium in Rovaniemi, Finland, August 21-23, 1996. Program and abstracts. University of Turku, Division of geology and mineralogy 33, p. 49.
- Bayanova, T. B. & Mitrofanov, F. P. 2005.** Layered Proterozoic PGE intrusions in Kola region: new isotope data. In: Törmänen, T. O. & Alapieti, T. T. (eds) *10th International Platinum Symposium*, August 8-11, 2005, Oulu. Extended abstracts. Geological Survey of Finland, 289–291.
- Bayliss, P. 1987.** Mineral nomenclature: scapolite. *Mineralogical Magazine* 51, p. 176.
- Berg, J. H. 1980.** Snowflake troctolite in the Hetasch Intrusions, Labrador: Evidence for Magma-Mixing and Supercooling in a Plutonic Environment. *Contributions to Mineralogy and Petrology* 72, 339–351.
- Bogdanova, S. V. & Bibikova, E. V. 1993.** The "Saamian" of the Belomorian Mobile Belt: new geo-chronological constraints. *Precambrian Research* 64, 131–152.
- Boudreau, A. E. & McCallum, I. S. 1986.** Investigations of the Stillwater Complex: III. The Picket Pin Pt/Pd Deposit. *Economic Geology* 81, 1953–1975.
- Boudreau, A. E., Mathez, E. A. & McCallum, I. S. 1986.** Halogen Geochemistry of the Stillwater and Bushveld Complexes: Evidence for Transport of the Platinum-Group Elements by Cl-Rich Fluids. *Journal Of Petrology* 27, 967–986.
- Boudreau, A. E. 1988.** Investigations of the Stillwater Complex. IV. The role of volatiles in the petrogenesis of the J-M Reef, Minneapolis Adit Section. *Canadian Mineralogist* 26, 193–208.
- Boudreau, A. E. & McCallum, I. S. 1989.** Investigations of the Stillwater Complex: Part V. Apatites as indicators of evolving fluid composition. *Contributions to Mineralogy and Petrology* 102, 138–153.
- Boudreau, A. E. & McCallum, I. S. 1992.** Concentrations of Platinum-Group Elements by Magmatic Fluids in Layered Intrusions. *Economic Geology* 87, 1830–1848.
- Bowen, N. L. 1928.** *The Evolution of the Igneous Rocks*. Princeton: Princeton University Press. 332 p. (1956 reprint)
- Bowles, J. F. W. 1977.** A method of tracing the temperature and oxygen-fugacity histories of complex magnetite-ilmenite grains. *Mineralogical Magazine* 136, 103–109.
- Bowles, J. F. W. 1988.** Definition and range of composition of naturally occurring minerals with the pseudobrookite structure. *American Mineralogist* 73, 1377–1383.
- Brandeis, G., Jaupart, C. & Allègre, C. J. 1984.** Nucleation, crystal growth, and thermal regime of cooling magma. *Journal of Geophysical Research* 89, 10161–10177.
- Brandeis, G. & Jaupart, C. 1986.** On the interaction between convection and crystallization in cooling magma chambers. *Earth and Planetary Science Letters* 77, 345–361.

- Brooks, C., Hart, S. R. & Wendt, I. 1972.** Realistic Use of Two-Error Regression Treatments as Applied to Rubidium-Strontium Data. *Reviews of Geophysics and Space Physics* 10, 551–577.
- Brown, G. M. 1957.** Pyroxenes from the early and middle stages of fractionation of the Skaergaard intrusion, East Greenland. *Mineralogical Magazine* 31, 511–543.
- Brown, G. M. & Vincent, E. A. 1963.** Pyroxenes from the late stages of fractionation of the Skaergaard intrusive, East Greenland. *Journal of Petrology* 4, 175–197.
- Buddington, A. F., Fahey, J. & Vlisidis, A. 1963.** Degree of oxidation of Adirondack iron oxide and iron-titanium oxide minerals in relation to petrogeny. *Journal of Petrology* 4, 138–169.
- Buddington, A. F. & Lindsley, D. H. 1964.** Iron-Titanium Oxide Minerals and Synthetic Equivalents. *Journal of Petrology* 5, 310–357.
- Buiko, A. K., Levchenkov, O. A., Turchenko, S. I. & Drubetskoi, Ye. E. 1995.** Geology and isotopic dating of the early Proterozoic Sumian-Sariolan Complex in northern Karelia (Paanajärvi-Tsipringa structure). *Stratigraphy, Geological Correlation* 3, 16–30. (in Russian)
- Cabella, R., Gazzotti, M. & Lucchetti, G. 1997.** Loveringite and baddeleyite in layers of chromian spinel from the Bracco Ophiolitic unit, Northern Apennines, Italy. *Canadian Mineralogist* 35, 899–908.
- Cameron, E. N. 1978.** An unusual titanium-rich oxide mineral from the Eastern Bushveld Complex. *American Mineralogist* 63, 37–39.
- Campbell, I. H. & Borley, G. D. 1974.** The geochemistry of Pyroxenes from the Lower Layered Series of the Jimberlana Intrusion, Western Australia. *Contributions to Mineralogy and Petrology* 47, 281–297.
- Campbell, I. H. & Kelly, P. R. 1978.** The geochemistry of loveringite, a uranium-rare-earth-bearing accessory phase from the Jimberlana Intrusion of Western Australia. *Mineralogical Magazine* 42, 187–193.
- Campbell, I. H., Naldrett, A. J. & Barnes, S. J. 1983.** A Model for the Origin of the Platinum-Rich Sulfide Horizons in the Bushveld and Stillwater Complexes. *Journal Of Petrology* 24, 133–165.
- Campbell, I. H. 1987.** Distribution of orthocumulate textures in the Jimberlana intrusion. *Journal of Geology* 95, 35–54.
- Carmichael, I. S. E. 1967.** The Iron-Titanium Oxides of Salic Volcanic Rocks and their Associated Ferromagnesian Silicates. *Contributions to Mineralogy and Petrology* 14, 36–64.
- Carstens, H. 1958.** Layered basic xenoliths in some Norwegian gabbros. *Beiträge zur Mineralogie und Petrographie* 6, 139–146.
- Cawthorn, R. G. 1994.** Formation of chlor- and fluor-apatite in layered intrusions. *Mineralogical Magazine* 58, 299–306.
- Cawthorn, R. G., Merkle, R. K. W. & Viljoen, M. J. 2002.** Platinum-Group Element Deposits in the Bushveld Complex, South Africa. In: Cabri, L. J. (ed.) *The Geology, Geochemistry, Mineralogy and Mineral Beneficiation of Platinum-Group Elements*. Canadian Institute of Mining, Metallurgy and Petroleum, Special Volume 54, 389–429.
- Chai, G. & Naldrett, A. J. 1992a.** The Jinchuan Ultramafic Intrusion: Cumulate of a High-Mg Basaltic Magma. *Journal of Petrology* 33, 277–303.
- Chai, G. & Naldrett, A. J. 1992b.** PGE mineralization of the Jinchuan Ni-Cu sulfide deposit, NW China. *Economic Geology* 87, 1475–1495.
- Chapman, M. & Rhodes, J. M. 1992.** Composite layering in the Isle au Hait Igneous Complex, Maine: evidence for periodic invasion of a mafic magma into an evolving magma reservoir. *Journal of Volcanology and Geothermal Research* 51, 41–60.
- Chayes, F. & Métais, D. 1964.** On relation between suites of CIPW and Barth-Niggli Norms. *Carnegie Institution, Annual Report of the Director of the Geophysical Laboratory 1963-1964*, 193–195.
- Chistyakov, A. V., Sharkov, E. V., Grokhovskaya, T. L., Bogatikov, O. A., Muravitskaya, G. N. & Grinevich, N. G. 2002.** Petrology of the Europe-Largest Burakovka early Paeoproterozoic layered pluton (Southern Karelia, Russia). *Russian Journal of Earth Sciences* 4, 35–75.
- Collerson, K. D. & Sheraton, J. W. 1986.** Age and Geochemical Characteristics of a Mafic Dyke Swarm in the Archaean Vestfold Block, Antarctica: Inferences about Proterozoic Dyke Emplacement in Gondwana. *Journal of Petrology* 27, 853–886.
- Compston, W. & Arriens, P. A. 1968.** The Precambrian geochronology of Australia. *Canadian Journal of Earth Sciences* 5, 561–583.
- Crocket, J. H., Teruta, Y. & Garth, J. 1976.** The Relative Importance of Sulfides, Spinel, and Platinoïd Minerals as Carriers of Pt, Pd, Ir, and Au in the Merensky Reef at Western Platinum Limited, near Marikana, South Africa. *Economic Geology* 71, 1308–1323.
- Cross, W., Iddings, J. P., Pirsson, L. V. & Washington, H. S. 1902.** A quantitative chemico-mineralogical classification and nomenclature of igneous rocks. *Journal of Geology* 10, 555–690.
- Dedeev, A. V., Khashkovskaya, T. N. & Galkin, A. S. 2002.** PGE Mineralization of the Monchegorsk Layered Mafic-Ultramafic intrusion of the Kola

- Peninsula. In: Cabri, L. J. (ed.) *The Geology, Geochemistry, Mineralogy and Mineral Beneficiation of Platinium-Group Elements*. Canadian Institute of Mining, Metallurgy and Petroleum, Special Volume 54, 569–577.
- Deer, W. A., Howie, R. A. & Zussman, J. 1995.** *An Introduction to the Rock-Forming Minerals*. Second Edition. Harlow: Longman Group Limited. 696 p.
- DePaolo, D. J. & Wasserburg, G. J. 1976.** Nd isotopic variations and petrogenetic models. *Geophysical Research Letters* 3, 249–252.
- DePaolo, D. J. 1981.** Neodymium isotopes in the Colorado Front Range and crust-mantle evolution in the Proterozoic. *Nature* 291, 193–196.
- Dokuchaeva, V. S., Razhev, S. A., Ryungenen, G. I., Gannibal, L. F., Zhuravlev, D. S., Koshcheev, O. A., Balashov, Yu. A. & Bayanova, T. B. 1990.** Fyodorov-Panski intrusive. In: Mitrofanov, F. P. & Balashov, Yu. A. (eds) *Geochronology and genesis of layered basic intrusions, volcanites and granite-gneisses of the Kola Peninsula*. The U.S.S.R Academy of Sciences, Kola Science Centre, 4–10.
- Dokuchaeva, V. S. & Yakovlev, Yu. N. 1994.** Monchegorsk Pluton. In: Mitrofanov, F. & Torokhov, M. (eds) *7th International Platinum Symposium, July 27-31, 1994, Apatity, Russia. Guide to the pre-symposium field trip*. Geological Institute KSC RAS, 71–104.
- Donaldson, C. H. 1974.** Olivine Crystal Types in Harrisitic Rocks of the Rhum Pluton and in Archean Spinifex Rocks. *Geological Society of America, Bulletin* 85, 1721–1726.
- Droop, G. T. R. 1987.** A general equation for estimating  $Fe^{3+}$  concentrations in ferromagnesian silicates and oxides from microprobe analyses, using stoichiometric criteria. *Mineralogical Magazine* 51, 431–435.
- Enkovaara, A., Härme, M. & Väyrynen, H. 1953.** Oulu-Tornio. General Geological Map of Finland 1:400 000, Explanation to the Map of Rocks, Sheets C5-B5. Geological Survey of Finland. 153 p.
- Emeleus, C. G. 1987.** The Rhum Layered Complex, Inner Hebrides, Scotland. In: Parsons, I. (ed.) *Origins of Igneous Layering*. NATO ASI Series C 196, D. Reidel Publishing Company, 263–286.
- Emeleus, C. H., Cheadle, M. J., Hunter, R. H., Upton, B. G. J. & Wadsworth, W. J. 1996.** The Rum Layered Suite. In: Cawthorn, R. G. (ed.) *Layered Intrusions*. Amsterdam-Lausanne-New York-Oxford-Shannon-Tokyo: Elsevier Science, 403–440.
- Fenner, C. N. 1929.** The crystallization of basalts. *American Journal of Sciences* 18, 225–253.
- Frenkel, M. Ya., Ariskin, A. A., Barmina, G. S., Korina, M. I. & Koptev-Dvornikov, Ye. V. 1988.** Geochemical thermometry of magmatic rocks – principles and examples. *Geochemistry International* 25, 35–50.
- Frisch, T., Jackson, G. D., Glebovitsky, V. A., Yefimov, M. M., Bogdanova, M. N. & Parrish, R. R. 1995.** U-Pb geochronology of zircon from the Kolvitsa gabbro-anorthosite complex, southern Kola Peninsula, Russia. *Petrologiya* 3, 248–254. (in Russian)
- Gammons, C. H., Bloom, M. S. & Yu, Y. 1992.** Experimental investigation of the hydrothermal geochemistry of platinum and palladium: I. Solubility of platinum and palladium sulfide minerals in  $NaCl/H_2SO_4$  solutions at 300 °C. *Geochimica et Cosmochimica Acta* 56, 3881–3894.
- Gatehouse, B. M., Grey, I. E., Campbell, I. H. & Kelly, P. 1978.** The crystal structure of loveringite - a new member of the crichtonite group. *American Mineralogist* 63, 28–36.
- Glebovitsky, V. G., Semenov, V. S., Belyatsky, B. V., Koptev-Dvornikov, E. G., Pchelintseva, N. F. & Kireev, B. S. 2001.** The structure of the Lukkulaisvaara intrusion, Oulanka group, Northern Karelia: Petrological implications. *Canadian Mineralogist* 39, 607–637.
- Glikson, A. Y. 1996.** Mega-impacts and mantle-melting episodes: tests for possible correlations. *AGSO Journal of Australian Geology and Geophysics* 16, 587–607.
- Grokhovskaya, T. L., Distler, V. V., Klyunin, S. F., Zakharov, A. A. & Laputina, I. P. 1992.** Low-sulfide platinum group mineralization of the Lukkulaisvaara pluton, northern Karelia. *International Geology Review* 34, 503–520.
- Grout, F. F. 1918.** Two-phase convection in igneous magmas. *Journal of Geology* 26, 481–499.
- Habekost, E. M. & Wilson, J. R. 1989.** Raft-like Metabasaltic Inclusions in the Fongen-Hyllingen Layered Intrusive Complex, Norway, and their Implications for Magma Chamber Evolution. *Journal of Petrology* 30, 1415–1441.
- Halkoaho, T. A. A., Alapieti, T. T. & Lahtinen, J. J. 1989a.** The Sompujärvi PGE Mineralization in the Penikat Layered Intrusion, Northern Finland. In: Alapieti, T. T. (ed.) *5th International Platinum Symposium, August 4-11, 1989, Espoo, Finland. Guide to the post-symposium field trip*. Geological Survey of Finland, Guide 29, 71–92.
- Halkoaho, T. A. A., Alapieti, T. T. & Lahtinen, J. J. 1989a.** The Ala-Penikka PGE Mineralization in the Penikat Layered Intrusion, Northern Finland. In: Alapieti, T. T. (ed.) *5th International Platinum Symposium, August 4-11, 1989, Espoo, Finland. Guide to the post-symposium field trip*. Geological Survey of Finland, Guide 29, 93–122.

- Halkoaho, T. A. A., Alapieti, T. T. & Lahtinen, J. J. 1990a.** The Sompujärvi PGE Reef in the Penikat Layered Intrusion, Northern Finland. *Mineralogy and Petrology* 42, 39–55.
- Halkoaho, T. A. A., Alapieti, T. T. & Lahtinen, J. J. 1990b.** The Ala-Penikka PGE Reefs in the Penikat Layered Intrusion, Northern Finland. *Mineralogy and Petrology* 42, 23–38.
- Halkoaho, T. 1993.** The Sompujärvi and Ala-Penikka PGE Reefs in the Penikat Layered Intrusion, Northern Finland: implications for PGE reef-forming processes. *University of Oulu, Acta Universitatis Ouluensis A* 249, 122 p.
- Halkoaho, T., Alapieti, T. & Huhtelin, T. 2005.** The Sompujärvi, Ala-Penikka and Paasivaara PGE reefs in the Penikat layered intrusion, Northeastern Finland. In: Alapieti, T. T. & Kaukonen, R. J. (eds) 10th International Platinum Symposium, August 8–11, 2005, Oulu. Field trip guidebook. Geological Survey of Finland, Guide 51a, 33–76.
- Halls, H. C., Kumar, A., Srinivasan, R. & Hamilton, M. A. 2007.** Paleomagnetism and U-Pb geochronology of easterly trending dykes in the Dharwar craton, India: feldspar clouding, radiating dyke swarms and the position of India at 2.37 Ga. *Precambrian Research* 155, 47–68.
- Hamlyn, P. R., Keays, R. R., Cameron, W. E., Crawford, A. J. & Waldron, H. M. 1985.** Precious metals in magnesian low-Ti lavas: Implications for metallogenesis and sulfur saturation in primary magmas. *Geochimica et Cosmochimica Acta* 49, 1797–1811.
- Hamlyn, P. R. & Keays, R. R. 1986.** Sulfur Saturation and Second-Stage Melts: Application to the Bushveld Platinum Metal Deposits. *Economic Geology* 81, 1431–1445.
- Hanley, J. J., Mungall, J. E., Pettke, T., Spooner, E. T. C. & Bray, C. J. 2005.** Fluid and Halide Melt Inclusions of Magmatic Origin in the Ultramafic and Lower Banded Series, Stillwater Complex, Montana, USA. *Journal of Petrology* 49, 1133–1160.
- Hanski, E., Walker, R. J., Huhma, H. & Suominen, I. 2001a.** The Os and Nd isotopic systematics of c. 2.44 Ga Akanvaara and Koitelainen mafic layered intrusions in northern Finland. *Precambrian Research* 109, 73–102.
- Hanski, E., Huhma, H., Rastas, P. & Kamenetsky, V. S. 2001b.** The Palaeoproterozoic Komatiite-Picrite association of Finnish Lapland. *Journal of Petrology* 42, 855–876.
- Hatton, C. J. 1989.** Densities and liquidus temperatures of Bushveld parental magmas as constraints on the formation of the Merensky Reef in the Bushveld Complex, South Africa. In: Prendergast, M. D. & Jones, M. J. (eds) *Magmatic sulphides - Zimbabwe Volume*. London: The Institution of Mining and Metallurgy, 87–93.
- Heaman, L. M. 1988.** A precise U-Pb zircon age for a Hearst Dyke. Geological Association of Canada, Mineralogical Association of Canada, Canadian Society of Petroleum Geologists, Joint Annual Meeting. Program with abstracts 13, p. A-53.
- Heaman, L. M. & Tarney, J. 1989.** U-Pb baddeleyite ages for the Scourie dyke swarm, Scotland: evidence for two distinct intrusion events. *Nature* 340, 705–708.
- Hess, H. H. 1941.** Pyroxenes of common mafic magmas. Part 2. *The American Mineralogist* 26, 573–594.
- Hess, H. H. 1960.** Stillwater Igneous Complex, Montana, A Quantitative Mineralogical Study. Geological Society of America, Memoir 80, 230 p.
- Himmelberg, G. R. & Ford, A. B. 1977.** Iron-titanium oxides of the Dufek intrusion, Antarctica. *American Mineralogist* 62, 623–633.
- Hinchey, J. G., Hattori, K. H. & Lavigne, M. J. 2005.** Geology, Petrology, and Controls on the PGE Mineralization of the Southern Roby and Twilight Zones, Lac des Iles Mine, Canada. *Economic Geology* 100, 43–61.
- Hoffman, E. L., Naldrett, A. J., Alcock, R. A. & Hancock, R. G. V. 1979.** The noble-metal content of ore in the Levack West and Little Stobie mines, Ontario. *Canadian Mineralogist* 17, 437–451.
- Hoffman, E. L. & Dunn, B. 2002.** Sample Preparation and Bulk Analytical Methods for PGE. In: Cabri, L. J. (ed.) *The Geology, Geochemistry, Mineralogy and Mineral Beneficiation of Platinum-Group Elements*. Canadian Institute of Mining, Metallurgy and Petroleum, Special Volume 54, 1–11.
- Honkamo, M. 1979.** Rytinki. Geological Map of Finland 1:100 000, Pre-Quaternary Rocks, Sheet 3541. Geological Survey of Finland.
- Hoover, J. D. 1989.** The Chilled Marginal Gabbro and Other Contact Rocks of the Skaergaard Intrusion. *Journal of Petrology* 30, 441–476.
- Huhma, H., Cliff, R. A., Perttunen, V. & Sakko, M. 1990.** Sm-Nd and Pb isotopic study of mafic rocks associated with early Proterozoic continental rifting: the Peräpohja schist belt in northern Finland. *Contributions to Mineralogy and Petrology* 104, 369–379.
- Huhma, H., Mutanen, T., Hanski, E., Räsänen, J., Manninen, T., Lehtonen, M., Rastas, P. & Juopperi, H. 1996.** Sm-Nd isotopic evidence for contrasting sources of the prolonged Palaeoproterozoic mafic-ultramafic magmatism in northern Finland. In: IGCP project 336 symposium, August

- 21–23, 1996, Rovaniemi, Finland. Program and abstracts. University of Turku, Division of geology and mineralogy 33, p. 17.
- Huhtelin, T. A., Alapieti, T. T. & Lahtinen, J. J. 1989a.** The Paasivaara PGE mineralization in the Penikat layered intrusion, Northern Finland. In: Alapieti, T. T. (ed.) 5th International Platinum Symposium, August 4–11, 1989, Espoo, Finland. Guide to the post-symposium field trip. Geological Survey of Finland, Guide 29, 123–144.
- Huhtelin, T. A., Lahtinen, J. J., Alapieti, T. T., Korvuo, E. & Sotka, P. 1989b.** The Narkaus intrusion and related PGE and sulphide mineralizations. In: Alapieti, T. T. (ed.) 5th International Platinum Symposium, August 4–11, 1989, Espoo, Finland. Guide to the post-symposium field trip. Geological Survey of Finland, Guide 29, 145–161.
- Huhtelin, T. A., Alapieti, T. T. & Lahtinen, J. J. 1990.** The Paasivaara PGE Reef in the Penikat Layered Intrusion, Northern Finland. *Mineralogy and Petrology* 42, 57–70.
- Huppert, H. E. & Sparks, R. S. J. 1989.** Chilled margins in igneous rocks. *Earth and Planetary Science Letters* 92, 397–405.
- Ikramuddin, M. & Steuber, A. M. 1976.** Rb-Sr ages of Precambrian dolerites and alkaline dikes, southeastern Mysore State, India. *Lithos* 9, 235–241.
- Iljina, M. J., Alapieti, T. T., Lahtinen, J. J. & Lerssi, J. M. 1989.** The Suhanko-Konttijärvi intrusion and related sulphide and PGE mineralizations. In: Alapieti, T. T. (ed.) 5th International Platinum Symposium, August 4–11, 1989, Espoo, Finland. Guide to the post-symposium field trip. Geological Survey of Finland, Guide 29, 163–187.
- Iljina, M. 1994.** The Portimo Layered Igneous Complex, with emphasis on diverse sulphide and platinum-group element deposits. University of Oulu, *Acta Universitatis Ouluensis A* 258. 158 p.
- Iljina, M., Karinen, T. & Räsänen, J. 2001.** The Koillismaa Layered Igneous Complex: general geology, structural development and related sulphide and platinum-group element mineralization. In: Piestrzynski, A. et al. (eds) *Mineral deposits at the beginning of the 21st century. Proceedings of the joint Sixth Biennial SGA-SEG Meeting*, August 26–29, 2001, Kraków, Poland, 653–656.
- Iljina, M. 2004.** Tutkimustyöselostus valtausalueilla Koskiahon 1-2, Kuusi 4-23, Maaselkä 1-14, Murto 1-2 sekä Portti 1-37 Pudasjärven, Taivalkosken ja Posion kunnissa suoritetusta tutkimuksesta vuosina 1996–2002. *Mineral exploration report of relinquished claims of Koskiahon 1-2, Kuusi 4-23, Maaselkä 1-14, Murto 1-2 and Portti 1-37.* Geological Survey of Finland, unpublished report M 06/3543/2004/1/10. 25 p. + 33 appendices. (in Finnish with extended English summary)
- Iljina, M. 2005.** Portimo Layered Igneous Complex. In: Alapieti, T. T. & Kärki, A. J. (eds) 10th International Platinum Symposium, August 8–11, 2005, Oulu. Field trip guidebook. Geological Survey of Finland, Guide 51a, 77–100.
- Iljina, M. & Hanski, E. 2005.** Layered mafic intrusions of the Tornio-Näränkäväära belt. In: Lehtinen, M., Nurmi, P. A. & Rämö, O. T. (eds) *Precambrian Geology of Finland. Key to the Evolution of the Fennoscandian Shield.* Elsevier B. V., Developments in Precambrian Geology 14, 101–137.
- Iljina, M., Heikura, P. & Salmirinne, H. 2005.** The Haukiahon and Kaukua PGE-Cu-Ni-Au prospects in the Koillismaa Layered Igneous Complex, Finland. Geological Survey of Finland, unpublished report M06/3543, 3544/2005/1/10. 20 p. + 3 appendices. (in Finnish with extended English summary)
- Irvine, T. N. & Baragar, W. R. A. 1971.** A Guide to the Chemical Classification of the Common Volcanic Rocks. *Canadian Journal of Earth Sciences* 8, 523–548.
- Irvine, T. N. 1982.** Terminology for Layered Intrusions. *Journal of Petrology* 23, 127–162.
- Irvine, T. N. & Sharpe, M. R. 1982.** Source-rock compositions and depths of origin of Bushveld and Stillwater magmas. *Carnegie Institution of Washington Year Book* 1982, 294–303.
- Irvine, T. N. 1987.** Appendices. (Appendix 1: Glossary of terms for layered intrusions & Appendix 2: Processes involved in the formation and development of layered igneous rocks.). In: Parsons, I. (ed.) *Origins of Igneous Layering.* D. Reidel Publishing Company, NATO ASI Series C 196, 641–656.
- Isophanni, M. 1976.** Porttivaaran ja Syötteen emäkisten kerrosintrusioiden sisäisestä sulfidialminmuodostuksesta Koillismaalla. M. Sc. Thesis, University of Oulu, Department of Geology. 122 p. (in Finnish)
- James, R. S., Jobin-Bevans, S., Easton, R. M., Wood, P., Hrominichuk, J. L., Keys, R. R. & Peck, D. C. 2002.** Platinum-Group Element Mineralization in Paleoproterozoic basic Intrusions in central and northeastern Ontario, Canada. In: Cabri, L. J. (ed.) *The Geology, Geochemistry, Mineralogy and Mineral Beneficiation of Platinum-Group Elements.* Canadian Institute of Mining, Metallurgy and Petroleum, Special Volume 54, 339–365.
- Jaupart, C. & Tait, S. 1995.** Dynamics of differentiation in magma reservoirs. *Journal of Geophysical Research* 100, 17615–17636.
- Jensen, L. S. 1976.** A new cation plot for classifying subalkalic volcanic rocks. Ontario Division of Mines, *Miscellaneous paper* 66. 22 p.

- Jones, A. P., Smith, J. V. & Dawson, J. B. 1982.** Mantle metasomatism in 14 veined peridotites from Bultfontein Mine, South Africa. *Journal of Geology* 90, 435–453.
- Juopperi, H. 1976.** Kuusijärvi-Lipeävaaran alueen kallioperä. M. Sc. Thesis, University of Oulu, Department of Geology. 87 p. (in Finnish)
- Juopperi, A. 1977.** The magnetite gabbro and related Mustavaara vanadium ore deposit in the Porttivaara layered intrusion, north-eastern Finland. Geological Survey of Finland, Bulletin 288. 68 p.
- Kalfoun, F., Ionov, D. & Merlet, C. 2002.** HFSE residence and Nb/Ta ratios in metasomatised, rutile-bearing mantle peridotites. *Earth and Planetary Science Letters* 199, 49–65.
- Karinen, T. 1998.** Posion Kuusijärven alueen stratigrafia ja rakennegeologia. M. Sc. Thesis, University of Oulu, Department of Geology. 110 p. (in Finnish)
- Karinen, T. & Salmirinne, H. 2001.** Koillismaan kerrosintruusiokompleksin läntisen osan geologin evoluutiomalli. Geological Survey of Finland, unpublished report M19/3543/2001/2. 19 p. + 1 appendix. (in Finnish)
- Karinen, T. & Iljina, M. 2009.** Structural history of the western part of the Koillismaa Layered Igneous Complex. In: Mitrofanov, F., Iljina, M. & Zhironov, D. (eds) *An Interreg-Tacis Project: Strategic Mineral Resources of Lapland - Base for the Sustainable Development of the North*. Project publication, volume II. Kola Science Center of Russian Academy of Sciences, 46–50.
- Kärki, A. 1995.** Palaeoproterozoic shear tectonics in the central Fennoscandian Shield, Finland. University of Oulu, *Res Terrae A* 10. 37 p.
- Kaulina, T. V. 1996.** Results of U-Pb dating of rock from the Tolstik Peninsula, northwestern region of the White Sea. In: Golubev, A. (ed.) *Problems of geology of the Karelia and Kola regions*. Petrozavodsk: Akademiya Nauk, Karel'skiy Nauchnyy Tsentr, 64–71. (in Russian)
- Kazanov, O. V. & Zaytseva, T. S. 1999.** Critical events in the ore-forming systems of layered intrusions. *Proceedings of the 5th Biennial SGA Meetings* 5. Society for Geology Applied to Mineral Deposits, 733–736.
- Kazanov, O. V., Koptev-Dvornikov, E. V., Berezovskaya, N. V., Bychkova, Y. V., Epifanova, T. A. & Pchelintseva, N. F. 2005.** The Oulanka (Olanga) Complex and related PGE deposits, Russian Karelia. In: Alapieti, T. T. & Kaukonen, R. J. (eds) *10th International Platinum Symposium*, August 8–11, 2005, Oulu. Field trip guidebook. Oulu University Press, University of Oulu. 31 p.
- Keays, R. R. & Campbell, I. H. 1981.** Precious metals in the Jimberlana Intrusion, Western Australia: Implications for the Genesis of Platiniferous ores in Layered Intrusions. *Economic Geology* 76, 1118–1141.
- Kelly, P. R., Campbell, I. H., Grey, I. E. & Gatehouse, B. M. 1979.** Additional data on loveringite (Ca, REE) (Ti, Fe, Cr)<sub>21</sub>O<sub>38</sub> and mohsite discredited. *Canadian Mineralogist* 17, 635–638.
- Kelsey, C. H. 1965.** Calculation of the C.I.P.W. norm. *Mineralogical Magazine* 34, 276–282.
- Kerkkonen, O. 1976.** Koillismaan emäksisten intrusiivien jalkapuolen reunavyöhykkeen sulfidimineralisaatio ja sen synty. M. Sc. Thesis, University of Oulu, Department of Geology. 80 p. (in Finnish)
- Kirkpatrick, R. J., Klein, L., Uhlmann, D. R. & Hays, J. 1979.** Rates and Processes of Crystal Growth in the System Anorthite-Albite. *Journal of Geophysical Research* 84, 3671–3676.
- Kirkpatrick, R. J. 1983.** Theory of nucleation in silicate melts. *American mineralogist* 68, 66–77.
- Kojonen, K. & Iljina, M. 2001.** Platinum-group minerals in the Early Proterozoic Kuusijärvi Marginal Series, Koillismaa Layered Igneous Complex, northeastern Finland. In: Piestrzynski, A. et al. (eds) *Mineral deposits at the beginning of the 21st century*. Proceedings of the joint Sixth Biennial SGA-SEG Meeting, August 26–29, 2001, Kraków, Poland, 649–652.
- Kouvo, O. 1977.** The use of mafic pegmatoids in geochronometry. Fifth European Colloquium of Geochronology, Cosmochronology and Isotope Geology, Pisa, September 5–10, 1977. Abstract. 1 p.
- Krogh, T. E., Davis, D. W. & Corfu, F. 1984.** Precise U-Pb Zircon and baddeleyite Ages for the Sudbury Area. In: Pye, E. G., Naldrett, A. J. & Giblin, P. E. (eds) *The Geology and Ore Deposits of the Sudbury Structure*. Ontario Geological Survey, Special Volume 1, 431–446.
- Kruger, F. J. & Marsh, J. S. 1982.** The significance of <sup>87</sup>Sr/<sup>86</sup>Sr ratios in the Merensky cyclic unit of the Bushveld Complex. *Nature* 298, 53–55.
- Kruger, F. J. & Marsh, J. S. 1985.** The Mineralogy, Petrology, and Origin of the Merensky Cyclic Unit in the Western Bushveld Complex. *Economic Geology* 80, 958–974.
- Kruger, F. J., Kinnaird, J. A., Nex, P. A. M. & Cawthorn, R. G. 2002.** Chromite is the Key to PGE. In: Boudreau, A. (ed.) *9th International Platinum Symposium*, July 21–25, 2002, Montana, USA. Extended abstract. 3 p.
- Kudryashov, N. M. & Balagansky, V. V. 1999.** U-Pb ages from Zhemchuznyi drusite massif in the Belomorian region (Russia): Geological implications. *Journal of Conference Abstracts* 4, European Union of Geosciences conference abstracts, p. 137.

- Lahti, S. & Honkamo, M. 1980.** Loukusa. Geological map of Finland 1:100 000, Pre-Quaternary Rocks, Sheet 3543. Geological Survey of Finland.
- Lahtinen, J. J. 1985.** PGE-bearing copper-nickel occurrences in the marginal series of the early Proterozoic Koillismaa layered intrusion, northern Finland. In: Papunen, H. & Gorbunov, G. I. (eds) Nickel-copper deposits of the Baltic Shield and Scandinavian Caledonides. Geological Survey of Finland, Bulletin 333, 161–178.
- Lahtinen, J. J., Alapieti, T. T., Halkoaho, T. A. A., Huhtelin, T. A. & Iljina, M. J. 1989.** PGE mineralization in the Tornio-Näränkäväära layered intrusion belt. In: Alapieti, T. T. (ed.) 5th International Platinum Symposium, August 4–11, 1989, Espoo, Finland. Guide to the post-symposium field trip. Geological Survey of Finland, Guide 29, 43–58.
- Lambert, D. D. & Simmons, E. C. 1983.** Platinum-Group Element Ore-Forming Process in Mafic Layered Intrusions: Geochemical Evidence From the Stillwater Complex, Montana. *Mining Engineering* 35, 1291–1297.
- Lambert, D. D., Morgan, J. W., Walker, R. J., Shirey, S. B., Carlson, R. W., Zientek, M. L. & Koski, M. S. 1989.** Rhenium-Osmium and Samarium-Neodymium Isotopic Systematics of the Stillwater Complex. *Science* 244, 1169–1174.
- Landén, L. 1999.** Koillismaan kerrosintruusiokompleksin yhteydessä esiintyvät felsiset kivilajit. M. Sc. Thesis, University of Helsinki, Department of Geology. 55 p. (in Finnish)
- Latypov, R. M. & Chistyakova, S. Yu. 2001.** Physicochemical Aspects of Magnetite Gabbro Formation in the Layered Intrusion of the Western Pansky Tundra, Kola Peninsula, Russia. *Petrology* 9, 24–45.
- Latypov, R. M. 2003a.** The origin of Marginal Compositional Reversals in Basic-Ultrabasic Sills and Layered Intrusions by Soret Fractionation. *Journal of Petrology* 44, 1579–1618.
- Latypov, R. M. 2003b.** The Origin of Basic-Ultrabasic Sills with S-, D-, and I-shaped Compositional Profiles by in Situ Crystallization of a Single Input of Phenocryst-poor Parental Magma. *Journal of Petrology* 44, 1619–1656.
- Latypov, R. M., Chistyakova, S. Yu. & Alapieti, T. T. 2008a.** Fine-grained mafic bodies as preserved portions of magma replenishing layered intrusions: the Nadezhda gabbro-norite body, Lukkulaivaara intrusion, Fennoscandian Shield, Russia. *Mineralogy and Petrology* 92, 165–209.
- Latypov, R. M., Chistyakova, S. Yu. & Alapieti, T. T. 2008b.** PGE reefs as an in situ crystallization phenomenon: the Nadezhda gabbro-norite body, Lukkulaivaara intrusion, Fennoscandian Shield, Russia. *Mineralogy and Petrology* 92, 211–242.
- Lauder, W. R. 1970.** Origin of the Merensky Reef. *Nature* 227, 355–356.
- Lauri, L. S. & Mänttari, I. 2002.** The Kynsijärvi quartz alkali feldspar syenite, Koillismaa, eastern Finland - silicic magmatism associated with 2.44 Ga continental rifting. *Precambrian Research* 119, 121–140.
- Lauri, L. S., Rämö, O. T., Huhma, H., Mänttari, I. & Räsänen, J. 2006.** Petrogenesis of silicic magmatism related to ~2.44 Ga rifting of the Archean crust in Koillismaa, eastern Finland. *Lithos* 86, 137–166.
- Leake, B. E. 1978.** Nomenclature of Amphiboles. *Mineralogical Magazine* 42, 533–563.
- Leake, B. E., Woolley, A. R., Arps, C. E. S., Birch, W. D., Gilbert, M. C., Grice, J. D., Hawthorne, F. C., Kato, A., Kisch, H. J., Krivovichev, V. G., Linthout, K., Laird, J., Mandarino, J., Maresch, W. V., Nickel, E. H., Rock, N. M. S., Schumacher, J. C., Smith, D. C., Stephenson, N. C. N., Ungaretti, L., Whittaker, E. J. W. & Youzhi, G. 1997.** Nomenclature of Amphiboles: Report of the Subcommittee on Amphiboles of the International Mineralogical Association Commission on New Minerals and Mineral Names. *Mineralogical Magazine* 61, 295–321.
- Le Bas, M. J., Le Maitre, R. W., Streckeisen, A. & Zanettin, B. 1986.** A Chemical Classification of Volcanic Rocks Based on the Total Alkali-Silica Diagram. *Journal of Petrology* 27, 745–750.
- Le Maitre, R. W. 1976.** Some Problems of the Projection of Chemical Data into Mineralogical Classifications. *Contributions to Mineralogy and Petrology* 56, 181–189.
- Le Maitre, R. W., Streckeisen, A., Zanettin, B., Le Bas, M. J., Bonin, B., Bateman, P., Bellieni, G., Dudek, A., Efremova, S., Keller, J., Lameyre, J., Sabine, P. A., Schmid, R., Sørensen, H. & Woolley, A. R. 2002.** *Igneous Rocks. A Classification and Glossary of Terms. Recommendations of the International Union of Geological Sciences Subcommission on the Systematics of Igneous Rocks.* Cambridge University Press. 236 p.
- Longhi, J., Wooden, J. L. & Coppinger, K. D. 1983.** The petrology of high-Mg dikes from the Beartooth Mountains, Montana: A search for the parent magma of the Stillwater Complex. *Journal of Geophysical Research* 88, B53–B69.
- Lorand, J.-P., Cottin, J.-Y. & Parodi, G. C. 1987.** Occurrence and petrological significance of loveringite in the Western Laouini layered complex, Southern Hoggar, Algeria. *Canadian Mineralogist* 25, 683–693.

- Maier, W. D., Barnes, S.-J., Gartz, V. & Andrews, G. 2003.** Pt-Pd reefs in magnetites of the Stella layered intrusion, South Africa: A world of new exploration opportunities for platinum group elements. *Geology* 31, 885–888.
- Maier, W. D., Gomwe, T., Barnes, S. J., Li, C. & Theart, H. 2004.** Platinum Group Elements in the Uitkomst Complex, South Africa. *Economic Geology* 99, 499–516.
- Mäkelä, T. 1975.** Emäksisen magman kiteytymisen ja differentiaatio Porttivaaran alueella, Koillismaalla. M. Sc. Thesis, University of Oulu, Department of Geology. 103 p. (in Finnish)
- Mangan, M. T. & Marsh, B. D. 1992.** Solidification Front Fractionation in Phenocryst-Free Sheet-Like Magma Bodies. *The Journal of Geology* 100, 605–620.
- Manhes, G., Allègre, C. J., Dupré, B. & Hamelin, B. 1980.** Lead isotope study of basic-ultrabasic layered complexes: Speculation about the age of the earth and primitive mantle characteristics. *Earth and Planetary Science Letters* 47, 370–382.
- Manninen, T., Pihlaja, P. & Huhma, H. 2001.** U-Pb geochronology of the Peurasuvanto area, northern Finland. In: Vaasjoki, M. (ed.) Radiometric age determinations from Finnish Lapland and their bearing on the timing of Precambrian volcano-sedimentary sequences. Geological Survey of Finland, Special Paper 33, 189–200.
- Mathez, E. A. 1995.** Magmatic metasomatism and formation of the Merensky reef, Bushveld Complex. *Contributions to Mineralogy and Petrology* 119, 277–286.
- Mathez, E. A., Hunter, R. H. & Kinzler, R. 1997.** Petrologic evolution of partially molten cumulate: the Atok section of the Bushveld Complex. *Contributions to Mineralogy and Petrology* 129, 20–34.
- Mathison, C. I. 1975.** Magnetites and ilmenites in the Somerset Dam layered basic intrusion, south-eastern Queensland. *Lithos* 8, 93–111.
- Mathison, C. I. 1987.** Pyroxene oikocrysts in troctolitic cumulates - evidence for supercooled crystallization and postcumulus modification. *Contributions to Mineralogy and Petrology* 97, 228–236.
- Matthess, S. & Schubert, W. 1971.** Der Original-Beerbachit im Odenwald, ein Amphibolit-Hornfels in Pyroxen-Hornfelsfazies. *Contributions to Mineralogy and Petrology* 33, 62–86.
- McBirney, A. R. & Noyes, R. M. 1979.** Crystallization and Layering of the Skaergaard Intrusion. *Journal of Petrology* 20, 487–554.
- McClay, K. R. & Campbell, I. H. 1976.** The structure and shape of the Jimberalana intrusion, Western Australia, as indicated by an investigation of the Bronzite Complex. *Geological Magazine* 113, 129–139.
- Mertanen, S., Pesonen, L. J., Huhma, H. & Leino, M. A. H. 1989.** Palaeomagnetism of the Early Proterozoic layered intrusions, northern Finland. Geological Survey of Finland, Bulletin 347. 40 p.
- Miller, C. 1974.** Reaction Rims between Olivine and Plagioclase in Metaperidotites, Ötztal Alps, Austria. *Contributions to Mineralogy and Petrology* 43, 333–342.
- Mitrofanov, F. P., Balagansky, V. V., Balashov, Yu. A., Gannibal, L. F., Dokuchaeva, V. S., Nerovich, L. I., Radchenko, M. K. & Ryungenen, G. I. 1995.** U-Pb age of gabbro-anorthosite massifs in the Lapland Granulite Belt. In: Roberts, D. & Nordgulen, Ø. (eds) *Geology of the eastern Finnmark - western Kola Peninsula region*. Norges Geologiske Undersøkelse, Special Publication 7, 179–183.
- Morimoto, N. 1988.** Nomenclature of pyroxenes. *Mineralogical Magazine* 52, 535–550.
- Morse, S. A. 1986a.** Thermal structure of crystallizing magma with two-phase convection. *Geological Magazine* 123, 205–214.
- Morse, S. A. 1986b.** Convection in aid of adcumulus growth. *Journal of Petrology* 27, 1183–1214.
- Morse, S. A. 1988.** Motion of crystals, solute, and heat in layered intrusions. *The Canadian Mineralogist* 26, 209–224.
- Mountain, B. W. & Wood, S. A. 1988.** Chemical Controls on the Solubility, Transport, and Deposition of Platinum and Palladium in Hydrothermal Solutions: A Thermodynamic Approach. *Economic Geology* 83, 492–510.
- Mutanen, T. 1976.** Koitelaisen malmitutkimukset. Geological Survey of Finland, unpublished report M19/3741/76/1/10. 45 p. + 8 appendices. (in Finnish)
- Mutanen, T. 1997.** Geology and petrology of the Akanvaara and Koitelainen mafic layered intrusions and the Keivitsa-Satovaara layered complex, northeastern Finland. Geological Survey of Finland, Bulletin 395. 233 p.
- Mutanen, T. & Huhma, H. 2001.** U-Pb geochronology of Koitelainen, Akanvaara and Keivitsa. In: Vaasjoki, M. (ed.) Radiometric age determinations from Finnish Lapland and their bearing on the timing of Precambrian volcano-sedimentary sequences. Geological Survey of Finland, Special Paper 33, 229–246.
- Myers, J. & Eugster, H. P. 1983.** The System Fe–Si–O: Oxygen Buffer Calibrations to 1500K. *Contributions to Mineralogy and Petrology* 82, 75–90.
- Naldrett, A. J., Gasparrini, E. C., Barnes, S. J., Von Gruenewaldt, G. & Sharpe, M. S. 1986.** The Upper Critical Zone of the Bushveld Complex and

- the Origin of Merensky-type Ores. *Economic Geology* 81, 1105–1117.
- Naldrett, A. J. 2004.** Magmatic Sulfide Deposits. *Geology, Geochemistry and Exploration*. Berlin-Heidelberg-New York: Springer. 668 p.
- Naslund, H. R. 1984.** Supersaturation and crystal growth in the roof-zone of the Skaergaard magma chamber. *Contributions to Mineralogy and Petrology* 86, 89–93.
- Nolan, K. M. & Morse, S. A. 1986.** Marginal rocks resembling the estimated bulk composition of the Kiglapait Intrusion. *Geochimica et Cosmochimica Acta* 50, 2381–2386.
- Ohenoja, V. 1968.** Porttivaaran ja Kuusijärven alueen kallioperä. M. Sc. Thesis, University of Oulu, Department of Geology. 88 p. (in Finnish)
- Page, N. J. 1979.** Stillwater Complex, Montana - Structure, Mineralogy, and Petrology of the Basal Zone with emphasis on the Occurrence of Sulfides. United States Geological Survey, Professional Paper 1038. 69 p.
- Page, N. J., Von Gruenewaldt, G., Haffty, J. & Aruscavage, P. J. 1982.** Comparison of Platinum, Palladium, and Rhodium Distributions in Some Layered Intrusions with Special Reference to the Late Differentiates (Upper Zone) of the Bushveld Complex, South Africa. *Economic Geology* 77, 1405–1418.
- Pang, K.-N., Zhou, M.-F., Lindsley, D., Zhao, D. & Malpas, J. 2008.** Origin of Fe–Ti Oxide Ores in Mafic Intrusions: Evidence from the Panzhihua Intrusion, SW China. *Journal of Petrology* 49, 295–313.
- Peck, D. C., Keays, R. R., James, R. S., Chubb, P. T. & Reeves, S. J. 2001.** Controls on the Formation of Contact-Type Platinum-Group Element Mineralization in the East Bull Lake Intrusion. *Economic Geology* 96, 559–581.
- Perttunen, V. & Vaasjoki, M. 2001.** U-Pb geochronology of the Peräpohja Schist Belt, northwestern Finland. In: Vaasjoki, M. (ed.) Radiometric age determinations from Finnish Lapland and their bearing on the timing of Precambrian volcano-sedimentary sequences. Geological Survey of Finland, Special Paper 33, 45–84.
- Piirainen, T., Hugg, R., Isohanni, M. & Juopperi, A. 1974.** On the geotectonics and ore forming processes in the basic intrusive belts of the Kemi-Suhanko, and Syöte-Näränkäväära. Geological Society of Finland, Bulletin 46, 93–104.
- Piirainen, T., Alapieti, T., Hugg, R. & Kerkkonen, O. 1977.** The marginal border group of the Porttivaara layered intrusion and related sulphide mineralization. Geological Society of Finland, Bulletin 49, 125–142.
- Piirainen, T., Hugg, R., Aario, R., Forsström, L., Ruotsalainen, A. & Koivumaa, S. 1978.** Koillismaan malmikirittisten aluiden tutkimusprojektin loppuraportti 1976. Geological Survey of Finland, Report of investigation 18. 51 p.
- Piispanen, R. & Tarkian, M. 1984.** Cu-Ni-PGE Mineralization at Rometölväs, Koillismaa Layered Igneous Complex, Finland. *Mineralium Deposita* 19, 105–111.
- Prendergast, M. D. & Keays, R. R. 1989.** Controls of platinum-group element mineralization and the origin of the PGE-rich Main Sulphide Zone in the Wedza Subchamber of the Great Dyke, Zimbabwe: implications for the genesis of, and exploration for, stratiform PGE mineralization in layered intrusions. In: Prendergast, M. D. & Jones, M. J. (eds) *Magmatic sulphides – Zimbabwe Volume*. London: The Institution of Mining and Metallurgy, 43–69.
- Posey, E. S. 2001.** Koillismaa Joint Venture, Finland - Interim Progress Report, August 15<sup>th</sup>, 2001. North Atlantic Natural Resources. 97 p. (unpublished)
- Puchtel, I. S., Hofmann, A. W., Mezger, K., Shchipansky, A. A., Kulikov, V. S. & Kulikova, V. V. 1996.** Petrology of a 2.41 Ga remarkably fresh komatiitic basalt lava lake in Lion Hills, central Vetryny Belt, Baltic Shield. *Contributions to Mineralogy and Petrology* 124, 273–290.
- Puchtel, I. S., Haase, K. M., Hofmann, A. W., Chauvel, C., Kulikov, V. S., Garbe-Schönerberg, C. -D. & Nemchin, A. A. 1997.** Petrology and geochemistry of crustally contaminated komatiitic basalts from the Vetryny Belt, southeastern Baltic Shield: Evidence for an early Proterozoic mantle plume beneath rifted Archean continental lithosphere. *Geochimica et Cosmochimica Acta* 6, 1205–1222.
- Ramdohr, P. 1980.** The ore minerals and their intergrowths. Oxford: Pergamon Press. 1207 p.
- Räsänen, J., Iljina, M., Karinen, T., Lauri, L., Salmirinne, H. & Vuollo, J. 2003.** Geological map of the Koillismaa area, northeastern Finland 1: 200 000. Geological Survey of Finland. (in electronic format, data available at the database of the Geological Survey of Finland, Rovaniemi)
- Rasilainen, K., Lahtinen, R. & Bornhorst, T. J. 2007.** The Rock Geochemical Database of Finland Manual. Geological Survey of Finland, Report of Investigation 164. 38 p.
- Rice, A. 2002.** Layered, PGE-Bearing Magma Chambers in a Single Pulse. In: Boudreau, A. (ed.) 9th International Platinum Symposium, July 21-25, 2002, Montana, USA. Extended abstract. 2 p.
- Rowell, W. F. & Edgar, A. D. 1986.** Platinum-Group Element Mineralization in a Hydrothermal Cu-Ni-

- Sulfide Occurrence, Rathbun Lake, Northeastern Ontario. *Economic Geology* 81, 1272–1277.
- Ruotsalainen, A. 1977.** Koillismaan intrusioiden rakenteen geofysikaalisesta tulkinnasta. M. Sc. Thesis, University of Oulu, Department of Geology. 64 p. (in Finnish)
- Săbău, G. & Alberico, A. 2003.** A new loveringite occurrence: oriented rods in garnet from the Foltea lherzolite, South Carpatians, Romania. *Acta Mineralogica-Petrographica, Abstract Series* 1, p. 92.
- Saini-Eidukat, B., Alapieti, T. T., Thalhammer, O. A. R. & Iljina, M. J. 1997.** Siliceous high-magnesium parental magma compositions of the PGE-rich early Palaeoproterozoic layered intrusion belt of northern Finland. In: Rongfu, P. (ed.) *Proceedings, 30<sup>th</sup> International Geological Congress* 9, 177–197.
- Saviaro, K. 1976.** Geofysikaalisia tutkimuksia Koillismaan gabrointrusioiden alueella. Ph. Lic. Thesis, University of Oulu, Department of Geology. 72 p. (in Finnish)
- Schiffries, G. M. 1982.** The Petrogenesis of a Platinumiferous Dunite Pipe in the Bushveld Complex: Infiltration Metasomatism by a Chloride Solution. *Economic Geology* 77, 1439–1453.
- Schissel, D., Tsvetkov, A. A., Mitrofanov, F. P. & Korchagin, A. U. 2002.** Basal Platinum-Group Element mineralization in the Fedorov Pansky Layered Mafic Intrusion, Kola Peninsula, Russia. *Economic Geology* 97, 1657–1677.
- Scoon, R. N. & Teigler, B. 1994.** Platinum-Group Element Mineralization in the Critical Zone of the Western Bushveld Complex: I. Sulfide Poor-Chromitites below the UG-2. *Economic Geology* 89, 1094–1121.
- Semenov, V. S., Beljatsky, B. V., Baltibaev, Sh. K., Glebovitsky, V. A., Koltsov, A. B. & Koptev-Dvornikov, E. V. 1998.** Fe-Ni-Cu sulfide and platinum mineralization in the Lukkulaivaara layered mafic intrusion (Northern Karelia, Russia). In: Laverov, N. P. & Distler, V. V. (eds) *International Platinum*. St. Petersburg – Athens: Theophrastus Publications, 79–91.
- Semenov, V., Klepinin, S., Koltsov, A. & Semenov, S. 2000.** The origin of the fine-grained rocks and PGE mineralization in the Lukkulaivaara Layered Intrusion (Northern Karelia, Russia). In: Kojonen, K., Carlson, L., Hölttä, P. & Lahti, S. (eds) *MSF Mini-Symposium*, June 11-17, 2000, Espoo, Finland. Geological Survey of Finland, Guide 48, 75–79.
- Sharpe, M. R. 1985.** Strontium isotope evidence for preserved density stratification in the main zone of the Bushveld Complex, South Africa. *Nature* 316, 119–126.
- Sharpe, M. R. & Hulbert, L. J. 1985.** Ultramafic Sills beneath the Eastern Bushveld Complex: Mobilized Suspensions of Lower Zone Cumulates in a Parental Magma with Boninitic Affinities. *Economic Geology* 80, 849–871.
- Sheraton, J. W. & Black, L. P. 1981.** Geochemistry and Geochronology of Proterozoic Tholeiite Dykes of East Antarctica: Evidence for Mantle Metasomatism. *Contributions to Mineralogy and Petrology* 78, 305–317.
- Silvennoinen, A. 1991.** Kuusamon ja Rukatunturin kartta-alueiden kallioperä. Summary: Pre-Quaternary rocks of the Kuusamo and Rukatunturi map-sheet areas. Geological Map of Finland 1:100 000, Explanation to the maps of Pre-Quaternary rocks, Sheets 4524, 4542 and 4613. Geological Survey of Finland. 62 p.
- Smith, D. 1970.** Mineralogy and Petrology of the Diabasic Rocks in a Differentiated Olivine Diabase Sill Complex, Sierra Ancha, Arizona. *Contributions to Mineralogy and Petrology* 27, 95–113.
- Söderholm, K. & Inkinen, O. 1982.** The Tornio layered intrusion - a recently discovered intrusion with chromitite horizons in Northern Finland. *Geological Society of Finland, Bulletin* 54, 15–24.
- Spencer, K. J. & Lindsley, D. H. 1981.** A solution model for coexisting iron-titanium oxides. *American Mineralogist* 66, 1189–1201.
- Stevens, R. E. 1944.** Composition of some chromites of the Western Hemisphere. *American Mineralogist* 29, 1–29.
- Stumpff, E. F. 1974.** The genesis of platinum deposits: Further thoughts. *Minerals Science and Engineering* 6, 120–141.
- Stumpff, E. F. & Rudlicke, J. C. 1982.** The Platinumiferous Dunite Pipes of the Eastern Bushveld. *Economic Geology* 77, 1419–1431.
- Stumpff, E. F. & Ballhaus, C. G. 1986.** Stratiform platinum deposits: New data and concepts. *Fortschritte der Mineralogie* 64, 205–214.
- Subcommittee on Pyroxenes 1989.** Nomenclature of Pyroxenes. *Canadian Mineralogist* 27, 143–156.
- Sun, S.-S. & McDonough, W. F. 1989.** Chemical and isotopic systematics of oceanic basalts: implications for mantle composition and processes. In: Saunders, A. D. & Norry, M. J. (eds) *Magmatism in the Ocean Basins*. Geological Society Special Publication 42, 313–345.
- Tarkian, M. & Mutanen, T. 1987.** Loveringite from the Koitelainen Layered Intrusion, Northern Finland. *Mineralogy and Petrology* 37, 37–50.
- Taylor, S. R. & McLennan, S. M. 1985.** *The Continental Crust: its Composition and Evolution*. Oxford: Blackwell Scientific Publications. 312 p.
- Tegner, C., Wilson, J. R. & Brooks, C. K. 1993.**

- Intraplutonic Quench Zones in the Kap Edward Holm Layered Gabbro Complex, East Greenland. *Journal of Petrology* 34, 681–710.
- Tegner, C. & Wilson, J. R. 1995.** Textures in a poikilitic olivine gabbro cumulate: evidence for supercooling. *Mineralogy and Petrology* 54, 161–173.
- Teertstra, D. K. & Sherriff, B. L. 1997.** Substitutional mechanism, compositional trends and end-member formulae of scapolite. *Chemical Geology* 136, 233–260.
- Thériault, R. D. & Barnes, S.-J. 1998.** Compositional variations in Cu-Ni-PGE sulfides of the Dunka Road deposit, Duluth Complex, Minnesota: The importance of combined assimilation and magmatic processes. *Canadian Mineralogist* 36, 869–886.
- Thériault, R. D., Barnes, S.-J. & Severson, M. J. 2000.** Origin of Cu-Ni-PGE Sulfide Mineralization in the Partridge River Intrusion, Duluth Complex, Minnesota. *Economic Geology* 95, 929–943.
- Todd, S. G., Keith, D. W., Le Roy, L. W., Schissel, D. J., Mann, E. L. & Irvine, T. N. 1982.** The J-M platinum-palladium reef of the Stillwater Complex, Montana: I. Stratigraphy and petrology. *Economic Geology* 77, 1454–1480.
- Tolstikhin, I. N., Dokuchaeva, V. S., Kamensky, I. L. & Amelin, Yu. A. 1992.** Juvenile helium in ancient rocks: II. U-He, K-Ar, Sm-Nd, and Rb-Sr systematics in the Monche Pluton.  $^3\text{He}/^4\text{He}$  ratios frozen in uranium-free ultramafic rocks. *Geochimica et Cosmochimica Acta* 56, 987–999.
- Turchenko, S. I., Semenov, V. S., Amelin, Yu. V., Levchenkov, L. A., Neymark, L. A., Buiko, A. K. & Koptev-Dvornikov, Je. V. 1991.** The Early Proterozoic riftogenic belt of Northern Karelia and associated Cu-Ni, PGE and Cu-Au mineralizations. *Geologiska Föreningens i Stockholm Förhandlingar* 113, 70–72.
- Turchenko, S. I. 1992.** Precambrian metallogeny related to tectonics in the eastern part of the Baltic Shield. *Precambrian Research* 58, 121–141.
- Väyrynen, H. 1954.** Suomen kallioperä, sen synty ja geologinen kehitys. Helsinki: Otava. 260 p. (in Finnish)
- Vermaak, C. F. 1976.** The Merensky Reef - Thoughts on its Environment and Genesis. *Economic Geology* 71, 1270–1298.
- Von Gruenewaldt, G. 1973.** The modified differentiation index and the modified crystallization index as parameters of differentiation in layered intrusions. *Transactions of the Geological Society of South Africa* 76, 53–61.
- Von Gruenewaldt, G. 1979.** A Review of some recent concepts of the Bushveld Complex, with particular reference to sulfide mineralization. *Canadian Mineralogist* 17, 233–256.
- Volborth, A., Tarkian, M., Stumpfl, E. F. & Housley, R. M. 1986.** A Survey of the Pd-Pt mineralization along the 35-km strike of the J-M Reef, Stillwater Complex, Montana. *Canadian Mineralogist* 24, 329–346.
- Vuollo, J. 1994.** Paleoproterozoic basic igneous events in Eastern Fennoscandian Shield between 2.45 Ga and 1.97 Ga, studied by means of mafic dyke swarms and ophiolites in Finland. University of Oulu, Acta Universitatis Ouluensis A 250. 47 p.
- Wadsworth, W. J. 1961.** The ultrabasic rocks of southwest Rhum. *Philosophical Transactions of the Royal Society of London B244*, 21–64.
- Wager, L. R. 1960.** The major element variation of the layered series of the Skaergaard intrusion and a re-estimation of the average composition of the hidden layered series and of the successive residual magmas. *Journal of Petrology* 1, 364–398.
- Wager, L. & Brown, G. 1967.** Layered Igneous Rocks. San Francisco: W. H. Freeman and Company. 588 p.
- Wang, L., Essene, E. & Zhang, Y. 1999.** Mineral inclusions in pyrope crystals from Garnet Ridge, Arizona, USA: implications for processes in the upper mantle. *Contributions to Mineralogy and Petrology* 135, 164–178.
- Watkinson, D. H. & Ohnenstetter, D. 1992.** Hydrothermal origin of platinum-group mineralization in the Two Duck Lake intrusion, Coldwell Complex, Northwestern Ontario. *Canadian Mineralogist* 30, 121–136.
- Wells, P. R. A. 1977.** Pyroxene Thermometry in Simple and Complex Systems. *Contributions to Mineralogy and Petrology* 62, 129–139.
- Wiebe, R. A. & Snyder, D. 1993.** Slow, dense replenishments of a basic magma chamber: the layered series of the Newark Island layered intrusion, Nain, Labrador. *Contributions to Mineralogy and Petrology* 113, 59–72.
- Williamson, J. H. 1968.** Least-squares fitting of a straight line. *Canadian Journal of Physics* 46, 1845–1847.
- Wilson, A. H. 1982.** The Geology of the Great “Dyke”, Zimbabwe: The Ultramafic Rocks. *Journal of Petrology* 23, 240–292.
- Wilson, G. 1988.** A critique of the normalization of PGE to 100 % sulphide. In: Macdonald, A. & Chery, M. (eds) *The Platinum Group of Elements in Ontario*. Ontario Geophysical Survey, Open File Report 5681, 173–176.
- Wilson, J. R. & Larsen, S. B. 1985.** Two-dimensional study of a layered intrusion - The Hyllingen Series, Norway. *Geological Magazine* 122, 97–124.
- Wilson, J. R. & Sørensen, H. S. 1996.** The Fongen-Hyllingen Layered Intrusive Complex, Norway. In:

- Cawthorn, R. G. (ed.) Layered Intrusions. Amsterdam-Lausanne-NewYork-Oxford-Shannon-Tokyo: Elsevier Science, 303–329.
- Wood, B. J. & Banno, S. 1973.** Garnet-Orthopyroxene and Orthopyroxene-Clinopyroxene Relationship in Simple and Complex Systems. *Contributions to Mineralogy and Petrology* 42, 109–124.
- Wood, S. C., Mountain, B. W. & Fenlon, B. J. 1989.** Thermodynamic constraints on the solubility of platinum and palladium in hydrothermal solutions: Reassessment of hydroxide, bisulfide, and ammonia complexing. *Economic Geology* 84, 2020–2028.
- York, D. 1969.** Least squares fitting of a straight line with correlated errors. *Earth and Planetary Science Letters* 5, 320–324.
- Zientek, M. L., Cooper, R. W., Corson, S. R. & Geraghty, E. P. 2002.** Platinum-Group Element Mineralization in the Stillwater Complex, Montana. In: Cabri, L. J. (ed.) *The Geology, Geochemistry, Mineralogy and Mineral Beneficiation of Platinum-Group Elements*. Canadian Institute of Mining, Metallurgy and Petroleum, Special Volume 54, 459–482.

## APPENDIX: DATA CD

- Appendix 1. Summary of isotopic ages of the early Palaeoproterozoic basic-ultrabasic intrusions in Finland.
- Appendix 2. Summary of isotopic ages of the early Palaeoproterozoic basic-ultrabasic intrusions in Russia.
- Appendix 3. Microprobe analyses of olivines.
- Appendix 4. Selected microprobe analyses of Ca-rich pyroxenes.
- Appendix 5. Selected microprobe analyses of Ca-poor pyroxenes.
- Appendix 6. Selected microprobe analyses of feldspars.
- Appendix 7. Selected microprobe analyses of amphibole group minerals.
- Appendix 8. Selected microprobe analyses of epidote group minerals.
- Appendix 9. Selected microprobe analyses of scapolite group minerals.
- Appendix 10. Selected microprobe analyses of phlogopite-biotites.
- Appendix 11. Selected microprobe analyses of chlorites.
- Appendix 12. Selected microprobe analyses of spinel group minerals.
- Appendix 13. Spinel classification parameters used in the thesis.
- Appendix 14. Selected microprobe analyses of ilmenites.
- Appendix 15. Selected microprobe analyses of garnets.
- Appendix 16. Selected microprobe analyses of lovozerites.
- Appendix 17. Selected microprobe analyses of rutiles, pseudobrookite, zircons and baddeleyites.
- Appendix 18. Selected microprobe analyses of apatites.
- Appendix 19. Selected microprobe analyses of principal base metal sulphides.
- Appendix 20. Selected analyses of accessory base metal sulphides.
- Appendix 21. Selected analyses of altaites, telluribismuthites and grains of an undefined mineral.
- Appendix 22. Selected analyses of PGE-minerals.
- Appendix 23. Chemical compositions of noncumulus-textured igneous rocks of the Koillismaa Intrusion area.
- Appendix 24. Chemical compositions of the Koillismaa Intrusion Marginal Series rocks.
- Appendix 25. Chemical compositions of the Koillismaa Intrusion Layered Series rocks.
- Appendix 26. Chemical compositions of the Koillismaa Intrusion Layered Series rocks and granophyre.
- Appendix 27. Detection limits.
- Appendix 28. Literature source for Figs 7.24 and 7.25.
- Geochemical analyses in 19 files.

www.gtk.fi  
info@gtk.fi



This study deciphers the genesis of a PGE-Cu-Ni sulphide-mineralized layer referred to as the Rometölväs Reef of the 2440 Ma old Koillismaa Intrusion.

The author concludes that the origin of the mineralization of the Rometölväs Reef was triggered by emplacement of dykes of a new magma pulse into partially consolidated cumulates of the Koillismaa Intrusion. These dykes are presently represented by the noncumulus-textured gabbronorite bodies of the reef.

ISBN 978-952-217-092-7 (paperback)

ISBN 978-952-217-093-4 (PDF)

ISSN 0367-522X



9 789522 170927